CONTENTS

FOREWORD

The main scope of the MEMSWAVE conference is to bring together scientists from different universities, research institutes, industrial companies interested in the development of the RF-MEMS field, to create a forum for the knowledge exchange between the RF-MEMS players, provide a qualified international forum for researchers and people from the industry, interested in the area and introduce to the most recent advances and achievements, especially on European activities.

The MEMSWAVE workshop was generated by the European project “Micromachined Circuites for Microwave and Millimeter Wave Applications” <<MEMSWAVE>> (1998-2001) coordinated by IMT-Bucharest. The project was nominated between the ten finalists (from 108 participants) to the Descartes Prize 2002.

The first 2 editions were organized at Sinaia (Romania) in 1999 and 2001. A special volume in the series Micro and Nanoengineering “Micromachined Microwave Devices and Circuits” of the Romanian Academy Press, was dedicated to the second edition of the workshop and was published in 2002.

Starting from 2002, the MEMSWAVE workshop is an itinerant European event and has become a reference point for the field, gathering interest from all over Europe and the rest of the world.

The next editions were held in Heraklion and Toulouse. From 2004 the MEMSWAVE workshop was connected to the European FP6 Network of Excellence in RF MEMS “AMICOM” and was strongly supported by this network. Most of the European teams involved in these challenging topics were partners in the AMICOM project. The workshop was organized in Uppsala (2004), Lausanne (2005), Orvieto (2006), Barcelona (2007) and became conference being important instruments for knowledge dissemination of the AMICOM network results.

In 2008 at Fodele, Greece, took place the first MEMSWAVE conference following the completion of AMICOM. In 2009, the conference was organized by the MemSRaD Research Group of the Fondazione Bruno Kessler (FBK), in 2010 by Universita del Salento, Lecce and in 2011 by University of Athens.

The conference is technically sponsored by the European Microwave Association (EuMA). However, the significant number of contribution has manifested the lasting support of the European RF MST community to this event.

It is now a tradition to publish the papers in the Series of Micro and Nanotechnologies of the Romanian Academy Press. Previous volumes may be requested at IMT-Bucharest (print@imt.ro). The present volume contains the papers presented at the 12th edition of the MEMSWAVE conference organized by University of Athens, in June 2011, in Athens, Greece.

The editors
May 2012

Reconfigurable RF-MEMS Circuits and Low Noise Amplifiers Fabricated Using a GaAs MMIC Foundry Process Technology

R. MALMQVIST[1], C. SAMUELSSON[1], A. GUSTAFSSON[1], D. SMITH[2], T. VÄHÄ-HEIKKILÄ[3], R. BAGGEN[4]

[1]Swedish Defence Research Agency (FOI), Olaus Magnus väg 42, SE-58330 Linköping, Sweden

[2]OMMIC, 22 Avenue Descartes-B.P. 11, 94453 Limeil-Brevannes, Cedex, France

[3]VTT Technical Research Centre of Finland, Tietotie 3, P.O. Box 1000, 02044 VTT, Espoo, Finland

[4]IMST GmbH, Carl-Friedrich-Gauss-Str.2, D-47475 Kamp-Lintfort, Germany

Abstract. We present key building blocks for monolithically integrated (*i.e.* single-chip) RF-MEMS enabled reconfigurable low-noise amplifiers and RF front-ends that have been fabricated on a GaAs wafer using a MMIC foundry process technology. Measured results of a tunable (frequency-agile) 16-24 GHz GaAs MMIC based RF-MEMS impedance matching network show 0.4 dB of minimum in-band insertion loss and an on-chip integrated wideband (unmatched) LNA circuit present 15-20 dB of gain together with 2 dB of noise figure at 6-26 GHz, respectively. Simulated results of a GaAs MEMS-MMIC based 15-20 GHz tunable (dual-band) LNA circuit show 12-17 dB and 2.5- 5.5 dB of in-band gain and noise figure, respectively.

1. Introduction

Today, there is an increasing interest in making RF systems self-adjusting or "cognitive" [1]. Such a unique ability is expected to lead to very efficient RF systems with reduced complexity, power and cost. Frequency-agile (tunable) frontend architectures using RF Micro Electro Mechanical Systems (MEMS) is an enabling technology proposed to achieve those highly attractive benefits. Reconfigurable MEMS circuits could be utilised to implement tunable (multi-band) Low Noise/Power Amplifiers (LNA/PA) and filters that can be commercially very attractive since such devices could be useful for different frequency bands and applications. For example, today's wireless RF systems for point-to-point communication can operate at many different frequencies (sub-bands) within the

5 to 40 GHz range and a use of such highly adaptive (frequency-agile) front-end components could result in a reduced system complexity and cost savings due to component re-use. By monolithic integration of RF-MEMS and MMICs, a higher degree of functionality would be possible, e.g. in active reconfigurable multi-band front-ends. RF-MEMS together with active RF-circuitry have so far with a few notable exceptions mostly been realized as hybrid circuits and also mainly up to 5-10 GHz (see e.g. [2-6]) which still leaves room for significant improvements to be made with respect to RF-performance, frequency range, functionality as well as to achieve reduced complexity (higher level of integration) and lower costs. To the best of our knowledge, the X-band switched dual-path PAs and LNAs reported in [2-3] are the first and to this date only real example of a successful monolithic integration of active RF devices with MEMS switches in a GaAs MMIC process.

In this paper, we build on our previous work described in [7] that presented experimental s-parameter data of two (10-16 GHz and 15-23 GHz) Co-Planar Waveguide (CPW) type of loaded-line RF-MEMS matching networks implemented on a 600 µm thick GaAs substrate. Different types of MEMS circuits together with monolithically integrated (on-chip) active devices have recently been fabricated by the foundry OMMIC (within the EC FP7 ICT project MEMS-4-MMIC) on a 100 µm thick GaAs wafer with via holes. Here, we will present a GaAs MMIC based 16-24 GHz reconfigurable MEMS matching network together with an on-chip 6-26 GHz (unmatched) LNA circuit that both were implemented as micro-strip designs to facilitate the monolithic integration of a GaAs MEMS tunable (dual-band) LNA. Such MEMS based frequency-agile MMICs can be regarded as a first step towards realising highly integrated (potentially single-chip) reconfigurable active microwave/mm-wave circuits and frontends. Fig. 1 shows an exemplary circuit schematic of a tunable LNA architecture using on-chip GaAs MEMS based reconfigurable input/output impedance matching networks.

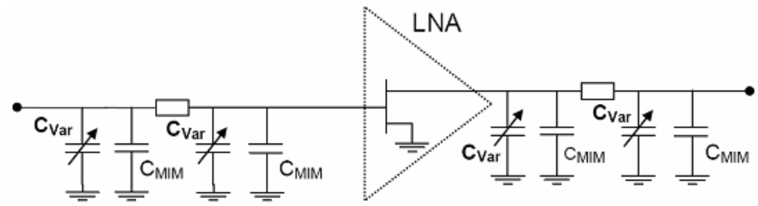

Fig. 1. Circuit schematic of a frequency-agile LNA architecture using on-chip GaAs RF-MEMS based reconfigurable impedance matching networks.

2. RF-MEMS Matching Networks and LNAS Fabricated Using a GaAs MMIC Foundry Process

Fig. 2 shows a photograph of a 1-bit loaded-line type of RFMEMS impedance matching network (top) and a wideband two-stage (unmatched) LNA circuit (bottom) with dimensions of 700 μm × 1100 μm and 1300 μm × 700 μm, respectively (incl. RF and DC pads). The ohmic contact type of MEMS switch used here was developed by OMMIC using a GaAs MMIC foundry process technology [8]. For the MEMS switches on the fabricated GaAs MMIC wafer that were used here the actuation voltage typically was found to vary between 20-40 V.

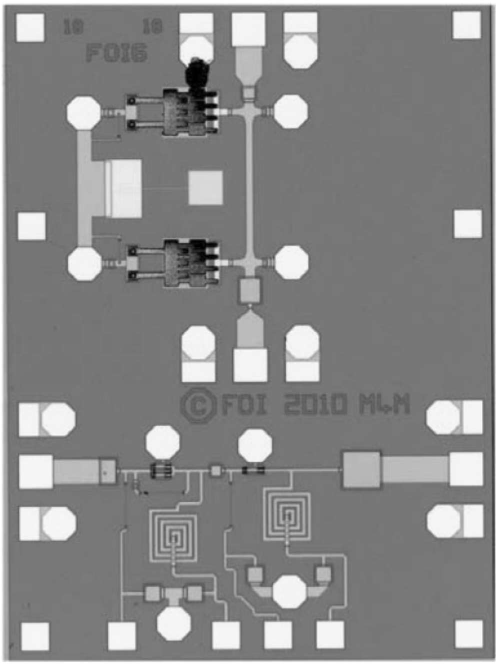

Fig. 2. Photograph of an RF-MEMS reconfigurable matching network (top) and a wideband (unmatched) LNA circuit (bottom) that have been fabricated on the same GaAs wafer using an MMIC foundry process technology.

Fig. 3 shows measured transmission (S_{21}) and input reflection (S_{11}) of the GaAs MMIC based 1-bit RF-MEMS input matching network shown in Fig. 2 when the two MEMS switches used were both switched ON (Down state) and OFF (Up state), respectively. The two possible tuning states shown here correspond to a centre frequency (f_c) for the input impedance matching that is equal to 16.2 GHz and 24.1 GHz, respectively (*i.e.* 40% tuning range). At the two frequencies, s_{11} and s_{21} are equal to -12.8 dB and -4.5 dB and -22.2 dB and -0.4 dB, respectively. The measured results of the reconfigurable matching network also compare relatively well with the corresponding EM-simulated data if we assume a contact resistance (R_{on}) of 4 Ω for the two MEMS switched used in parallel (the MEMS switch capacitance in the Up state Cup equal 10 fF). Simulations further indicate that it should be possible to achieve a low transmission loss for the MEMS matching network also within the Down state (*i.e.* when both switches are ON) if R_{on} would be reduced to 1-2 Ω (*i.e.* by obtaining an improved contact). This would then also result in a higher in-band small-signal gain and lower in-band Noise Figure (NF) of a tunable LNA that were using such types of RF-MEMS matching networks.

The experimental s-parameter data presented here were measured between 5-40 GHz due to the RF probes and the onchip calibration standard that were used in this case. Furthermore, the s-parameters of the GaAs RF-MEMS matching network were measured at two different RF input power levels (-25 dBm and 9 dBm, respectively). As is shown in Fig. 3, the measured RF performance of the GaAs MEMS matching network is largely the same at these two power levels thus indicating the relatively highly linear properties of this type of reconfigurable MEMS matching network.

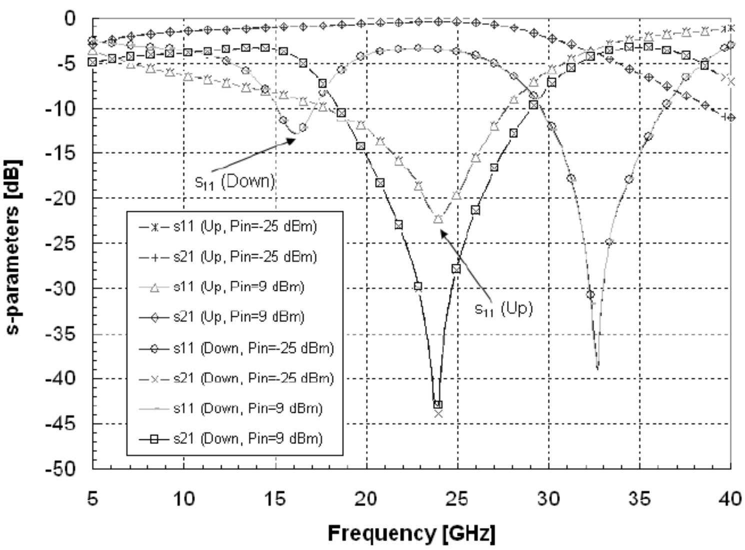

Fig. 3. Measured transmission S_{21} and input reflection S_{11} of a GaAs MMIC based 1-bit RF-MEMS input matching network when the two MEMS switches used were both switched ON (Down state) and OFF (Up state), respectively.

Fig. 4 shows measured s-parameter data and noise figure of the two-stage wideband (unmatched) LNA MMIC shown in Fig. 2. The LNA presents a gain of 15-20 dB at 6-26 GHz and NF=2 dB within this frequency range (NF could be measured up to 26.5 GHz due to a limitation with respect to the noise figure measurement equipment used). The (fixed) wideband LNA MMIC was intentionally made without any input and output impedance matching networks which explains the quite moderate values obtained for the LNA input and output return losses (S_{11} and S_{22} above of -8 dB at 5-40 GHz, respectively). The P_{DC} of the unmatched GaAs LNA MMIC was in this case equal to 60 mW. The measured results of the GaAs 1-bit MEMS matching network and unmatched LNA (see Fig. 3-4) have further been used in simulations to be able to predict the expected RF performance of a corresponding GaAs RF-MEMS based (single-chip) tunable LNA MMIC design.

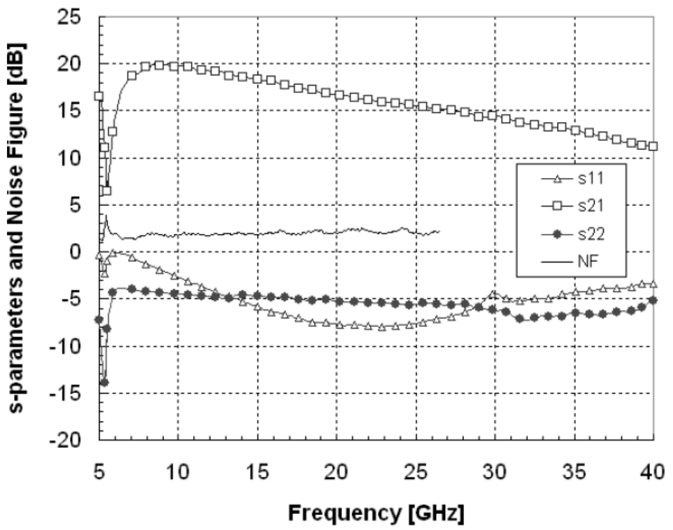

Fig. 4. Measured s-parameters and noise figure of a two-stage wideband (unmatched) LNA MMIC fabricated on the same GaAs wafer as a 1-bit RFMEMS matching network (see Fig. 2).

Fig. 5 shows simulated small-signal results of a tunable dualband LNA design based on the measured s-parameter data of a 1-bit GaAs MEMS input/output matching network and a wideband (unmatched) LNA circuit (both shown in Fig. 2). The two centre frequencies obtained for the tunable LNA correspond to when the two MEMS switches used within each MEMS matching network are either in the Up state or in the Down state, respectively (corresponding to the two tuning states shown in Fig. 3). The results show that it can be possible to achieve a high in-band tunable LNA gain (12-17 dB) together with relatively low values of return losses within the two frequency bands at 15 GHz and 20 GHz, respectively (corresponding to a tuning range of 29%). Measured data of a 1-bit GaAs MEMS matching network and a 6-26 GHz wideband (unmatched) LNA together with corresponding simulated results of a tunable dual-band LNA design are summarized in Table 1. Compared with simulated tunable LNA gain and NF at f_c=20 GHz, the in-band gain and NF is 5 dB lower and 3 dB higher at f_c=15 GHz which can be explained by the 3 dB higher measured losses of the GaAs MEMS matching network at this frequency when the two MEMS were activated (Down state). Simulations further indicate it should be possible to obtain a similar high in-band gain and low NF for a GaAs MEMS based tunable LNA circuit if the MEMS switch contact resistance could be made sufficiently small (R_{on}=1-2 Ω).

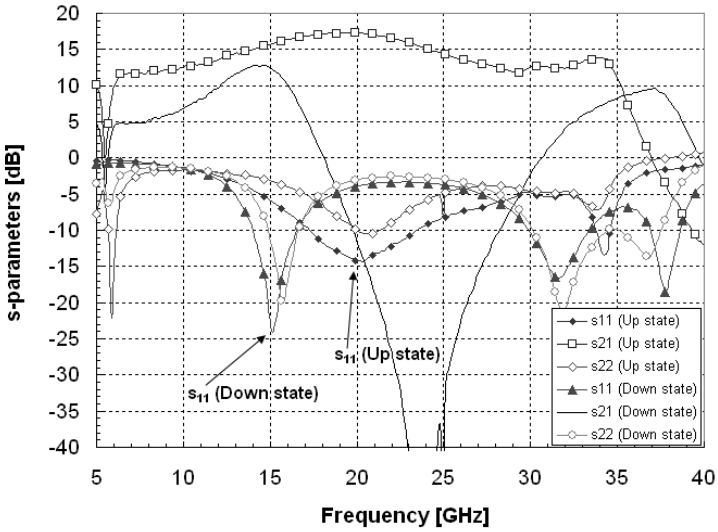

Fig. 5. Simulated s-parameters of a tunable dual-band LNA design based on the measured data of a 1-bit GaAs RF-MEMS (input/output) matching network and an unmatched LNA circuit (both shown in Fig. 2).

Table 1. Results of RF-MEMS and LNA circuits made on GaAs

Circuits	**Gain [dB]**	**Imput matching [dB]**	**NF [dB]**
MEMS matching network	-3.5(@ 15GHz) -0.6(@ 20GHz)	-10.0(@ 15GHz) -12.3(@ 15GHz)	N/A N/A
Wideband LNA	-18.3(@ 15GHz) -16.6(@ 20GHz)	-5.9(@ 15GHz) -7.7(@ 20GHz)	-1.9(@ 15GHz) -1.9(@ 20GHz)
Tunable LNA (sim.)	-12.3(@ 15GHz) -17.3(@ 15GHz)	-24.0(@ 15GHz) -14.8(@ 20GHz)	-5.5(@ 15GHz) -2.5(@ 20GHz)

3. Conclusion

We presented a frequency-agile 16-24 GHz 1-bit RF-MEMS matching network and a wideband (unmatched) LNA circuit that have been fabricated on the same GaAs substrate using a MMIC foundry process technology. The GaAs MEMS based matching network and unmatched LNA are both implemented as micro-strip designs to facilitate the monolithic integration of an RF-MEMS enabled tunable (dual-band) LNA MMIC. The 1-bit GaAs MEMS matching network has 0.4 dB of minimum in-band transmission loss (in the up state) and the on-chip integrated unmatched LNA design shows 15-20 dB of gain together with 2 dB of noise figure at 6-26 GHz, respectively.

Simulated results of a 15-20 GHz tunable dual-band LNA design (based on the measured data of the 1-bit GaAs MEMS input/output matching network and the unmatched LNA) show that it can be possible to achieve a high in-band gain of 12-17 dB and low values of return losses within the two frequency bands (corresponding to a tuning range of 29%). Simulations further indicate that the tunable LNA gain and noise figure at the lower frequency band (i.e. when all the MEMS switches used are in the down-state) are primarily limited by the MEMS switch contact resistance. The initial prototypes of GaAs RFMEMS based tunable MMICs presented in this paper can be regarded as a first step towards realising highly integrated (potentially single-chip) reconfigurable active microwave/mmwave circuits and front-ends.

References

[1] E.J. MARTINEZ, *Transforming MMIC's*, Proc. of the Gallium Arsenide Integrated Circuits Symposium 2002, 24th Annual Tachnical Digest, pp. 7–10, Oct. 2002.

[2] M. KIM, J.B. HACKER, R.E. MIHAILOVICH, and J.F. DeNATALE, A monolithic MEMS switched dual-path power amplifier, IEEE Microw. And Wireless Comp. Letters, **11**(7), pp. 285–286, July 2001.

[3] E.A. SOVERO, R. MIHAILOVICH, D.S. DEAKIN, J.A. HIGGINS, J.J. YAO,, J.F. DENATALE and J.H. HONG, *Monolithic GaAs PHEMT MMICs integrated with high performance MEMS microrelays*, Proc. of the 1999 Int. Microwave and Optoelectronics Conf., pp. 257–260, Aug. 1999.

[4] T. MUKHERJEE, and G.K. FEDDER, *RF-CMOS-MEMS based frequencyreconfigurable amplifiers*, IEEE Custom Integrated Circuit Conf. Dig., pp. 81–84, Sept. 2009.

[5] K. JOSHIN, Y. KAWANO, X. MI, O. TOYODA, T. SUZUKI, T. HIROSE and S. UEDA, *K-band CMOS-based power amplifier module with MEMS tunable bandpass filter*, *Proc. of the 5th European Microwave Integrated Circuits Conf.,* pp. 440–443, Sept. 2010.

[6] F. CRISPOLDI, A. PANTELLINI, S. LAVANGA, A. NANNI, P. ROMANINI, L. RIZZI, P. FARINELLI, and C. LANZIERI, *Full integrated process to manufacture RF-MEMS and MMICs on GaN/Si substrate*, Int. Journal of Microwave and Wireless Technlogies, **2**(3-4), pp. 333–339, 2010.

[7] R. MALMQVIST, C. SAMUELSSON, P. RANTAKARI, T. VÄHÄ-HEIKKILÄ, D. SMITH, J. VARIS, and R. BAGGEN, *RF MEMS and MMIC based reconfigurable matching networks for adaptive multi-band RF front-ends*, IEEE Int. Microw. Workshop Series on RF Front-ends for Software Defined and Cognitive Radio Solutions, pp. 77–78, Feb. 22-23, 2010.

[8] R. MALMQVIST, C. SAMUELSSON, W. SIMON, P. RANTAKARI, D. SMITH, M. LAHDES, M. LAHTI, T. VÄHÄ-HEIKKILÄ, J. VARIS, and R. BAGGEN, *Design, packaging and reliability aspects of RF MEMS circuits fabricated using a GaAs MMIC foundry process technology*, Proc. of the 40th European Microwave Conference, pp. 85–88, Sept. 2010.

Tunable Via-free Microstrip Composite Right/Left-Handed Transmission Lines Using MEMS Technology

Taeyoung KIM, Larissa VIETZORRECK

Technische Universität München, Lehrstuhl für Hochfrequenztechnik, Arcisstraße 21, 80333 München, Germany

Tel.:(+49) 89 289 23377

Abstract. In this contribution a tunable via-free microstrip composite right/left-handed transmission line (CRLH-TL) is designed and simulated. To add tunability RF MEMS elements are implemented in the interdigital capacitors and stub inductors, which match the line impedance during tuning. The via-free design enables easy and low-cost fabrication. Additionally, tunable zero-order resonators (ZORs) using two and three-cell CRLH-TL units, which have the resonant frequency tuning capability, are designed and simulated to verify the size-independent characteristic of ZORs.

1. Introduction

Metamaterials are of interest in order to realize novel components. They are artificial structures with electromagnetic properties not commonly found in nature. Typical realizations are three-dimensional structured materials containing cells with split-ring resonators (SRRs) or composite right/left-handed transmission lines (CRLH-TLs) [1]. But for those SRRs are based on the resonant phenomenon, their inherent drawbacks such as narrow bandwidth, high loss and fabrication difficulties limit the application to the microwave engineering. CRLH –TLs are a more practical approach, which are made up with additional series capacitance (C_L) and shunt inductance (L_L) other than unavoidable parasitic series inductance (L_R) and shunt capacitance (C_R) of the line as depicted in Figure 1. CRLH-TLs exhibit left-handed (LH) and right-handed (RH) behavior in the lower and upper frequency range. Since CRLH-TLs have unique characteristics such as negative phase constant, backward propagation and non-linear phase, many studies have been done to apply CRLH-TLs in various microwave engineering areas such as antennas, resonators and filters, etc.

Of increasing interest is the possibility to make those CRLH components tunable in order to provide various functionalities in one component. Many researchers have developed tunable CRLH-TLs to enhance their performance and widen its application areas by adding tunability. Those researches are mainly focused on changing the parameters of reactive loads, which have been realized with varactor diodes, pin-diodes or ferroelectric/superconductive materials. However those approaches suffer from high loss, poor yield, narrow tuning range, low operating frequency and low temperature condition for superconducting. Recently, Micro-Electro-Mechanical Systems (MEMS) are referred to be the best candidate which meet the challenging factors with low loss, high frequency operation, high linearity and virtually no power consumption, etc. Other features to be considered in the tuning of CRLH-TLs are impedance matching and balancing. In general, CRLH-TLs can only be matched in a restricted frequency band. However, as the formulae in Figure 1, when a purely right hand impedance (Z_R) and a purely left hand impedance (Z_L) are equal to the line impedance (Z_0), the CRLH-TLs are matched over an infinite bandwidth, which also allows balanced conditions where the shunt resonant frequency (ω_{sh}) is identical to the series one (ω_{se}). If only one load is tuned, the CRLH-TL, which is initially impedance matched and balanced, is no more matched and balanced, so at least two loading parameters should be tuned at the same time [2, 3].

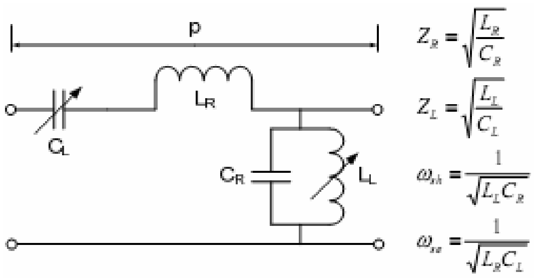

Fig. 1. Equivalent circuit of tunable CRLH unit cell with physical length p.

In this work, we propose a tunable CRLH-TL based on a microstip and monolithically integrated on a MEMS process. As conventional designs, the CRLH cell is designed by inserting tunable series capacitance (C_L) and shunt inductance (L_L) as in Figure 1. The cell simultaneously tunes C_L and L_L to account for the impedance change by reactive component change whereas many conventional ways are through tuning of only one component. Comparatively, a better matching is achieved. This is also advantageous to realize balanced CRLH-TLs, which is required to the specific application like broadband side radiating leaky wave antennas. The proposed structure is designed by a single planar metal layer and is via-free, which introduces low parasitic and loss besides simple fabrication process. By introducing radial stubs for grounding, we avoid the complex via penetrating process which deters cost effective fabrication. As another approach, the coplanar waveguide configuration, where the grounding is much easier for the ground conductors are same plane as signal's, can be considered, but it is not suitable for some applications like 2D texture surfaces [4, 5]. The MEMS elements in this study are based on the design by EADS Germany as reported in [6]. Compared to the conventional ones, they introduce low parasitic for their fabrication process and geometries are simple, which are advantageous to control and design.

2. Design and Simulation of Unit CRLH Cell

A. Tunable interdigital capacitor

In terms of the capacitance control, the Metal-Insulator-Metal (MIM) approach is more advantageous of realizing high capacitance due to the confined and dense electric field between metal electrodes. However, to avoid the fabrication complexity, we adopt planar interdigital capacitors (IC), which are easy to implement, as opposed to the MIM approaches which require complicated process. Figure 2 describes a tunable interdigital capacitor with two MEMS cantilever beams (IC1, IC2) for capacitance tuning. When the beam is down, the finger is more coupled with its neighboring finger, which leads to an increase of the capacitance. Likewise, the up-positioned beam decreases the capacitance. Consequently, an IC has maximum capacitance when all beams are down and minimum when they are in up-position. Unlike a normal switching operation, the beams in the IC have no contact parts, so are free of the contact problems. To achieve good impedance matching and balancing, the dimensions of IC are carefully determined by lumped element parameter extraction.

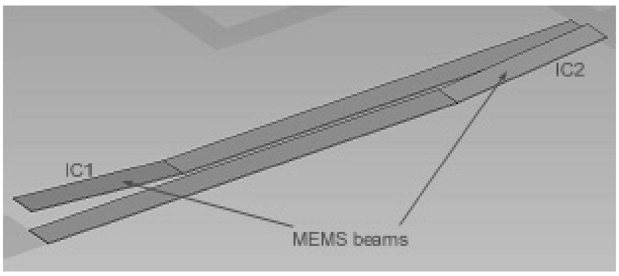

Fig. 2. Tunable interdigital capacitor.

B. Tunable stub inductor using radial stub

The tunable stub inductor is shown in Figure 3. Short circuited stubs which have three meander lengths make three different shunt inductances according to the state of six switches (RS1, RS2 and RS3). The switches are controlled by three signals. When a certain stub is connected to the main line, only two switches in one line are down whereas the other four switches are up. For stub grounding, a radial stub is introduced to avoid via-hole fabrication and achieve broadband operation, which also enables easy and cost effective fabrication.

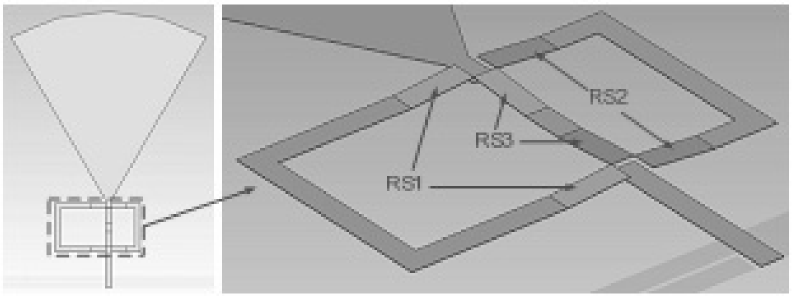

Fig. 3. Tunable stub inductor using radial stub.

C. Tunable CRLH cell

Figure 4 and Table 1 show the assembled CRLH unit cell and beam/switch state assignments to control it into three states while maintaining impedance matched and balanced conditions. In Figure 5(a), S_{21} parameters of CRLH lines with three CRLH-TL states are depicted through the simulation by CST Microwave Studio [7]. In the figure, we can see the frequency at which the phase of S_{21} is zero is changed for each state by 7.3, 8.2 and 9.6 GHz. Those frequencies are transition points between LH and RH regions on each state. The propagation constant (β) of one CRLH cell can be easily calculated from its ABCD parameter. For a reciprocal network which has the physical length p the following equation (1) is valid [8].

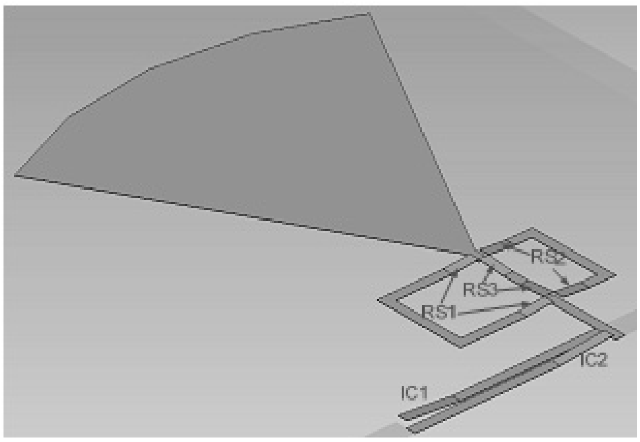

Fig. 4. Assembled CRLH unit cell.

Table 1. Beam/switch state assignments

	IC1	IC2	RS1	RS2	RS3
State 1	Down	Down	On	Off	Off
State 2	Up	Down	Off	On	Off
State 3	Up	Up	Off	Off	On

$$\alpha + j\beta = \frac{1}{p}\cosh^{-1}\frac{A+D}{2} \tag{1}$$

Generally, the right side term of (1) is a complex value and its imaginary part corresponds to the propagation constant β. Figure 5(b) shows calculated dispersion curves for each state. The figure depicts dispersion curve changes by reactive load tuning. At about 8 GHz, the wave propagates forward in state 1 (β>0). But in state 3 the propagation occurs in reverse direction (β<0) and even remains in the same position in state 2 (β=0). If our design frequency is 8 GHz, we can switch one state to another by changing beam/switch states. At other frequencies, we can still tune the propagation behavior just by the MEMS element state change without circuit modifications.

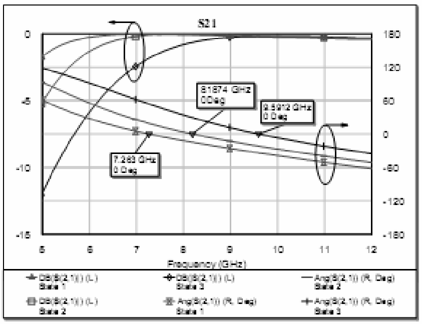

a)

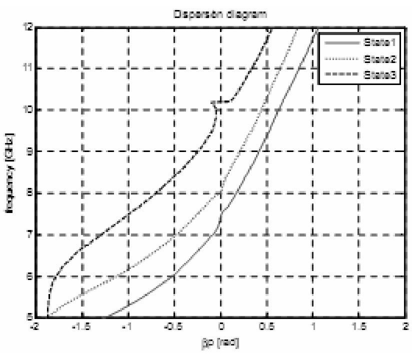

Fig. 5. (a) Magnitude and phase of S_{21} according to the state (b) Dispersion diagram.

Initially, all the states are designed to be always balanced regardless of tuning. However, state 1 and 2 are slightly unbalanced and clearly on state 3. This is mainly due to the loading parameter changes by element couplings, which is not considered in the parameter extraction before assembly. Moreover, compared to the reported CRLH design (mainly based on the Rogers material), the structure is much smaller and denser where a small coupling makes considerable changes to the loading parameters.

3. Zero Order Resonators

Open ended transmission lines produce standing waves due to the boundary condition and become resonators. The CRLH-TL resonators have unusual characteristics which allow negative and zero order resonant mode besides positive order operation as in normal transmission lines. The most interesting mode is zero order (β=0) where the CRLH-TL resonates at the infinite wavelength regardless of the transmission line length. In unbalanced case, it is shown that the resonant frequency of open ended resonators is determined by shunt components, which is different from the balanced frequency [1].

In Figure 6(a) open circuited CRLH-TL based ZORs of two- and three-cell configurations are shown. The cells are cross positioned to avoid radial stub overlap between cascading cells. On the same position of each cell, the switches are simultaneously controlled to get same loads. In Figure 6(b) it is observed that the resonating frequencies for each state are approximately the same regardless of the cell number, which verifies the zero order resonance.

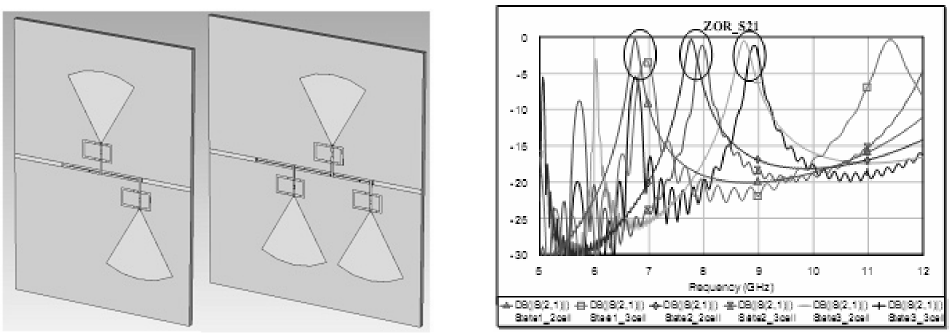

a) b)

Fig. 6. (a) ZORs with 2, 3 CRLH unit cells (b) S21 on each state.

4. Conclusion

Tunable via-free, single-layered microstrip CRLH-TLs using RF MEMS technology are designed and simulated. MEMS beams and switches are used for changing reactive loads, which simultaneously tunes series conductance and shunt inductance for impedance matching and CRLH balancing. According to the beam/switch states, the propagation mode of CRLH-TL is changed, which is investigated by β-ω dispersion curves. The exact matching and balancing are still a significant developing task. Two designs of ZOR are simulated and discussed to confirm the infinite wavelength resonant characteristic. The resonant frequencies are not a function of line length but of the loading elements which are controlled by MEMS elements.

References

[1] C. CALOZ, T. ITHO, *Electromagnetic Metamaterials: Transmission line Theory and Microwave Applications*, Wiley 2006.

[2] S. LIM, C. CALOZ, T. ITOH, *Metamaterial-based electronically controlled transmission-line structure as a novel leaky-wave antenna with tunable radiation angle and beamwidth*, IEEE Transactions on Microwave Theory and Techniques, **52**(12), pp. 2678–2690, Dec. 2004.

[3] Yi WANG, M.J. LANCASTER, F. HUANG, P.M. SUHERMAN, D.M. HOLDOM, T.J. JACKSON, *Superconducting Tunable Composite Right/Left-Handed Transmission Lines Using Ferroelectric Thin Films with a Resistive Bias Network*, Microwave Symposium, IEEE/MTT-S International, pp. 1415–1418, 3-8 June 2007.

[4] Sung-Hyun HWANG, Taehee JANG, Yong-Seung BANG, Jong-Man KIM, Yong-Kweon KIM, Sungjoon LIM, Chang-Wook BAEK, *Tunable composite right/left-handed transmission line with positive/negative phase tunability using integrated MEMS switches*, 2010 IEEE 23rd International Conference on Micro Electro Mechanical Systems (MEMS), pp.763–766, 24-28 Jan. 2010.

[5] G. NAGA SATISH, K.V. SRIVASTAVA, A. BISWAS, D. KETTLE, *A via-free left-handed Transmission Line with Radial Stubs*, Asia Pacific Microwave Conference, APMC 2009., pp.2501–2504, 7-10 Dec. 2009.

[6] C. SIEGEL, V. ZIEGLER, B. SCHOENLINNER, U. PRECHTEL, H. SCHUMACHER, *Simplified RF-MEMS Switches Using Implanted Conductors and Thermal Oxide*, The 1st European Microwave Integrated Circuits Conference, 2006, pp. 509–512, 10-13 Sept. 2006.

[7] CST GmbH, Germany, CST STUDIO SUITE

[8] David M. POZAR, Microwave engineering(3rd edition), Wiley 2005.

Waveguide-Mounted RF MEMS for Tunable W-band Analog Type Phase Shifter

D. PSYCHOGIOU[1], J. HESSELBARTH[1],
Y. LI[2], S. KÜHNE[2], C. HIEROLD[2]

[1]Laboratory for Electromagnetic Fields and Microwave Electronics (IFH)
[2]Group of Micro and Nanosystems (MNS) Swiss Federal Institute of Technology Zurich (ETH), 8092 Zurich, Switzerland

Abstract. A novel MEMS enabled W-band waveguide transmission phase shifter is presented. It consists of a ridge waveguide half-wavelength long resonator and an electrostatically actuated tilting micro-mirror MEMS. Operation is described as a distributed variable shunt capacitance realized by rotating, anti-parallel oriented MEMS conductive fingers. A deflection of the fingers of 0º…7.5º results in a phase shift variation of 0º…35 at 102GHz with an insertion loss of less than 0.73 dB.

1. Introduction

The specific properties of millimeter-waves enable the development of high-capacity communication links, high resolution imaging, radar and sensing systems. Millimeter-wave phase shifters are fundamental components of phased arrays and beam steering systems used in such applications.

W-band (frequency 75 GHz…110 GHz) phase shifters presented in the literature are typically based on switched transmission lines or variable capacitive loads using RF MEMS [1, 2]. Alternatively, the material properties of ferroelectrics and ferrites are tuned by external E-field or H-field, resulting in a phase shifting operation [3]. The first approach is limited by low power handling capability, high dissipation loss and discrete phase shift. In the second approach, continuous phase shift is feasible but leads to bulky structures and increased dissipated power due to the large dielectric loss of the materials.

Mounting the MEMS inside an air filled metal waveguide has the potential to overcome the obstacles mentioned above [4]. The waveguide-MEMS concept was first introduced in [5, 6] for the application of waveguide switches at frequencies up to 16 GHz.

A subsequent development showed a reflection-type W-band phase shifter based on a MEMS-tunable reflector using the high-impedance surface (HIS) concept [7]. When expressing phase shifter performance in terms of a figure of merit (FOM) defined by the ratio of maximum relative phase shift to the maximum insertion loss (degrees per dB), the HIS-based reflection phase shifter achieves a FOM of 68º/dB (based on simulated data given in [7]).

In this paper, we present a novel MEMS enabled W-band transmission phase shifter. The proposed device consists of a ridge waveguide resonator and an electrostatic actuated tilting micro-mirror MEMS as a tuning element placed beneath the ridge. Then, variation of transmission phase is achieved by means of a variable distributed capacitive loading of this resonant ridge waveguide section. The packaging concept proposes a multilayer circuit board (*e.g.*, LTCC) to accommodate the MEMS, covered a by three-dimensional ridge waveguide structure which can be produced by conventional and electron-discharge machining techniques.

2. Phase Shifter Concept

The variation of transmission phase by means of a variable shunt capacitor is limited by the effect of increased input reflection. For example, a shunt capacitor C in a transmission line environment of characteristic impedance Z (see Fig. 1a) and operating at frequency f, shows an input reflection S_{11} and transmission S_{21} of respectively:

$$S_{11} = \frac{-y}{2+y}, \quad S_{21} = \frac{2}{2+y}, \quad y = 2j\pi f CZ \tag{1}$$

From eq. (1), there is zero mismatch for C=0, whereas a larger C results in mismatch and increased transmission phase. Assuming a worst-case input reflection of –15 dB (corresponding to a worst-case insertion loss of –0.14 dB), the maximum achievable phase shift (that is, variation of transmission phase) is about 10.2º.

Phase shift can be increased at the cost of reduced frequency bandwidth, by placing the variable capacitor in a resonator. Then, the worst-case input reflection (and insertion loss) may occur at both the minimum and the maximum capacitance settings. For example, a half-wavelength transmission line resonator of characteristic impedance $Z_R \neq Z$, with a centered variable shunt capacitance, can be used as a transmission phase shifter. Example structures shown in Fig. 1b and Fig. 1c both realize about twice the maximum achievable phase shift, compared to the structure of Fig. 1a.

More complicated structures comprising variable shunt capacitors and transmission line sections can be envisaged. The structure shown in Fig. 1d, comprising of three variable shunt capacitors separated by two identical short transmission line sections, can realize a large maximum achievable phase shift. Assuming the center capacitance equaling n = 3.5 times one end-capacitance, the maximum achievable phase shift in transmission (for worst-case input reflection of −15 dB) is about 128º.

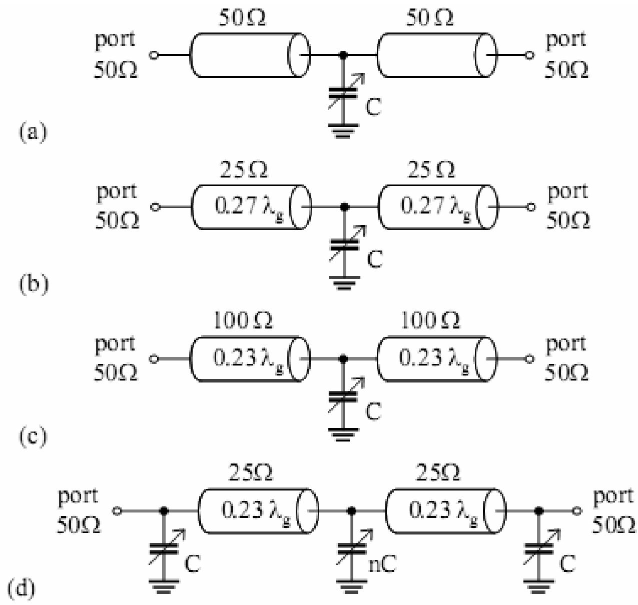

Fig. 1. Phase shifter equivalent circuits. For identical conditions (S11 below −15dB, S_{21} better than − 0.14dB), circuit (a) gives a transmission phase variation of about 10º, (b) and (c) each give about 20º, and (d) gives about 128º with n = 3.5.

Note that there is a tremendous increase of the transmission phase shift range between the structures of Fig. 1a,b,c and the one of Fig. 1d. The idea of the proposed waveguide-MEMS phase shifter is to approximate a structure shown in Fig. 1d using a single MEMS. The actuated part of this MEMS shall be large (that is, not small compared to the wavelength) such that its spatially distributed influence on the electromagnetic fields can indeed be approximated by the circuit of Fig. 1d.

The proposed MEMS chip is placed beneath the waveguide ridge as shown in Fig. 2. It consists of two sets of conductive fingers which are either set flat in the waveguide bottom wall, or rotate in an anti-parallel fashion out of the bottom wall plane and towards the ridge. By doing so, the distance between the respective ends of the fingers and the low-impedance ridge varies, forming the two outer variable capacitors of Fig. 1d. The part in the center of the fingers also moves with respect to the central part of the low-impedance ridge, thereby approximating the middle variable capacitor of the equivalent circuit of Fig. 1.

The length of a finger (and also the length of the low-impedance ridge section) is approximately slightly less than half a wavelength, thereby approximating the transmission line sections of the equivalent circuit of Fig. 1d.

The ridge waveguide is proposed to be formed from a three-dimensional machined part connected to the flat metalized surface of a circuit board (*e.g.*, LTCC). The MEMS chip is then placed in an open cavity of the circuit board. The connection between board and waveguide is helped by alignment pins and uses conductive glue. Bias wiring is embedded in the circuit board. Fig. 3 highlights this assembly concept.

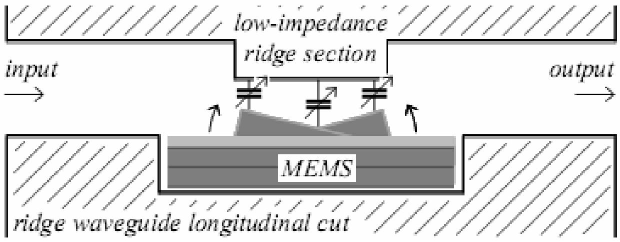

Fig. 2. Waveguide-MEMS phase shifter concept. Beneath a low-impedance ridge section of length of somewhat less than half a guided wavelength, two sets of conductive fingers rotate upwards in an anti-parallel fashion.Fig. 3.

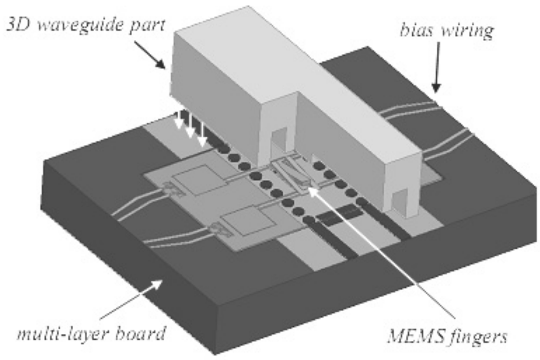

Fig. 3. Waveguide-MEMS assembly concept. The MEMS is located in an open cavity of a multi-layer circuit board. The machined waveguide part comes on top.

3. MEMS Design

RF-MEMS chip design is based on an electrostatic actuated tilting micro-mirror. In [8], the feasibility of an RF variable ratio power divider tuned by a double-side tilting micro mirror is shown. Here, a MEMS design based on bulk silicon micromachining and electrostatic actuation mechanism for a torsional mode of movement is proposed (Fig. 4). High aspect-ratio vertical comb drives and a polymeric SU8 spring allow for large static deflection (0º…7.5º) at low actuation voltage (30 V). A stack of 3 double side polished mono-crystalline Silicon (100) wafers (starting from top: device layer thickness 100 μm, stator layer 180 μm, handle layer 400 μm) and top and intermediate metallization layers are fabricated in a 5 mask process [8]. Specific features improve the RF performance and the phase shifter FOM:

- Geometry: two single-side micro-mirrors arranged in an interdigitated anti-parallel fashion. Such a configuration approximates a multiple-capacitor-loaded resonator. A large beam length keeps the micro-mirrors apart from the comb drive actuators. Accordingly, the chip size is 4 mm × 8 mm.
- Materials: highly conductivity Si is used (σ~75'000 S/m) so as to prevent excessive insertion loss due to E-field penetration into the chip. Low conductivity Si would allow the appearance of RF cavity resonances inside the MEMS chip, which would in turn increase dissipative RF loss.
- Functionality: single-side torsional actuation with a maximum tilt angle of 7.5º at 30 V.

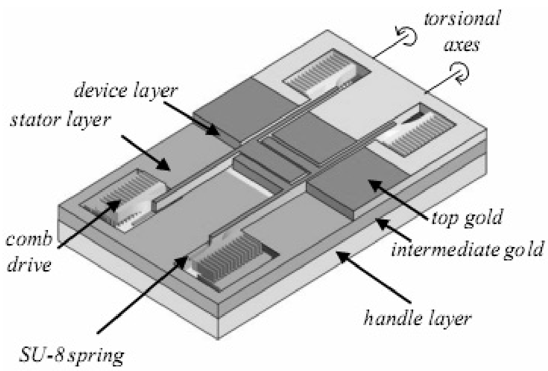

Fig. 4. Dual-axis tilting micro-mirror MEMS schematic.

4. Results and Discussion

The device was simulated using a finite element solver, Ansoft HFSS V13, taking into account all geometrical and material parameters. The simulation results are shown in Fig. 5. At 102 GHz, the maximum transmission phase shift is 35.5^0 with a maximum insertion loss of 0.73 dB.

The phase shift obtained is much smaller than the one obtained from the (idealized) equivalent circuit of Fig. 1d. It is, nevertheless, almost twice as large as expected from a lumped shunt capacitor equivalent circuit, such as shown in

Fig. 1b. This clearly shows that the distributed nature of the interaction of MEMS and electromagnetic field results in an increased performance.

Simulation of the different loss contributions show that more than half of the loss originates from the MEMS silicon. The use of higher conductivity silicon would reduce the loss and increase the FOM. Another significant loss contribution comes from electromagnetic energy channeling through the beam openings in the waveguide wall.

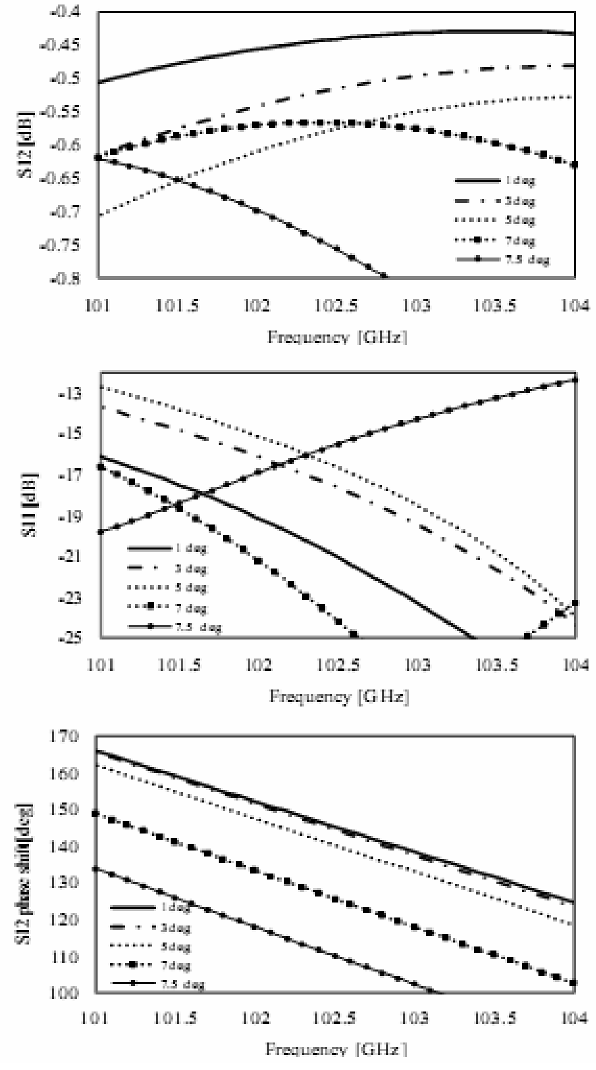

Fig. 5. Simulated phase shifter performance. At 102 GHz, input match is below –15 dB, transmission is above–0.73 dB, and the transmission phase variation is about 35.5º, resulting in a FOM of about 49º/dB.

5. Conclusion

A novel waveguide-MEMS transmission phase shifter is proposed. A tilting micro-mirror MEMS device with anti-parallel fingers realizes a variable distributed capacitive load to a ridge waveguide resonator. For a deflection angle varying between 0º and 7.5º, a transmission phase variation of 35.5º is obtained at an insertion loss of less than 0.73 dB at a frequency of 102 GHz, corresponding to a FOM of 49º/dB. A packaging concept based on a single metal 3D machined part placed on top of a structured multi-layer circuit board is proposed.

Acknowledgement–This work was supported in part by the Swiss National Science Foundation (SNF) under Grant 200021_129832.

References

[1] J.-J. HUNG, L. DUSSOPT, G.M. REBEIZ, *Distributed 2- and 3-bit W-band phase shifters on glass substrates*, IEEE Trans. Microw. Theory Tech., **52**(2), Feb. 2004.

[2] A. STEHLE, G. GEORGIEV, V. ZIEGLER, B. SCHOENLINNER, U. PRECHTEL, H. SEIDEL, U. SCHMID, *RF-MEMS switch and phase shifter optimized for W-band*, 38th Europ. Microw. Conf., EuMC, pp. 104–107, 2008.

[3] M.A. POPOV, I.V. ZAVISLYAK, G. SRINIVASAN, *Magnetic field tunable 75-110 GHz dielectric phase shifter*, Electronics Lett., 15th , **46**(8). Apr. 2010.

[4] J. HESSELBARTH, R. VAHLDIECK, *Concepts for waveguide-MEMS phase shifters*, Microwave Optical Techn. Lett., **52**(2), 5 May 2010.

[5] M. DANESHMAND, R.R. MANSOUR, N. SARKAR, *RF MEMS waveguide switch*, IEEE IMS Int. Microwave Symp., pp. 589–592, 2004.

[6] M. DANESHMAND, R.R. MANSOUR, *Multi-port MEMS-based waveguide and coaxial switches*, IEEE Trans. Microw. Theory Tech., **53**(11), Nov. 2005.

[7] D. CHICHERIN, M. STERNER, J. OBERHAMMER, S. DUDOROV, J. ABERG, A.V. RÄISÄNEN, *Analog type millimeter wave phase shifters based on MEMS tunable high-impedance surface in rectangular metal waveguide*, IEEE IMS Int. Microwave Symp., pp. 61–64, 2010.

[8] Y. LI, S. KÜHNE, D. PSYCHOGIOU, J. HESSELBARTH, C. HIEROLD, *Large deflection actuator for variable-ratio RF MEMS power divider application*, 21st Micromechanics and Microsystems Europe Workshop, Enschede, Sept. 2010.

MEMS-Based Frequency-Tunable Reflect-Line Phase Shifter

Fabrizio CONGEDO[1], Giuseppina MONTI[1], Luciano TARRICONE[1], Paola FARINELLI[2], Roberto SORRENTINO[2], Jacopo IANNACCI[3], Viviana MULLONI[3], Benno MARGESIN[3]

[1]University of Salento, Dept. Innovation Engineering, Via Monteroni, 73100, Lecce, Italy

[2]University of Perugia, Dept. of Electronic and Information Engineering, Via G. Duranti, 93 - I-06125 Perugia, Italy

[3]FBK-irst, MEMS Research Unit, Via Sommarive 18, 38050 Povo, Trento, Italy

Abstract. This paper presents a reflect-line phase shifter with a frequency reconfigurable behaviour. The proposed design approach uses Metal-Insulator-Metal (MIM) capacitors as loads of a branch-line coupler. The reconfigurability is obtained by means of RF-MEMS switches. Results referring to a 90° differential phase shifter able to work at two different frequencies (7.7 GHz and 9.76 GHz) are reported and discussed. It will be shown that the use of RF-MEMS switches combined with MIM capacitors results in compact dimensions and good performance in terms of bandwidth, thus demonstrating that the proposed approach is an optimum candidate for designing frequency reconfigurable phase shifters.

1. Introduction

Microwave Phase Shifters (PSs) are key elements of modern telecommunication systems [1], [2]. On the other hand, devices with a frequency reconfigurable behaviour are desirable. Accordingly, in this paper we present a reflection-type differential PS whose operating frequency can be tuned by means of RF-MEMS switches. The architecture of the proposed device is illustrated in Fig. 1: it consists of a 3-dB Branch Line Coupler (BLC) terminated with MIM-capacitors [3], [4]. Both the BLC and the MIM loads have been designed with a frequency reconfigurable behaviour.

In the literature, several approaches are available for designing BLCs with a reconfigurable frequency response [5]-[7]; among these, in [7] the electrical length of the BLC arms is modified by means of four varactor diodes. In this paper, in order to tune the BLC working frequency, MEMS switches in series with MIM capacitors are used instead of varactors (see Fig. 2a). Similarly, each load of the BLC coupled ports consists of a MIM capacitor selected by means of MEMS switches. Fig. 1 shows the schematic corresponding to the application of the proposed approach in order to design a differential PS with two possible operating frequencies; it can be observed that eight MIM capacitors, each one selected by a series MEMS switch, have been used. Similarly, N possible operating frequencies can be obtained by using 6-N 4 MIM capacitors and the same number of series MEMS switches.

2. Simulated Risults

As an example of application of the proposed approach, we design a PS able to exhibit a 90° differential phase shift at two different frequencies: 9.76 GHz and 7.33 GHz. Referring to Fig. 1, we first optimized the MIM capacitances from C_1 to C_4 in order to ensure the BLC frequency reconfigurabilty; consequently, we optimized the MIM capacitances from C_5 to C_8 in order to ensure the 90° Differential Phase Shift (DPS). More in detail, C_5 and C_7 determine the DPS at 9.76 GHz, whereas C6 and C8 determine the DPS at 7.33 GHz.

The schematic obtained this way has been implemented in coplanar waveguide technology on a 525 μm high-resistivity Silicon substrate within the 8-masks MEMS realization process available at FBK laboratories [8]. The corresponding layout is illustrated in Fig. 2a; the insert shows the dimensions of the series MEMS switches which have been designed according to the process described in [8]. Table 1 summarizes the switch configurations at the two operating frequencies. The layouts corresponding to these configurations have been analysed by means of full-wave simulations; results obtained this way are given in Figs. 3-4.

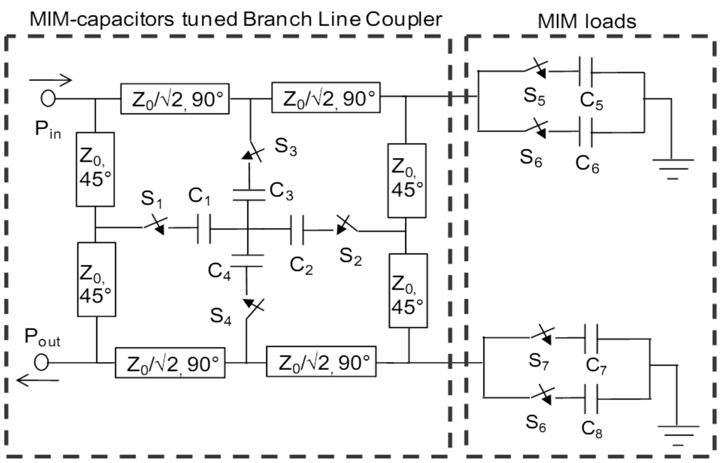

Fig. 1. Schematic representation of the proposed frequency reconfigurable PS.

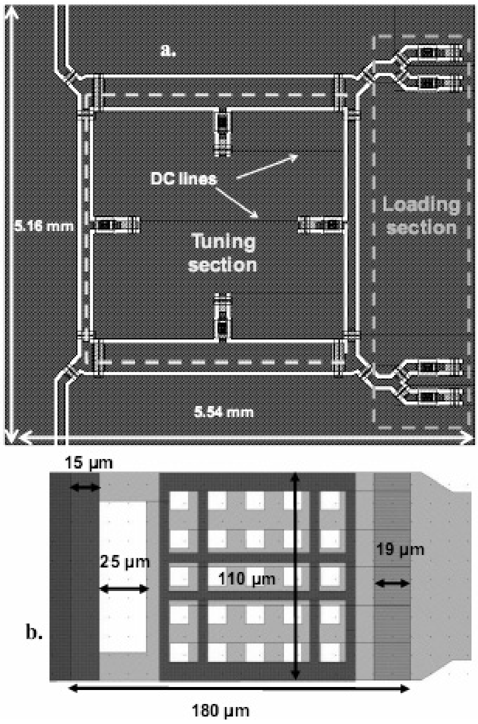

Fig. 2. Layout of the proposed frequency tunable PS (a.). MEMS switch layout and dimensions (b.).

It is evident that good performance have been obtained at both working frequencies.

The calculated differential phase shift is 90.024° at 9.76 GHz (relative phase error equal to 0.03%) and 89.716° at 7.33 GHz (relative phase error equal to 0.3%). Furthermore, from Fig. 2a it can be noticed that the proposed device occupies a very compact area (5.54×5.16 mm^2).

Table 1. Combination of the switch configurations Corresponding to the two working frequencies.

Switch	Frequency	
	9.76 [GHz]	**7.33 [Ghz]**
S_1	Off	On
S_2	Off	On
S_3	Off	On
S_4	Off	On
S_5	On/Off	Off
S_6	Off	On/Off
S_7	On/Off	Off
S_8	Off	On/Off

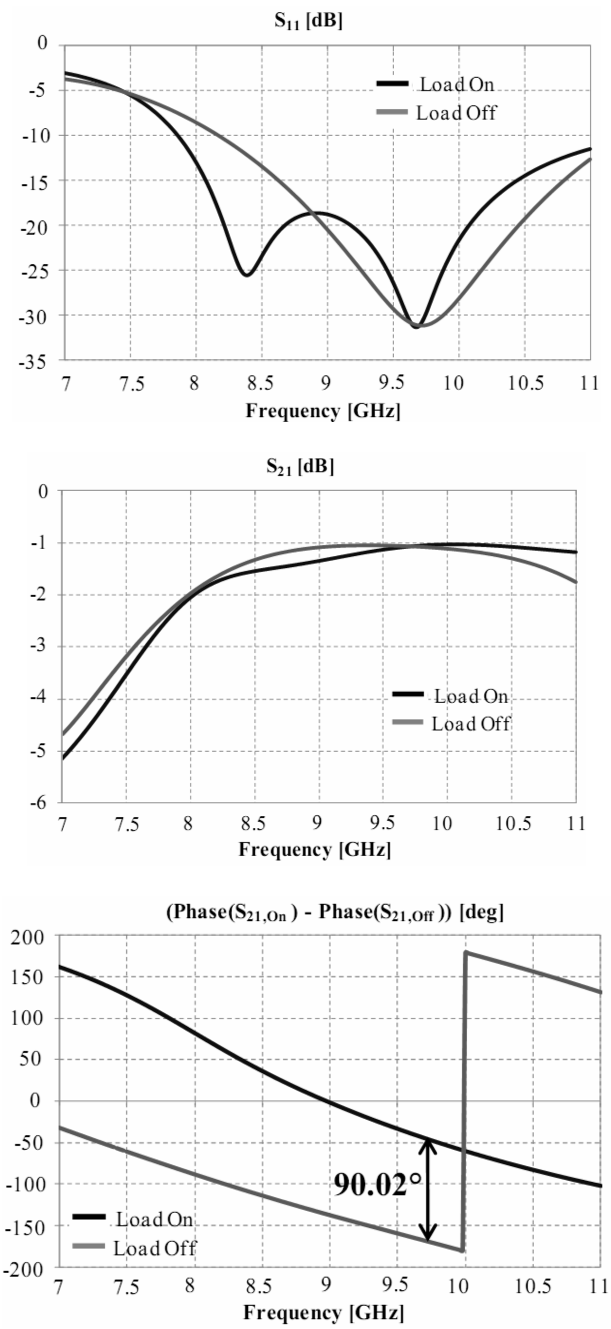

Fig. 3. Numerical results calculated for the proposed PS when the switch combination is the one corresponding to the 9.76 GHz operating frequency.

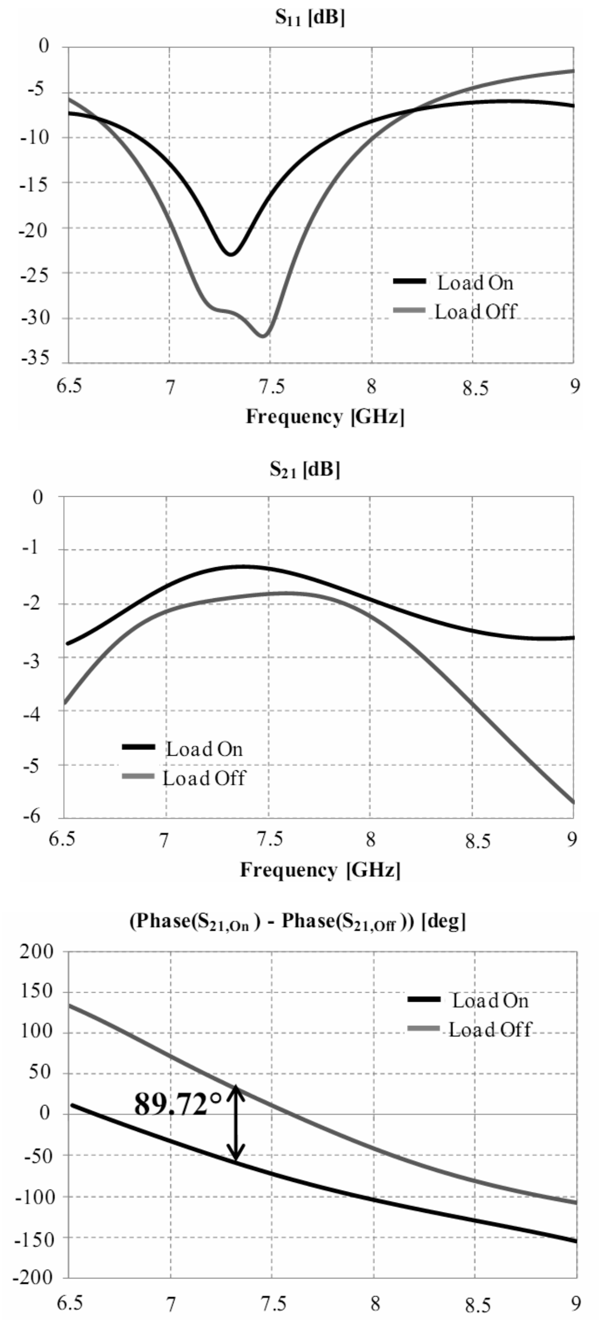

Fig. 4. Numerical results calculated for the proposed PS when the switch combination is the one corresponding to the 7.33 GHz operating frequency.

Acknowledgement. This work was supported by OPTEL (Consorzio Nazionale di Ricerca per le Tecnologie Optoelettroniche dell'InP) in the framework of the MUR funded project "Tecnologie Abilitanti di nuova generazione per Sistemi di trasmissione e ricezione a Microonde".

References

[1] S. KOUL and B. BHAT, *Microwave and Millimeter Wave Phase Shifters*, Norwood, MA: Artech, 1991.

[2] G.M. REBEIZ, *RF MEMS Theory, Design, and Technology*, New York: Wiley, 2003.

[3] M.H. KORI and S. MAHAPATRA, *Switched reflection phase shifter*, Electronics Letters, **22(**10), pp. 550–551, May 1986.

[4] C.-S. LIN, S.-F. CHANG and W.-C. HSIAO, *A full-360° reflection-type phase shifter with constant insertion loss*," IEEE Microwave and Wireless Components Letters, **18**(2), pp. 106–108, Feb. 2008.

[5] Chul-Soo KIM, Jun-Seok PARK, Dal AHN and Jae-Bong LIM, *Variable directional coupler with LC resonator*, Electronics Letters, **36**(18), pp. 1557–1559, August 2000.

[6] D. DRASKOVIC and D. BUDIMIR, *An optically reconfigurable dual-band branch-line coupler with artificial transmission lines*, in Proc. of IEEE Antennas and Propagation Society International Symposium, San Diego, CA, pp. 1–4, 5-11 July 2008.

[7] E.A. FARDIN, K. GHORBANI and A.S. HOLLAND, *A varactor tuned branch-line hybrid coupler*, in Proc. of APMC2005, 4-7 Dec. 2005.

[8] A. OCERA, P. FARINELLI, F. CHERUBINI, P. MEZZANOTTE, R. SORRENTINO, B. MARGESIN, F. GIACOMOZZI, *A MEMS reconfigurable power divider on high resistivity silicon substrate*, in Proc. of the IEEE MTT-S International Microwave Symposium, Honolulu, pp. 501–504, 3-8 June 2007.

9.6-11.7 GHz Analogically Tuned Band Stop Filter Based on RF-MEMS Varactors

David MARDIVIRIN, Fabien BARRIÈRE, Arnaud POTHIER, Aurélian CRUNTEANU, Pierre BLONDY

XLIM Research Institute – UMR 6172, Université de Limoges / CNRS, 123 Avenue Albert Thomas, 87060 Limoges Cedex, France

Abstract. Tunable 9.6 GHz to 11.7 GHz bandstop filters are presented. Tuning is done using RF MEMS structure with analogical capacitance variation, from 25 fF to 225 fF [1]. Filter is designed with ring resonators coupled on a 50 Ohms micro-strip transmission line. To optimize microwave performances, a 2 pole is presented with a half-wave line arranged between two resonators with a zero refection mode. This configuration permits to enhanced rejection and minimizes the out of band losses. The measured performances are -35 dB of rejection at 9.6 GHz, shifting to -42 dB at 11.7 GHz. The losses below the rejected band are less than -1 dB. This device has also been measured under variable RF power and has shown handling at 6 W.

1. Introduction

MEMS technology is an attractive solution for microwave component switching and tuning. For instance, micro-electromechanical analog tunable capacitors enable wide tuning ranges and high quality factors, compared to the existing solid state varactors, which typically have small tuning ratios, high resistive losses and low self-resonances. Due to their superior RF performance (low loss, low power and low intermodulation distorsion), RF MEMS have been used in different RF circuit applications: tunable microwave filters [2], tunable phase shifters [3] and tunable antennas. One type of tunable filter that is very important in RF receivers for communication and radar systems is the bandstop filter.

In this work, RF MEMS are used as analog varactors, to change the operating frequency of a band reject filter. MEMS based tunable split ring resonator can be easily tuned using a variable capacitor since the arms of the ring are in opposite phase. Using 2 pole filters, the performances at the working frequency can be improved, with the 2 pole tuned at the same frequency. Also, the filtered can be widened, by appropriate separate tuning of the resonators. For band stop filter applications, the use of ring resonators designs also permits to improve the filter performances along with tuning, as the electromagnetic energy can be coupled using a magnetic field coupling inside the ring. This device has also been measured under variable RF power.

2. Tunable Band Stop Filter

The band stop filter developed is designed on 50 Ohms micro-strip waveguide, on a 530 µm fused silica substrate with a 400 nm AlN dielectric insulating layer. The design of this filter is shown on Fig. 1.

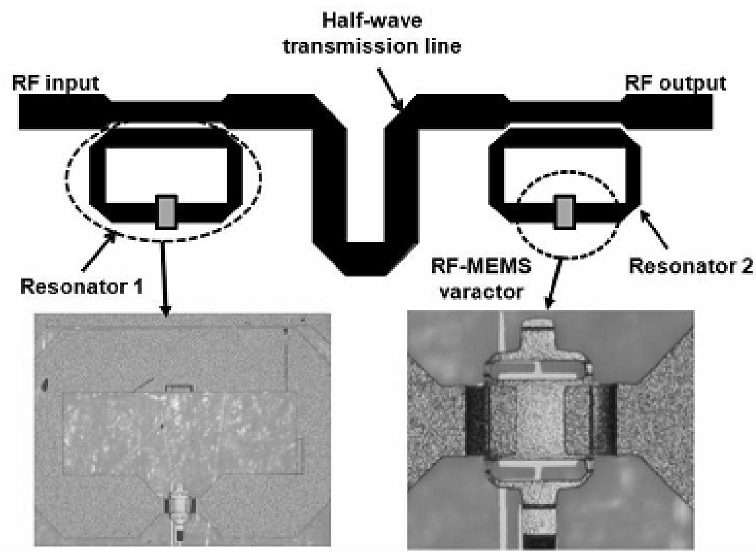

Fig. 1. Design of the 2 pole tunable X-band rejecter filter based on RF-MEMS varactor.

The filter rejection is made with ring resonators. There are two of these as the filter operates with 2 pole. The operating frequency of these resonators without loading is 12 GHz, changed by the charged impedance presented by the RF-MEMS varactors. The RF-MEMS used is based on a technology development already presented in [1]. It is composed of an electroplated gold bridge raised above an actuation electrode made in chromium, and an aluminum nitride dielectric layer. The microwave input and output are standing above the bridge, with an air gap between both. The varactor corresponds to two capacitance in series located at the RF input of the bridge (metal-air-metal capacitance), and the same with the output. These two capacitances will decrease by applying bias, which reduce the bridge height, and increase the distance with microwave inputs.

These tuning devices are located at the opposite of the micro-strip line (on the rings), where the accumulated EM field is maximum. This permits to maximize the effect of tuning devices on the filter. The two rings are arranged in series with a half-wave line between them (9 GHz). This disposition is used to create two reflections zero, which reduces losses outside of the rejected band. A second zero reflection point exists for the frequency of 12 GHz, due to combination of this half-wave line with the resonators.

Two types of application on this filter can be considered. On the one hand, the two pole are working at the same frequency, and so, the rejected performance is enhanced with high selectivity. On the other hand, the two poles can be adjusted on near frequencies, so the rejection bandwidth is improved.

This design had been simulated under ADS MOMENTUM software, and compared with measurement, for each pole centered at 10.95 GHz, on Fig. 2.

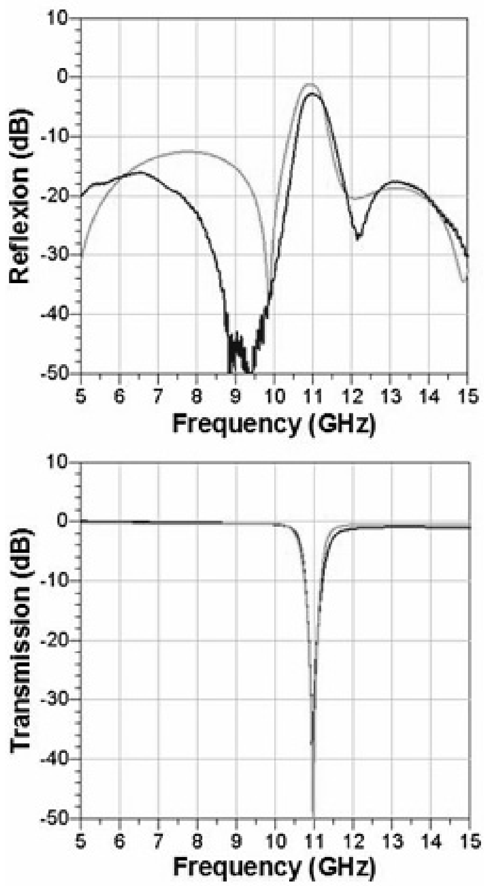

Fig. 2. Microwave simulation of the filter (red) and measurement (blue).

Thus, this design of filter shows potential rejection performances better than -50 dB rejected at 11 GHz. The measurements show rejection of -42 dB.

3. Measurements

The filter has been realized, and measured with the 2 pole working at the same frequency. A picture of the filter in its package is shown on Fig. 3.

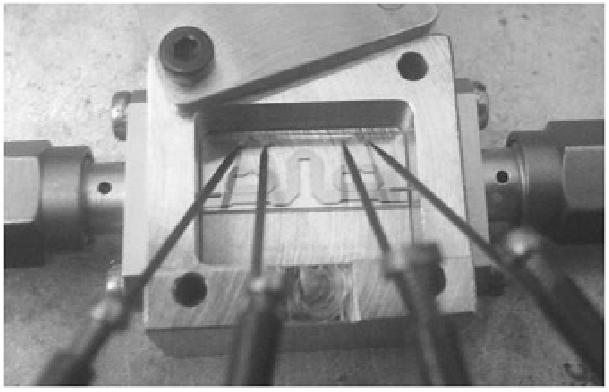

Fig. 3. Photography of the filter set in case with SMA connection accesses.

The microwave signal is brought with two SMA connectors, and the bias is applied with external pads on the filter. On the picture, two bias signals are applied using DC probes on the two varactors. In the final development of this device, bias will be applied using a specific plug system. Reflection and transmission performances are shown on Fig. 4.

We can see the influence of the two zero reflection points at 9.5 GHz and 12 GHz. The first of these permits to enhance the return loss with increasing working frequency, up to -30 dB at 9.6 GHz (with rejection set at 10.8 GHz). The 12 GHz zero reflection point permits to have return loss under -16 dB between 12 GHz and 12.5 GHz.

In transmission, this filter shows tunability on X-band between 9.6 GHz to 11.7 GHz. This tunability allows rejecting all possible frequencies in this frequency band, since the matching devices (RF-MEMS varactors) are analogically actuated. The isolation due to rejection are from -35 dB at 9.6 GHz, improved to -42 dB at 11.7 GHz. Performances are better for higher frequencies because the resonator are design at 12 GHz (considering no bridges), also measured at 12.2 GHz. The bandwidth measured for -20 dB rejection increases from 50 MHz at 9.6 GHz, to 250 MHz rejected at 11.7 GHz operating frequency.

Another essential point on this design concerns insertion losses outside the rejected band. Using the two zero reflection points seen before, these are limited to low values. This is presented in Fig. 5.

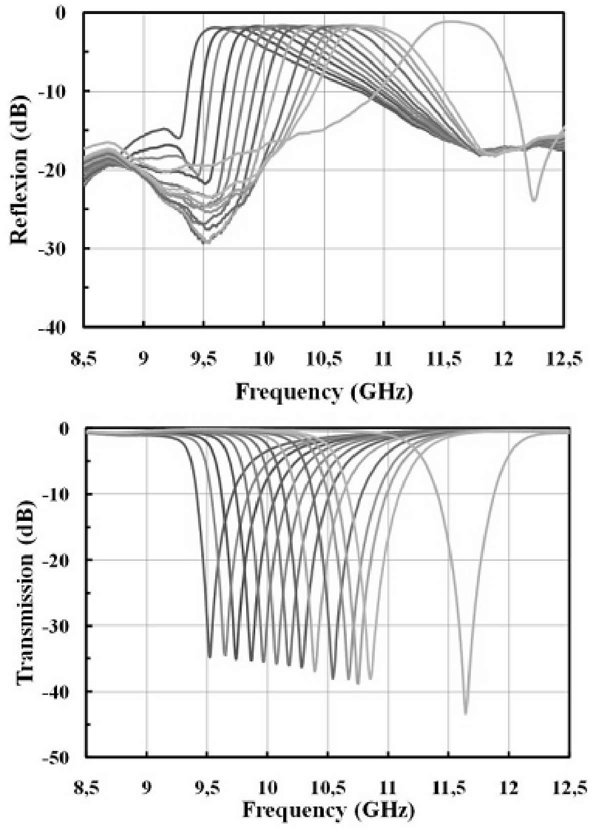

Fig. 4. Microwave performances of the filter, on top the reflection, and down the transmission. The measurements are realized for different applied voltages, from 0 V to 90 V on the two varactors.

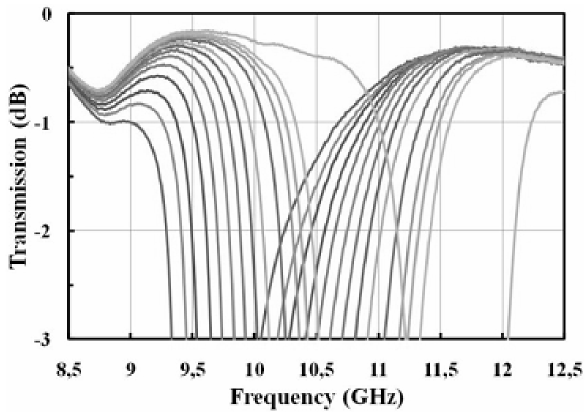

Fig. 5. Expanded view on transmission. Insertion losses are low outside of the rejected band.

Moreover, this filter has been caracterized in response of a power effect.

Sensivity to radio-frequency power provokes drifts of the resonant frequencies of each pole. This drift is depending of the electromagnetic energy located between MEMS bridges and RF electrodes. Thus, capacitance values are changed by power effect, and then will increase with higher power applied, due to the inverted electromechanical principle of the actuators. Capacitance variations can be compensated thanks to several volts of applied voltage added on the actuators. This is shown on Fig. 6 with different values of power, between 100 mW and 250 mW. With 1.5 V added on the first pole and 9 V added on the second pole, drift of the RF power variation from 100 mW to 250 mW is cancelled.

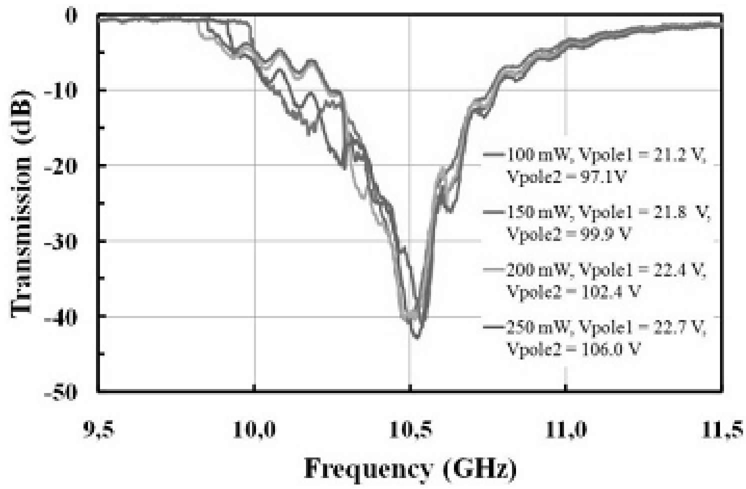

Fig. 6. Compensated power effect on the device to obtain fixed 10.5 GHz resonant frequency.

Futhermore, this device has been tested at highest resonant frequency, with variable RF power. In this case, applied power will have the lowest influence on the filter stability because MEMS bridges are contacting on the ALN dielectric. This has been measured, and shown on Fig. 7.

Thus, with all RF MEMS in the down state, the resonant frequency of the two pole filter is 11.65 GHz, also with 100 mW RF power applied. Then, the transmission response is measured for variable power until 6 W, with inchanged bias. At 1 W power applied, disturbances are low on the filter, and at 2 W applied, we can see that these disturbances are found by drift of the resonance frequency of almost 500 MHz. More, we can see that the rejection at 11.65 GHz is still strong with -30 dB of transmission at 6 W of power applied.

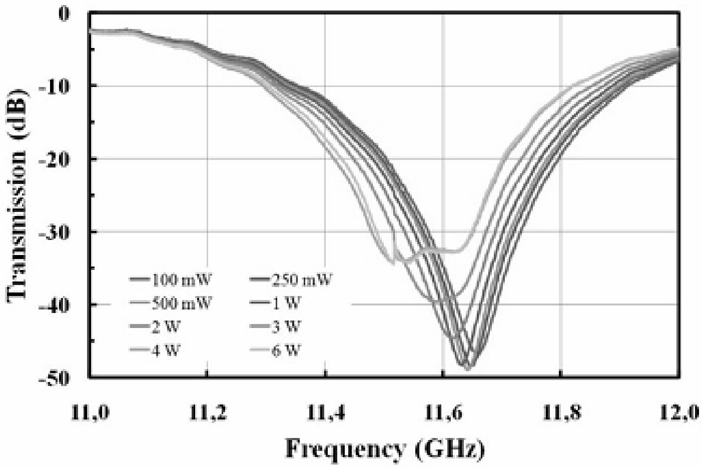

Fig. 7. Influence of RF power on rejection when RF MEMS are in the down state.

4. Conclusion

A high performance tunable X-band bandstop filter for interference management applications is presented. RF-MEMS are used as tuning devices for their interests in microwave performances, with high Q factor. Here we used analog RF-MEMS varactors which present low values of capacitance (25 fF to 225 fF), in order to tune the center frequency of two ring resonators coupled to a micro-strip line. Measurements have shown that tuning effect operate between 9.6 GHz to 11.7 GHz with rejection about -35 dB to -42 dB. Furthermore, this bandstop filter has shown power handling performances under 6 W with disturbances compensation possibility.

Acknowledgement. Authors want to acknowledge the French Ministry of Defense for their supports in this work.

References

[1] F. BARRIERE, A. CRUNTEANU, A. POTHIER, M. CHATRAS, P. BLONDY, *A Low Value Normally On RF-MEMS Switches Capacitor for High Q Millimeter Wave Tuning*, IEEE SIRF Conference, pp. 77–79, Jan 2010.

[2] E.R. BROWN, *RF MEMS switches for reconfigurable integrated circuits*, IEEE Trans Microwave Theory, pp. 1845–1880, 1998.

[3] N.S BARKER and G.M. REBEIZ, *Distributed MEMS true-time delay phase shifters and wide-bands switches*, IEEE Trans Microwave Theory, pp. 1881–1890, 1998.

Design of Ultra-Wideband Filter with Embedded RF-MEMS based Reconfigurable Notched Band

Luca PELLICCIA, Federico CASINI, Fabrizio CACCIAMANI, Paola FARINELLI, Roberto SORRENTINO

University of Perugia, DIEI, Via G. Duranti 93, 06125 Perugia, Italia

Phone: +39-075-585-3658,

E-mail: luca.pelliccia, federico.casini, fabrizio.cacciamani, paola.farinelli, roberto.sorrentino}@diei.unipg.it

Abstract. This paper presents the design of a compact ultra-wideband (UWB) bandpass planar filter with a tunable notched band within the bandwidth. The filter can be used for wireless communications within the unlicensed UWB range (3.1-10.6 GHz). The UWB filter is based on external interdigitated quarter-wavelength microstrip resonators and a central half-wave microstrip resonator embedding a reconfigurable open-circuited stub. The stub introduces a narrow rejection band inside the UWB filter bandwidth. The frequency tuning of the notched band is obtained by sequentially activating three RF MEMS ohmic switches placed in series along the embedded stub. HFSS® simulations of a 5^{th} order UWB filter show very low return (>13dB) and insertion losses (<0.3dB) in all stub states and good selectivity performance of the notched bands (up to -18dB of rejection). The device is being fabricating at FBK on quartz substrate; experimental results will be available soon.

1. Introduction

Since 2002, when the Federal Communication Commission (FCC) authorized the unlicensed use of the frequency band from 3.1 to 10.6 GHz for commercial communication applications [1], considerable research efforts have been put into ultra-wideband (UWB) radio technology worldwide. For the indoor use, the UWB frequency band of 3.1 to 10.6 GHz may be interfered by the wireless local area network radio signals. So, a communication system working in this UWB frequency band requires a bandpass filter with tunable notched bands to avoid being interfered by the WLAN radio signals.

In recent years several techniques have been introduced to generate a single or multi notched bands into UWB bandpass filters. In [2] an asymmetric parallel-coupled line structure is developed in a multi-mode resonator UWB filter and in

[3] an asymmetric dual-line coupling structure is employed for multiple-notch implementation in UWB filters. In [4] and in [5] stepped-impedance resonators are coupled to the UWB filter to achieve a narrow notched band. In [6] open stubs are embedded in a microstrip-to-SIW transitions to generate the frequency notch in a UWB filter realized combining the responses of a highpass filter in Substrate Integrated Waveguide (SIW) technology and a step-impedance lowpass filter. Embedded open-circuited stubs have been proposed to introduce a fixed notched band in a UWB filtering response, such as in [7], [8], [9].

In this paper, a UWB 5^{th} order bandpass filter with an embedded RF-MEMS based reconfigurable notched band is presented. The UWB filter is composed by external interdigitated quarter wavelength microstrip resonators and a central half-wave microstrip resonator [2], embedding a MEMS-reconfigurable open stub. Such a solution allows for lower loss contribution and narrower rejection bandwidth if it is compared to other solutions developed so far which employ pin diodes [10].

Moreover, the MEMS-based open-circuited stub yielding the tunable notched bands is embedded in the 5^{th} order filter thus unchanging the filter footprint and achieving a very compact structure (2×35 mm).

2. Filter Design

The layout of the UWB filter is shown in Fig. 1. At both extremities, three λ/4 (at 6.5 GHz central frequency) open-circuited lines are parallel-coupled in an interdigitated configuration producing four filtering function poles. The additional pole of the filter is due to the central λ/2 resonator. The UWB filter structure is characterized by the presence of a length-reconfigurable open-circuited stub that is directly embedded within the central λ/2 resonator (Fig. 2).

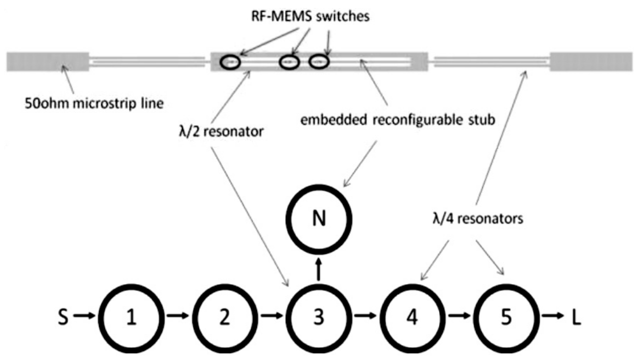

Fig. 1. Layout and scheme of the UWB bandpass 5^{th} order filter.

Three RF-MEMS cantilever switches are placed in series along the open-circuited stub to vary its length L_{notch} and consequently tune the notch frequency.

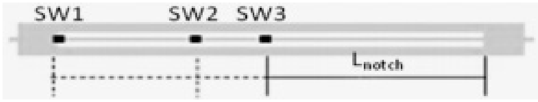

Fig. 2. Reconfigurable open-circuited stub with three RF-MEMS switches embedded in the UWB filter central resonator.

The cantilever MEMS switch consists of a gold membrane suspended above the interrupted microstrip stub and anchored at one end. The membrane has a size of 110μm×170μm and an air gap of 2.7μm (Fig. 3). In the off-state the switch provides very high wide-band isolation from DC up to high frequencies, virtually realizing an ideal open-circuit. In the on-state, on the contrary, the cantilever is lowered by electrostatic forces applied on the actuation pad and contacts the interrupted signal line.

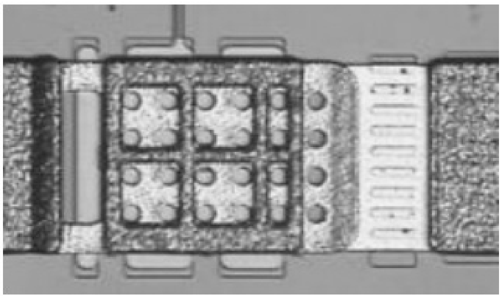

Fig. 3. Photo of the series ohmic cantilever switch used as building block of the filter.

Similar switches in coplanar or microstrip technology have already been manufactured at FBK (Fondazione Bruno Kessler) on high resistivity silicon substrate showing equivalent on-state resistance of 0.9Ohm and off-state capacitance of about 10fF [11], [12].

3. Simulated Results

Fig. 4 shows the Ansoft HFSS® model of the MEMS-based 5th order UWB filter. Each MEMS switch has been modeled as a series capacitance of 10fF or a series resistance of 1Ohm for the cantilever in up (off-state) or down position (on-state) respectively. The filter footprint is 2×35 mm.

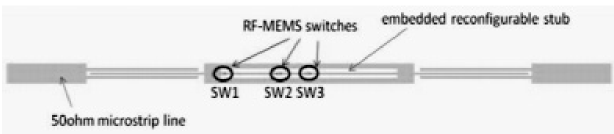

Fig. 4. HFSS® model of the MEMS-based 5th order UWB filter.

When all switches are activated (on-state), the line is uninterrupted and no selective stop band is visible. Fig 5 shows the full wave simulated results via Ansoft HFSS® [13] for this configuration. As can be seen, return loss and insertion loss better than 20 dB and 0.25 dB have been obtained from 3.5 GHz to 9.5 GHz.

When switch #1 is deactivated and the other ones are in the on-state, the embedded line is interrupted introducing the notch stop-band response at 4.3 GHz. When also switch #2 is deactivated, the length of the stub is reduced so as to produce a rejected band exactly at the center of the filter band, *i.e. at* 6.5GHz. Similarly when switch #3 is deactivated as well, the notched band is moved to the upper bandwidth, *i.e*. at 8.5GHz.

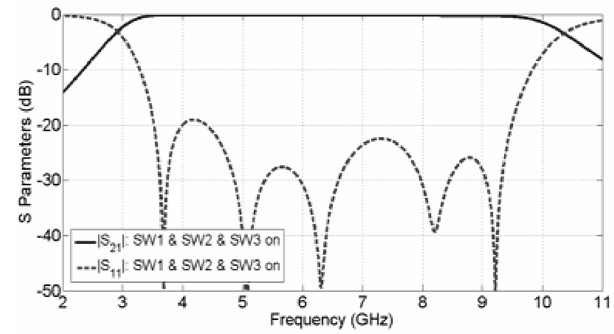

Fig. 5. Full wave HFSS® simulated performance of the UWB filter with no rejected band: |S21| (solid blue line) and |S11| (dashed red line).

Fig. 6 shows the comparison in terms of insertion loss in these three configurations. As can be seen, the 3dB rejection bandwidth is very narrow (5-6% depending on the stub state) because of the very low coupling between the central resonator and the embedded stub [9].

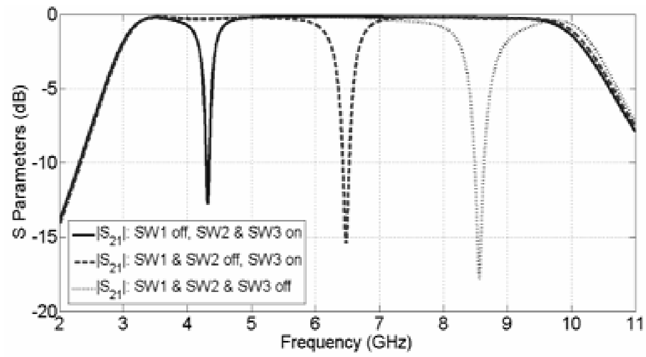

Fig. 6. Comparison among the UWB filter |S21| responses of the three different stub configurations (HFSS®).

The rejection ranges from -13dB up to -18dB depending on the stub configuration. The insertion loss of the UWB filter is insensitive to the embedded stub state and is below 0.3dB in all cases. Fig. 7 shows the filter responses in terms of return loss for different states of the embedded stub. The stub introduces a small degradation of the filter matching: the return loss is however better than 13 dB over the whole filter bandwidth in all cases.

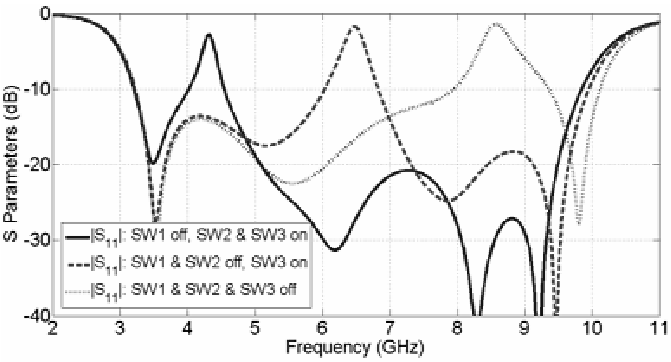

Fig. 7. Comparison among the UWB filter |S11| responses of the three different stub configurations (HFSS®).

The device is being fabricated on quartz substrate by using the 8-mask MEMS process developed by FBK in Trento [11]. RF performance and reliability tests will be carried out for a complete characterization. The experimental results will be available soon.

4. Conclusions

The design of a compact UWB 5th order bandpass filter with a tunable notched band has been presented. A variable length λ/4 open stub is embedded in the central λ/2 resonator of the UWB filter. Three RF-MEMS cantilever switches have been placed in series to the open stub allowing for selecting four possible filter states: no notch, notch in the lower bandwidth, notch at centre frequency, notch in the higher bandwidth. The Ansoft HFSS® filter simulations show very good return loss (>13 dB), insertion loss (<0.3dB) in the entire bandwidth and rejection of notched band up to -18dB in all configurations. The presented device is being fabricated at FBK.

References

[1] *Revision of Part 15 of the Commission's Rules Regarding Ultra-Wide- band Transmission System*, ET-Docket, pp. 98–153, First note and order, Federal Communication Commission, Feb. 14, 2002.

[2] H. SHAMAN, J.S. HONG, *Asymmetric parallel-coupled lines for notch implementation in UWB filters*, IEEE Microw. Wireless Compon. Lett., 17(7), pp. 516–518, Jul. 2007.
[3] K. SONG, Q. XUE, *Asymmetric dual-line coupling structure for multiple-notch implementation in UWB bandpass filters*, Electronics Letters **46**(20), 30th September 2010.
[4] Chun-Ping CHEN, Y. TAKAKURA, H. NIHIE, M. ZHEWANG, T. ANADA, *Design of compact notched UWB filter using coupled external stepped-impedance resonator*, Microwave Conference, APMC 2009, Asia Pacific, pp. 945–948, 7-10 Dec. 2009.
[5] Hussein SHAMAN, Jia-Sheng HONG, *Ultra-wideband (UWB) Microstrip Bandpass Filter With Narrow Notched Band*, Proceedings of the 38th European Microwave Conference, October 2008, Amsterdam, The Netherlands.
[6] Wei QIN, Wei HONG, Hong Jun TANG, Jing WANG, *Design and Implementation of UWB Bandpass Filter with a Frequency Notch for Choking Back the Interference from Narrow Band Wireless Communication Systems*, ICUWB 2009, September 9-11, 2009.
[7] Min-Hang WENG, Chihng-Tsung LIAUH, Hung-Wei WU, Hung-Wei WU, *An Ultra-Wideband Bandpass Filter With an Embedded Open-Circuited Stub Structure to Improve In-Band Performance*, IEEE Microwave and Wireless Components Letters, **19**(3), March 2009.
[8] Binyan YAO, Qunsheng CAO, Yonggang ZHOU, *Ultra-Wideband (UWB) Bandpass Filter With Embedded BandNotch Structures*, ICMMT2008 Proceedings.
[9] Hussein SHAMAN, Jia-Sheng HONG, *Ultra-Wideband (UWB) Bandpass Filter With Embedded Band Notch Structures,* IEEE Microwave and Wireless Components Letters, **17**(3), March 2007.
[10] Young-Hoon CHUN, Hussein SHAMAN, Jia-Sheng HONG, *Switchable Embedded Notch Structure for UWB Bandpass Filter*, IEEE Microwave and Wireless Components Letters, **18(**9), September 2008.
[11] A. OCERA, P. FARINELLI, F. CHERUBINI, P. MEZZANOTTE, R. SORRENTINO, B. MARGESIN, F. GIACOMOZZI, *A MEMS-Reconfigurable Power Divider on High Resistivity Silicon Substrate*, IEEE MTT-S International Microwave Symposium, Honolulu, 3-8 June 2007.
[12] F. CASINI, *et al*., *Design of mm-wave 5-bit phase shifters for Phased Array Antenna Systems*, MEMSWAVE Conference Proceedings, July 2010.
[13] www.ansoft.com

Low-Loss Distributed 2-bit RF MEMS Phase Shifter for 60GHz Applications

Cheikh NDIAYE[1], Arnaud POTHIER[1], Cyril GUINES[1], Pierre BLONDY[1]

[1]XLIM UMR 6172, Université de Limoges /CNRS, 123 avenue Albert Thomas, 87060 Limoges, France
E-mail: cheikh-tidiane.ndiaye@xlim.fr, arnaud.pothier@xlim.fr, pierre.blondy@xlim.fr

Abstract. This paper presents the design of a low loss 2-bit digital phase shifter using a high-impedance coplanar transmission line periodically loaded with miniature RF-MEMS switched capacitors. This phase shifter is designed to generate four phase states with an accuracy of better than 2° and should be integrated to allow electronic steering of patch antenna in SIP complete communication module operating at 54.5 GHz. This phase shifter is composed of the series association of 18 unit cells organized in 2 independent bits thanks to DC biasing though decoupling MIM capacitors. At 54.5 GHz the targeted reflection loss matching should be better than -12 dB with insertion loss of as low as 1.5 dB whatever the phase state generated.

1. Introduction

Since a couple of years, phase shifters appear to be key components in any communication module that requires antenna with scanning and beam forming capabilities.

Several technologies are today available to produce highly integrated and high performance phase shifters in the millimeter wave frequencies spectrum. Hence phase shifter design using semiconductor components technology like FET or PIN diode have been for a long time favored ensuring high integration level and very fast reconfiguration capabilities (1-100ns) [2]. But nevertheless this technology generally implies high insertion losses as well linearity and power consumption troubles [3-4].

Today, other candidates are under study to overcome these drawbacks, as ferroelectric capacitors [5-8] that still requires doing compromises between loss and tunability capabilities or also RF-MEMS components ensuring both low insertion loss and power consumption with monolithic integration capabilities [9] with sometime some limitation in term of switching speeds and power handling.

Today there are three main topologies that have been exploited to achieve phase shifter design based on RF MEMS component technology. The first is based on the phase shift induced by a reflection line design which usually requires couplers or circulators The second is based on switchable delay line topology whereas the third uses the principle of a slow wave transmission line periodically loaded with switches or MEMS switched capacitors well known as DMTL (Distributed MEMS Transmission Lines) on which the phase shift introduced when MEMS are activated is given by [1]:

$$\Delta\phi = \frac{360\, fsZ_0\sqrt{\varepsilon_{eff}}}{c}\left(\frac{1}{Z_{lu}} - \frac{1}{Z_{ld}}\right)\frac{\deg\text{rees}}{\sec\text{tion}} \tag{1}$$

It is expressed in terms of:

- f the operating frequency in Hz
- s the spacing between the MEMS switches in m
- Z_0 the characteristic impedance of the line in Ω
- ε_{eff} the effective dielectric constant of the substrate.
- c is the speed of light in vacuum in m/s
- Z_{lu} and Z_{ld} the impedances of the loaded line corresponding to up and down states of MEMS switches respectively in Ω.

The aim of our study is to prototype high performance 2-bit phase shifters combining low losses and low power consumption, able to generate four phase states [0°, 65°, 130°, 195°] to ensure the targeted 20 degrees beam steering on the radiating pattern of a millimeter frequencies antenna based on a four patches array. The targeted frequency band is quite wide (52-57GHz) implying to achieve a broadband performance, that why DMTL phase shifter topology has been favored. This approach is also compatible with the final SIP (System in Package) integration expected in this work.

2. Operating Principle of a DMTL Phase Shifter

As illustrated in Fig. 1, one approach to design a DMTL phase shifter in millimeter frequency band is to use a high-impedance coplanar line periodically loaded by MEMS switched capacitors. Thus the phase shifter design consists in cascading identical unit cells that allows obtaining a phase shift proportional to the number of cells used. By appropriately sizing the MEMS components and their periodic spacing on the transmission line, we can lower the impedance of the transmission line from its unloaded value Z_0 to loaded impedance given by [10]:

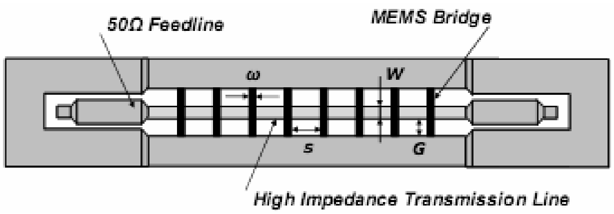

Fig. 1. Structure of the DMTL phase shifter from the top view.

$$Z_l = \sqrt{\frac{L_t}{C_t + C_b / s}} \tag{2}$$

where C_t and L_t are the per unit-length capacitance and inductance of the unloaded high-impedance transmission line and C_b (C_{bu} for the OFF state and ON state for C_{bd}) and s are the RF-MEMS switch capacitance and periodic spacing, respectively. In addition to changing the transmission-line impedance, phase velocity is also decreased due to the capacitive load and is given by [10]:

$$v_l = \sqrt{\frac{1}{L_t(C_t + C_b / s)}} \tag{3}$$

So the maximum expected return loss level RL_{max} can be set judiciously choosing the optimal impedance for loaded transmission line.

Thus the periodically loaded transmission line can operate over a wide frequency range from DC up to Bragg frequency of the device corresponding to a cutting frequency where the propagated wavelength begins to be very close to the RF-MEMS switches period spacing. This frequency can be easily computed using (6) and set the size of the phase shift elementary cell as function of the targeted bandwidth of operation of the phase shifter [11]:

$$f_{Bragg} = \frac{1}{\pi \cdot s\sqrt{L_t(C_t + C_b / s)}} \tag{4}$$

3. RF Design

A. Miniature MEMS switched capacitors

For the switched capacitors design that will load periodically the slow wave coplanar line used as phase shifter, we have opted for a miniature MEMS component topology whose dimensions are 5 to 10 times lower than conventional RF MEMS components. As shown in [12], this approach also allows to achieve switching times of less than one microsecond but also to be less sensitive to temperature changes and the effects of charge trapping at the root of many failures encountered in the conventional RF MEMS components. As illustrated in Fig. 2, these MEMS two states capacitors are based on a 60×30µm^2 gold movable membrane 350 nm thick and suspended 1µm above the lower capacitor RF electrode also used as biasing electrode. This electrode is covered with an insulating AlN film 200 nm thick. According to finite element electromechanical simulations performed using ANSOFT ANSYS, with this design these switches should require actuation voltages from 20 up to 30V and can generate a change in capacitance from 15fF to 90fF once actuated.

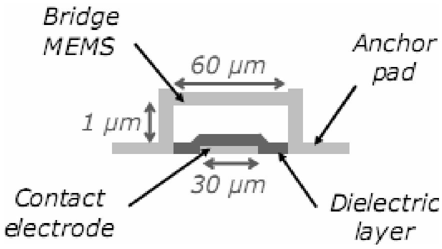

Fig. 2. Miniature RF-MEMS switched capacitor cross-view section.

B.2 bits DMTL phase shifter design

As shown in Fig. 3, each MEMS switched capacitor (C_{bu}, C_{bd}) is associated in series with a MAM capacitor C_s (Metal Air Metal) in order to avoid RF MEMS capacitance value dispersion in their down state. Indeed, the specificity of the MAM capacitor is to be mechanically unmoving allowing to ensure a fixed capacitance value.

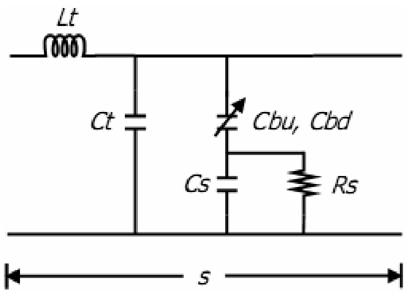

Fig. 3. Unit cell equivalent circuit model with the MEMS bridge.

Thus the load capacitance seen by the line is the series combination of the MEMS bridge capacitance C_b and the total lumped capacitance C_s (45fF) and is:

$$C_l = C_s\, C_b / \left(C_b + C_s\right) \tag{5}$$

when the MEMS bridge is in the up-state position, the bridge capacitance C_{bu} (15fF) is, in the limit, much smaller than C_s (45fF) and the effective capacitance seen by the transmission line, is $C_{lu} \approx C_{bu}$. When a bias is applied on the line and the MEMS bridge is in the down-state position, the bridge capacitance C_{bd} (expected to be at least higher than 90fF) increases by a factor of 6 and becomes much larger than C_s (45fF)) thereby resulting in a load capacitance of $C_{ld} \approx C_s$. The distributed capacitance can therefore be discretely controlled by the independent choice of C_{bu} and C_s. Our unit cell is designed to achieve 11 degrees phase shift at 54.5 GHz. Thus as shown in Fig. 4, by cascading 6 unit cells, a 65° degrees phase shift section is obtained whereas using 12 cells a 130 degrees phase shift can be achieved. For each of these group of cells, activation of MEMS switched capacitors will collectively and synchronous and independently from each other through the integration of DC decoupling MIM capacitors (300 fF) between the two bits. It allows generating the intermediate phase states (*i.e.* 65° and 130°). As illustrated in Fig. 4, the MEMS biasing is ensured by separate commands related to the central conductor of the waveguide through high impedance integrated resistor R_s (50-100kΩ). These resistances allow us to prevent any leakage of the RF signal into the bias network and maintain a low loss performance phase shifter.

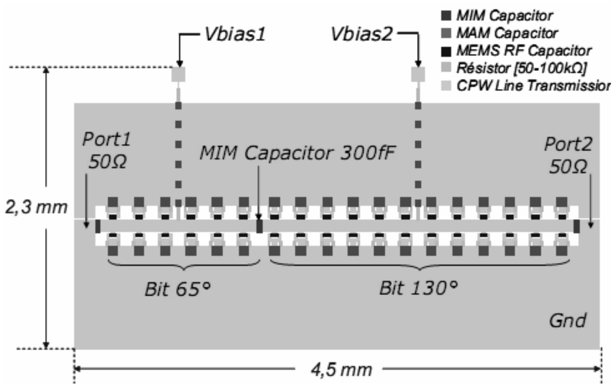

Fig. 4. Layout of the DMTL 2-bit phase shifter.

4. Conclusions

This paper illustrates the potential of miniature RF-MEMS switched capacitors to design low-loss digital type distributed RF-MEMS phase shifters in millimeter frequencies. The electromagnetic simulations performed on this design using the software 2.5 D Momentum confirmed that the number of cells retained will achieve the desired level of total phase shift with a phase error acceptable. Also as shown in Fig. 5-(a) and 5-(b), the matching level remains well below -12 dB in the frequency range covered (52-57 GHz), while the total loss level is estimated better than 1.5 dB regardless the phase state looked for. Thus, at 54.5 GHz, as well Table 1 summarizes simulations results that seem very promising. The first phase-shifters fabrication is still on-going in our laboratory

(Fig. 6). Unfortunately, on the first fabrication run the biasing resistances were not working properly due to fabrication process troubles. This problem will be normally fixed quickly. First RF measurements (Fig. 7) are still in good agreement with expected performances, but since bit cannot be activated for instance, only one state has been successfully measured. A second fabrication run is running, last results with operating MEMS capacitors are expected in the following weeks and will be presented during the MEMSWAVE conference this year.

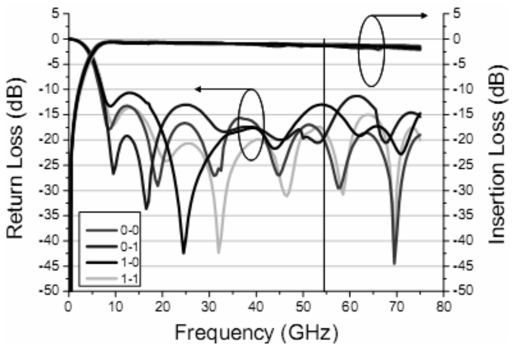

a)

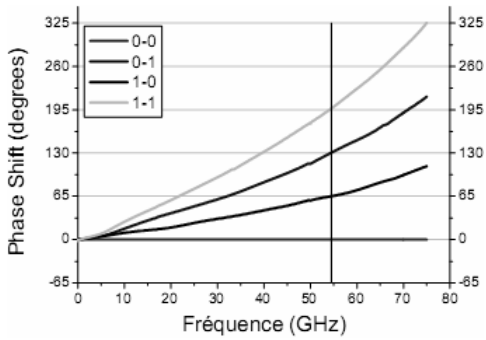

b)

Fig. 5. Simulation results of the 2-bit DMTL phase shifter.
(a) Return Loss and Insertion Loss, (b) Phase Shft.

Table 1. Expected Performance of th 2-Bit MEMS Phase Shifter at 54.5 GHz

Binary combination	0-0	1-0	0-1	1-1
Desired phase shift	0,0°	65,0°	130,0°	195,0°
Simulated phase shift	0,0°	65,4°	129,4°	193,8°
Phase error	0,0°	0,4°	0,6°	1,2°
Return loss (dB)	-20	-13	-19,5	-18
Insertion loss (dB)	-0.8	-1,2	-1,1	-1,2

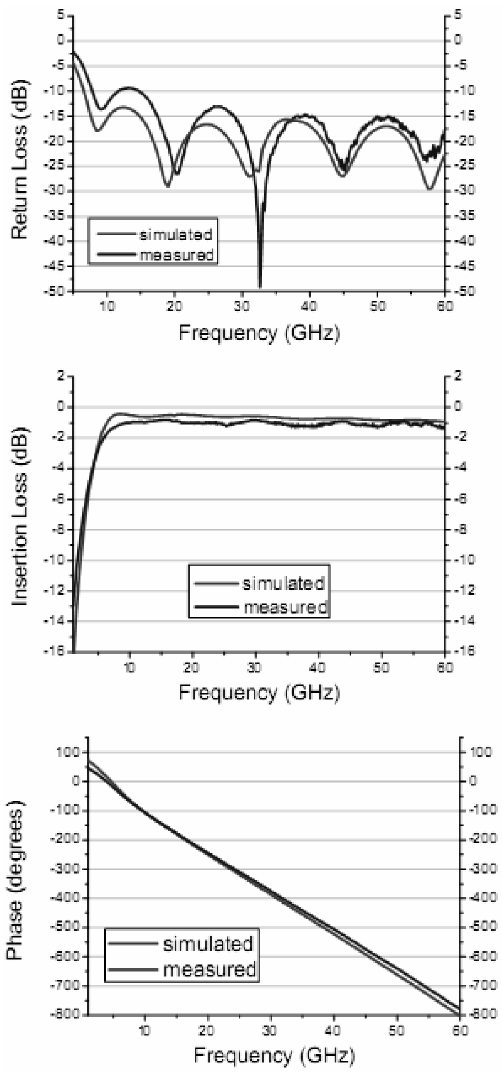

Fig. 7. RF performance of phase shifter in their 0-0 state.

References

[1] J.S. HAYDEN and G.M. REBEIZ, *2-bit MEMS distributed X -band phase shifters*, IEEE Microwave Guided Wave Lett., **10**, pp. 540–542, Dec. 2000.
[2] B. GLANCE, *A fast low-loss microstrip P-I-N phase shifter*, IEEE Trans. On Microwave Theory Tech., **27**(1), pp. 14-–16, January 1979.
[3] K. MARUHASHI, *et al*, *A Ka-band 4-bit monolithic phase shifter using unresonated FET switches*, IEEE MTT-S Int. Microwave Symp. Dig., pp. 51–54, June 1998.
[4] J. WALLACE, *et al*, *Low cost MMIC DBS chip sets for phase array applications*, IEEE MTT-S Int. Microwave Symp. Dig., Anaheim, CA, pp. 677–680, June 1999.

[5] Wenfei HU, *et al*, *Cost effective ferroelectric thick film phase shifter based on screen-printing technology*, In Proc. IEEE MTT-S Int. Microwave Symp. Digest, 2005.

[6] V. SHERMAN, *et al*, *Digital reflection-type phase shifter based on a ferroelectric planar capacitor*, **11**(10):, pp. 407–409, 2001.

[7] V. SHERMAN, *et al*, *Design and investigation of ferroelectric digital phase shifter*, In Proc 31st European Microwave Conf, pp. 1–4, 2001.

[8] O.G. VENDIK, *Insertion loss in reflection-type microwave phase shifter based on ferroelectric tunable capacitor*, **55**(2), pp. 425–429, 2007.

[9] H.T. KIM, *et al*, *V -Band 2-b and 4-b Low-Loss and Low-Voltage Distributed MEMS Digital Phase Shifter Using MAM Capacitors*, IEEE Trans. Microwave Theory Tech., **50**(12), Dec. 2002.

[10] S. BARKER and G.M. REBEIZ, *Distributed mems true-time delay phase shifters and wide-band switches*, IEEE Transactions on Microwave Theory and Techniques, **46**(11), pp. 1881–1890, 1998.

[11] M.J.W. RODWELL, *et al*, *Active and nonlinear wave propagation devices in ultrafast electronics and optoelectronics*, Proceedings of the IEEE, **82**(7), pp. 1037–1059, 1994.

[12] B. LACROIX, *et al*, *Sub-microsecond rf mems switched capacitors. Microwave Theory and Techniques*, IEEE Transactions on, **55**(6), pp. 1314–1321, 2007.

Optimization of a High-Power Ka-Band RF MEM 2-Bit Phase Shifter on Sapphire Substrate

B. ESPANA[1], B. BELENGER[1], S. COURRÈGES[2], P. BLONDY[2], O. VENDIER[1], D. LANGREZ[1], J.-L. CAZAUX[1]

[1]Thales Alenia Space, 26 av JF Champollion, 31037 Toulouse Cedex1, France
E-mail: beatrice.espana@thalesaleniaspace.com
benoit.belenger@thalesaleniaspace.com

[2]XLIM, UMR CNRS n°6672, Université de Limoges, 123 av A. Thomas, 87060 Limoges Cedex, France

Abstract. In this paper, the optimization of a low-loss radio frequency (RF) microelectromechanical (MEMS) 2-Bit Ka-Band monolithic Phase Shifter for high-power application is presented. These micro-strip circuits are fabricated on 0.254mm-thickSapphire substrate and are based on a reflection topology using 3-dB branch line coupler. The insertion loss of the circuit varies from –2 dB for the state (0°) to –2.6 dB for the highest state (225°). The return loss is better than -15 dB and the phase shift is steady within the aimed frequency range [25.7 –27] GHz. Power stress with 1 dB step measurements have been done on a 1-bit 45°cell . No significant phase change has been observed in down-state for an input power variation from 0 dBm to +32 dBm. In up-state only 3.3° deviation is recorded.

Index Terms: Microelectromechanical systems (MEMS), phase shifters, switches, high-power.

1. Introduction

With the progress of the MEMS technology , new antenna solutions are arising, achieving reconfigurability at moderate cost. It could be an answer to new needs for Space telecoms with Flexible Payloads (coverage flexibility, frequency resource flexibilities and power flexibility) [1].

Microwave and millimetre-wave phase shifters are essential components in phase array antennas for telecommunication and radar applications. Low loss and high frequency phase shifter has been presented in reference [2] or [3] but those works did not address power handling capabilities. Other works such as [4] present phase shifter designs using high power MEMS switches but not necessarily suited for Ka band application nor constant phase shift response versus frequency requirement [5], [6].

This paper proposes an optimized Ka-Band 2-bit phase shifter careful design using capacitive MEMS switches with high-power handling capabilities. This phase shifter has been designed for the particular need of Ka-Band phase array antennas which use ferrites as a reference solution. Two bits only are necessary in our application with the respective values of 45° and 180°. The circuit has been designed within the frequency range [25.7-27] GHz, and the operating power requirement is 4.6W CW. Thus, the RF power applied to MEMS switches is 3dB less than the circuit input power.

Manufacturing of the devices has been performed at XLIM laboratory. Design, probing and measurements were carried out at TAS.

The measured performances of the Ka-Band 2-bit phase shifter are presented in [9] and main results are recalled in section 3. In this paper, back simulations and optimization have been done in order to achieve an accurate response and get the correct phase shifts within the frequency range (see section 4).

2. Circuit Design and Fabrication

In addition to the 2-bit 45°/180° phase shifter (Figure 1), a 1-bit 45° (Figure 2) and a 1-bit 180° phase shifters (Figure 3) have been also designed. The three circuits have been fabricated on a 254 μm-thick Sapphire substrate.

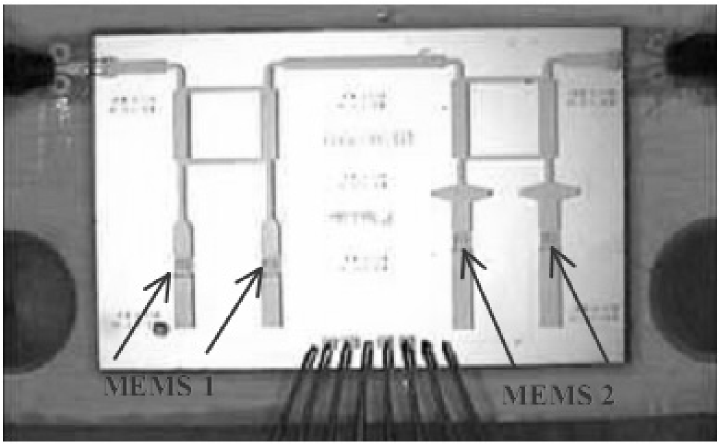

Fig. 1. 2 bit Ka band phase shifter.

The elementary 1-bit phase shifter is based on reflection type topology [7] [8] which consists of a 3-dB branch line coupler and identical transmission lines at the direct and coupled ports loaded with capacitive MEMS Switch taken from XLIM Technology Basic Building blocks (Figure 5).

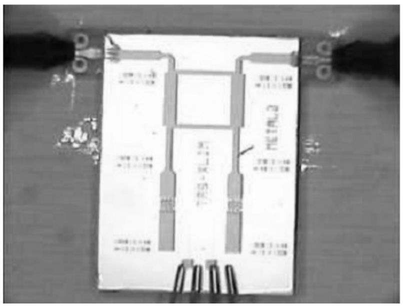

Fig. 2. 1-bit 45° phase shifter.

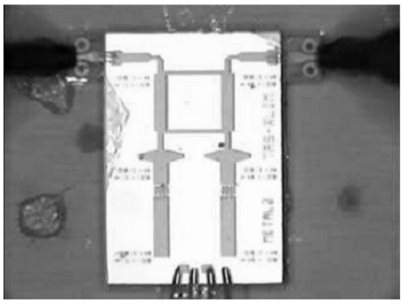

Fig. 3. 1-bit 180° phase shifter.

Fabrication process starts with the deposition of a 60/1500A Cr/Au metal deposition (fig. 5 (a)), followed by a 0.4 µm thick AlN sputtered layer (b).

Next, a 100Kohm.square doped carbon resistive layer is deposited and patterned to provide a low loss bias network of the components. Next, a two steps sacrificial layer is deposited and patterned (c-d), in order to define the areas where the MEMS devices will be separated from the substrate. A second 2.5 µm thick gold layer is then deposited and patterned, to define the MEMS moveable parts (e). Finally, the devices are diced, released (f) and dried in a critical point drying system.

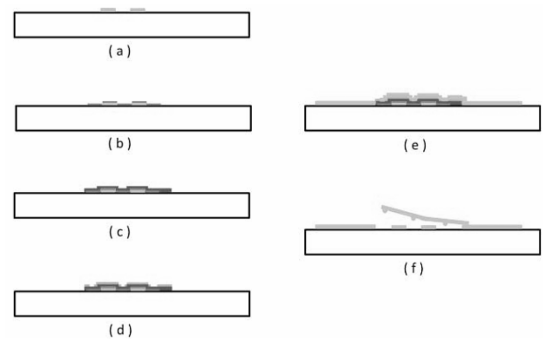

Fig. 4. Fabrication process.

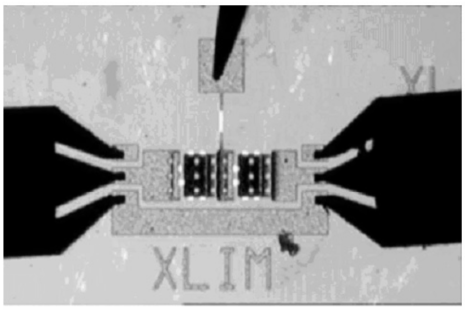

Fig. 5. XLIM elementary capacitive MEMS Switch.

3. Measurements

S-parameters and phase shift of each circuit (1-bit 45° phase shifter, 1-bit 180° phase shifter and 2-bits phase shifter) have been presented in [9]. The three circuits are mounted on a Copper-Tungsten base-plate and are wire-bounded using three parallel wires (length 200µm, diameter 25µm) to JMT© transition (used to transform CPW connection to micro strip).

A. 1-bit 45° phase shifter measured performance

The performance of the 1-bit 45° phase shifter is recalled in Figure 6 and TABLE 1. The input and output reflection losses are better than –11 dB from 25.7 GHz to 27 GHz and the average insertion loss is -0.7 dB for down or up state. The delta fundamental phase state is within 2.3°.

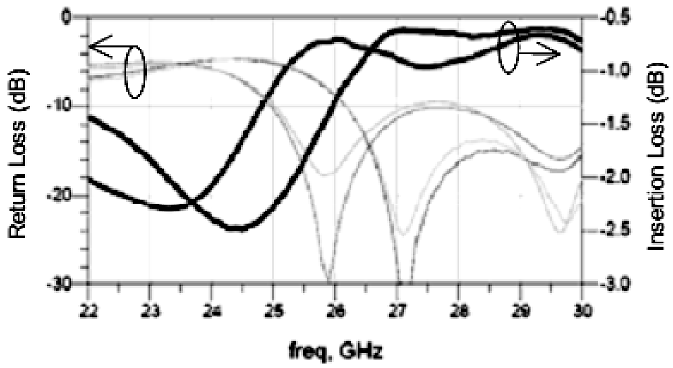

Fig. 6. 1-bit 45 ° phase shifter performance.

Table 1. 1-bit phase data at 26.4 GHz

Phase State	45.0
Measuured	42.7
Delta	-2.3

For this design, we note that, in down-state, insertion loss and phase shift measurement is reproducible. Phase shift response is very close to simulation results (Table 1). Nevertheless, we observed that phase shift value decreases after few actuations down to a stabilized value of 25° due to the influence of charging effects phenomena.

The input power hardness has also been characterized. Figure 7 shows relative AM/PM curves in up- and down-states for three frequency points in the band of interest.

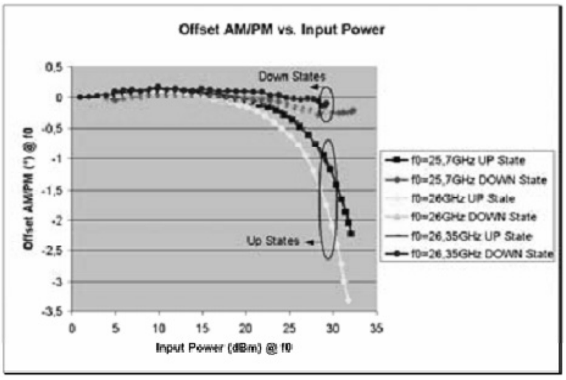

Fig. 7. AM/PM measurement of 45° phase shifter.

Measurement results show a good sturdiness of both the design and the RF-MEMS for an high input power range. The worst case AM/PM variation is 3.3° in up-state and 0.3° in down-state. The input power was voluntarily limited to +32 dBm in order to avoid probes damage.

B. 1-bit 180° phase shifter measured performance

The performance of the 1-bit 180 ° phase shifter is drawn in Figure 8. The input and output reflection losses are better than –10 dB from 25.7 GHz to 27 GHz and the average insertion loss is –1.5 dB for down or up-state.

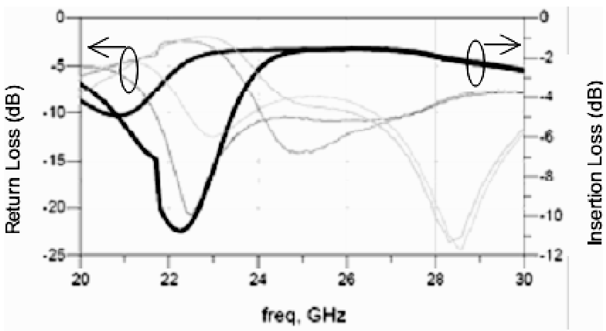

Fig. 8. 1-bit 180 ° phase shifter performance.

On this circuit, input and output matching performance is deteriorated compared to simulation results. Insertion losses are 0.8 dB poorer than simulation. The measured phase shift at ambient temperature is 170°, for an aimed 180° value.

However this performance is obtained at 23 GHz instead of 26.5 GHz indicated a shift in frequency.

After twelve hours at hot temperature (75°C) in environmental chamber, the 170° phase shift value has been now measured at 120°. Charging effect phenomena of the dielectric of the MEMS Switch, not totally reset during a thermal stage, has an influence on the phase shift variation. It shows that packaging is here needed to have reproducible results.

C. 2-bit phase shifter measured performances

The performance for two manufactured samples of the 2-bit phase shifter for up and down-states are shown in Figure 9 and Figure 10 for three MEMS switches configuration.

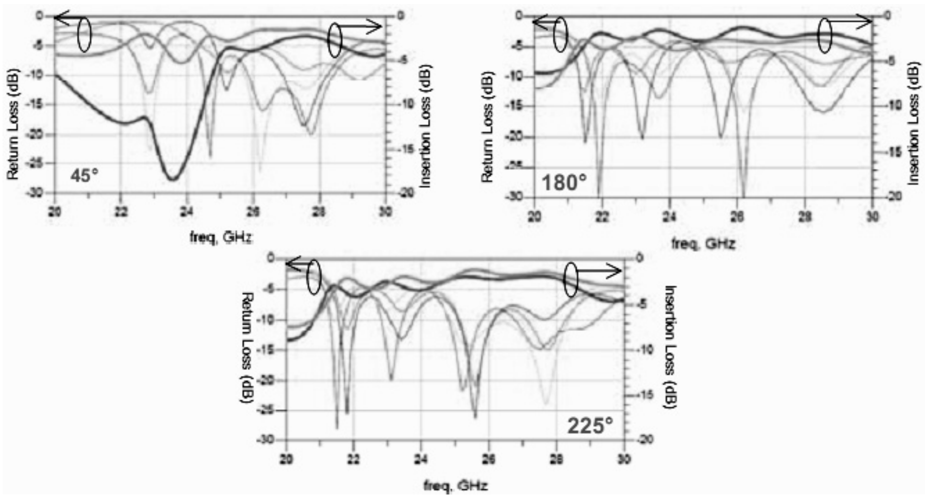

Fig. 9. 2-bit 180° phase shifter RF performances.

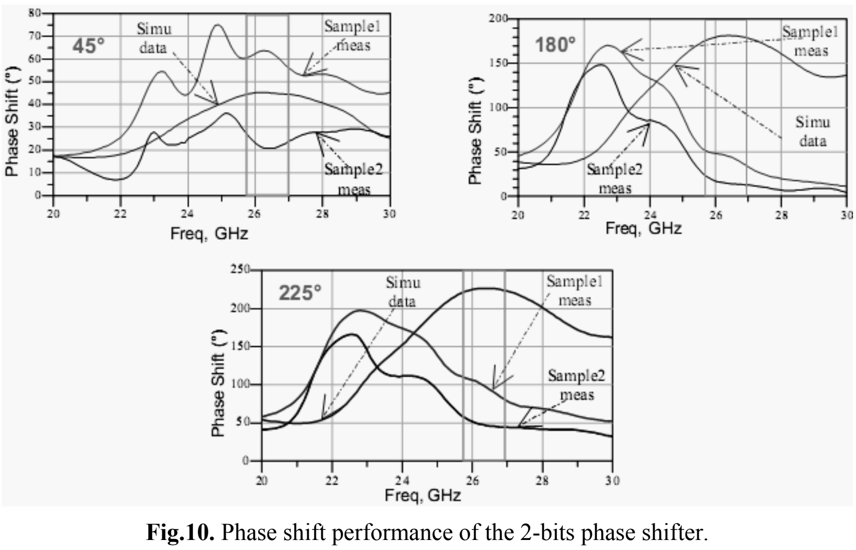

Fig.10. Phase shift performance of the 2-bits phase shifter.

The influence of the 180° cell behaviour could have been recognize on the 2-bit phase shifter measurement. Moreover, it has been noticed that measurement (in particular for phase shift parameter), is not reproducible over several samples. This phenomena could be explain by dispersion on physical parameters of MEMS switches and/or their C_{Down}/C_{Up} ratio.

We observed that:

• The input and output reflection loss are higher than simulation predictions but they are in line with the measurement obtained on the single 180° cell.

• Phase shift curves for 180° and 225° states are shifted by 3 GHz towards low frequencies like the 180° cell.

The results showed an average insertion loss of about -2 or -3dB in the operating frequency band, in any case higher than the simulation. This can be due to metal and/or substrate losses underestimation.

3. Feedback Simulation and Optimization

Retro simulations with Agilent ADS circuit software have been done to better explain the discrepancy between measured and simulated results. The design of each function has been optimized for a second run, taking into account substrate and MEMS switches technological parameters uncertainties. We have been keeping in mind that these uncertainties could have a significant influence on the totally circuit performance.

Regarding substrate technological parameters uncertainties, we paid a particular attention to the properties of sapphire substrate (Table 2) and especially its anisotropic permittivity value. Measurement fitting was performed by sweeping the effective dielectric constant value. The best result was obtained with an ε_r of 11.6 (ε_r=11 for the initial design). Thus, this value have been kept for design optimization.

Table 2. Properties of Sapphire substrate

	Value
Crystalline structure	rhombohedral
Tear in a stocking parameter (nm)	0.348
Permittivity: ε_r	9.3 to 11.6(anisotropic)
Tan δ	3.8 10^{-8} at 80K and 10 GHz
CTE(10^{-6}/K)	7

Since the dielectric properties of sapphire substrate are anisotropic, the relative dielectric constant is not a single value but a tensor. It could have an impact on the behaviour of single micro-strip lines by the variation of their local impedance, and could explained frequency shift, high insertion losses, and incorrect phase shift.

Width and length dimensions of each discontinuities as bend or taper elements have been also analyzed and optimized to reduce their sensitivity to variation of effective dielectric constant.

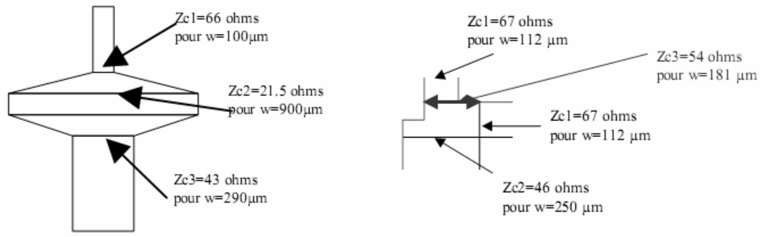

Fig. 11. Layouts of micro-strip elements sensitive to ε_r variation.

For MEMS switches technological parameters uncertainties we have looked a design sensitivity to the dispersion on physical parameters of MEMS switches and /or their C_{DOWN}/C_{UP} ratio which have a direct impact on phase shift value at given frequency.

More attention has been given to improve the 180° cell behaviour. The optimization of this design has been done in order to get better input and output matching performance, better insertion loss and a correct phase shift centred at 26.5 GHz (Figure 14). Thereby, we have taken into account:

• the technological parameters (including tan δ parameter new value),

• the influences of every discontinuity, keeping in mind that they could have a significant influence on the presented impedances, and consequently on the totally 180° cell performance.

Further, the proposed structure of the 1-bit 180° phase shifter design (Figure 13) has been done to be close to the 1-bit 45° phase shifter, whose measured performance and simulated behaviour are similar.

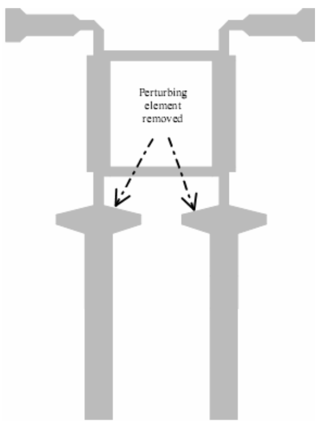

Fig. 12. Previous1-bit 180° cell layout.

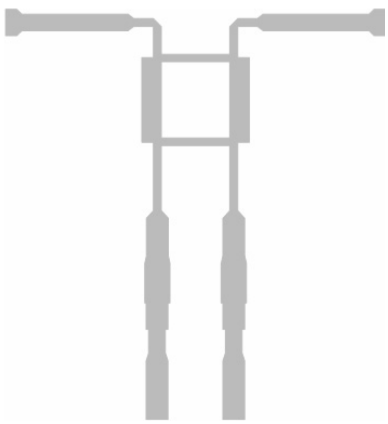

Fig. 13. 1-bit 180° cell optimized layout.

Simulated performances are very encouraging for the phase shift parameter. It can be seen on Figure 14 that, a flat phase shift value within the operating range can be expected.

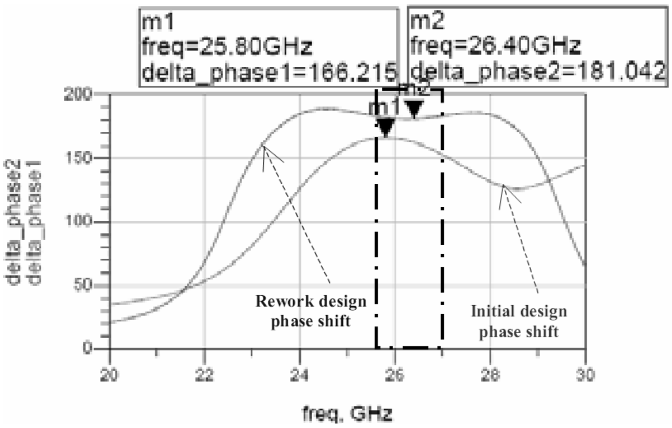

Fig, 14. Phase shift of optimized 180° device.

Figure 15 and Table 3 show the simulated result of the 2-bit phase shifter optimized design.

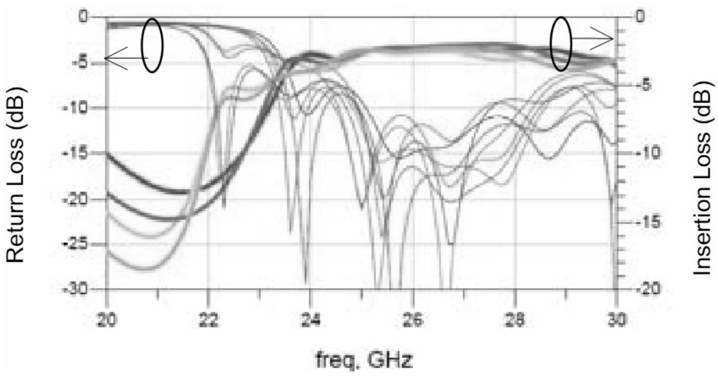

Fig. 15. 2-bit phase shifter performance.

Table 2. 2-bit phase shifter simulated phase shift value

Phase State	45.0	180.0	225.0
Simulated data @26.4 GHz	40	175	216
Delta	-5	-5	-9

The insertion loss of the phase shifter at 26.5 GHz varies from -2 dB for the state (0°) to -2.6 dB for the highest state (225°). The return loss is better than -15 dB for all states within the [25.7-27] GHz frequency range.

5. Conclusion

A 2-bit Ka-Band monolithic phase shifter with XLIM elementary MEMS switches for high power applications has been designed and on-probe measured. The average insertion loss of the circuit is -2.3 dB with a return loss >10 dB within the aimed frequency range [25.7-27] GHz. Power handling capability of a 1-bit 45° phase shifting cell over a wide input power range shows a good behaviour. No self actuation of RF-MEMS has been observed up to an input power of +32 dBm which confirms the interest in XLIM capacitive MEMS technology for power applications.

Taking into account technological parameters uncertainties which have a direct impact on device behaviour and phase shift parameter, back simulations have been done. Redesign of corrected and optimized 45° 1-bit, 180° 1-bit and 2-bit phase shifters have been achieved. Manufacturing of these MEMS based phase shifters will be performed by XLIM laboratory.

Acknowledgment. This work has been performed with the sponsorship of the FILTRAMEMS project led by Thales Communications and supported by French Ministry of Defense. The authors would like to thank E. Gatard from AMCAD for power characterizations.

References

[1] J.-L. CAZAUX, M. FEUDALE, C. DREVON, J.-F.VILLEMAZET, S. DI NARDO, O. VENDIER, S. FORESTIER, *New Technologies for Future Flexible Satellite Payloads: Where are we?*, International Journal of Microwave and Optical Technology, Special Issue Containing Selected Papers of ISMOT-2007, **3**(3). July 2008.

[2] C. PALEGO, Z. PENG, J.C. M. HWANG, D. SCARBROUGH, D.I. FOREHAND C.L. GOLDSMITH, *Compact Ka-Band Phase Shifters Using MEMS Capacitive Switches*, Proc. of EMICC, Sept. 2009.

[3] R. MALMQVIST, C. SAMUELSSON, B. CARLEGRIM, P. RANTAKARI, T. VÄHÄ-HEIKKILÄ, A. RYDBERG, J. VARIS, *Ka-Band RF MEMS Phase Shifters For Energy Starved Millimetre-Wave Radar Sensors*, Semiconductor Conference (CAS), 2010.

[4] J. LAMPEN, S. MAJUMDER, C. JI ,J. MACIEL, *Low-Loss, MEMS Based, Broadband Phase Shifters*, Phased Array Systems and Technology, 2010 Int. Symposium.

[5] F. MAURY, A. POTHIER, A. CRUNTEANU, F. CONSEIL, P. BLONDY, *RF-MEMS Switched Varactors for Medium Power Applications*, DTIP MEMS/MOEMS Symposium, Apr.2008.

[6] C. PALEGO, A. POTHIER, T. GASSELING, A. CRUNTEANU, C. CIBERT, C. CHAMPEAUX, P. TRISTANT, A. CATHERINOT, P. BLONDY, *RF-MEMS Switched Varactor for High Power Applications*, Microwave Symposium Digest, IEEE MTT-S International, pp. 35–38, 11-16 June 2006.

[7] H. ZHANG, A. LAWS, K.C. GUPTA, Y.C. LEE, V.M. BRIGHT, *MEMS Variable-Capacitor Phase Shifters Part II: Reflection-Type Phase Shifters*, Int J RF Microwave CAE 13, pp. 415–425. 2003.

[8] G.M. REBEIZ, G.-L. TAN, J.S. HAYDEN, *RF MEMS Phase Shifters: Design and Applications*, IEEE Microwave Magazine, June 2002.

[9] B. BÉLENGER, B. ESPANA, S. COURRÈGES, P. BLONDY O. VENDIER, D. LANGREZ, J.-L. CAZAUX, *A High-Power Ka Band RF-MEMS 2-Bit Phase Shifter on Sapphire Substrate*, submitted for the publication to EuMIC 2011 Conference.

Design of selectable-band patch filter for WiMax applications using MEMS varactor

G. REHDER, A.L.C. SERRANO, F.S. CORRERA, M.N.P. CARREÑO

Laboratory of Microelectronics, University of São Paulo,
CP 61548, CEP 05424-970, São Paulo, SP, Brazil
E-mail: grehder@lme.usp.br

Abstract. A selectable-band triangular patch filter for WiMax application using MEMS varactors is proposed. The MEMS varactor was designed based on the envisioned fabrication process and the required capacitances to be incorporated to the filter using a flip-chip process and a final MEMS release after incorporation. The filter was simulated by an EM-simulator using the extracted equivalent electrical circuit model for the MEMS varactor. The widths of the 2.5 GHz and 3.5 GHz passbands are 8.35 % and 4.84 %, respectively. The insertion loss within both bandwidths is better than 2.6 dB and the return loss is better than 10 dB.

1. Introduction

Currently, different wireless communication standards such as GSM, WCDMA, WLAN and WiMAX are using more than one operating band to handle more efficiently the information in wireless communication systems. As a consequence, RF/microwave selectable-band circuits are essential for further developments in wireless systems.

The use of MEMS as tuning elements is interesting for their higher performance in terms of loss and nonlinearity when compared to traditional tuning elements such as PIN or varactors diodes, and provides a simple integration with planar resonators, offering a compact size and a wide tuning range On the other hand, planar patch resonators are very attractive for applications in satellite and mobile communication systems where low insertion loss and high power handling are required [1], besides its simple low cost fabrication [2]-[3].

In this paper, MEMS varactors are integrated to a patch filter through a flip-chip process in order to change the filter center frequency. The selected frequencies are the ones assigned to WiMAX frequency bands. The design of a selectable-band patch filter at 2.5 GHz and 3.5 GHz is proposed with a detailed description of the envisaged MEMS varactors fabrication process.

2. Tunable Filter Design

The design of the patch filter in this work is based on the analysis of the dual-mode triangular patch filter with inverted "T" slots of reference [4]. This topology was chosen due to its flexibility shown by the possibility of controlling independently the frequency of each fundamental degenerate mode.

The tunability concept illustrated in [5] was applied to the triangular patch filter in order to obtain a multi-band reconfigurable filterIn [5], two face-to-face varactors diodes were used across each of the four slots of a circular patch filter to change its center frequency and bandwidth. The face-to-face configuration was required to correctly bias the varactors.

Here, in order to simplify the polarization scheme and simply the topology of the MEMS varactor, the triangular patch was divided in four smaller patches. Each of the smaller patches is connected to its neighbor by a varactor. Thus, the varactor can be biased by applying a dc voltage between any two of the smaller patches. The layout of this patch filter is shown in Fig. 1.

The patch resonator is formed by an equilateral triangle with base of 10.8 mm. All the gaps and slots in the layout are 200-μm wide. The small vertical and horizontal slots in Fig. 1 are 1.55-mm and 3.1-mm long, respectively, and they are used to reduce the frequency of the resonant modes, yielding greater miniaturization. The feed lines were designed to have a characteristic impedance of 50 Ω, considering a commercial substrate (Rogers 3010 with ε_r=10.2 and thickness of 25 mils). The varactors C1, C2, C3 and C4 were placed strategically where their influence on the resonant modes are the strongest. The input capacitors (C_{in}=1 pF) are used to achieve a stronger coupling between the feed lines and the resonator.

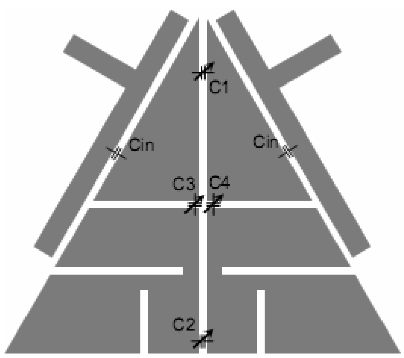

Fig. 1. Layout of the selectable multiband triangular patch filter.

The patch filter of Fig. 1 was simulated with a 3D-planar electromagnetic simulator (Momentum - Agilent) considering the dielectric and conductor losses of the substrate. The influence of ideal varactors on the filter response was simulated with a circuit simulator (ADS - Agilent Technologies) using simple capacitances. The capacitances were varied in order to obtain passbands with center frequencies assigned to WiMax applications *i.e.* 2.3 GHz, 2.5 GHz, 3.5 GHz and 5.8 GHz. Fig. 2 shows the filter frequency responses with different bands and Table 1 lists the insertion and return losses, the 3 dB bandwidth and the capacitances (C1, C2, C3 and C4) required to obtain the related central frequency, Fc. The results demonstrated great center frequency tuning flexibility.

Table 1. Multi-band filter responses and capacitances

Fc (GHz)	Insertion Loss (dB)	Return Loss (dB)	3 dB Bandwidth (%)	C1 (pF)	C2 (pF)	C3 (pF)	C4 (pF)
2.3	1.8	10.4	5.2	7.1	7.1	100	0.85
2.5	1.4	10.6	7.2	7.1	7.1	100	0.3
3.5	2.2	10.2	3.45	2.75	2.75	2.7	0.3
5.8	1.8	15.7	3.8	1.8	1.8	0.2	0.3
3.5/5.8	2.0/1.8	24.5/15.8	4.6/3.8	1.8	1.8	4.5	0.3

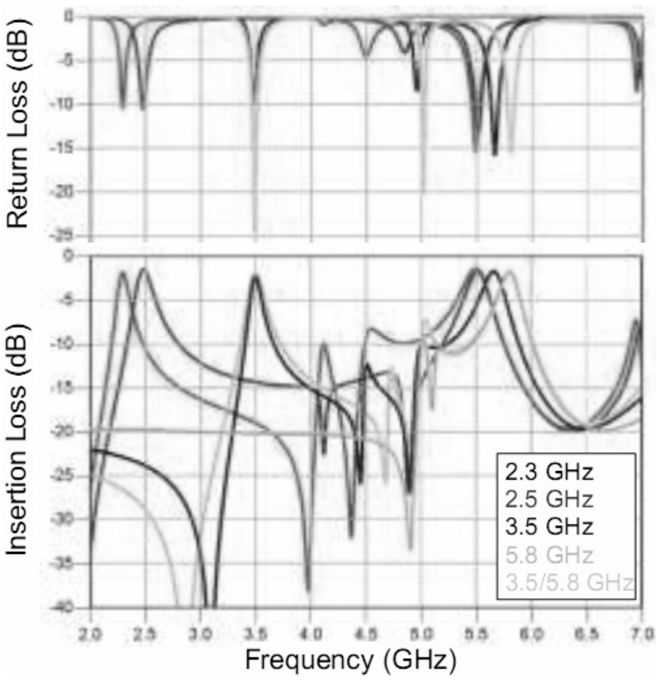

Fig. 2. Performance of the triangular patch filter with capacitances.

The filter frequency responses shown in Fig. 2 are not the only possible ones, since it is possible to arrive at similar results with different combinations of capacitances. For example, the value of C3 could be reduced down to 53 pF with only a small increase in the insertion loss (IL) at the 2.3 GHz and 2.5 GHz passbands. Considering this change, all the capacitances can be obtained with commercial varactors. However, the series resistances of these devices range from 0.8 Ω up to 3.15 Ω [6], which completely degrades the filter response, highly increasing its IL. In fact, resistances greater than 0.1 Ω result in IL greater than 3 dB for most of the passbands of this filter. For this reason, MEMS varactors were developed to tune the filter.

3. MEMS Varactor Design and Modeling

Considering the capacitances ranges required to obtain all the passbands illustrated in Fig. 2, MEMS varactors with up to four positions would be necessary. To simplify the MEMS design and the filter complexity, only two passbands were selected as a proof-of-concept: 2.5 GHz and 3.5 GHz. Simulations showed that it is possible to switch between these two passbands using only MEMS with up to two positions. In this case, C1 is not required, C2 and C4 have the same capacitances of 70 pF (DOWN position) and 2.45 pF (UP position), while maintaining C3 and Cin constant at 3.9 pF and 1 pF, respectively.

The MEMS varactors were designed to be fabricated using the process described in Fig. 3. The main idea is to fabricate the patch filter using conventional printed circuit board technology on commercial RF substrates and to incorporate the MEMS with a flip-chip process.

The MEMS is to be fabricated using conventional microelectronic processes on low-cost glass substrate. In the envisioned fabrication process (Fig. 3), a sacrificial film, such as SiO_2, is deposited over the substrate to allow the structure to be released from the substrate after it integration to the patch filter. A seed layer of titanium, used for adherence, followed by a layer of copper, is deposited over the sacrificial layer (Fig. 3a).

Then, the geometry of the MEMS structure, with 500 μm by 500 μm parallel plates, is defined with conventional photolithography. The photoresist is used as mask to electroplate a thicker copper film (1μm) that will be the structural material of the MEMS varactor. After that, an insulator (Si_3N_4–85 nm) and another sacrificial layer

(SiO_2 –1 μm) are deposited and patterned (Fig. 3b). Once again, a seed layer of Ti/Cu is deposited and the geometry of the copper supports is defined on a photoresist. A thick copper film (10 μm) is then electroplated to form the supports that will be attached to the patch filter (Fig. 3c). These supports are bonded using solder spheres to the patch filter and a final release step (Fig. 3d) removes the sacrificial films, freeing the MEMS varactor and eliminating the glass substrate.

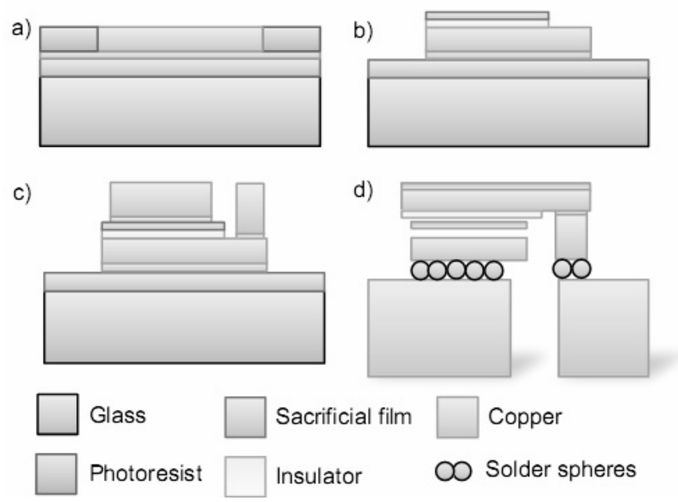

Fig. 3. Fabrication process flow for the MEMS varactor.

Based on the fabrication process described above, the MEMS varactor, shown in Fig. 4, was simulated using a full-wave 3D electromagnetic simulator (HFFS – Ansoft).

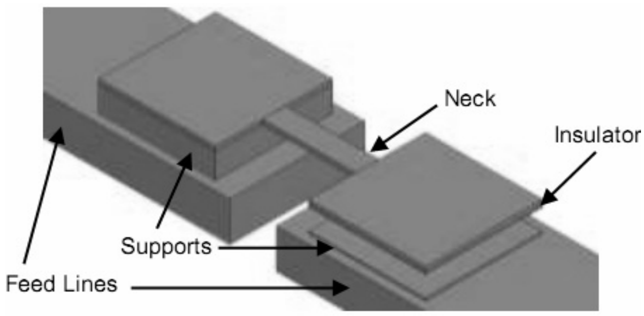

Fig. 4. Topology of the MEMS varactor in the UP position.

Considering the dimensions of the neck (400 μm × 100 μm), a low pull-in voltage is estimated of approximately 8 V, based on [7]. The capacitance in the DOWN position is expected to be 70 pF and in the UP position, 2.45 pF.

By comparing the HFSS simulated results with an equivalent RLC circuit, it was possible to extract values for the equivalent capacitance, resistance and inductance of the MEMS varactor, shown in Fig. 5.

Fig. 5. RLC equivalent circuit for the UP position (2.45 pF) and the DOWN position (70 pF).

Fig. 6 shows that the HFSS simulation results of the MEMS structure and the equivalent electrical circuit model results agree considerable well.

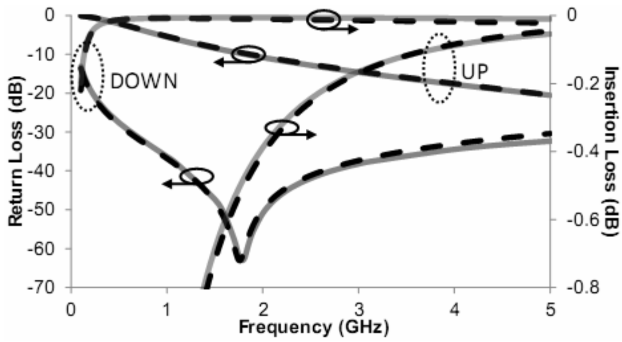

Fig. 6. Comparison between the results of the HFFS model (solid line) and the equivalent RLC circuit (dashed line) for the MEMS varactor in the UP and DOWN positions.

The equivalent RLC circuit was incorportated into the patch filter model (Fig. 1). The capacitances at the UP and DOWN positions and the filter layout had to be adjusted to account for the parasitic inductance of the MEMS model. The small vertical and horizontal slots were increased to 1.75 mm and 3.4 mm long, respectively. The UP and DOWN capacitance were changed to 2.65 pF and 65 pF, respecively, and C3 was changed to 3.8 pF. Fig. 7 shows the performace of the triangular patch filter with the MEMS varactors. In theses simulations, the substrate losses were considered.

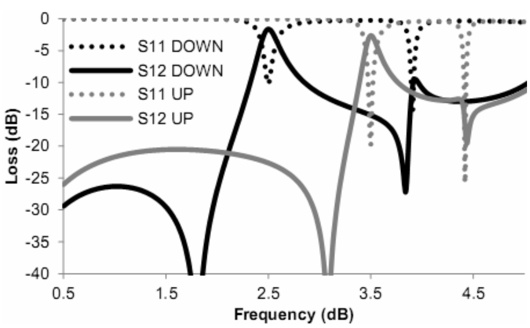

Fig. 7. Simulated performance of the selectable band patch filter with MEMS varactor.

In the selectable band patch filter, the bandwidths of the 2.5 GHz and 3.5 GHz passbands are 8.35 % and 4.84 %, respectively. The insertion loss within the passbands is better than 2.6 dB and the return loss is better than 10 dB.

4. Conclusion

A selectable-band filter was designed for integration with MEMS varactors through a flip-chip process. Two-position MEMS varactors were designed with 65 pF and 2.65 pF capacitances and modeled based on the proposed low-cost fabrication process. The simulated filter response demonstrates that the filter can be switched rom 2.5 GHz to 3.5 GHz using a low bias voltage of approximately 8 V, maintaining adequate performance.

Acknowledgement. The authors wish to acknowledge the financial support of the Brazilian agency FAPESP.

References

[1] J. HELSZAJN and D.S. JAMES, *Planar triangular resonators with magnetic walls*, IEEE Transactions on Microwave Theory and Techniques, **26**(2), pp. 95–100, February 1978.
[2] J.S. HONG and S. LI, *Theory and experiment of dual-mode microstrip Triangular Patch Resonators and Filters*, IEEE Transactions on Microwave Theory and Techniques, **52**(4), pp. 1237–1243, April 2004.
[3] L. ZHU, *et al.*, *Miniaturized Dual-Mode Bandpass Filter Using Inductively Loaded Cross-Slotted Patch Resonator*, IEEE Microwave and Wireless Components Letters, **15**(1), pp. 838–840, Dec 2005.
[4] A.L.C. SERRANO and F.S. CORRERA, *A Triple-Mode Bandpass Filter Using a Modified Circular Patch Resonator*, Microwave and Optical Technology Letters, **51**(1), pp. 2897–2902, January 2009.
[5] A.L.C. SERRANO, T.P. VUONG, F.S. CORRERA, P. FERRARI, P.O. BOX and S. PAULO, *A Tunable Bandpass Patch Filter with Varactors*, in Microwave Symposium Digest (MTT), Anaheim, May 2010, pp. 1752–1755.
[6] http://www.skyworksinc.com/
[7] S.D. SENTURIA, Microsystem Design, Kluwer Academic Publishers, 2001.

Tunable Metamaterial Devices by means of Two-Hot-Arm Electrothermal Actuators

A.X. LALAS, N.V. KANTARTZIS, T.V. YIOULTSIS, T.D. TSIBOUKIS

Department of Electrical and Computer Engineering, Aristotle University of Thessaloniki, GR-54124, Thessaloniki, Greece
E-mail: tsibukis@auth.gr

Abstract. A reconfigurable metamaterial, obtained from the combination of two-hot-arm electrothermal actuators with a split-ring resonator, is presented in this paper. Offer-ing a reliable control of the tip displacement, the selected actuators overcome the undesired bandwidth constraints of existing structures and establish significant levels of tunabil-ity. To this goal, the actuator is realized as an integrated part of the resonator. The proposed design is numerically verified through several setups which prove its left-handed behavior.

1. Introduction

Metamaterials, as artificially engineered electromag-netic media, exhibit unique electromagnetic properties not available in nature. Among the multitude of contemporary applications, their combination with nanostructures has been intensively researched [1]-[4]. Nonetheless, such implementations are still rather limited, mainly due to the lack of a wide spectral bandwidth. So, the design of meta-materials with a controllable operating frequency is deemed critical to overcome the prior constraints. To this aim, various tuning mechanisms have been proposed [5]-[8]. However, the excellent features of radio-frequency microelectromechanical systems (RF-MEMS) [9]-[11] offer the most viable solutions, as they introduce the de-sired tunability which circumvents bandwidth restrictions.

A noteworthy design of RF-MEMS switches that can provide robust control of the tip displacement, and hence fulfill the above requirements, is the two-hot-arm thermal actuator [12], [13]. This type of electrothermally actuated apparatus may be used as a powerful switching element or as a part of a tuning mechanism, *e.g.* a reconfigurable capacitor with an externally movable dielectric. In the former case, the actuator causes a negligible impact in the overall performance of the controllable device, while in the latter it is responsible only for the device's rear-rangement. Although various interesting studies have been presented, to the best of our knowledge, the association of the two-hot-arm thermal actuator with an electromag-netic structure as a fully operational component has not been yet numerically explored. Therefore, it is the goal of this paper to examine the combination of the aforemen-tioned actuator with a split-ring resonator (SRR) in order to obtain a reconfigurable metamaterial. The proposed design launches the actuator as an integral component of the SRR and supports its claims by a set of accurate nu-merical results with a left-handed profile.

2. Design of the Electrothermal Actuator

The two-hot-arm design approach of a thermal actuator exhibits some important advantages over existing realiza-tions, such as increased power consumption efficiency and thinner flexure, which lead to enhanced levels of deflection. Its principal operation is summarized in the asymmetric thermal expansion of the hot and cold arms, while an electric circuit is created by setting a potential difference between them. In this manner, electric current travels along the hot arms, resulting in resistive heating and thermal expansion, whereas the thicker arm remains cold, since it is not part of the electric circuit. Conse-quently, a deflection occurs owing to the expansion dif-ference between hot and cold arms.

The design parameters of the PolySilicon two-hot-arm horizontal thermal actuator, as depicted in Fig. 1, are: L_1 = 252 μm, L_2 = 220 μm, L_3 = 162 μm, L_4 = 38 μm, w_1 = 21 μm, w_2 = 14 μm, w_3 = 14 μm, d = 2 μm, and g = 5 μm. Also, the height of dimples and anchors is set to 2 μm, while the height of the remaining actuator is 2 μm.

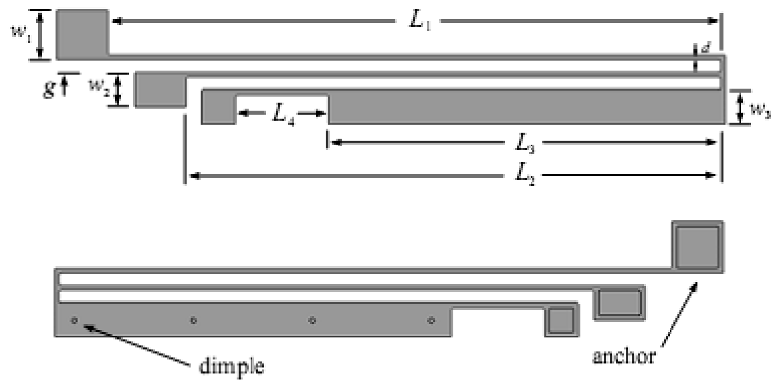

Fig. 1. Front and back side of the two-hot-arm actuator.

A cou-pled electric, thermal and structural analysis along with a parametric study for the actuation voltage are conducted in order to identify the primary characteristics of the device. In this framework, the displacement of the actuator's tip versus the actuation voltage is illustrated in Fig. 2.

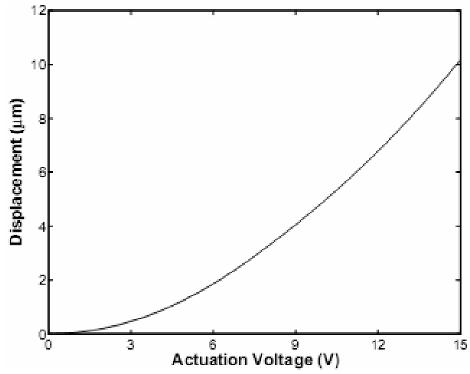

Fig. 2. Maximum tip displacement for different values of the actuation voltage.

To avoid the presence of unwanted short circuits that may degrade the device's performance, the operational range is limited to 15 V. Based on the above notions, Fig. 3 presents the deformed geometry of the actuator together with its corresponding total displacement distribution.

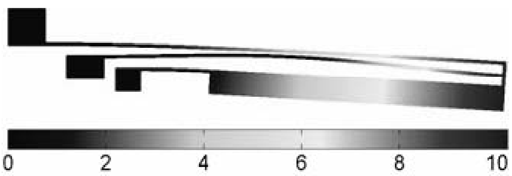

Fig. 3. Total displacement distribution on the actuator (in μm) at the actuation voltage of 15 V.

3. Controllable Metamaterial Unit Cell

The geometry of our controllable 550×473 μm meta-material unit cell – formed via the gap between the actua-tors and the SRR – is given in Fig. 4.

When a voltage is applied to the actuator's arms, a deformed structure oc-curs and the gap is shortened. Therefore, variations in voltage levels introduce a tunable gap and as a conse-quence a reconfigurable SRR. The width of its metal strip is 28 μm, the cell period is 650 μm, the height of the SRR is 4 μm, and the thickness of the Si_3N_4 substrate is 20 μm. Furthermore, the length and the width of the cou-pling bar between the two independent actuators are 150 μm and 14 μm, respectively. Bearing in mind the prior structural data, all numerical simulations are performed by means of the finite element method. In order to extract the S-parameters, a parallel-plate waveguide approach is adopted, which requires the use of PEC and PMC bound-ary conditions instead of the conventional periodic boundary conditions. Also, a robust homogenization method [14] is utilized to retrieve the constitutive effec-tive parameters of the proposed metamaterials. In this context, Fig. 5 illustrates the magnitude of the S_{11}- and S_{21}-parameter of the reconfigurable metamaterial at the actuator voltage of 0 V.

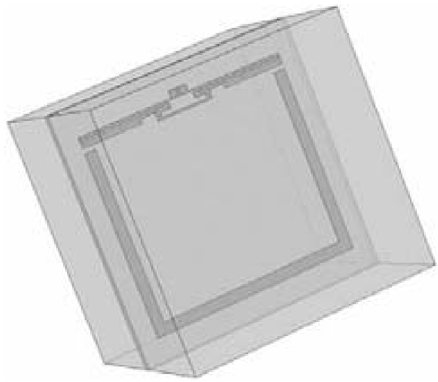

Fig. 4. Geometry of the electrothermally controlled, in terms of two independent actuators, metamaterial unit cell.

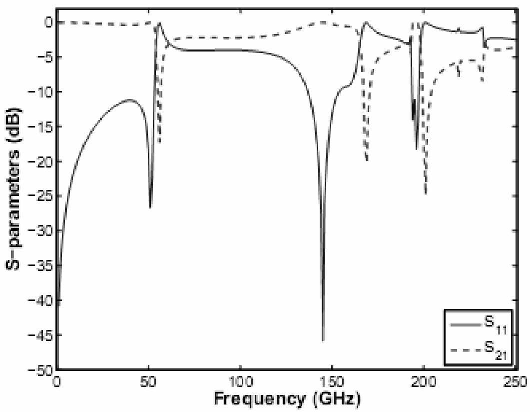

Fig. 5. S-parameters of the reconfigurable device at the ac-tuation voltage of 0 V.

Results indicate the pres-ence of three acute resonant frequencies for the S_{21}-parameter, *i.e.* at 56 GHz, 169 GHz, and 201 GHz. To this direction, the left-handed behavior of the combined structure can be substantiated in Fig 6, which illustrates the variation of the real and imaginary part of both effec-tive constitutive parameters.

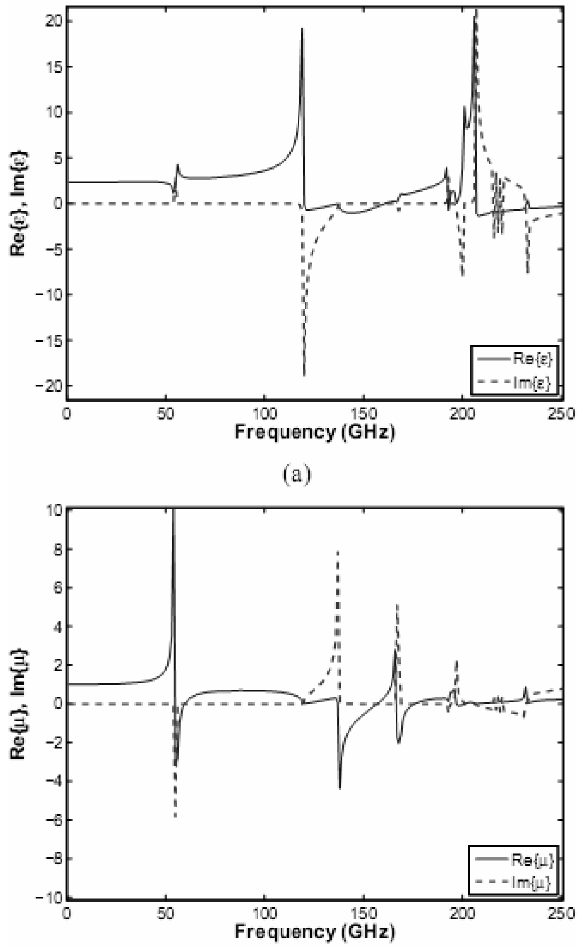

(b)

Fig. 6. Left-handed performance at the actuation voltage of 0 V. (a) Effective dielectric permittivity and (b) effective mag-netic permeability.

However, in order to ensure the validity of the homogenization technique the opera-tional wavelength must be higher than the cell period by a factor of 8 at least. Thus, the presence of three distinct negative μ frequency regions is easily discerned, but only the first is identified as a left-handed resonance. Addi-tional evidence of the enhanced tunability accomplished by our controllable device can be obtained from Figs 7 and 8, where the variation of the S_{11}- and S_{21}-parameter is -l examined for different actuation voltages. In fact, as the actuation voltage increases from 0 V to 15 V, a certain shift (around 2-3 GHz) at all resonant frequencies is achieved.

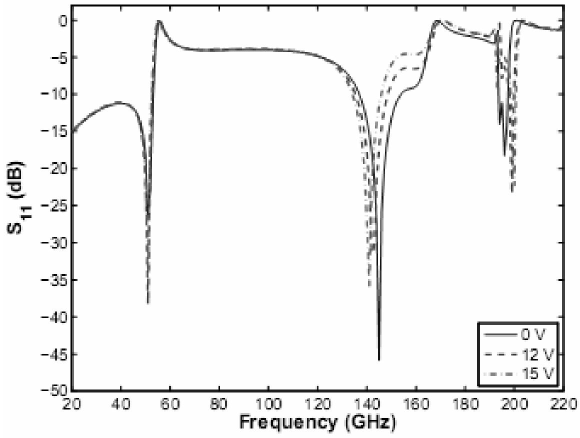

Fig. 7. Tunable behavior at several actuation voltages in terms of S_{11}-parameter.

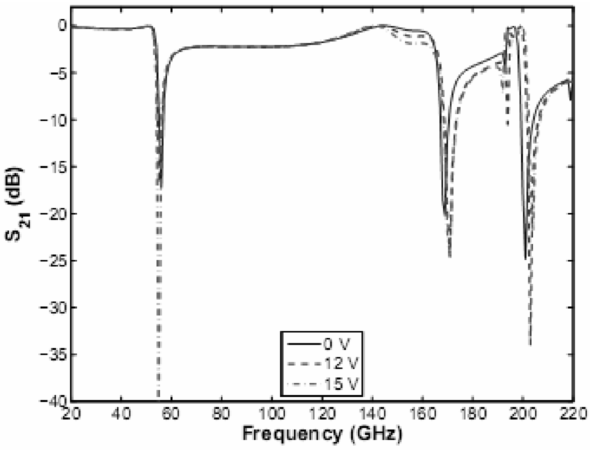

Fig. 8. Tunable behavior at several actuation voltages in terms of S_{21}-parameter.

Similar deductions may be drawn from the shift of the real part of the effective magnetic permeabil-ity in Fig. 9, while Fig. 10 presents two snapshots of the electric field at two resonant frequencies of the device for an actuation voltage of 0 V.

Concentrating on the results so far acquired, it has to be stressed that, despite initial theoretical predictions, a nontrivial number of multiple gaps is involved in the overall analysis. This simply implies that multiple reso-nant frequencies are sufficiently amplified, thus compli-cating the investigation of such devices. Moreover, it becomes apparent that the use of two independent electro-thermal actuators enables the fine tuning of the resulting metamaterial – with respect to the actuator voltage of 0 V– on condition that the proper bias network (separate for each actuator) is employed.

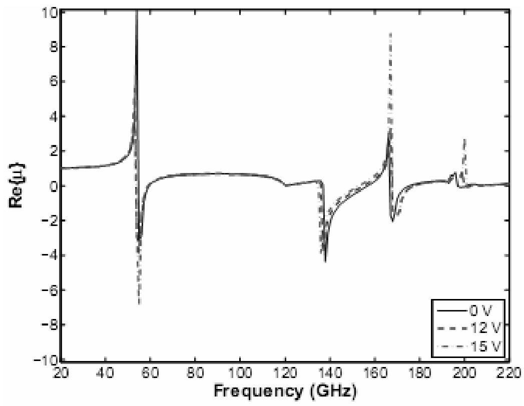

Fig. 9. Tunable left-handed performance at several actuation voltages in terms of effective magnetic permeability.

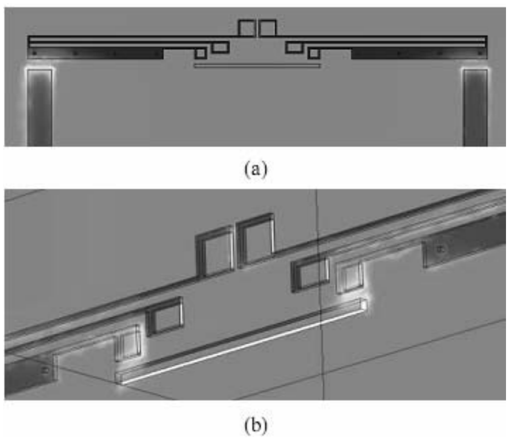

Fig. 10. Electric field snapshots of the electrothermally con-trolled, in terms of two independent actuators, metamaterial unit cell at (a) 56 GHz and (b) 201 GHz.

Should we have required a simpler configuration with only one bias network, the novel double parallel actuated structure of Fig. 11 can be considered. However, this simplification is at a slight expense of fine tunability, as the double parallel actuator is proven more rigid. So, this tradeoff between bias network complexity and fine tuna-bility must be taken into account during the design of such devices, depending on the operational priorities.

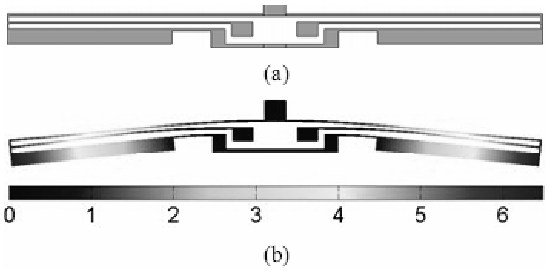

Fig. 11. (a) Geometry of the double parallel actuated device and (b) its total displacement distribution (in μm) at the actua-tion voltage of 12 V.

Taking into account the aforementioned properties, a reconfigurable metamaterial unit cell, which incorporates the double parallel actuated device, is designed and nu-merically investigated. The enhanced tunability achieved by our controllable device can be confirmed via Fig. 12, where the variation of the S_{11}- and S_{21}-parameter is exam-ined for different actuation voltages.

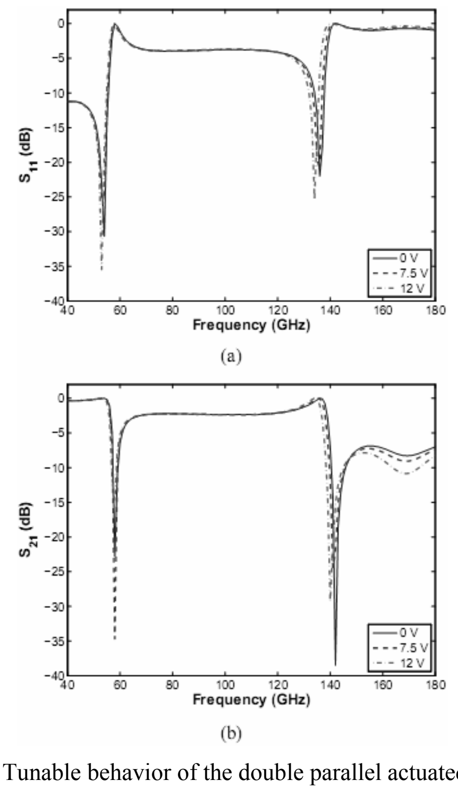

Fig. 12. Tunable behavior of the double parallel actuated de-vice at several actuation voltages in terms of (a) S_{11}-parameter and (b) S_{21}-parameter.

At 0 V, the presence of two acute resonant frequencies for the S_{21}-parameter, *i.e.* at 58 GHz and 142 GHz, is revealed. However, as the actuation voltage increases from 0 V to 12 V, a certain shift (around 1-2 GHz) at all resonant frequencies is observed. Congruent deductions may be obtained from the shift of the real part of the effective magnetic perme-ability in Fig. 13, while the homogenization condition, denoting a left-handed performance, is only satisfied for the first resonance. Finally, Fig. 14 presents a snapshot of the electric field at the first resonant frequency of the device for an actuation voltage of 12 V.

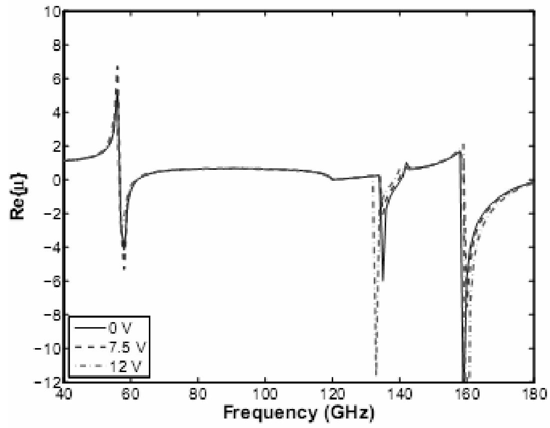

Fig. 13. Tunable left-handed performance of the double parallel actuated device at several actuation voltages in terms of effective magnetic permeability.

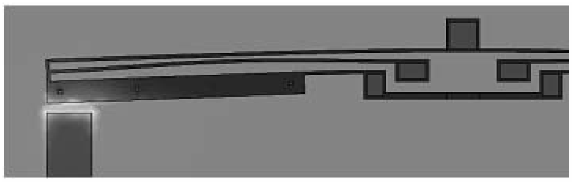

Fig. 14. Electric field snapshot of the double parallel actuated device at 58 GHz.

The reconfigurable unit cells presented herein exhibit left-handed behavior as well as conventional performance depending on the frequency region utilized. In both cases, the tuning property in terms of bandwidth and frequency shifting is accomplished, thus allowing the design of sev-eral applications, such as millimeter wave filters and modulators. Moreover, the electrothermal principle of controllability provided by the two-hot-arm horizontal thermal actuator enables driving these devices by means of a low voltage. Hence, the controllable unit cells may be incorporated in mobile apparatus, where low voltage specifications are enforced by limited power availability.

4. Conclusion

The use of two-hot-arm thermal actuators in the effi-cient design of finely tunable metamaterials has been analyzed and numerically studied in this paper. A left-handed performance has been attained for several states, leading to useful millimeter wave implementations.

Acknowledgement. This work was supported by the National Scolarships Foundation of Greece (IKY), under Grant No. 5282.

References

[1] J.F. O'HARA, R. SINGH, I. BRENER, *et al.*, *Thin-film sensing with planar terahertz metamaterials: sensitivity and limita-tions*, Opt. Express, **16**, pp. 1786–1795, 2008.

[2] L. SOLYMAR and E. SHAMONINA, Waves in Metamaterials, 1st ed., Oxford University Press, Inc., 2009.

[3] A.E. NIKOLAENKO, F. DE ANGELIS, S.A. BODEN, *et al.*, *Car-bon nanotubes in a photonic metamaterial*, Physical Re-view Letters, **104**, art. no. 153902(1-4), 2010.

[4] R. SINGH, I.A.I. AL-NAIB, M. KOCH and W. ZHANG, *Asymmetric planar terahertz metamaterials*, Opt. Ex-press, **18**, pp. 13044–13050, 2010.

[5] H. TAO, A.C. STRIKWERDA, K, FAN, *et al.*, *Reconfigurable terahertz metamaterials*, Phys. Rev.Lett. **103**, 147401, 2009.

[6] J.M. MANCEAU, N.H. SHEN, M. KAFESAKI, *et al.*, *Dynamic response of metamaterials in the terahertz regime: Blue-shift tunability and broadband phase modulation*, Appl. Phys. Lett. **96**, 021111, 2010.

[7] W.M. ZHU, H. CAI, T. BOUROUINA, *et al.*, *A MEMS tunable metamaterial filter*, in Proceedings of the 23rd Interna-tional Conference on MEMS, pp. 196–199, Hong Kong, China, January 2010.

[8] X.-J. HE, Y. WANG, J.-M. WANG and T.-L. GUI, *MEMS switches controlled multi-split ring resonator as a tunable metamaterial component*, Microsystem Technology, **16**, pp. 1831–1837, 2010.

[9] G.M. REBEIZ, *RF MEMS: Theory, Design, and Technol-ogy*, 1st ed., John Wiley & Sons, Inc., 2003.

[10] C. LUGO, G. WANG, J. PAPAPOLYMEROU, *et al.*, *Frequency and bandwidth agile millimeter-wave filter using ferroelec-tric capacitors and MEMS cantilevers*, IEEE Transactions on Microwave Theory and Techniques, **55**(2), pp. 376–382, 2007.

[11] S. LUCYSZYN (Ed.), Advanced RF MEMS, 1st ed., Cam-bridge University Press, 2010.

[12] D. YAN, A. KHAJEPOUR and R. MANSOUR, *Modeling of two-hot-arm horizontal thermal actuator*, Journal of Microme-chanics and Microengineering, **13**, pp. 312–322, 2003.

[13] D. GIRBAU, M. LLAMAS, *et al.*, *A low-power-consumption out-of-plane electrothermal actuator*, Journal of Micro-electromechanical Systems, **16**, pp. 719–727, 2007.

[14] X. CHEN, T.M. GRZEGORCZYK, B.I. WU, J. PACHECO and J.A. KONG, *Robust method to retrieve the constitutive ef-fective parameters of metamaterials*, Physical Review E, **70**(1), art. no. 016608(1–7), 2004.

Design of Ohmic Miniature MEMS Components for Fast Reconfiguration

Aurélie VERGER[1], Arnaud POTHIER[1], Cyril GUINES[1], Aurelian CRUNTEANU[1], Pierre BLONDY[1], JeChristophe ORLIANGES[2], Jérémie DHENNIN[3], Frédéric COURTADE[4], Olivier VENDIER[5]

[1]XLIM UMR6172–Université de Limoges/CNRS, 123 avenue Albert Thomas, 87060 Limoges, Franc
[2]SPCTS UMR 6638–Université de Limoges/CNRS, 123 avenue Albert Thomas, 87060 Limoges, Franc
[3]NOVAMEMS, 10 avenue de l'Europe, 31520 Ramonville, France
[4]CNES, 18 avenue Edouard Belin, 31401 Toulouse Cedex9, France
[5]Thales Alenia Space, 26 avenue Jean-François Champollion, 31100 Toulouse, France

Abstract. A miniature multilayer beam (alumina / aluminum / alumina) has been recently proposed for capacitive ultra fast RF MEMS switches design and fabrication. This component presents a 40 V pull-in voltage and is able to achieve the switching time as low as 50 ns once biased with 80 V actuation voltage which is the faster RF MEMS capacitor reported up to now. Based on this setup, this paper describes our current work on ohmic contact switch design based miniature and multilayer high stiffness beam geometry. The presented concept is expected to achieve switching time lower than 300 ns considering a 7 V pull-in voltage.

1. Introduction

RF-MEMS switches and switchable capacitor should be promised to a fruitful future. Their impressive linearity capabilities, their superior RF performances and their very small DC consumption requirements make them serious competitors for semiconductor technologies. Huge research efforts are currently done to bring solutions to their reliability limitation and lead this MEMS technology to the maturity required for industrial applications. However, RF MEMS components still suffer from limitation; their switching time, generally of few microseconds is one of them [1-2]. It is usually limited by the time required to move physically the beam mechanical structure. Hence, this time limits the use of MEMS components for fast reconfigurable application.

In order to improve the switching time, some studies were already made. Rebeiz [3], from San Diego University, showed that downsize the beam compare to the actual common sizes, results in high mechanical resonance frequency able to reach high switching speed. Indeed, with a 20 µm long and 9 µm large beam, switching times below 500 ns could be measured. Lacroix [4], from XLIM laboratory, demonstrates by reducing the beam dimensions and adding simple bent sides on conventional beam edges, strongly increases the beam mechanical stiffness. With this setup, he obtained 200 ns switching time. Another study has been made by Berkeley laboratory [5]. It demonstrated the use of micro electromechanical component in logic application. With this setup, 300 ns switching time was achieved.

50 ns are achieved, for capacitive components, made of a multilayer beam alumina/aluminum/alumina [6]. The beam, whose dimensions are 30 µm long by 25 µm large, presents a 40 V pull-in voltage. From this setup, in this paper, an ohmic contact RF MEMS component design is presented based on with nanogap electrostatic actuators. The miniature membrane consists also in a composite structure of three layers alumina/aluminum/alumina supporting a gold based contacting electrode. Thanks to this setup and an appropriated mechanical design, pull-in voltage under 10 V can be achieved for switching time close to 250 ns.

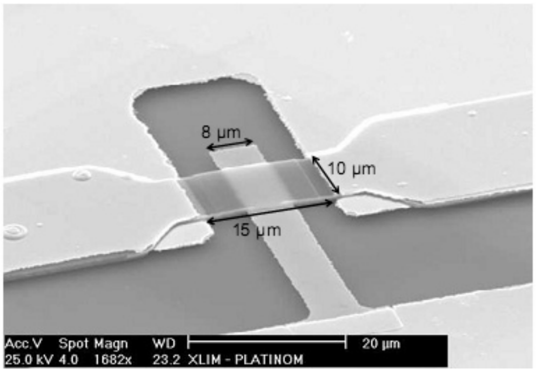

Fig. 1. SEW view of fabricated bridges structure; beam dimension 15 µm long and 10 µm wide.

To increase the beam mechanical resonance frequency, a first approach is to miniaturize the mobile structure [4]. A second approach is to use for the mobile structure, one or combination of materials with enhanced mechanical properties.

In a previous study [6], we designed suspended miniature structures made with several thin film materials stacked to achieved a high mechanical performance membrane that have been implemented on a CPW line to form ultra fast switchable capacitors (Figure 1). Thus, aluminum has been favored since it is a very good conductor and also because it's a very light material (2.7 g/cm^3) that will allow to guaranty high mechanical resonance frequencies for the MEMS structure. To enhance its mechanical capabilities, aluminum layer has been encapsulated between two others material layers. For this stack, alumina was a good candidate because of its very low density (3.9 g/cm^3), but also its high Young's modulus (380 GPa) which allow to achieve a high stiffness thin film. Based on this alumina / aluminum / alumina structural material with respective thickness of 100 nm / 200 nm / 100 nm, some MEMS components have been developed based on fixed-fixed miniature beams geometry. This setup ensures high mechanical resonant frequencies in the range of several MHz, compared to few tens of kHz for conventional RF MEMS components.

In fact, once looking for high MEMS device structural material stiffness that allows reaching fast switching speed, also impacts on the beam pull-in voltage. This voltage is related to the beam stiffness and the gap between the beam and the actuation electrode. This electrode was recovered of a 200 nm aluminum nitride dielectric layer to ensure a RF capacitive contact. Thus, to keep reasonable lower voltages, the air gap was reduced by a factor of 10 compared to conventional values. With a gap of 300 nm, lower voltages than 50 V should be sufficient to actuate the component. From this configuration, in order to reach sub-microseconds switching time range with this device, it's necessary to tune the beam sizes (length, width, thickness). In Table 1, some geometry which have been designed and fabricated as a proof of concept of ultra fast switched MEMS capacitors are shown.

The beam mechanical resonance frequency and the pull-in voltage were simulated using 3D Finite Element Method Ansys mechanical simulations [7]. Then, the switching time values were calculated from the computed beam mechanical resonance frequency and the equation (1) [8] considering a V_{app}/V_p ratio of 1.5. The computed results for the several designs are summarized in Table 1.

Table 1. Summary of Expected and Measured Values for Several Designs

Beam length (µm)	Bean witdh (µm)	Actuation electrode witdh (µm)	Computed beam mechanical resonance frequency (MHz)	Measured beam mechanical resonance frequency (MHz)	Computed switching time (ns) @1.5×Vp	Measured switching time (ns) @1.5×Vp	Computed pull-in voltage (V)	Measured pull-in voltage (V)
15	10	8	18.7	18.9	21	40*	120	76
20	15	13	10.6	10.5	37	65	68	54
25	15	18	6.8	6.5	57	75	44	30
30	25	23	4.8	4.7	82	110	31	40
35	25	28	3.5	3.5	111	130	22	42

* @ 1.2×Vp

$$t_s \approx 3{,}67 \frac{V_p}{2\pi V_{app} f_0} \quad (1)$$

From specific test bench, the beam mechanical resonance frequency and the switching time have been measured and demonstrated good performances (Table 1). Indeed, switching times below 100 ns are achieved and the beam pull-in voltages are close to 50 V.

Moreover, the fabricated switched RF performances have also been measured. To evaluate the off-state and the on-state capacitances, the S_{21} parameters measurements are itting with an equivalent circuit using Agilent Momentum electromagnetic simulator [9]. Table 2 summarizes the RF performance measurements for several designs.

As we can see in Table 1, the smaller components have a low switching time, but also a low contrast corresponds at these components. This is the price of small contacting surface associated to very small air gap distance design.

Table 2. RF Performance Measurements

Beam length (µm)	Actuation electrode witdh (µm)	C_{off} (fF)	C_{on} (fF)	C_{on}/C_{off}
15	8	8	15	1.9
20	13	10	30	3
25	18	13	42	3.2
30	23	18	82	4.6
35	28	19	110	5.8

3. Mechanical Design for Ohmic Contact Relays

From this concept, to improve the contrast and to use low actuation voltage, a design of a miniature ohmic component has been studied. In this case, we keep the miniature multilayer membrane (alumina / aluminum / alumina) geometry and thickness (100 nm / 200 nm / 100 nm). A carbon pull down electrode coated by a dielectric layer has been added since in this case the contact electrode could not be used as electrostatic actuator electrode. An evaporated titanium/gold metallization layer takes place to define the RF contact area at the extremity of the RF line discontinuity. The multilayer membrane is suspended 300 nm above these contact electrodes and is anchored between two metallization layer to mechanically fixe the beam extremities.

To allow the RF transmission signal once the membrane will be pulled down, a gold contact bar including dimples are added below the multilayer membrane. RF signal will be transmitted along.

In order to have a beam pull-in voltage smaller than 10V, several designs are considered. Figure 3 shows the pull-in voltage for a fixed-fixed multilayer beam for several lengths considering a 30 µm large beam. The gold contact dimple dimensions are 28 µm long and 10 µm large. We can see that the pull-in voltage is smaller than 10 V for beam length higher than 42 µm.

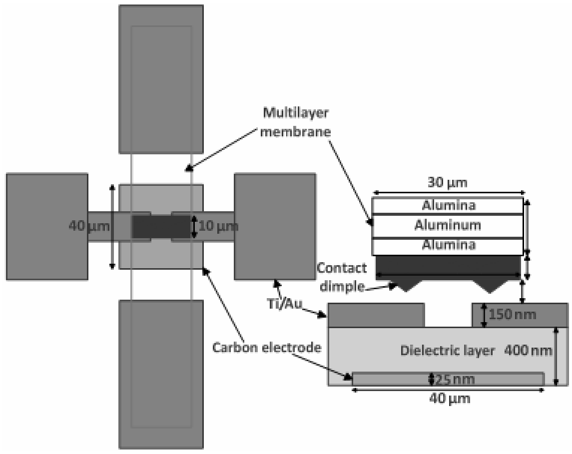

Fig. 2. Design of ohmic contact miniature MEMS relay.

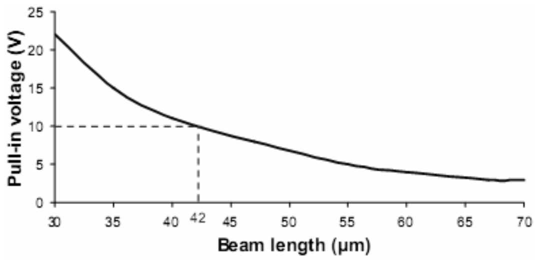

Fig. 3. Effect of the beam length on the pull-in voltage.

The corresponding switching time is shown on Figure 4. For beam length higher than 42 µm, the switching time is higher than 200 ns. We chose to have a small pull-in voltage in despite of a switching time higher than 200 ns. For example, for a 50 µm long beam, the pull-in vol tage is 7 V and the switching time is 285 ns considering 10.5 V actuation voltage.

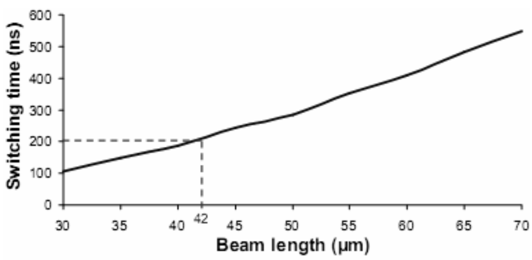

Fig. 4. Effect of the beam length on the switching time.

In order to have switching time below 200 ns and actuation voltage below 10 V the gap should be decreases. But with gap under 300 ns, the technology process becomes complex especially to realize efficient gold dimple contact.

For this design, the contact force per contact area is evaluated to be in the 8 μN range once actuation voltage reaches 10.5 V. When the contact force increases, the insertion losses are reduced.

Beam tests structures are actually in fabrication. The latest experimental results will be presented during the conference.

4. Conclusion

An approach to design miniature ohmic RF MEMS component has been presented. This multilayer beam alumina / aluminum / alumina with gold dimple contact allows reaching pull-in voltage below 10 V with switching time in the 250 ns range. To valid the presented concept, beam tests structures are being fabricated.

References

[1] Z.J. YAO, S. CHEN, S. ESHELMAN, D. DENNISTON and C. GOLDSMITH, *Micromachined low-loss microwave systems*, IEEE Journal of Microelectromechanical Systems, **8**(2), pp. 129–134, 1999.

[2] B. Mc CARTHY, G.G. ADAMS, N.E. MC GRUER and D. POTTER, *A dynamic model, including contact bounce, of an electrostatically actuated microswitch*, Journal of microelectromechanical Systems, **11**(3), pp. 276–283, 2002.

[3] B. LAKSHIMINARAYANAN, D. MERCIER and G. REBEIZ, *High-reliability miniature RF-MEMS switched capacitors*, IEEE Trans. Microwave Theory & Tech., **56**(4), pp. 971–981, Apr. 2008.

[4] B. LACROIX, A. POTHIER, A. CRUNTEANU, C. CIBERT, F. DUMAS-BOUCHIAT, C. CHAMPEAUX, A. CATHERINOT and P. BLONDY, *Sub-Microsecond RF MEMS Switched Capacitors*, IEEE Trans. Microwave Theory & Tech., **55**(6), pp. 1314–1320, Jun. 2007.

[5] H. KAM, V. POTT, R. NATHANAEL, J. JEON, E. ALON and T.-J. KING LIU, *Design and reliability of a micro-relay technology for zero-standby-power digital logic applications*, IEDM Tech. Dig., pp. 809–812, 2009.

[6] A. VERGER, A. POTHIER, C. GUINES, A. CRUNTEANU, P. BLONDY, J.C. ORLIANGES, J. DHENNIN, F. COURTADE, O. VENDIER, *Sub-hundred nanosecond reconfiguration capabilities of nanogap RF MEMS switched capacitor*, IEEE MTT-S International Microwave Symposium Digest, pp. 1238–1241, 2010.

[7] Ansoft Ansys, www.ansys.com

[8] N.S. BARKER, *Distributed MEMS Transmission Lines*, Michigan PhD Dissertation, 1999.

[9] Agilent Technologies, www.agilent.com.

Capacitance Tuning Behavior of a BiCMOS Embedded RF-MEMS Switch

M. KAYNAK[1], M. WIETSTRUCK[1], W. ZHANG[1], R. SCHOLZ[1], B. TILLACK[1,2]

[1]IHP, Im Technologiepark 25, 15236 Frankfurt (Oder), Germany
[2]Technische Universität Berlin, Berlin, Germany
Tel: (+49) 335 5625 707, Fax: (+49) 335 5625 327,
Email: kaynak@ihp-microelectronics.com

Abstract. The capacitance tuning behavior of a BiCMOS embedded RF-MEMS switch is investigated. The novel switch electrode configuration allows precisely obtaining intermediate capacitance values between the off-state (Coff) and on-state (Con) capacitances under specific AC signal conditions. The stable capacitance tunability is demonstrated by both optical and electrical methods. For AC amplitudes up to 400mV, capacitance tuning with a ratio of 1:10 is achieved without any pull-in effect. The results show that the RF-MEMS switch can be used as a tunable capacitor for mm-wave applications.

Index Terms: Embedded MEMS, RF-MEMS switch, mm-wave circuits, varactor, tunable capacitor.

1. Introduction

Latest developments in RF-MEMS technology have opened the way for achieving high performance and IC-integrated MEM devices/systems, especially RF-MEMS switches and tunable capacitors. RF-MEMS components are considered as one of the key components for the development of the next generation multi/wide band communication systems [1, 2]. Many communication systems such as satellite communication or wireless local area networks (WLAN) require tunable components to have multi-band or wide-band operation [3]. P-N junction or inversion MOS types of varactors are the main components in BiCMOS technologies to achieve capacitance tuning with limited capacitance ratios. However, the quality factors of such devices are limited especially for mm-wave frequency ranges. RF-MEMS tunable capacitors are used in voltage-controlled oscillators, matching networks and tunable filters and provide a wide capacitance tuning and a high quality factor, especially for the frequency below 10GHz [4, 5]. There is a strong need of a tunable capacitor in mm-wave frequency range which has a high capacitance ratio and a high quality factor. Recently, a BiCMOS embedded RF-MEMS switch was demonstrated with an excellent performance and very good reliability [6, 7]. The capacitive-type RF-MEMS switch shown in Fig. 1 provides a C_{off} /C_{on} ratio larger than 1:10 and is therefore a potential candidate for using it as a tunable capacitor especially due to the electrode configuration which provides a continues control of the movable membrane displacement without any pull-in effect.

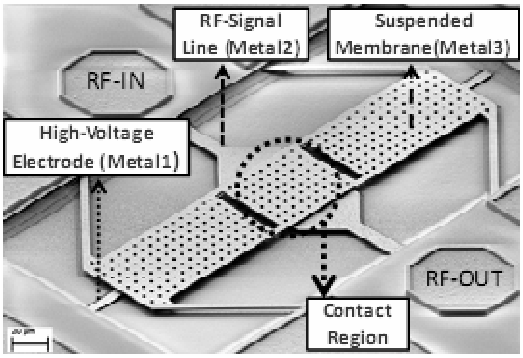

Fig. 1. BiCMOS embedded RF-MEMS switch [6].

In this work, the mechanical and electrical performance of a BiCMOS embedded RF-MEMS switch which is used as a tunable capacitor have been demonstrated. The electrode configuration allows to precisely achieving the intermediate capacitance values between the off-state (C_{off}) and the on-state (C_{on}) capacitances under specific AC signal conditions. The mechanical and the electrical characteristics have been investigated by different methods to overcome the specific measurement effects. Measurement results show that the RF-MEMS switch can be used as a tunable capacitor with a C_{off} /C_{on} capacitance ratio of 1:10. The advantage of electrode configuration which provides a mechanical movement without any pull-in effect is detailed.

RF power handling performance of the tunable capacitor is also analyzed.

2. Technology

The fully embedded RF-MEMS switch has been built between the Metal2 (M2) and Metal3 (M3) of BEOL metallization of IHP's 0.25µm SG25H1 BiCMOS process (Fig. 1) [5]. The specific RF-MEMS switch consists of M1 used as high voltage electrodes for electrostatic actuation and the stress-compensated M3 stack which is used as the movable membrane (Fig. 2). The original RF-MEMS switch process is slightly modified and the initial gap between M3 and M2 is lowered from 1300nm to 900nm to have a better tuning capability. The Con/Coff ratio is higher than 1:10 and makes the RF-MEMS switch feasible to use it as a tunable capacitor with a wide and continues tuning range.

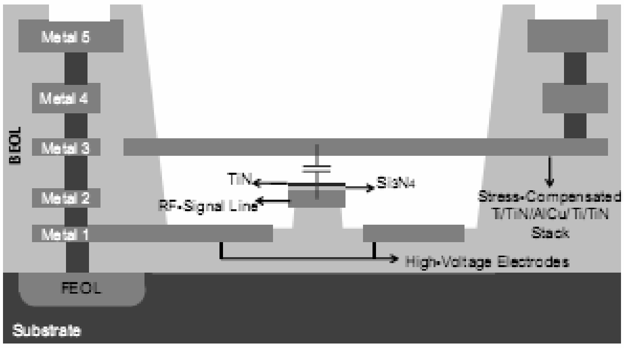

Fig. 2. Cross-section view of RF-MEMS Varactor.

3. RF-MEMS Tunable Capacitor

The nonlinear behavior of the electrostatic actuation with the characteristic pull-in effect is one of the main reasons which limit the tuning range of MEMS tunable capacitors. The equation (1) gives the relation between the applied voltage and the changing gap where the A is the area, go is the initial gap and the g is the displacement [8].

$$\frac{\varepsilon_0 \cdot \varepsilon_r \cdot A \cdot U^2}{2 \cdot g^2} = k \cdot (g_0 - g) \tag{1}$$

After the voltage pull-in voltage (U_{pi}) is reached i becomes equal to (2) and pull-in occurs. At this voltage the membrane suddenly moves down to the contact and canno be held in a stable position [8]. By the help of (1) and (2), it can be shown that the displacement can be controlled only for the first 1/3 of the initial distance between the movable membrane and the high-voltage electrodes [8]. This phenomenon limits capacitance tuning of electrostatic actuated MEMS varactors because the higher capacitance values are achieved when the membrane is close to the contact.

$$U_{pi} = \sqrt{\frac{8 \cdot k}{27 \cdot \varepsilon_0 \cdot \varepsilon_r \cdot A} \cdot g_0^3} \tag{2}$$

The BiCMOS embedded RF-MEMS switch in this study has a specific electrode configuration. The details are given in Fig. 4. As can be seen from

Fig. 4, the high voltage electrodes (M1) are in a lower position than the contact level (M2).

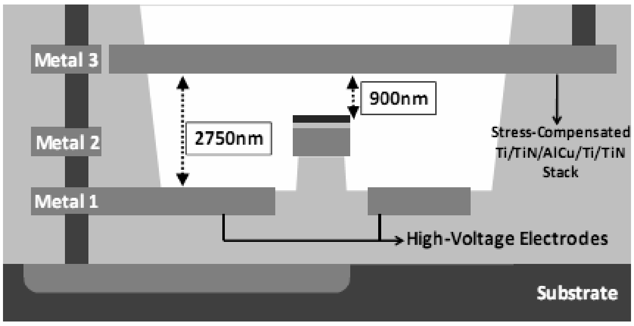

Fig. 3. Detailed cross-section of the RF-MEMS varactor.

Different principles have already been proposed in literature to prevent from nonlinearities of the pull-in effect such as three-plate configuration or separation of actuation electrodes and signal-line [9, 10]. The present RF-MEMS varactor is based on the second principle and therefore is insensitive to the nonlinear characteristic of electrostatic actuation. The initial distance between the membrane (M3 and the electrode (M1) is 2750nm while the gap between th signal line (M2) and the membrane (M3) is 900nm. Th movable membrane can be controlled in every position between M3 and M2. The specific electrode configuration allows using the MEMS switch as a MEMS variable capacitor. Furthermore, the electric field occurs only from the sides of the movable membrane (Fig. 3) which also helps to prevent from pull-in effect.

Although the standalone DC actuation voltage does no cause any pull-in effect, the AC signal on the signal lin (M2) can also affect the mechanics of membrane and pull-in can occur due to the high amplitude of AC signal [11]. The membrane is very sensitive to the AC signal amplitude when it is too close to signal line (M2). This effect obviously limits the power handling of the MEMS structur when it considered to be used as a variable capacitor Furthermore, precise capacitance measurements require specific voltage level which influences the C-V behavio during measurements. Therefore both optical and electrica measurements have been performed to distinguish between different effects which can result with pull-in of the switch.

4. Experimental Results

To analyze the variable capacitor performance of the switch, optical and electrical measurements have been done The displacement of the membrane by applied voltage has extracted using optical methods while the electrical method has provided the capacitance versus applied voltage curve Finally, the results from different methods have been correlated.

A. Optical Measurements

Optical measurements have been performed to investigate the deflection of the membrane with respect to the applied voltage which is related to the contac capacitance between M2 and M3. In comparison to electrical measurements, it provides a membrane deflection without any applied signal on M2 and therefore prevent from the mentioned pull-in effect which can occur due to high amplitude of AC signal on the signal line (M2). The Laser-Doppler-Vibrometer MSA-500 from Polytec® (LDV has been used to measure the maximum deflection in the middle of the contact area with respect to the actuation voltage which has been changed with 100mV steps between 13V to 20V. The result of the displacement-voltag behavior is shown in Fig. 4.

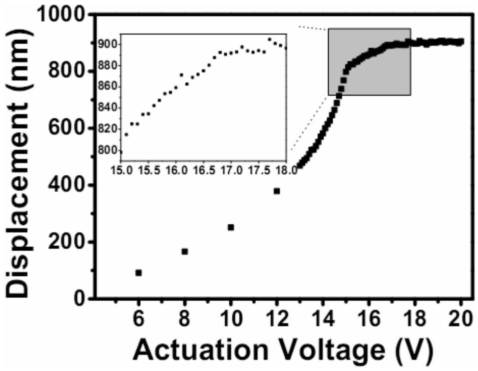

Fig. 4. LDV measurement of RF-MEMS varactor: Displacement versus actuation voltage. Every point in figure shows a measurement point.

The total displacement is approximately 900nm with a required voltage of 14-18V (Fig. 4). 100mV voltage steps are applied between 13V to 20V to better extracting the tuning region. All the measurement points show the stable membrane position which approves that the MEMS switch can be easily controlled with 100mV voltage steps.

B. Electrical Measurements

Although the optical results show that the mechanics of the RF-MEMS switch is suitable to use it as a variable capacitor, appropriate electrical performance is also necessary. Therefore, the contact capacitance measurements between M2 and M3 have been performed using Agilent® 4294A Precision

Impedance Analyzer. The measurement frequency of the AC signal was taken as 100 kHz to measure the capacitance. AC signal is applied to M2, resulting in an influence on the mechanical behavior of the membrane. If the amplitude of this signal is too high, this can also affect the mechanical behavior of the switch.

Therefore, the AC signal amplitude was chosen as 100mV not to affect the dynamics of the switch. The total capacitance from signal line (M2) to substrate without a suspended membrane (M3) has been removed from the total measured capacitance to extract the pure contact capacitance for both off and on states. A switch without any membrane was used to measure the coupling capacitance from signal line (M2) to substrate. The de-embedded contact capacitance between M2 and M3 is given in Fig. 5. The off-state and the on-state contact capacitances have been measured as 16fF and 165fF, respectively. Fig. 5 shows almost continues C-V curve for an AC voltage increment of 100mV. The intermediate capacitance values between off and on states have been achieved by applying 100mV actuation voltage steps. On the other hand, it is noted that such small amplitude (100mV) of the measurement signal has no effect on the mechanics of membrane. Under such low amplitude of AC signal, electrical measurements also provide acceptable variable capacitor performance.

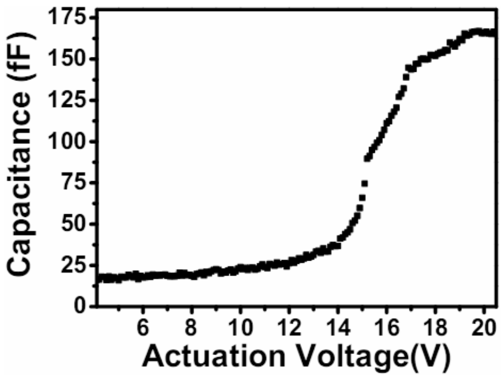

Fig. 5. De-embedded contact capacitance versus actuation voltage. Every point in figure shows a measurement point.

C. Nonlinear Movement

As illustrated in Fig. 6, there are three main different regions in case of the displacement-voltage and capacitance-voltage behavior (Fig. 6). The main reason for such behavior is the nonlinear movement of the membrane and the specific electrode configuration. The LDV with the scanning option has been used for better understanding the different effects on dynamic behavior. Following effects have been observed after detailed analyses of the dynamics: In region A, the whole membrane (the middle region and the side parts) moves down and at the end of region A, the sides stop to move. In region B, only the middle part moves down and the sides almost do not move. The first contact between M2 and M3 is achieved at the end of the region B. This can also be seen from the displacement curve because the displacement finishes at the end of region B. Region C helps to define the real contact and the final position of the membrane. In region C, there is no remarkable displacement but a significant capacitance increase can be observed.

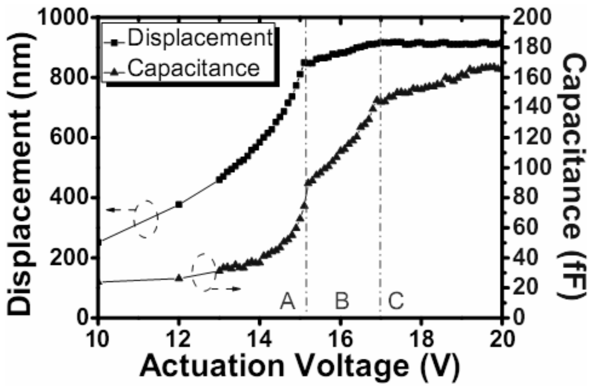

Fig. 6. Different regions of membrane movement. Every point in figure shows a measurement point.

5. RF Power Handling

As mentioned in previous parts, the amplitude of the AC signal on the signal line (M2) has a strong effect on the dynamics of the RF-MEMS switch if it is used as a variable capacitor. The capacitance measurements have been repeated using different AC signal amplitudes to define the maximum allowable amplitude that can be used on the RF line (M2). An AC signal with a frequency of 100kHz and amplitude values ranging from 100mV to 800mV has been used. Fig. 7 shows the C-V curve for different amplitudes of AC measurement signal. It is clearly seen that the increase of the amplitude results with a stronger pull-in effect. Up to 400mV, almost all the intermediate capacitance values can be achieved using 100mV actuation voltage steps but using 800mV amplitude of AC signal, the capacitance values between 50fF to 150fF cannot be achieved due to the strong pull-in effect (Fig. 7).

Table 1 summarizes the dependency of the C_{on}/C_{off} ratio and pull-in effect to AC signal amplitude. No real pull-in effect was observed for the AC signal amplitudes of 100mV, 200mV and 400mV. At 800mV amplitude of AC signal, strong pull-in effect was observed due to the high amplitude of the AC signal.

For the first three cases, the capacitance tunability is almost the same like in case of 100% tunability with capacitance ratio of 1:10 because there is no real pull-in effect. But in case of 800mV AC signal amplitute, the maximum tuning range reduces to 1:3.7 because the intermediate capacitance values between 50fF to 150fF cannot be achieved using 100mV actuation voltage steps. It is obvious that if the RF-MEMS switch wanted to be used as a variable capacitor with a 100mV actuation voltage steps, the AC signal amplitude on the signal line should be kept below 400mV to achieve a continues tuning range.

Such power levels are enough for most of the mm-wave SiGe applications. Another approach to handle more RF signal amplitude would also be using an actuation voltage steps smaller than 100mV.

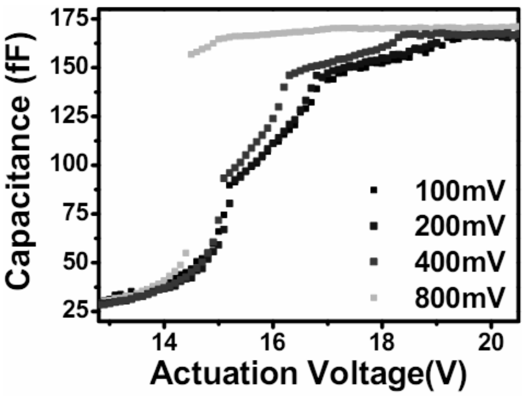

Fig. 7. De-embedded contact capacitance versus actuation voltage curves for different amplitudes of AC signal used for capacitance measurements. Every point shows a measurement point with an increment of 100mV.

Table 1. Dependency to AC signal amplitude

Umeas [mV]	Con/Coff	Pull-In Effect [V]
100	10.8	No Pull-in
200	10.9	No Pull-in
400	10.8	No Pull-in
800	11	~ 14.5

6. Conclusion

A BiCMOS embedded RF-MEMS switch has been used as tunable capacitor. The stable capacitance tunability has been demonstrated using electrical measurement supported by optical measurement to understand the effect of the AC signal amplitude. Up to 400mV AC signal amplitude, continues tuning ratio of 1:10 has achieved without any pull-in effect. A further increase of the AC signal amplitude leads to a strong pull-in effect and reduces the tuning ratio. The results show the feasible usage of RF-MEMS switch as a tunable capacitor for mm-wave applications.

Acknowledgement. The authors thank to the team of the IHP pilot line for excellent support and D. Knoll for valuable discussions. This work was supported by the European Commission under the contract No. 257335-FLEXWIN (www.flexwin.eu) and BMBF under the contract No. 03IS2011-NANETT "Nano-systemintegration" (http://www.nanett.org).

References

[1] G.M. REBEIZ, J.B. MULDAVIN, *RF MEMS switches and switch circuits*, Microwave Magazine, IEEE, **2**(4), pp. 59–71, 2001.
[2] S. PACHECO, *et al.*, Microwave and Optoelectronics Conference, pp. 770–777, 2007.
[3] A. DEC, *et al*., *Electro-mechanical properties of a micromachined varactor with a wide tuning range*, IEEE 1998.
[4] J. ETXEBERRIA, *et a.l*, *High Q factor RF MEMS Tunable Metallic Parallel Plate Capacitor*, IEEE 2007.
[5] S.P. NATARAJAN, S.J. CUNNINGHAM, A.S. MORRIS, D.R. DEREUS, *CMOS Integrated Digital RF MEMS Capacitors*, Digest of SiRF 2011.
[6] M. KAYNAK, *et al*., *BEOL Embedded RF-MEMS Switch for mm-Wave Applications*, IEDM 2009.
[7] M. KAYNAK, *et al*., *Robustness and Reliability of BiCMOS embedded RF-MEMS switch*, SiRF 2011
[8] G.M. REBEIZ, *RF MEMS: Theory, Design, and Technology*, John Wiley & Sons, 2003.
[9] D. PEROULIS, *et al*., *Electrostatically-Tunable Analog RF MEMS Varactors with Measured Capacitance Range of 300%*, IEEE 2007.
[10] M. SHAKHRAY, *Design and Investigation of Micromechanical (MEMS) Varactors*, 2005.
[11] H. NIEMINEN, *et al*., *Microelectromechanical capacitors for RF applications*, J. Micromech. Microeng. 2002.

Floating Electrode Microelectromechanical System Capacitive Switches: A Different Actuation Mechanism

E. PAPANDREOU[1], S. COLPO[2], M. KOUTSOURELI[1],
F. GIACOMOZZI[2], G. PAPAIOANNOU[1], B. MARGESIN[2]

[1]National Kapodistrian University of Athens, Solid State Physics Section of Physics Dpt., Panepistimiopolis Zografos, Athens 15784, Greece

[2]FBK- IRST, Via Sommarive 18, 38050 Povo Trento, Italy

Abstract. The paper investigates the actuation mechanism in floating electrode MEMS capacitive switches. It demonstrated that in the pull-in state the device operation turns from voltage to current controlled actuation. The current arises from Poole-Frenkel mechanism in the dielectric film and Fowler-Nordheim in the bridge-floating electrode air gap. The pull-out voltage seems to arise from the abrupt decrease of Fowler-Nordheim electric field intensity. This mechanism seems to be responsible for the very small difference with respect to the pull-in voltage.

The radio frequency (RF) microelectromechanical systems (MEMS) switches and varactors have been developed more than fifteen years ago for low loss switching/routing circuits and X-band to millimeter-wave (mm-wave) phase shifters, which have seen increasing applications in tunable filters, antennas and reconfigurable matching networks [1, 2]. Among the different designs, the capacitive switches proved to exhibit excellent RF performance and power handling [3, 4]. The performance of the capacitive switches depends on the down-state capacitance that can be limited by the finite roughness as well as the low planarity of both the dielectric layer and the beam [5, 6]. In order to diminish this effect and ensure a constant capacitance in the pull-in state, the deposition of an additional (electrically floating) metal layer on the dielectric layer was proposed [7, 8, 9]. Such devices are actuated through side actuation pads or by applying the bias directly to the transmission line. Among the two actuation methods, the former is similar to the one used in conventional capacitive switches and the pull-in condition has been analyzed in details in many papers including or not the charging effect, *e.g.* [1, 2, 10, 11. In these switches the actuation through the floating electrode has received no attention in spite of the dramatic change of bridge to floating electrode capacitance, hence the potential difference, upon the transition from pull-out to pull-in state. The aim of the present work is to analyze the actuation mechanism of the floating electrode capacitive switch, demonstrate that in the pull-in state the conventional condition $V \geq V_{pi}$ cannot further hold and the device turns from voltage to current actuation.

The switches used in present work were parallel single pole single through (SPST) cells. In the parallel (shunt) version of the SPST a metal membrane (movable air bridge) above the CPW substrate can electrically short the centre line to ground when electrostatically actuated, as shown in Figure 1a. Two side actuation pads were added in order to separate the DC bias from the RF signal on central line. These actuation pads were connected with polysilicon bias lines which were isolated with 300nm SiO_2 film from the ground plane and coplanar transmission line (fig. 1a). In the present work the bias was applied only to coplanar waveguide transmission line (CPW) and not to the side actuation pads. Under the bridge the central line was constituted by a metal multilayer (Ti-TiN-Al-Ti-TiN) covered by SiO_2 dielectric film (Low Temperature Oxide, LTO) with a thickness of about 100 nm. A floating metallic (Au) contact (90μm × 150μm) was deposited on the top surface of the dielectric film to ensure a constant capacitance during pull-in state where the device must behaved like MIM capacitor with a capacitance of $C_{MIM} \cong 4.66$pF.

The capacitance of the RF MEMS switches was measured at 1 MHz with a Boonton 72 B capacitance bridge that provided a resolution better than 0.5 fF. The current-voltage characteristic was measured at room temperature with a Keithley 6487 picoampere meter. All measurements were performed in vacuum and the surface humidity was removed by heating cycles at 140°C for two hours each time. Finally prior assessment the devices were stored in vacuum. Unipolar capacitance-voltage characteristic were obtained increasing the voltage from 0 to 50 V and then returning back to 0 V (fig. 1b). In all measurements the bias was applied to the transmission line with respect to the ground level. Unlike the conventional actuation without floating electrodes or by using the lateral pads, there was no apparent hysteresis. The two branches of CV curve for increasing and decreasing voltage are practically superimposed and the pull out and the pull in voltages are about the same.

As already mentioned a metal film floating electrode was deposited on the dielectric surface in order to ensure primarily a constant capacitance during pull-in. The presence of this metallic film cap leads to uniform charge injection and screens any potential fluctuation that may arise inside the insulating film. In absence of dielectric charging, if z_0 is the air gap at equilibrium, k the spring constant, A the switch area, d the dielectric film thickness ($d \ll z_0$) and V the applied bias the pull-in voltage will be given by:

$$V_{PI} = \left(1 + \frac{3d}{2\varepsilon_r z_0}\right) \cdot \sqrt{\frac{8k z_0^3}{27\varepsilon_0 A}} \tag{1}$$

where the first term is introduced by the capacitors voltage divider. The pull-out voltage cannot be calculated in the conventional way because of the following reasons: i) the absence of a dielectric film between the floating electrode and bridge, although the asperities and roughness will not allow the perfect contact between the electrodes and ii) the fact that as soon as the bridge lands on the floating electrode they attain the same potential and the electrostatic force vanishes. For an ideal dielectric, where no leakage occurs, the later will lead to a transitory actuation after which the bridge will return permanently to pull-out state. In Fig.1b the switch remains in the "pull-in" state, a fact that indicates the presence of electrostatic force.

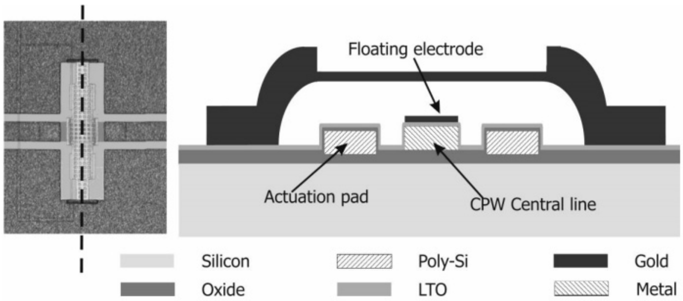

a)

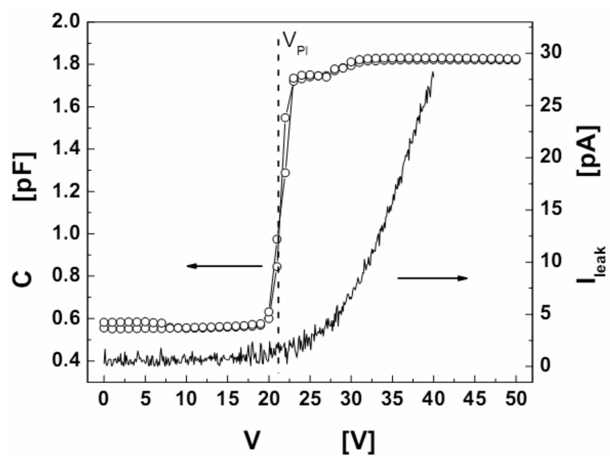

b)

Fig. 1. (a) Picture and cross-section of the device and (b) the unipolar capacitance-voltage and current-voltage characteristic of the MEMS switch.

The electric field between the bridge and floating electrode clearly denotes that, during contact, transferred charges are dissipated as soon as the contact is lost. The practically constant pull-in capacitance leads to the conclusion that charges are transferred from the bridge to the floating electrode and further through the insulating film to transmission line. Since the current may be injected through even one asperity, no further bridge flattening will occur when the applied bias increases. This current arises from field emission (Fowler-Nordheim, I_{FN}) in the gap and Poole-Frenkel (I_{PF}) in the dielectric film. According to this I_{FN} (V_{FN}) = I_{PF} (V_{PF}) while the applied bias will be given by $V=V_{FN} + V_{PF}$, where V_{FN} and V_{PF} are the voltages across the gap and the dielectric film controlling the Fowler-Nordheim and Pool-Frenkel effects respectively. Now, if w is the gap through which current flows, then the currents equality can be written as:

$$A \cdot C \cdot \left(\frac{V_{FN}}{w}\right)^2 \cdot \exp\left(-B\frac{w}{V_{FN}}\right) = M \cdot \left(\frac{V_{PF}}{d}\right) \cdot \exp\left[-\frac{q \cdot \left(\Phi - \sqrt{\frac{q}{\pi\varepsilon} \cdot \frac{V_{PF}}{d}}\right)}{kT}\right] \qquad (2)$$

where Φ is the trap emission barrier, $C = \frac{q^3}{8\pi h \Phi_1} = 2.96 \cdot 10^{-7}\ \mathrm{A/V^2}$ and $B = \frac{4\sqrt{2} \cdot \Phi_1^{3/2}}{3q\hbar} \cdot \frac{m^*}{m_e} = 81.0\ V/nm$, the numerical values obtained for the Au-vacuum potential barrier (Φ_1 = 5.2eV). Finally, M is a constant proportional to Poole-Frenkel conductivity. At this point we must stress that w is much smaller than the average gap measured through capacitance. The effective value of w arises from one or more asperities or surface roughness peaks that ensure the required current flow. Since (2) is valid only in the pull-in state it becomes obvious that the capacitance-voltage and current-voltage characteristics have to be monitored and plotted simultaneously. The two characteristics are presented in Fig. 1b and allow the determination of the onset of leakage current, which practically coincides with the transition to pull-in state. Here it must be pointed out that in spite of the fact that the experiment has been performed in vacuum the presence of surface leakage currents cannot be overruled. At pull-in the potential drop across the gap and w readjust in order to compensate the current through the dielectric film. Taking these into account and the fact that the Fowler-Nordheim current increases faster with the gap electric field than the Poole-Frenkel one with the electric field in the film, as deduced from (2), we are led to the conclusion that V_{FN} must not vary significantly above pull-in. This allows the fitting of Poole-Frenkel law to the measured current using V_{FN} as fitting parameter, as shown in Fig. 2.

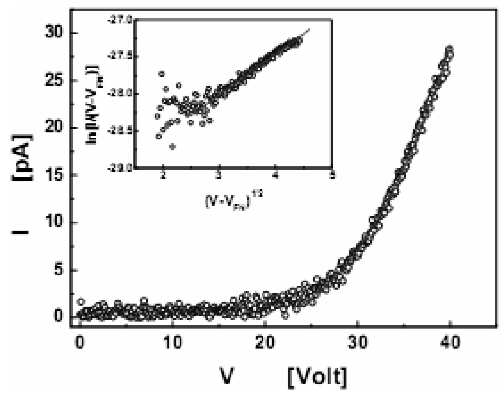

Fig. 2. Current-voltage characteristics of the MEMS switch. The inset shows the excellent agreement with Pool-Frenkel effect.

The calculated potential drop across the gap (V_{FN}) was found to be about 20.4 Volt, which is in good agreement with the pull-in voltage of V_{PI} = 21.4 Volt obtained from the capacitance-voltage characteristic (fig. 1b). The smooth transition to pull-in state, within 3 Volt, cannot be attributed to the bridge mechanical deformation, like in conventional switches, but rather to mechanism that controls the pull-in state. Nevertheless, this effect requires further investigation. The pull-out voltage (V_{PO}) when calculated in the conventional way, assuming the presence of an air gap in the pull-in state [12] and taking into account the capacitors divider, leads to:

$$\frac{V_{PO}}{V_{PI}} = \frac{3}{2} \cdot \frac{\varepsilon_r\, w_0 + d}{2\varepsilon_r\, z_0 + 3d} \cdot \sqrt{3 \cdot \frac{z_0 - w_0}{z_0}} \tag{3}$$

where w_0 is the average gap calculated from C-V characteristic in the pull-in state. For the present device, with an air gap of about 3μm, the theoretical and measured capacitances in the pull-out state are $C_{po\text{-}th} \approx 0.04$pF and $C_{po\text{-}meas} \approx 0.56$pF, the later arising from the parasitic capacitances introduced by the low frequency measurement setup. In the pull-in state on the other hand the measured pull-in capacitance is $C_{pi\text{-}meas}$ = 1.83pF and being further corrected to 1.31pF by considering the parasitic capacitances, leads to an average air gap $w_0 \approx 69$nm, which is in reasonable agreement with previously reported values by S. Melle *et al.* [5]. According to these values (3) leads to a very low pull-out voltage (4% of V_{PI}) that disagrees with data in Fig.1b and clearly indicates a different pull-out mechanism. Since the phenomena occurring at pull-out could not be analytically derived we calculated theoretically I_{PF}, using the previous fitting parameters, and from this the corresponding electric field intensity for the FN effect (E_{FN}), both as a function of applied voltageHere it is important to emphasize that E_{FN} is the electric field across the shortest distance between the floating electrode and the moving armature arising from asperities where the field emission current occurs in order to fulfill (2). The results are shown in Fig. 3 and indicate an abrupt decay of E_{FN} below pull-in voltage. The abrupt decrease of E_{FN} obviously results in a decrease of current and since the continuous flow cannot be further maintained the bridge is released. Here it must be pointed out that if the pull-out voltage was smaller, then at pull-in the leakage current would exhibit a sharp increase and vanish at pull-out as shown above.

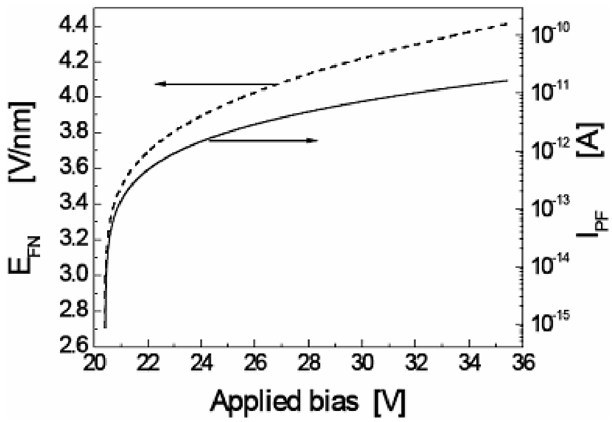

Fig. 3. Dependence on Poole-Frenkel current and corresponding Fowler-Nordheim electric field intensity of the applied bias to device terminals.

In conclusion, it has been demonstrated that in floating electrode MEMS capacitive switches the operation is different with respect to conventional ones. Although the transition to pull-in state is electrostatically controlled in the conventional way, the pull-in is sustained through current flow that allows the development of electrostatic force between the floating electrode and the moving armature. This process appears to control the pull-out voltage since the electric field in the gap vanishes as soon as the diminishing of the current through the dielectric cannot be sustained. Finally we should like to emphasize that this mechanism is promising because it can lead to new devices with properly engineered dielectric films that will efficiently mask the charging and produce a new generation of MEMS capacitive switches.

References

[1] G.M. REBEIZ, *RF MEMS: Theory, Design, and Technology*, Hoboken, NJ: Wiley, 2003.

[2] G. REBEIZ, K. ENTESARI, I.C. REINES, S.-J. PARK, M. EL-TANANI, A. GRICHENER and A.R. BROWN, IEEE Microwave Magazine **10**, 55, 2009.

[3] C.L. GOLDSMITH, J. EHMKE, A. MALCZEWSKI, B. PILLANS, S. ESHELMAN, Z. YAO, J. BRANK and M EBERLY, IEEE MTT-S Int. Microwave Symp. Digest, Long Beach, CA, 227, (2001)

[4] J.B. MULDAVIN, R. BOISVERT, C. BOZLER, S. RABE and C. KEAST, IEEE MTT-S Int. Microwave Symp. Dig., pp. 1915, Philadelphia, PA, June 2003.

[5] S. MELLE, D. De CONTO, D. DUBUC, K. GRENIER, O. VENDIER, J.-L. MURARO, J.-L. CAZAUX and R. PLANA, IEEE Trans. on Microwave Theory and Techniques MTT-**53**, 3482, 2005.

[6] H.M.R. SUY, R.W. HERFST, P.G. STENEKEEN, J. STULEMEIGER and J.A. BIELEN, NIST Proc. Nanotech, 1-5 June, Boston, 2008.

[7] Jae Y. PARK, Geun H. KIM, Ki W. CHUNG, Jong U. BU, Sensors and Actuators A **89(**88), 2001.

[8] X. ROTTENBERG, H. JANSEN, B. NAUWELAERS, P. FIORINI, W. De RAEDT, H.A.C. TILMANS, *Boosted RF-MEMS capacitive shunt switches*, Proceedings of Workshop on Semiconductor Sensor and Actuator, pp. 667–671, SeSens, Veldhoven, Nov. 2003, The Netherlands.

[9] C. CALAZA, B. MARGESIN, F. GIACOMOZZI, K. RANGRA and V. MULLONI, Microelectronic Engineering **84**, 1358, 2007.

[10] W. Merlijn van SPENGEN, Robert PUERS, Robert MERTENS and Ingrid de WOLF, J. Micromechanics Microengineering **14**, 514, 2004.

[11] X. ROTTENBERG, I. DE WOLF, B.K.J.C. NAUWELAERS, W. De RAEDT, H.A.C. TILMANS, W. De RAEDT and Harrie A.C. TILMANS, IEEE Journal of Microelectromechanical Systems **16**, 1243, 2007.

[12] H.J. De Los SANTOS, G. FISCHER, H.A.C. TILMANS and J.T.M. van BEEK, IEEE Microwave Magazine, pp. 36–49, Dev. 2004.

A Highly-Repeatable, Broadband 180º Phase Switch for Integrated MEMS Processes

Marco Antonio LLAMAS[1], David GIRBAU[2], Miquel RIBÓ[3], Lluís PRADELL[4], Flavio GIACOMOZZI[5], Sabrina COLPO[5], Fabio COCCETTI[6,7], Stéphane AOUBA[6,7]

[1]Baolab Microsystems, Ctra. N-150, Km 14.5, 08220 Terrassa, Spain

[2]Department of Electronic, Electrical and Automatic Control Engineering, Universitat Rovira i Virgili, 43007 Tarragona, Spain

[3]Department of Electronics and Telecommunications, La Salle, Universitat Ramon Llull, 08022 Barcelona, Spain

[4]Signal Theory and Communications, Universitat Politècnica de Catalunya, Campus Nord UPC, 08034 Barcelona, Spain
E-mail: pradell@tsc.upc.edu

[5]Fondazione Bruno Kessler, Center for Materials and Microsystems, via Sommarive 18, 38123, Trento, Italy

[6]LAAS CNRS, 7 Avenue du Colonel Roche, 31077 Toulouse Cedex 4, France

[7]Université de Toulouse ; UPS, INSA, INP, ISAE ; UT1, UTM, LAAS, F-31077 Toulouse, France

Abstract. A broadband 0º/180º phase switch based on a slotline-coplanar-waveguide cross loaded with two MEMS switches in opposed (ON/OFF or OFF/ON) states, is reported. The fabrication was made on high-resistivity silicon substrates using the FBK-irst and LAAS-CNRS surface micromachining processes, showing a high repeatability. The measured phase shift is 180º +0º/-7º in the extremely wide frequency range 1–30 GHz.

1. Introduction

Recent advances in two-state (0º/180º) phase switches have shown that uniplanar designs based on coplanar waveguide (CPW) [1], [2] feature a broadband phase-shift behavior with low insertion loss. In [1], a CPW/slotline design on alumina substrate using PIN diodes is reported, with a phase shift of 180º ± 2º and insertion loss ≤ 2.5 dB in the frequency range 24−37 GHz (42.6%). In [2], a phase switch based on switching between two out-of-phase back-to-back CPW-to-slotline transitions using two single-pole-double-through MEMS switches is presented, with a phase shift of 180º ± 5º and insertion loss ≤ 2 dB in the frequency range 14−20 GHz (35.3%). These figures are comparable or even better than those reported for microstrip-based MMIC phase switches [3] –[5]. In [3] an InP HEMT process is used, featuring a phase shift of 170º ± 10º and insertion loss of 3.5 ± 0.5 dB in the frequency range 26–36 (32.2%). The p-HEMT phase switch presented in [4] features a phase shift of 187º ± 7º in an ultra-wide bandwidth (0.5–20 GHz) with insertion loss of 3.7 ± 0.6 dB in the frequency band 6–20 GHz. The InP HBT phase switch presented in [5] features a phase shift of 180º ± 1º to 180º ± 5º with insertion loss of 2–5 dB in various 20%-bandwidth channels in the frequency range 30–100 GHz. Phase switches based on MEMS switches with electrostatic actuation [2], [6] present inherent low insertion loss and egligible DC-power consumption, which are attractive features for space applications. In [6] a distributed-MEMS phase shifter is reported, presenting a differential phase shift of 180º in a narrow band at 13.7 GHz, whereas in [2] the phase shift is broadband as described above.

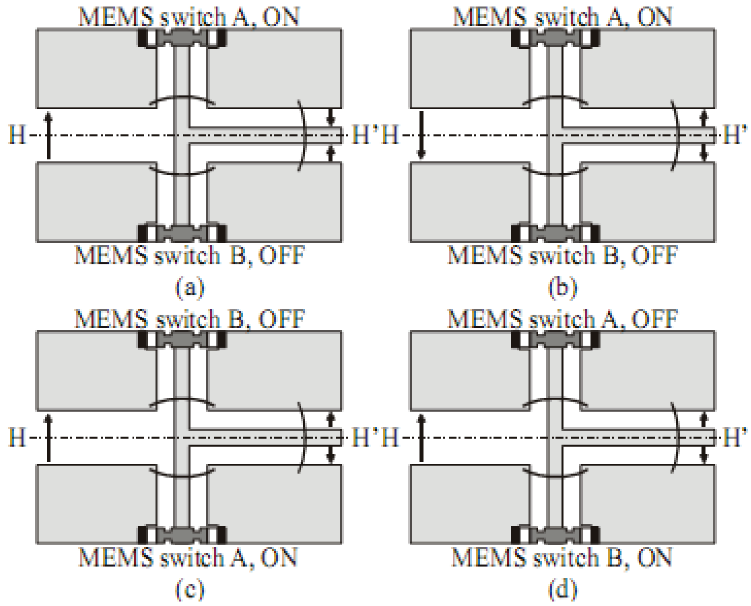

Fig. 1. Structure of the uniplanar 180º phase switch and its principle of operation. The arrows represent electric-field orientations. (a) One of the phase-switch states, with the exciting input slotline mode, and the obtained output CPW (even) mode. (b) Same MEMS switch states as in (a) but now reversing the sign of the incoming slotline field; by linearity, the output CPW field is reversed. (c) Same phase-switch as in (b) but mirrored along de H-H' axis. (d) Same phase-witch as in (c) but with the MEMS switches renamed (A↔B); thus, the other MEMS-switch state is obtained: the output CPW mode is sign-reversed with respect to (a), for the same field orientation of the input slotline mode.

In this paper, we report a broadband, uniplanar phase switch based on a slotline-CPW cross with capacitive-contact MEMS as switching elements. Fig. 1 illustrates its principle of operation. The two MEMS switches are always in opposed states (ON/OFF or OFF/ON, where OFF is used here for not-actuated MEMS and ON for actuated MEMS), thus defining the two phase-switch states (0º/180º). The phase switch features frequency-independent 180º phase-shift properties provided that the structure is symmetric along the axis H-H'. The underlying multimodal theory and design procedure of the phase switch are not covered here since they are extensively studied in [7]. The RF MEMS switches are described in section 2 and applied to the phase switch design in section 3. Section 4 summarizes the main results.

2. Fabrication Processes and MEMS Switches

The phase switch was fabricated using two different surface-micromachining MEMS processes, the FBK-irst eight-mask process [8] and the LAAS-CNRS process [9], both on high-resistivity silicon substrate. The substrate resistivity is higher than 5 KΩcm for the FBK process and 2 KΩcm for the LAAS process. Fig. 2 shows pictures of the capacitive-contact switches used in the design. A bridge topology was selected, with a pair of electrodes located symmetrically. The switch-membrane dimensions and electrode area of 620×100 μm^2 and 2×180×100 μm^2 (for the FBK process), and 800×50 μm^2 and 2×130×210 μm2 (for the LAAS process), respectively. The actuation voltages are 50 V (FBK) and 35 V (LAAS).

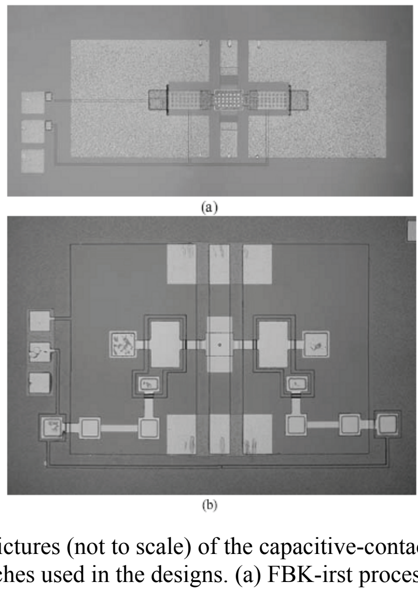

Fig. 2. Pictures (not to scale) of the capacitive-contact MEMS switches used in the designs. (a) FBK-irst process and (b) LAAS–CNRS process.

Fig. 3 illustrates the RF performance of the switches characterized up to 30 GHz with an AgilentTM N5242 network analyzer and a Cascade-MicrotechTM on-wafer probe station with ground-signal-ground probes. Within the phase-switch operating band (8-16 GHz), the FBK-switches OFF-state insertion loss is ≤ 0.3 dB and the return loss is ≥ 20 dB; the ON-state return loss is ≤ 0.5 dB and the isolation is ≥ 20 dB. For the same operating band, the LAAS-switches OFF-state insertion loss is ≤ 0.6 dB and the return loss is ≥ 20 dB; the ON-state return loss is ≤ 0.6 dB and the isolation is ≥ 15 dB.

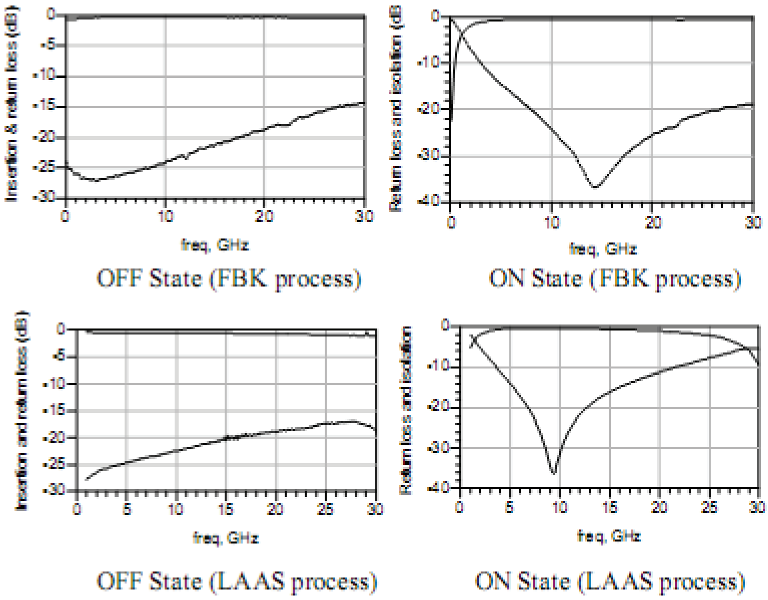

Fig. 3. Measured results of the capacitive-contact MEMS switches of Fig. 2.

3. 180º Phase Switch

A phase switch was designed. It uses the symmetric slotline-CPW cross shown in Fig. 1 loaded with capacitive MEMS switches in the two CPW opposed arms. Fig. 4 shows pictures of the fabricated phase switches using the two processes and the capacitive MEMS switches described in Section 2. Three devices were fabricated on different chips using the FBK process, and one device with the LAAS process. The design centre frequency is 12 GHz. The phase switch was simulated and designed using multimodal-analysis tools [7], which take into account the complex interaction between the CPW even and odd modes generated in the slotline-CPW cross. To obtain a perfect phase shift of 180º between the two phase-switch states, the CPW opposed arms must have equal lengths and be loaded with identical capacitive MEMS switches (but in opposed ON/OFF or OFF/ON states). Under these conditions, the 180º phase-shift is basically frequency-independent.

In Fig. 4, it is observed that a CPW-to-slotline transition of the type described in [10] is inserted prior to the slotline arm, in order to ease the phase-switch characterization using CPW ground-signal-ground wafer-probes.

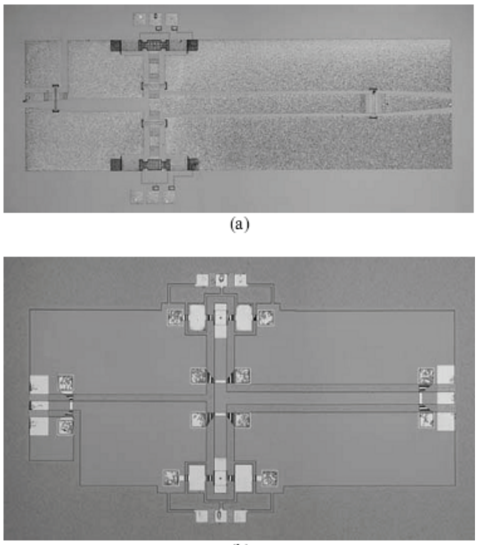

(a)

(b)

Fig. 4. Pictures (not to scale) of the implemented 180º phase switches. (a) FBK-irst process and (b) LAAS-CNRS process.

The simulated and measured performances are depicted in Fig. 5. Simulations were performed using electromagnetic tools (MomentumTM from Agilent). The simulations agree well with the measured results; in general, Momentum simulations predict quite accurately the phase-switch behavior, though they tend to underestimate the insertion loss. From Fig. 5(a) (FBK process) the insertion loss is ≤ 3 dB for 9–16.5 GHz, with a minimum of 1.9 dB at 13.5 GHz. The amplitude unbalance between both phase-switch states is small in a very wide band (± 0.5 dB for 1–20 GHz). Moreover, the amplitude differences between the three FBK devices for each state is minimum (± 0.25 dB for 9–16.5 GHz), demonstrating a very small dispersion in the fabrication process. Return loss is ≥10 dB for 7.7–16.7 GHz, with a maximum of 25 dB at 12.8 GHz. The measured phase shift is 180º +5º/−2º in a very wide band (1–18 GHz). Regarding the measured results of the phase switch manufactured with the LAAS process (Fig. 5(b)), they show an insertion loss ≤ 4.3 dB in the frequency range 7–15 GHz, with a minimum of 3.2 dB at 12.6 GHz. The amplitude unbalance between both phase-switch states is small in an extremely wide band (± 0.5 dB for 1–30 GHz). The return loss is ≥ 10 dB in the frequency range 10–16 GHz, with a maximum of 18 dB at 14 GHz. The measured phase shift is 180º +0º/−7º, also in an extremely wide band (1–30 GHz), showing the basic phase-shift frequency-independence property of this kind of phase switches. The somewhat higher measured insertion loss for this process is due to the lower resistivity of the silicon substrate.

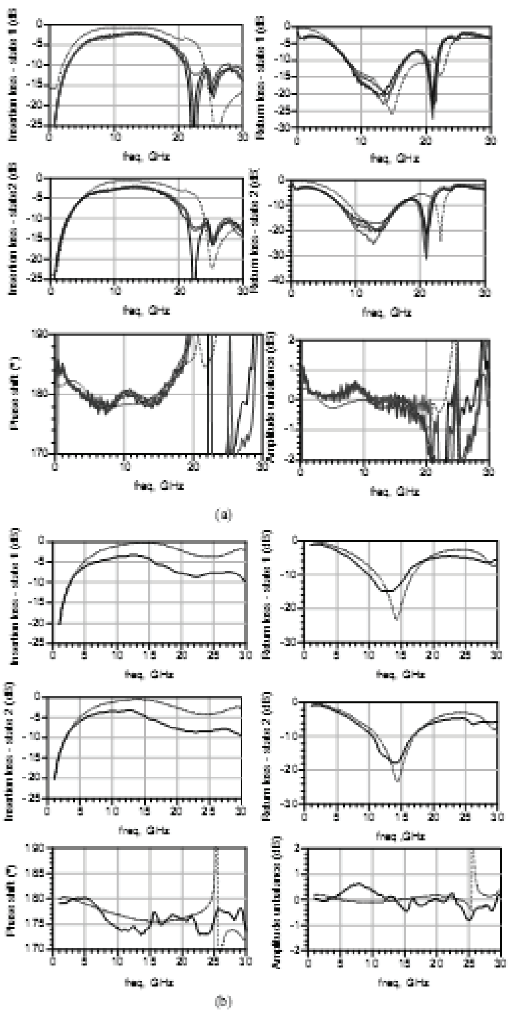

Fig. 5. Experimental results and electromagnetic simulations of the implemented phase switches: insertion and return loss for each state, phase shift and amplitude unbalance. (a) FBK-irst process. Solid line: measurements of chips 9A (red), 9B (orange), 10B (blue). Dotted line: electromagnetic simulation. (b) LAAS-CNRS process. Solid line: measurements. Dotted line: electromagnetic simulation.

4. Conclusion

In this paper, a broadband, uniplanar 180º phase switch, based on a slotline-CPW cross loaded with two capacitive MEMS switches in opposed states has been reported. The devices were fabricated on high-resistivity silicon substrates using two surface-micromachining processes (FBK-irst and LAAS-CNRS). The phase switches have proved to be highly repeatable over the two processes showing similar performance. They feature a 180º +0º/−7º phase-shift in an extremely wide frequency band (1–30 GHz) and insertion loss ≤ 3 dB in a 59% bandwidth (9–16.5 GHz).

Acknowledgement. This work was supported by Projects TEC2007-65705, TEC2008-06758-C02-02 and TEC2010-20318-C02 (Spanish Ministry of Science and Innovation), and by the former EU Network of Excellence AMICOM ref. FP6-IST-507352 (now EuMA Topical Group on RF-MEMS).

References

[1] E. VILLA, B. AJA, L. DE LA FUENTE and E. ARTAL, *Wideband uniplanar 180º phase switch*, Electronics Letters, **45**(11), pp. 556–557, May 2009.

[2] M.A. LLAMAS, D. GIRBAU, M. RIBÓ, L. PRADELL, A. LÁZARO, F. GIACOMOZZI and B. MARGEZIN, *MEMS-based 180º Phase Switch for Differential Radiometers*, IEEE Transactions on Microwave Theory Techniques, **58(**5), pp. 1264–1272, May 2010.

[3] D. KETTLE, N. RODDIS and R. SLOAN, *A Ka-band InP MMIC 180º phase switch*, IEEE Microw. Wireless Comp. Lett., **15**(6), pp. 425–427, Jun. 2005.

[4] K. MIYAGUCHI, M. HIEDA, K. NAKAHARA, H. KURUSU, M. NII, M. KASAHARA, T. TAKAGI and S. URASAKI, *An ultra-broad-band reflection-type phase-shifter MMIC with series and parallel LC circuits*, IEEE Trans. Microw. Theory Tech., **49**(12), pp. 2446–2452, Dec. 2001.

[5] R.J. HOYLAND, *A new MMIC, Wideband 180º Phase Switch Design for Millimeter Wave Applications*, in Proceedings of 3rd ESA Workshop on Millimetre Wave Technology and Applications, Espoo, pp. 305–310, May 2003, Finland.

[6] G. BARTOLUCCI, S. CATONI, F. GIACOMOZZI, R. MARCELLI, B. MARGESIN and D. POCHESCI, *Realisation of distributed RF MEMS phase shifter with very low number of switches*, Electronics Letters, **43**(23), pp. 1290–1292, Nov. 2007.

[7] M.A. LLAMAS, D. GIRBAU, M. RIBÓ, L. PRADELL, A. LÁZARO, F. GIACOMOZZI, S. COLPO, *RF-MEMS Uniplanar 180º Phase Switch based on a Multimodal Air-Bridged CPW Cross*, Accepted for publication in IEEE Transactions on Microwave Theory Techniques.

[8] F. GIACOMOZZI, L. LORENZELLI, B. MARGESIN, G. TURCO and R. MARCELLI, *MEMS Technology for RF Switches*, in Proceedings of Ottava Conferenza Nazionale Sensori e Microsistemi, pp. 392–397, Trento, Italy, Feb. 2003.

[9] C. VILLENEUVE, P. PONS, V. PUYAL and R PLANA, *Planarization optimization of RF-MEMS switches with a gold membrane*, Journal of Micromechanics and Microengineering, 20, 064013, 2010.

[10] M.A. LLAMAS, D. GIRBAU, M. RIBÓ and L. PRADELL, *Compact, Wideband CPW-to-Slotline Multimodal Transition*, in Proceedings of the 37th European Microwave Conference, pp. 897–900, Munich, Germany, Oct. 2007.

Large Fractional Bandwidth BAW Filter

M. CHATRAS[1], L. CATHERINOT[1], S. BILA[1], P. BLONDY[1], D. CROS[1], T. BARON[2], S. BALLANDRAS[2], P. MONFRAIX[3], L. ESTAGERIE[4]

[1]University of Limoges, XLIM-CNRS, 123 Av Albert Thomas, 87060 Limoges, France
Tel.: +33 587 50 67 34

[2]University of Besançon, FEMTO-ST, 32 Av de l'Observatoire, 25044 Besancon, France
Tel.: +33 381 40 28 34

[3]Thales Alenia Space, 26 Av JF Champollion, 31037 Toulouse, France
Tel.: +33 534 35 60 70

[4]CNES, 18 avenue Edouard Belin, 31 401 Toulouse, France
Tel.: +33 561 28 27 61

Abstract. A resonator using shear waves of lithium niobate is used in this paper to achieve large fractional bandwidth BAW filter. Electromechanical couplings in the 20–50 % range are obtained for the shear waves of a thin layer of Lithium Niobate suspended on a silicon substrate. By this way a filter with fractional bandwidth over 20% has been designed for space applications.

1. Introduction

Acoustic waves in elastic solids are used in numerous applications in signal processing, including frequency generation, control and filtering in modern wireless communication systems [1] [2]. With the growing demand for multimedia and mobile applications, the new generations of telecommunication satellites require higher performances, higher functionalities and still stronger cost and size constraints [3] [4]. In that context, Bulk Acoustic Waves (BAW) devices have many potentialities for the development of smart RF subsystems. For instance this technology is now used as alternative to Surface Acoustic Waves (SAW) filters in handset duplexers for UMTS and DCS standards around 2 GHz with Aluminum Nitride piezoelectric layers [5]. However, Aluminum Nitride is not suitable for large band applications, due to its electromechanical coupling coefficient. This material is mainly processed for local oscillators or narrowband filtering operations (<5%) [6] [7] [8].

Single crystal-based acoustic resonators for filtering have received a strong interest for many years. Various developments have been particularly achieved using Quartz with either SAW delay lines or resonators. However, most approaches have been developed exploiting quartz machining along standard etching, rarely compatible with batch processes as used for Micro-ElectroMechanical Systems (MEMS) [9][10][11].

That is why Lithium Niobate ($LiNbO_3$) layers bonded on silicon substrates are studied to reach large band pass specifications for satellite requirements. It is essential to maximize the values of the electromechanical coupling coefficient in Lithium Niobate, and to use wisely crystallographic cuts in order to perform the best results for longitudinal or transverse waves. Thanks to Lithium Niobate shear wave propagation behavior, it is possible to synthesis and to achieve band-pass filters with fractional bandwidth over 10 or 20 %. The resonant frequency of the resonator and the filter proposed in this paper is not given because the industrial partner of this project keeps this value confidential.

2. Electromechanical Coupling Coefficient

Mechanical and electric fields are coupled in piezoelectric solids, so both Maxwell and elastodynamic equations have to be solved [12]. The velocity of elastic waves in elastic solids is generally five orders of magnitude lower than the electric waves, which give much smaller circuits, mainly used for low frequency applications (100MHz ~ 3GHz). A quasi static approximation permits to obtain independent propagations for elastic and electric waves.

By solving the generalized Christoffel equation in piezoelectric materials, we can use tensorial expressions that give phase velocity and polarization [12]. For “z” propagation (fig1.), three plane waves are created, which have orthogonal polarization with different velocities.

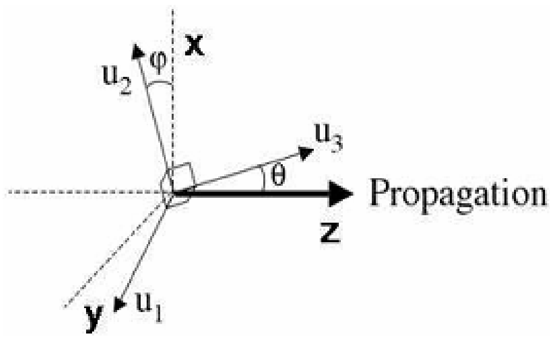

Fig. 1. Propagation in anisotropic crystal.

It results a thickness wave polarized along the "Z" axis, and two shear waves, polarized in the "XY" waves plane. These velocities permit to define very important parameters for BAW resonators: thickness, electromechanical coupling coefficient kt² and shear electromechanical coefficient ks².

The higher these coefficients are, the best electromechanical coupling the piezoelectric layer gives. The following expression describes the dependence of kt² (or ks²) according to resonance and anti-resonance.

$$k_t^2 = \frac{\pi^2}{4}\left(\frac{f_p - f_s}{f_p}\right) \quad (1)$$

It is not possible for Aluminum Nitride to have a coupling coefficient kt² higher than 7%. We propose to use two different cuts of Lithium Niobate: the (YXl)/ 36° and the (YXl)/163° cuts. The first one allows for the excitation of high velocity (7000 m.s-1) longitudinal modes whereas shear waves are used in the second one, allowing for electromechanical coupling. For these orientations we obtain ks² around 30% for the (YXl)/36° cut and around 45% for the (YXl)/163° cut.

3. 1D Simulation Results

The first step is to size the thicknesses of the several layers of the structure to reach the targeted frequencies. In the case of figure 2, we used the cut Y+36°; we obtain a coupling coefficient kt² equal to 33%. This resonator with very large electromechanical coupling will enable to reach easily fractional bandwidth filter over 10%.

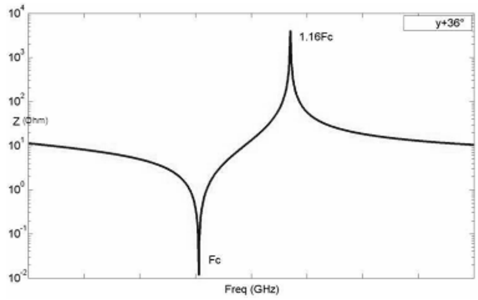

Fig. 2. Simulation response of a lithium niobate resonator (cut Y+36).

4. Fabrication and Measurements

In this work, we propose a filter fabricated on $LiNbO_3$/Silicon substrates obtained by Au/Au bonding at room temperature and a lapping/polishing on the upper face of the lithium niobate substrate. This approach allows for a collective and accurate production of filters, the filter frequency being controlled by the membrane thickness of the lithium niobate layer.

We based our device fabrication on gold bonding with a lapping/polishing process to prepare wafer compound to different devices. It allows us to manufacture a BAW resonator on $LiNbO_3$ membrane as shown in fig. 3. A gold thin layer (200nm) is deposited first by sputtering on both $LiNbO_3$ (bottom face) and silicon (top face) wafers.

Both wafers are then bonded together via gold layer compression into an EVG bonding machine. During this process, we apply a pressure of 65 $N.cm^{-2}$ to the whole contact surface, yielding a high quality bond. $LiNbO_3$ is subsequently thinned by lapping and polishing steps to an overall thickness of several microns. The resonator is finally suspended by etching the back side of the silicon substrate by DRIE. Aluminum electrodes are deposited on the $LiNbO_3$ upon the cavity to achieve working BAW resonators. A cross section of the resonator is presented figure 3.

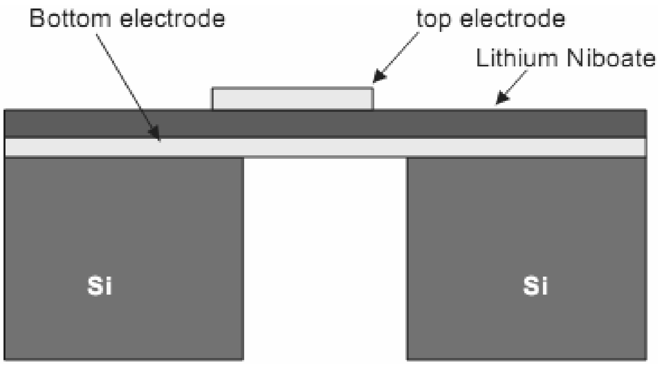

Fig. 3. Cross section of the structure.

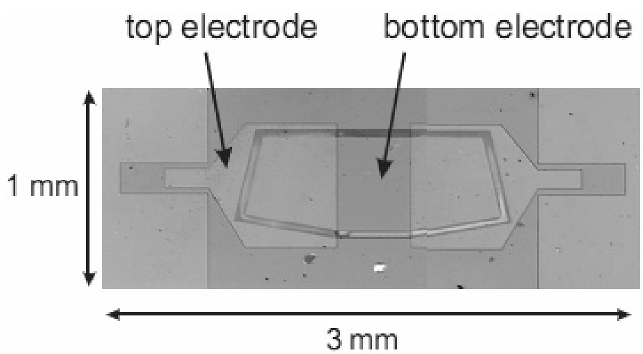

Fig. 4. Fabricated resonator (top view).

S21-parameter measurements for the structure shown in Fig. 4 were performed using a HP 8510 A network analyzer system. The measured response is presented Fig. 5.

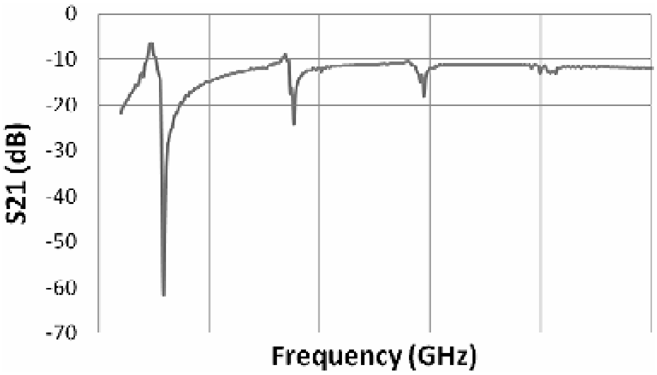

Fig. 5. Measured resonator.

It exhibits an electromechanical coupling of 30 %. This resonator can then been used to synthesis large fractional bandwidth filter. Figure 6 presents a lithium niobate based BAW 3 pole filter with a 3 dB fractional bandwidth of 22 % in a ladder configuration.

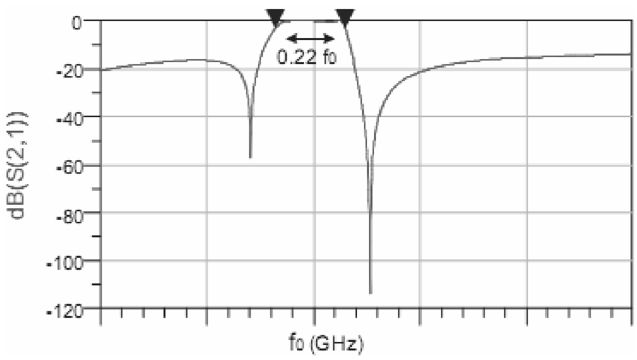

Fig. 6. Computed ladder 3 pole filter with large fractional bandwidth for space application.

5. Conclusion

In this paper an efficient method to compute BAW filter using shear waves has been presented using a scalar approach. By the way very important electromechanical coupling coefficients have been obtained with lithium niobate. Large band pass filter become then very easy to achieve for space applications.

Acknowledgement. This work is supported by the French Space Agency (CNES) (project FOVETTES) under grant# R&T R-S08/TC-0001-026.

References

[1] K.M. LAKIN, G.R. KLINE, K.T. McCARRON, *High-Q Microwave Acoustic Resonators and Filters*, IEEE Microwave Symp. Digest, **3**, pp. 1517–1520, 1993.

[2] R. AIGNER, *SAW and BAW Technologies for RF Filter applications: A Review of the Relative Strengths and Weaknesses*, Proceedings of IEEE Ultrasonics Symposium, Beijing/China, 2–5 Nov 2008.

[3] R. AIGNER, J. KAITILA, J. ELLÄ, L. ELBRECHT, W. NESSLER, M.HANDTMANN, T.-R. HERZOG and S. MARKSTEINER, *Bulk-Acoustic-Wave Filters: Performance Optimization and Volume Manufacturing*, proceedings of IMS-MTTS, Philadelphia, 2003.

[4] P. BAR, A. GIRY, P. TRIOLET, G. PARAT, D. PACHE, P. ANCEY, J.F. CARPENTIER, *Full deplex receiver and PA integration with BAW devices*, IEEE SiRF, pp. 9–12, 2008.

[5] S. GIRAUD, S. BILA, M. CHATRAS, D. CROS, M. AUBOURG, *Bulk acoustic Wave Filter Synthesis and Optimization for Multi-Standard communication Terminals*, IEEE TUFFC, **57**, pp. 52–58, January 2010.

[6] A. REINHARDT, G. PARAT, E. DEFAY, M. AID, F. DOMINGUE, *Acoustic technologies for advanced RF architectures*, IEEE Newcas conference, pp. 161–164, 2010.

[7] R. LANZ, P. MURALT, *Solidly Mounted BAW Filters for 8 GHz based on AlN Thin Films*, 2003 IEEE Ultrasonic Symp, pp. 178–181.

[8] C. ZUO, J. van der SPIEGEL, G. PIAZZA, *1.05 GHz CMOS Oscillator based on Lateral-Field-Excited Piezoelectric AlN Contour-Mode MEMS Resonators*, Proc. IEEE Int. Freq. Contr. Symp., pp. 70–74, 2009.

[9] A. VOLATIER, E. DEFAY, M. AID, A. NHARI, P. ANCEY, B. DUBUS, *Switchable and tunable strontium titanate electrostrictive bulk acoustic wave resonator integrated with a Bragg mirror*, Applied Physics Letters; **92**(3): 032906, 2008.

[10] G. PIAZZA, P.J. STEPHANOU, A.P. PISANO, *Piezoelectric AluminumNitride Vibrating Contour-Mode MEMS Resonators*, Journal of Microelectromechanical Systems, **15**(6), pp. 1406–1418, Dec. 2006.

[11] X. ZHU, V. LEE, J. PHILLIPS and A. MORTAZAWI, *Intrinsically switchable contour mode acoustic wave resonators based on barium titanate thin films*, Microwave Symposium Digest, 2009. MTT '09. IEEE MTT-S International, pp. 93–96, 7-12 June 2009.

[12] K.Y. HASHIMOTO, *RF Bulk Acoustic Wave Filters for Communications*, Artech House, 2009.

An Analogically Tuned Capacitor with RF MEMS Structure

F. BARRIERE, D. MARDIVIRIN, A. POTHIER,
A. CRUNTEANU, P. BLONDY

Xlim Research Institute–UMR 6172 University of Limoges/CNRS 123 avenue Albert Thomas, 87060 Limoges Cedex, France

Abstract. This paper presents a 102 fF to 18 fF analogically tuned capacitor, based on RF MEMS structure. It is composed of a beam electrostatically actuated with a polarization electrode under, and two RF electrodes above. Then, the operating MEMS principle is inverted, which permits to present a high capacitance variation in the analog motion of the beam, before its pull-down under 2/3 of the initial gap.

1. Introduction

RF-MEMS are emerging as a practical solution for high Q, wideband tuning of microwave elements. Recently, wide band tunable filters, cavities, and silicon integrated high Q tuners have been demonstrated by several laboratories and companies. Indeed, specific designs had to be made or very careful integration of varactors had to be conducted. Among the designs that have been made in RF-MEMS switched varactors, most were concentrated on high density capacitance designs, which resulted in moderate Qs, when they were switched in the down state. In the design presented in [1] and [2], the capacitance is operating in the opposite manner: the electrostatic gap is in the lower side of the capacitor, and the capacitance is decreased as the voltage is increased. Therefore, instability issues are occurring when the moveable plate is far from the actuation plate. Another approach could be to use a structure similar to ohmic contact switches with a capacitive contact instead of having an ohmic contact. This idea was developed in [3] and [4]. In this paper, we propose to develop novel air gap capacitance, with low values and high Q, and a normally on behavior, that is to say the device has its largest capacitance when no bias voltage is applied. A photograph of the RF MEMS varactor is presented in Fig. 1.

2. Operating and Fabrication

The varactor presented is based on an RF MEMS technology developed already, and presented in [5]. It is composed of an electroplated gold bridge raised above an actuation electrode made in chromium, and an aluminum nitride dielectric layer. The microwave input and output are standing above the bridge, with an air gap between both. The varactor corresponds to two capacitance in series located at the RF input of the bridge (metal-air-metal capacitance), and the same with the output. These two capacitances will decrease by applying bias, which reduces the bridge height, and increases the distance with microwave input and output.

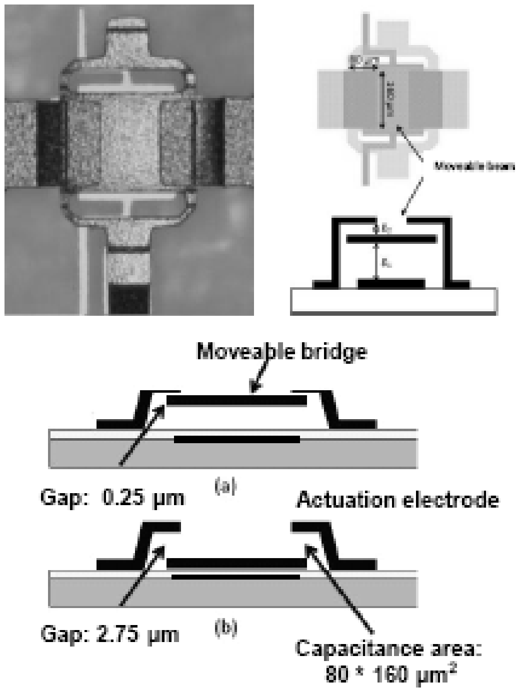

Fig. 1. Photograph of the micrometric RF MEMS varactor, and its operating sketch view under.

In order to reduce losses in the structure, the bridge and RF electrodes thickness are 3 µm thick. Thus, the series resistance due to metallization is strongly decreased, and the Q factor of the capacitance is less limited by this parameter. The bridge is raised upon the dielectric layer with a 2.50 µm height, leaving a variable distance from 0.25 µm to 2.75 µm with the RF electrodes. The AlN dielectric layer thickness is 400 nm. The fabrication process of this component is shown in Fig. 2.

This design of RF-MEMS allows a variation of capacitance in the 5 V to 30 V range.

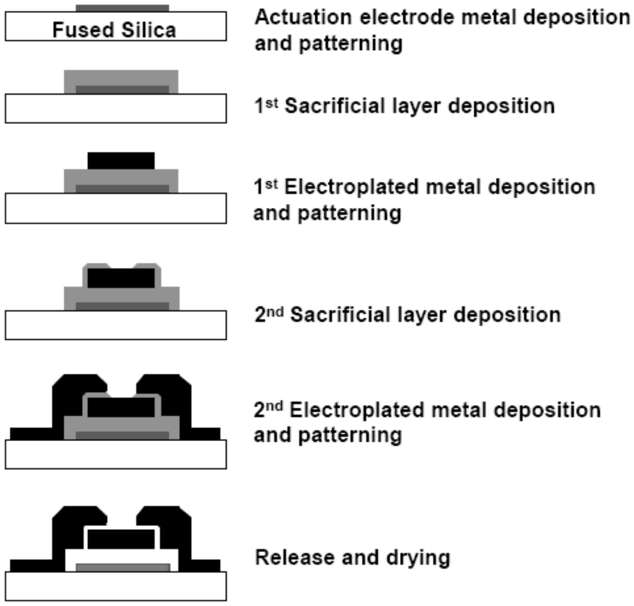

Fig. 2. Fabrication process of the RF MEMS based varactor.

3. Measurements

Measurements were taken on an Agilent-HP 8722 ES VNA, and cascade probe stations, as the component has been implemented on a coplanar waveguide. The values of the capacitors were fitted to an equivalent scheme composed of capacitance in series with a 0.29 nH inductance. The capacitance values were fitted to the measured curves, with relatively fair agreement. The measured up state capacitance 102 fF, and the down state capacitance is 12 fF, with the beam contact on the dielectric. The lowest capacitance measured in the analog range is 18 fF, with 35 V applied in the electrostatic actuator. Measurements are shown in Fig. 3., where we try to pick-up the varactor capacitance value each 0.5 dB of variation. On these curves the highest capacitance corresponds to the beam initial state, with no bias applied. Finally, this device presents analog capacitance variation with a ratio of 5.6, and a switched capacitance variation with 8.5.

Regarding loss, we were not able to measure any consistent value for the Q of these varactors. The modulus of the impedance of the series capacitance is over 1 KOhm at 2 GHz, even in the up state, and we estimate that the series resistance of this device is on the order of 0.1 Ohm.

We believe that the main loss contribution of such varactor mounted inside a microwave cavity will be the assembly loss. For instance, if the bonding resistance is Ohm, then the Q of this device would be better than 100 at 10 GHz, in the worst case, since the capacitance is low.

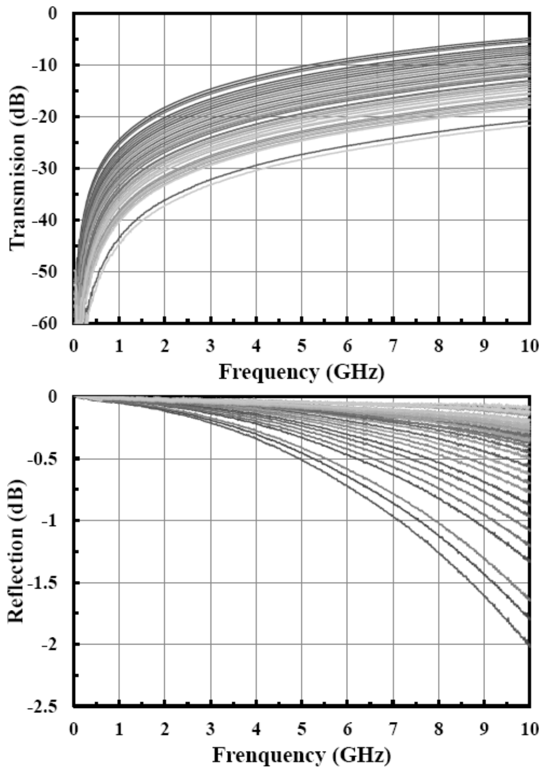

Fig. 3. RF measurements of the varactor under various bias, from 0 V applied (C = 102 fF) to 36 V (C = 12 fF). The lowest capacitance value in the analog part is obtain at 35 V with C = 18 fF.

4. RF-Power

On this type of structure, the RF electrodes are opposed to the actuator electrode, compared to the moveable beam. This is an important point, because the effect of RF power will applied on the beam a force opposed to the electrostatic force. Thus, failure modes like self-actuation can be compensate by applying an appropriate added voltage on the actuator. The Fig. 4. shows the effect of power on the varactor during a power sweep from 10 mW to 1 W for different initial capacitance values, and the power compensation with biasing. All RF power are applied at frequency constant wave of 3 GHz.

We can see first that the power effect increases the varactor’s capacitance value, especially when the beam is near RF electrodes. The failure by contact between the beam and RF electrodes is identified at 26 dBm applied for capacitance values of almost 100 fF. This failure happens with higher RF power when the capacitance is lower, as the beam goes away from RF electrodes, until no influence observed at the analog limit (S21=-26 dB @ 3 GHz), and after pull-down.

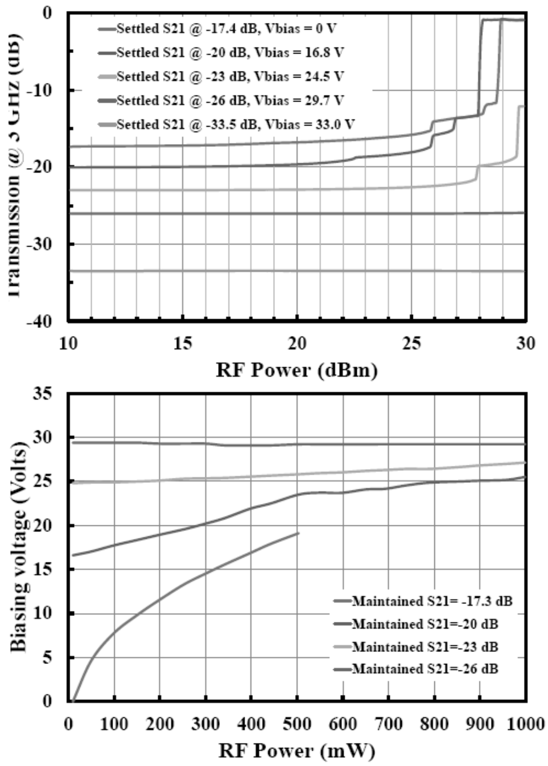

Fig. 4. On the top: effect of RF power on the varactor with fixed biasing voltages, the capacitance increase with power until failure. On the bottom: compensated RF power effect with biasing to fix the capacitance values.

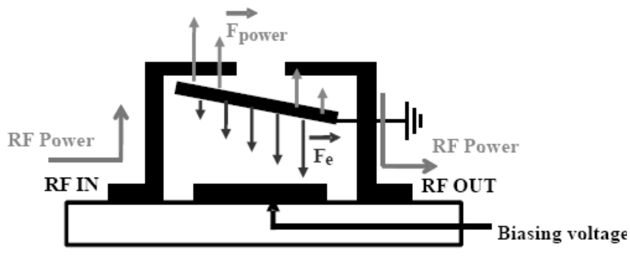

Fig. 5. The RF power effect compensation is limited, considering that the force induced by power is non-uniformly distributed on the moveable beam.

The power effect is compensated by applying higher bias voltage, so higher electrostatic force, which permits to equilibrate the beam height at a given position (also the RF transmitted response). At the initial state, the beam is near the RF electrode with no bias applied. When RF power increases, bias voltage is applied on the actuator to compensate. We can see that almost 20 V are needed to compensate 500 mW of power. After this step, the compensation cannot be established, because the mechanical force induced by power is not uniformly distributed on the beam, so the beam will be positioned slantwise, and failure by contact between beam and RF-electrode cannot be prevented (Fig. 5.).

For lower capacitance values, the beam is located lower, and the power effect can be compensated until 1 W.

5. Conclusion

We have presented an analogically tuned RF MEMS varactor, based on a reverse actuation principle. This type of structure shows the potential to design microwave devices with very high quality factor and enough wide accordability. Furthermore, high quality factor are developed on very low value of variable capacitances (<100 fF).

Capacitance range of this type of device can be easily changed in the conception, because it is almost only dependent of RF electrodes surfaces, considering that the mechanical part of the structure is not sensitive to this parameter.

Finally, another point can be interesting, considering that the biasing electrode can be used to compensate the effect of RF power, and then permit to increase the reliability of the device with high power handling.

Acknowledgment. Authors want to acknowledge the French Ministry of Defense for their support in this work.

References

[1] Xiaoguang LIU, Linda P.B. KATEHI, William J. CHAPPELL and Dimitrios PEROULIS, *A 3.4 - 6.2 GHz Continuously Tunable Electrostatic MEMS Resonator with Quality Factor of 460-530*, IEEE MTT-S Int. Microwave Symp. Dig., June 2009.

[2] J. HIMANSHU, H.H. SIGMARSSON, P. DIMITRIOS and W.J. CHAPPELL, *Highly loaded evanescent cavities for widely tunable high-Q filters*, IEEE MTT-S Int. Microwave Symp. Dig., pp. 2133–2136, June 2007.

[3] Alex GRICHENER, Balaji LAKSHMINARAYANAN and Gabriel M. REBEIZ, *High-Q RF MEMS Capacitor with Digital/Analog Tuning Capabilities*, IEEE MTT-S Int. Microwave Symp. Dig., June 2008.

[4] S. FOULADI, W. DONG YAN and R.R. MANSOUR, *Microwave Tunable Bandpass Filter with MEMS Thermal Actuators*, Proceedings of the 38th European Microwave Conference.

[5] F. BARRIERE, A. CRUNTEANU, A. POTHIER, M. CHATRAS, P. BLONDY, *A Low Value Normally On RF-MEMS Switches Capacitor For High Q Millimeter Wave Tuning*, IEEE SiRF Conference., pp. 77–79, Jan. 2010.

Quasi-Analog Multi-Step Tuning of Laterally-Moving Capacitive Elements Integrated in 3D MEMS Transmission Lines

U. SHAH, M. STERNER, J. OBERHAMMER

KTH- Royal Institute of Technology, Microsystem Technology Lab Department,
Osquldas väg 10, SE-100 44, Stockholm, Sweden
Phone: +46-87907782, Email: umers@kth.se

Abstract. This paper reports on multi-position RF MEMS digitally tuneable capacitor concept resulting in quasi-analog tuning with large tuning range. The capacitors are integrated inside a coplanar transmission line whose tuning is achieved by moving the sidewalls of the 3D micromachined transmission line, with the actuators being completely embedded and shielded inside the ground layer.

Devices with symmetrical two and three-stage actuators have been fabricated in an SOI RF MEMS process. A tuning range of C_{max}/C_{min}=2.41 with a total of 7 discrete tuning steps from 44 to 106 fF was achieved for the three-stage tuneable capacitors. Devices with actuator designs of different mechanical stiffness, resulting in actuation voltages of 16 to 73 V, were fabricated and evaluated. The robustness of the actuator to high-power signals has been investigated by a nonlinear electromechanical model, which shows that self actuation occurs for high-stiffness designs (73 N/m) not below 50 dBm, and even very low-stiffness devices (9.5 N/m) do not self-actuate below 40 dBm.

1. Introduction

Most RF MEMS capacitors are based on a switched or tuned, surface-micromachined, parallel-plate configuration [1]-[2]. However, such architectures are limited to low tuning range (analog tuning) or require large areas, as digitally tuning requires multiple devices, and require relatively complex fabrication. The devices presented in this paper are based on laterally moving structures fabricated in robust monocrystalline siliconon-insulator (SOI) device layer, already utilized by the authors for fabricating laterally moving switches [3]. The basic concept of utilizing such a technology for tuneable capacitors has recently been presented by the authors [4].

In the present paper, this process is utilized for a concept of multi-step quasi-analog tuneable capacitors utilizing laterally-moving multi-stage MEMS actuators.

2. Concept and Design

Fig. 1 shows the basic concept of the multi-stage tuneable capacitors. The sidewalls in a section of the ground plane of a 3D micromachined coplanar waveguide can be moved laterally and are thus changing the capacitive load of the transmission line [4].

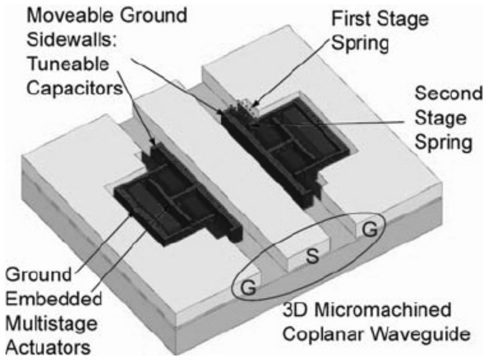

Fig. 1. 3D illustration of ground sidewall integrated multistage tuned capacitors.

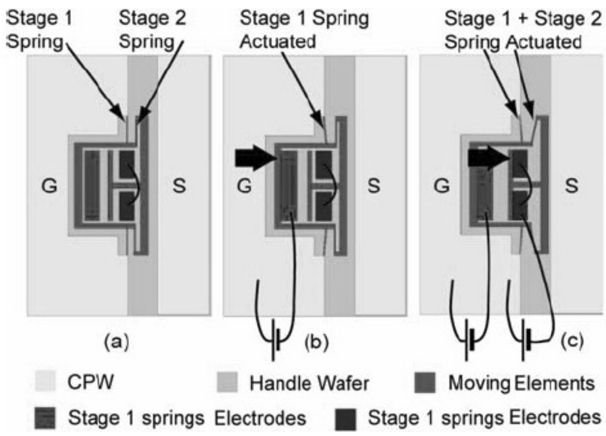

Fig. 2. Operation states of a two-stage actuator (only one side of the coplanar transmission line illustrated): (a) nonactuated; (b) stage 1 actuated (half displacement); (c) stage 1 and stage 2 actuated (full displacement).

The tuning range of the devices in this paper is much larger than conventional parallel-plate tuneable capacitors, as the actuation electrodes are de-embedded from the RF electrodes. Furthermore, a special multistage actuator is implemented, which offers large displacement at acceptable low voltages by splitting the total movements into smaller parts, which is achieved by a series of actuators which are sequentially operated, as shown in Fig. 2 for a two-stage design. For actuating a stage at low actuation voltage, all previous stages must already have been actuated. The tuning elements of one side are duplicated symmetrically in the ground layer of the other slot, and thus the number of possible states is higher than the number of actuator stages, as the transmission line can be loaded slightly unbalanced.

The advantages of this concept, over conventional electrostatic actuator based MEMS tuneable capacitors, are summarized as follows:

- moving sidewalls low-parasitic tuning concept;
- multi-step digital tuning with extended tuning range;
- ground layer-embedded, electrically shielded actuators;
- de-embedded RF and actuation electrodes;
- 3D micromachined transmission lines;
- all-metal actuators and metal-air-metal capacitor;
- single-mask fabrication.

3. RF and Actuator Evaluation

Fig. 3 and 4 show SEM pictures of fabricated two and three-stage devices respectively. The two ground sidewalls of a CPW can be tuned independently, resulting in additional states, as listed in Table I, together with the corresponding capacitance values extracted from S-parameter measurements (shown in Fig. 5) via an equivalent circuit model in Agilent Advanced Design System (ADS). The two-stage device has a total of 5 discrete states with capacitance values ranging from 48 to 105 fF (C_{max}/C_{min}=2.18), for a **capacitance gap from 6 to 2 µm**. The three-stage device has **7 discrete states** with capacitance values ranging from **44 to 106 fF (C_{max}/C_{min}=2.41)**.

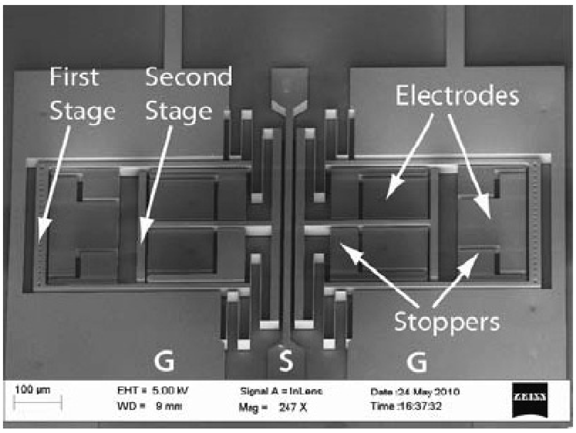

Fig. 3. SEM picture of a fabricated two-stage Tuneable capacitor.

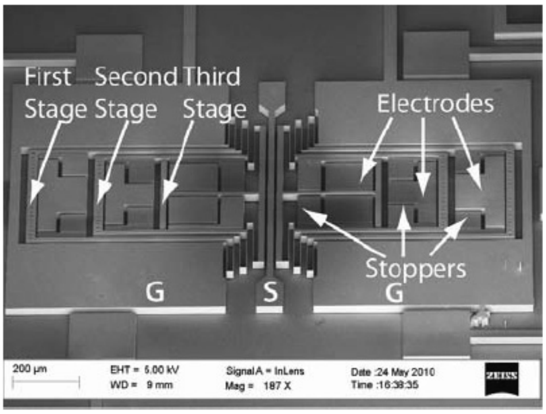

Fig. 4. SEM picture of a fabricated three-stage tuneable capacitor.

Table 1. Actuation states and corresponding capacitances Extracted from S-parameter measurements

Actuated stages (left) 12 21(right)	**Capacitance [fF] (measured)**
00 00	48
10 00	62
10 01	70
11 01	88
11 11	105

a) two- stage device

Actuated stages (left) 123 321(right)	**Capacitance [fF] (measured)**
000 000	44
100 000	47
100 001	50
110 001	58
110 011	64
111 011	86
111 111	106

b) three- stage device

The capacitive behavior and the varying capacitance is clearly visible in the measured return loss (S11) of the 50 Ω transmission line piece containing the tuneable capacitors, plotted in Fig. 5 for all states of the two and three-stage devices. The S-parameters could only be measured up to 40 GHz with our measurement setup.

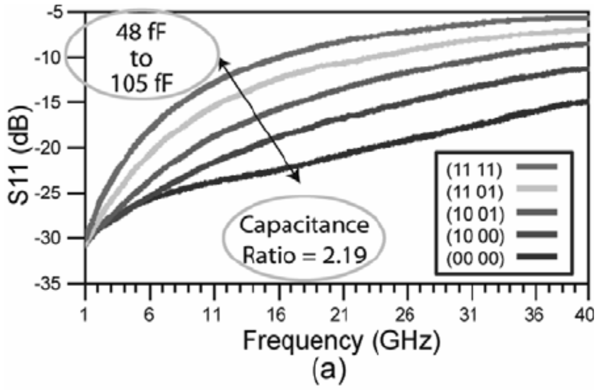

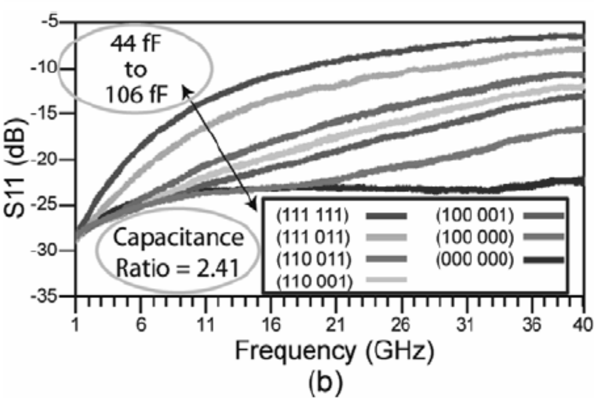

Fig. 5. Measured return loss (S11) of fabricated devices for all actuation states as listed in Table 1: (a) two-stage device; (b) three-stage device.

Fig. 6 shows the results of the actuator characterization, *i.e.* pull-in and release voltages for each stage of the two and three-stage devices, for 10 device designs with different mechanical spring constants. The actuation voltages for the different implemented spring designs are between 16 and 73 V. The overall device design is extraordinarily robust, since relatively stiff springs can be employed as the full tuning range is split up between different actuators, in contrast to conventional tuneable capacitors. This robustness is demonstrated by simulation results of a nonlinear electromechanical model in Agilent Advanced Design System (ADS) shown in Fig. 7, showing that selfactuation, *i.e.* pull-in resulting from very high signal power, occurs for the high-k designs only above 50 dBm, and even for the lowest-k devices not below 40 dBm.

The mechanical resonant frequency of one of the devices was measured to be 11.05 kHz. The fabrication process flow require only one photolithographical step, one metal deposition step, a deep-silicon etch step and wet-etching.

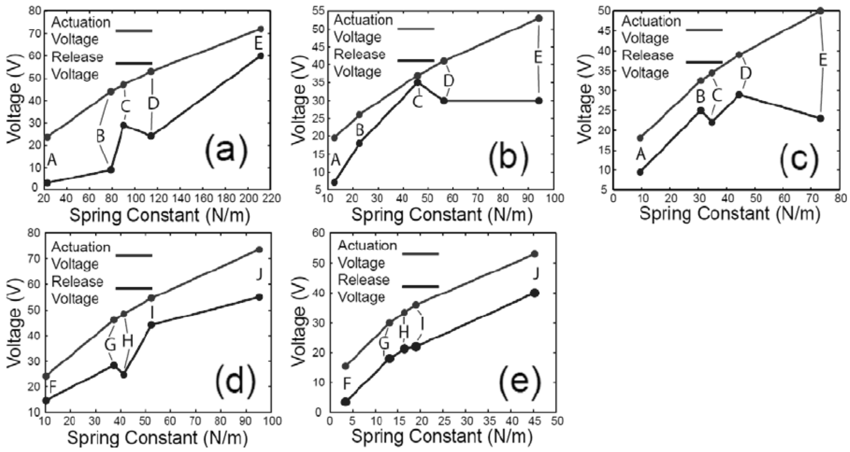

Fig. 6. Actuation and release voltages versus spring constants of 10 different actuator designs of varying mechanical stiffness, plotted or the individual stages of three-stage (A..E) and two-stage (F..J) devices: (a), (b), (c) three-stage devices, stages 1, 2, and 3, respectively; (d), (e) two-stage devices, stages 1 and 2, respectively.

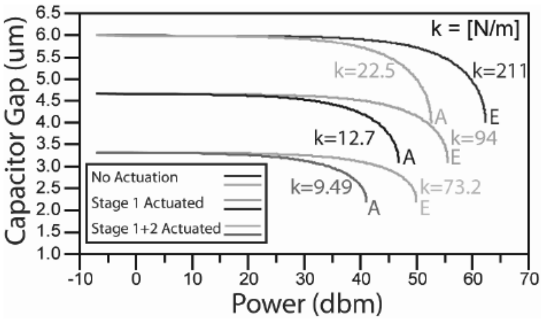

Fig. 7. Simulated self-actuation robustness for three-stage devices A (low k) and E (high k) from Fig. 7.

4. Conclusion

A novel concept of RF MEMS tuneable capacitors has been presented which offers the following advantages: multi-position digitally tuning; large tuning range; number of states independent on required transmission line length; low insertion loss by moveable sidewalls and by embedding the actuators inside the shielding ground layer; low-loss 3D micromachined transmission line; high self-actuation robustness; single-mask fabrication.

Acknowledgement. The authors wish to thank Alan Cheshire and Gabriel Roupillard from Applied Materials for the SiO_2 and Si deep etching on a prototype

Centura etching platform. The authors would also like to thank Andreas Fisher from Microsystem Technology Lab, KTH for his help with the wire bonding.

References

[1] L. DUSSOPT and G.M. REBIEZ, *High-Q Millimeter-Wave MEMS Varactors: Extended Tuning Range and Discrete-Position Designs*, 2002 IEEE MTT-S Int. Microwave Symp. Dig., **2**, pp. 1205–1208, 2002.

[2] C.L. GOLDSMITH, A. MALCZEWSKI, Z.J. YAO, Shea CHEN, J. EHMKE and D.H. HINZEL, *RF MEMs Variable Capacitors for Tunable Filters*, International Journal of RF and Microwave Computer-Aided Engineering, **9**(4), pp. 362–374, July 1999.

[3] M. STERNER, N. ROXHED, G. STEMME and J. OBERHAMMER, *Static Zero-Power-Consumption Coplanar Waveguide Embedded Dc-to-RF Metal-Contact MEMS Switches in Two-Port and Three-Port Configuration*, IEEE Transactions on Electron Devices, **57**(7), 2010.

[4] U. SHAH, M. STERNER, G. STEMME, J. OBERHAMMER, *RF MEMS tuneable capacitors based on moveable sidewalls in 3D micromachined coplanar transmission lines*, IEEE Asia-Pacific Microwave Conf. 2010, Yokohama, Japan, December 7-10, 2010.

[5] G.M. REBEIZ, *RF MEMS: Theory, Design and Technology*, New York, NY, USA: John Wiley & Sons, Inc, 2003.

Terahertz Diode on AlGaN Microcathode

N.M. GONCHARUK

Research Institute “Orion”, Egena Potie 8a, 03680 Kiev, Ukraine
Tel.: 38(044)4566071

Abstract. This paper deals with small-signal model of diode on base of electron field emission of AlGaN microcathode and electron transit in vacuum layer, which width is less than one micron. Electron emission delay time dependent on Al fraction in cathode is comparable with transit time and less than a picosecond for the diode.

Therefore we have included consideration of the emission delay when studying diode impedance characteristics. The investigations show that diode negative conductance spectrum being single-band or multiband depending on a ratio of emission delay time to alternating signal period is in terahertz frequency range. Maximal value of negative conductance in the spectrum and frequency of the maximum are the more than less emission delay time value.

1. Introduction

Negative conductance of available microwave semiconductor barrier-injection transit-time (BARITT) diode is a result of the electron transit delay effect alone because of negligible small electron injection delay time as compared with electron transit time. We have modified BARITT diode small-signal theory [1] to investigate vacuum barrier-emission transit-time diode on base of electron field emission of *AlGaN* microcathode and electron transit in vacuum. Time of electron tunneling under potential barrier of electron affinity energy in the emitter is comparable with transit time for the studied diode. Therefore in the small-signal model of the diode we unlike Sze [1] take into account delay both transit and emission as for a single-barrier diode in [2]. In addition an acceleration of electron in transit layer has been included into consideration as distinct from supposed in [1] and [2] constancy of electron drift velocity.

2. Model Description

Active layers of the diode studied are a layer of *AlGaN* emitter, a vacuum layer of potential barrier of electron affinity energy in the emitter and a vacuum transit layer. Fig. 1 shows energy diagram of the diode studied.

Time-independent current density of electron field emission is expressed as

$$J = A\int_{0}^{\infty} T_V \ln\left|1+\exp\left[\left(e_f - e_z\right)/ k_B T\right]\right| \mathrm{d}e_z \tag{1}$$

here $A = 4\pi q m_c m_e{}^* k_B T/h^3$, q and m_e^* are electron charge and effective mass in emitter, m_c degeneracy of emitter conduction band, k_B and h are Boltzmann and Plank's constants, e_f and e_z are Fermi energy and emitter electron energy component perpendicular to emitting surface, T is diode temperature and T_V permeability of the potential barrier for an emitted electron.

A tunnel resistance of the potential barrier is inverse to derivative of a current density on voltage. It is expressed for the diode as $r_t = b/\sigma$, where $\sigma = dJ/dF$ is positive differential emission conductivity of the diode. F is constant electric field in vacuum and b is potential barrier width for emitted electron which energy we suppose equal Fermi energy. At this assumption $b = (\chi - \varphi_s - e_f)/qF$ where χ and φ_s are the electron affinity energy and emitter conduction band bending on boundary with the barrier. Time of electron tunneling under the potential barrier $\tau_t = r_t c_t = \varepsilon_0/\sigma$, where $c_t = \varepsilon_0/b$ is barrier layer capacitance per unit area, ε_0 vacuum permittivity constant.

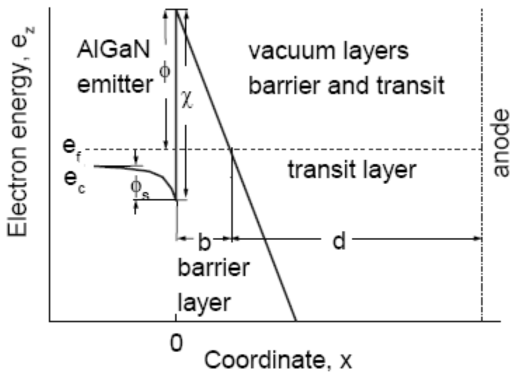

Fig. 1. Energy diagram of the diode.

Diode microwave impedance is calculated in framework of small-signal model like the same one developed by Sze [1] for BARITT diode but involving electron emission delay and acceleration of electron in vacuum transit layer. Expressions for active and reactive components of the impedance derived neglecting emitter conduction band bending are the following

$$r = a\left(a_1 \cos\varphi - a_2 b_2\right)/ z_1 + b\cos\varphi / \sigma z_2 + r_s \tag{2}$$

$$x = a\left(a_2 \cos\varphi - a_1 b_1\right)/ z_1 - b b_2 / \sigma z_2 - 1/ \omega c_d \tag{3}$$

here $a = u\sigma/\omega^4\varepsilon_0^2$, $a_1 = \cos\theta + \theta\sin\theta - 1$, $a_2 = \theta\cos\theta - \sin\theta$, $b_1 = 1/\varphi - \sin\varphi$, $b_2 = \varphi - \sin\varphi$, $z_k = \cos^2\varphi + b_k^2$, $\omega = 2\pi f$, f is alternating signal frequency, τ and $\theta = \omega\tau$ are time and angle of electron transit, $\varphi = \omega\tau_t$ is emission delay angle, $u = qF/m_0$ and m_0 are acceleration and mass of electron in vacuum transit layer, $c_d = \varepsilon_0/d$ is transit layer capacitance, $d = u\tau^2/2$ transit layer width, $r_s = \rho_c + \rho_e l_e$ is diode parasitic series resistance in absence contact spreading resistance, ρ_c contact specific resistance, ρ_e and l_e are resistivity and total width of semiconductor epitaxial layers of the diode.

3. Analysis of Numerical Calculation Results

Numerical calculations were conducted for three diodes with presented in Table 1 values of electron affinity energy in emitter which correspond with different values of *Al* fraction *x* in $Al_xGa_{1-x}N$ emitter. We suppose diode temperature 300*K*, an emitter doping level $5 \cdot 10^{18}$ cm^{-3} and the following parameters of the parasitic resistance l_e = 250 nm, $\rho_e = 10^{-3}$ Om×cm, $\rho_c = 10^{-7}$ Om×cm^2 [3].

Table 1. Diode Parameters And Emission Characteristics

Diode number	Electron affinity energy in emitter (eV)	Electric field (kV/cm)	Minimal tunneling time (ps)
1	0.18	$1.9\ 10^3$	$6\ 10^{-2}$
2	0.44	$6.5\ 10^3$	$2.5\ 10^{-1}$
3	0.61	$1.04\ 10^3$	$6\ 10^{-1}$

Dependences of differential emission conductivity on direct electric field in vacuum calculated for the diodes with the above mentioned values of potential barrier of electron affinity energy in emitter are shown in Fig. 2. The emission conductivity reaches maximum which value is the more and the maximum is reached at the less electric field value than the potential barrier is lower. Table 1 shows values of electric field and minimal emission delay time which correspond with the emission conductivity maxima for the diodes.

Microwave impedance characteristics per unit of diode cross-section area computed for the diodes with the minimal values of emission delay time are shown in Fig. 3–5. When analyzing the impedance characteristics it is seen that negative conductance spectra of all the diodes are in terahertz frequency range. The spectrum is singleband or multiband depending on frequency inverse to tunneling time is higher or lower than upper frequency of diode negative conductance frequency spectrum.

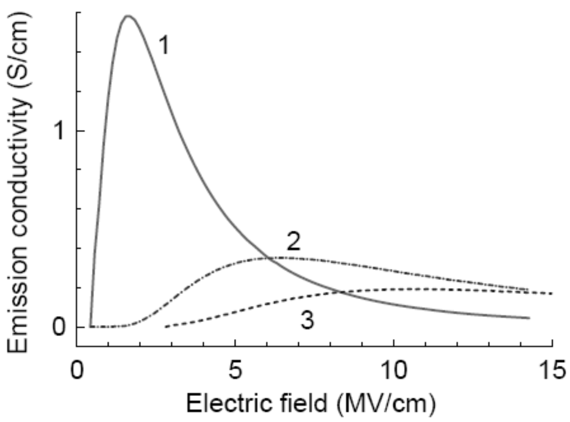

Fig. 1. Differential emission conductivity dependences on direct electric field in vacuum for the diodes with the electron affinity energy in emitter 0.18 eV, 0.44 eV, 0.61 eV.

Tunneling time is less than alternating signal period at all frequencies in negative conductance spectrum of the diode 1 so the spectrum is single-band. For the diodes 2 and 3 a ratio of tunneling time to alternating signal period is less than unit in lower part of negative conductance spectrum and it is more than unit in upper part of the spectrum. When frequency in the spectrum changes value and sign of the greatest first term in (2) oscilate due to oscilations included into it periodical functions of emission delay angle. The angle increases to about 0.9π, 5π and 11π when frequency increases to upper limits in the spectra of the diodes 1, 2 and 3 accordingly. This modulation of negative resistance frequency dependence results in multiband spectra of the diodes 2 and 3. Except the basic first band at frequencies less than emission delay frequency $f_t = 1/\tau_t$ additional bands are in the rest upper part of the spectrum.

Fig. 3. Frequency dependences of negative resistance (Fig. 3*a*) and negative conductance (Fig. 3*b*) of the diode 1 at transit angles $\theta = k\pi/5$, where k is curve number. Fig. 3 presents negative resistance and negative conductance frequency dependences for diode 1. There is one peak on every of the two dependences. Value of negative resistance peak increases and frequency of the peak lowers when transit angle increases. A value and frequency of negative conductance peak and a width of negative conductance frequency band depend on a ratio of transit time to tunneling time. When transit angle increases from zero to value of emission delay angle the band appears and broadens as its upper frequency increases and lower frequency decreases, frequency of negative conductance peak increases. When transit angle further increases to 2π frequencies upper and of the peak decrease, the band narrows and lowers. Negative conductance peak value reaches two maxima with transit angles about π/2 and 3π/2 accordingly and one minimum with transit angle near π. It tends to zero when the transit angle approaches to 2π.

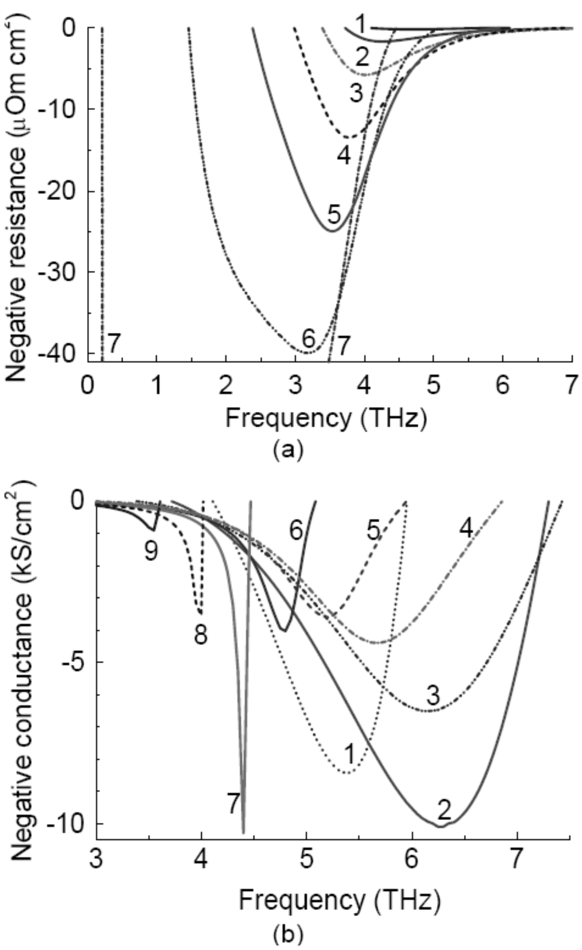

Fig. 3. Frequency dependences of negative resistance (Fig. 3*a*) and negative conductance (Fig. 3*b*) of the diode 1 at transit angles $\theta = k\pi/5$, where k is curve number.

Frequency dependences of negative resistance of the diode 2 at frequencies of the lowest first band are shown in Fig. 4a and at frequencies in the rest upper part of the spectrum in Fig. 4b. Two additional bands of negative resistance take place at frequencies near emission delay frequency and doubled this frequency accordingly. A value of negative resistance peak in a band increases and frequency of the peak decreases with transit angle increasing. A value of negative resistance peak in the basic first band is three orders more than the same one the second additional band.

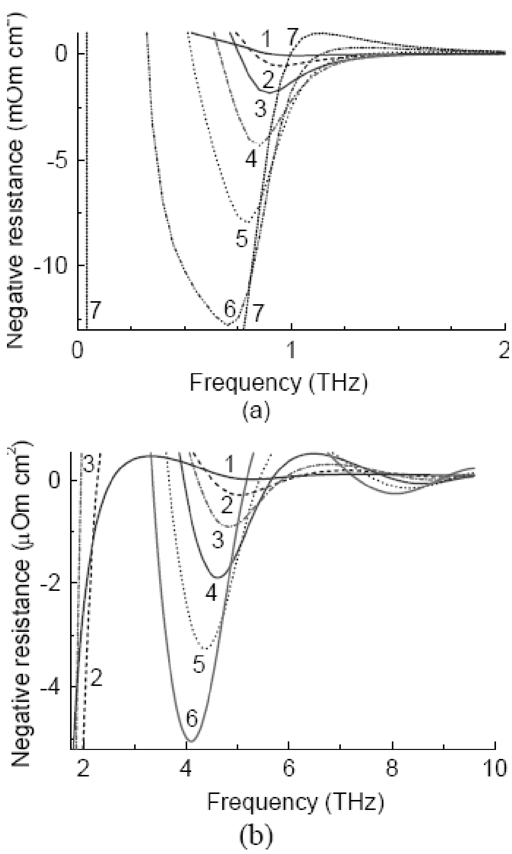

Fig. 4. Frequency dependences of negative resistance for the diodes 2 in lower (Fig. 4*a*) and upper (Fig. 4*b*) part of negative conductance frequency spectrum at transit angles $\theta = k\pi/5$, k is curve number.

Analysis of negative conductance multiband spectra the diodes 1 and 2 in Fig. 5 shows the more transit angle the lower frequency bands of negative conductance in the spectra. Maximal peak of negative conductance in a band takes place at transit angle near the least its value in the band. However lower limit of transit angle interval where negative conductance is present in a band increases with band number increasing. Therefore the transit angle corresponding with maximal negative conductance in band is the more than the band is higher. For both the diodes the greatest peak in the first band takes place near half of emission delay frequency and transit angle of $\pi/4$. When tunneling time increases the negative conductance spectrum widens; bands narrow and increase in the number; value, frequency and transit angle corresponding with the greatest peak in the spectrum decrease.

Admittance reactive component at frequency of the greatest negative conductance peak is comparable with the same active component for the diode 1 and of one order more for the diodes 2 and 3. Its value decreases with emission delay increasing.

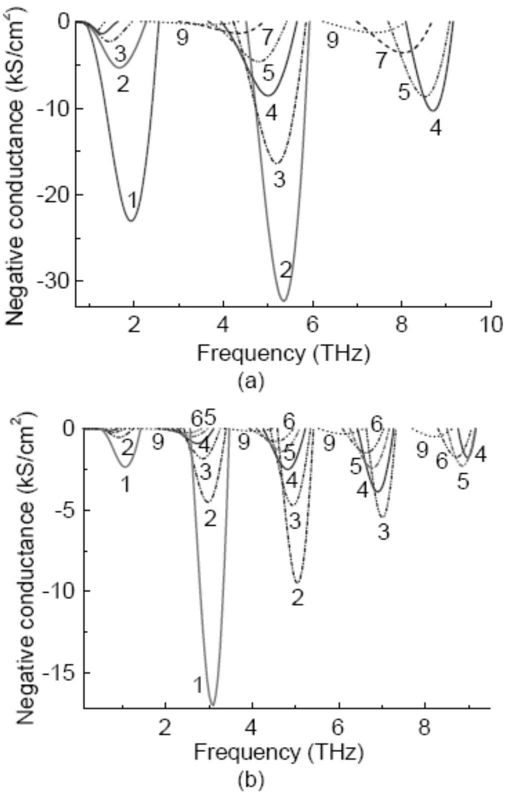

Fig. 5. Frequency dependences of negative conductance for the diodes 2 (Fig. 5*a*) and 3 (Fig. 5*b*) at transit angles $\theta = k\pi/5$, k is curve number.

Transit layer width values at frequencies of the greatest negative conductance peaks shown in Fig. 3b, 5a, 5b are close to 17 nm and 420 nm for the diode 1 with transit angles π/2 and 3π/2, 80 nm and 950 nm for the diodes 2 and 3 with the angle π/2 and π/4 accordingly.

4. Conclusion

Terahertz frequency spectrum of negative conductance of the diodes is single-band or multiband depending on emission delay frequency is more or less than upper frequency in the spectrum. Modulation period of negative resistance multiband spectrum is near emission delay frequency. The first negative conductance band in the spectrum is near one half of emission delay frequency. The less is emission delay time the more value, frequency and transit angle corresponding with the greatest peak of negative conductance in the spectrum. Advantage of the diode over semiconductor the same one [2] is higher operating frequency due to less barrier width which value is into interval from 0.9 nm to 0.6 nm for the diodes.

References

[1] S.M. SZE, *Physics of Semiconductor Devices*, **2**, Chapter 10, Section 7, New York: J. Wiley & Sons, 1981.

[2] N.M. GONCHARUK, S*ingle-Barrier Diode with Tunnel Injection*, in Proceedings of the 11th International Symposium on RF MEMS and RF Microsystems, MEMSWAVE 2010, Otranto, Italy, June 28-30, 2010.

[3] Q.Z. LIU, S.S. LAU, *A review of the metal-GaN contact technology*, Solid-State Electronics, **42**(5), pp. 677–691, 1998.

High Frequency CNT Based Resonator for DNA Detection

Alina CISMARU, Mircea DRAGOMAN, Antonio RADOI, M. VOICU ,
Alina BUNEA, Mihaela CARP, Adrian DINESCU

National Institute for Research and Development in Microtechnology (IMT),
P.O. Box 38-160, 023573 Bucharest, Romania

Abstract. The paper presents modeling and measurements of microwave propagation in CNTs based resonator for DNA detection. We report on sensing of adsorbed DNA on multi walled carbon nanotubes and deposited over a microwave IDT resonator. The DNA is revealed by a phase shift, of 20 degrees for the resonant frequency.

1. Introduction

The microwave devices based on carbon nanotubes (CNTs) constitute a promising area of research and many microwave devices, such as filters, resonators, amplifiers, and oscillators, which have been already built and tested in the frequency range of 0.5-100 GHz, and even beyond, up to THz. A recent review [1] gives a comprehensive overview of these efforts to bridge the nanotechnologies based on CNTs with microwave applications. The high impedance of CNTs make them very difficult to match CNTs-based RF devices or with any other RF device or circuit that have a standard impedance of 50 Ω. Recently, our group has obtained a resonator based on a CNT array in the microwave frequency range of 1–2 GHz. [2].

The detection of the deoxyribonucleic acid (DNA) represents a huge importance in molecular diagnosis of various diseases and early warning of serious illnesses. New DNA detection methods are required to be simple, fast and able to detect DNA with a reduced number of preliminary steps in the DNA sample processing. All these effective methods are termed free-label methods and carbon nanotubes (CNTs) play a leading role in them.[3] On the other hand, the dielectric properties of DNA are used to detect it at various electromagnetic frequencies.[4].

In this paper is reported the fabrication interdigitated structures IDT CNTs based resonators for DNA detection and also the experimental results at a high frequency.

2. Design and Modeling

The test structure was modeled and designed in frequency domain using CST Microwave Studio. CST uses time domain simulations and the port definition, S parameter extraction is optimized for electric field distribution (ideal for waveguide port and planar ports with multiple pins definition). The 3D view o resonator structure obtained by CST is presented in Fig. 1.

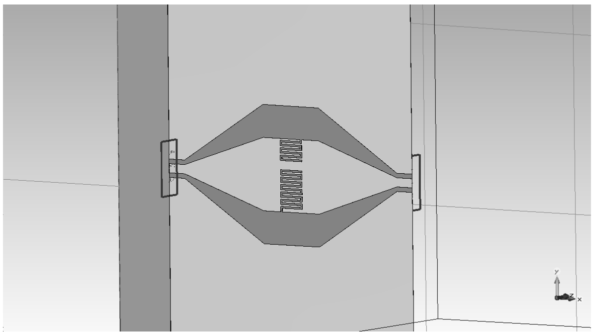

Fig. 3. D view of IDT resonator structure layout.

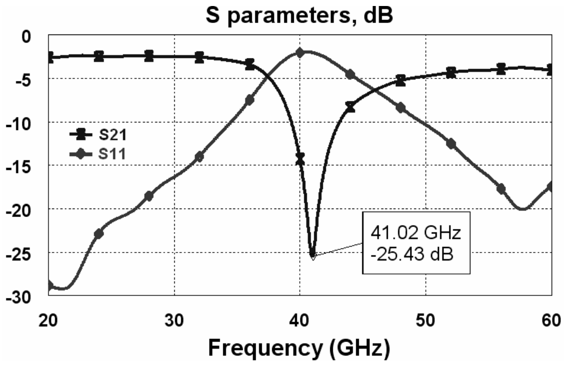

Fig. 2. Simulated S parameters for the IDT resonator.

The simulated S parameters are presented in Fig. 2. The simulated insertion losses are very good taking into account the large domain of frequency.

The design of the multilayer structure was made for a 10 (width)×140 (length) μm IDT structure having one large IDT for a 50 (width)×140(length) μm which transform a capacitor in a LC band stop resonator. The structure has been designed with the following layers:

- the substrate layer is Silicon, with high permittivity (11.9) and is 500 μm thick.

- the second layer is silicon dioxide (SiO_2), with a permittivity of 3.9 and 500 nm thick.

- the top layer is the metallization, where perfect electric conductor (PEC) was used, 500 nm thick.

The frequency bandwidth for this structure was 20-60 GHz and set in the environment. The next step was to set of some boundaries for the structure, so the open boundary was chosen for all the sides of the structure, and with space for the top side. In the final stage of the preparations for the simulation, the waveguide ports were designed, defining the coordinates for them, and selecting the type of the port, meaning Ground-Signal-Ground (GSG). The simulation was done using the Transient Solver, meaning time-domain.

3. Fabrication

The IDT structure was manufactured on a SiO_2/high resistivity wafer with the dielectric permittivity 11.9. The fabrication has been done following the steps: (a) cleaning of the Si wafer ($H_2SO_4 + H_2O_2$, HF + DIH_2O), (b) thermal oxidation (t_{ox} = 1μm), (c) optical lithography consisting of treatment on hot plate at 110^0C for 10 minutes, AZ5214 photoresist deposition by spinning with thickness of 1.5 μm, and UV exposure and developing), (d) e-beam Ti/Au deposition with heat treatment during vacuum step, with layers of thicknesses 20 nm/80 nm, (e) metal lift-off (treatment on hot plate at 110^0C for 1 minute, till cracks appear on the metal surface, followed by cooling down to room temperature and then immersion in acetone, and (f) cleaning in isopropylic alcohol and DI water in a ultrasonic bath for 1 minute.

In the area of the IDT we deposited a drop (0.3 μL) of the MWCNTs and DNA composite with the following concentrations: 10 g /l CNT and 0.5 g/l DNA which can be seen in Fig. 3 (a) and (b) of the sensing device. The morphological characterisation of IDT resonator structure covered by CNTs and DNA has been obtained using scanning electron microscopy (SEM). As you can seen in Fig. 4 (b) and (c) texture differences are clearly visible i.e. before and after the DNA immobilisation.

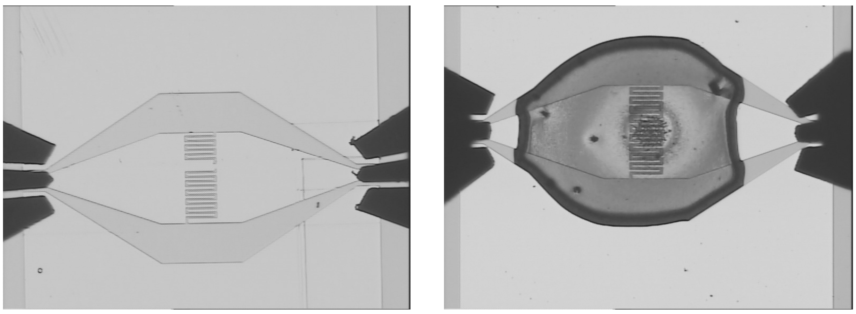

a) b)

Fig. 3. Optical photo of the structure during the microwave characterisation.

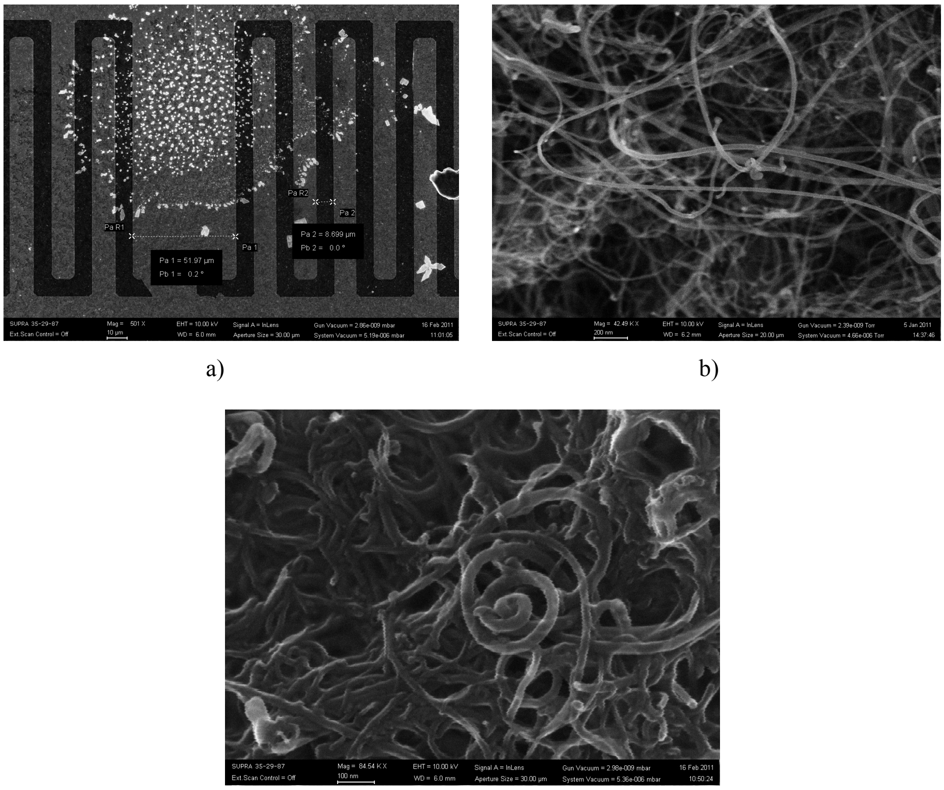

a) b)

c)

Fig. 4. The SEM photo showing the deposition of the DNA- MWCNTs composite in the area of the IDT is displayed in Fig. 4 (a), while Fig. 4 (b) illustrates a detail of the CNTs before DNA immobilization, Fig. 4 (c) illustrates the detail of CNTs DNA composite after DNA immobilization.

The functionalization of MWCNT started with dispersing them for 6 hours, with the aid of ultrasounds, in 300 mL of concentrated H_2SO_4/HNO_3 (3:1, v/v) mixture. The suspension of purified CNTs was then diluted up to 1500 mL with distilled water and filtered on a 0.45 µm (Isopore™) membrane, using a Büchner funnel. The filtrate was washed plenty with distilled water until the pH of the waste water became 6.0. The functionalized nanotubes were afterwards dried in oven, at 100°C, for 4 h and the FT-IR spectra were acquired, showing the characteristic absorption band ascribed to the carboxyl group -COOH, situated at 1740 cm^{-1}. The interaction of λ-DNA (0.5 g/L) with MWCNTs-COOH (0.04 g/L), mixed at 1:1 v/v, was assayed spectrophotometrically (Fig. 5), using a photodiode array spectrophotometer (U-0080D Diode Array Bio-Spectrophotometer, Hitachi). At the working pH, the adsorption process of λ-DNA on the MWCNTs-COOH backbone is much facilitated, being known that minimum influences on the adsorption processes concerning the immobilization of DNA on solid substrates are manifested in the 6.4 - 8.5 pH range when. We can see from Fig.5 that the composite DNA-functionalized MWCNTs displays a shape containing the spectral peaks of its constituents.

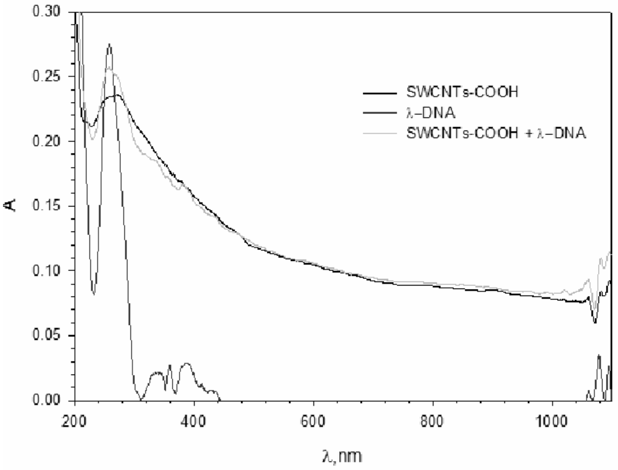

Fig. 5. UV-VIS spectra (in arbitrary units) of multi-*walled carbon nanotubes* (*MWCNTs,* black) and functionalized carbon nanotubes (MWCNTs-COOH, red) monitored spectrophotometrically (U-0080D Diode Array Bio-Spectrophotometer, Hitachi) is marked by the green color.

4. Measurement Results

Further, we have performed the microwave measurements and for this purpose we have used two types of depositions made on the same wafer: IDT structure covered only with MWCNTs and IDT structure covered with the composite DNA - MWCNTs with the same concentrations as mention before. The two IDT structures covered with MWCNT and with DNA- MWCNTs functionalised were measured directly on-wafer with a vector network analyzer (VNA) -Anritsu - 37397D connected to a Karl-Suss PM5 on-wafer probe station. The SOLT calibration standard was used to calibrate the system.

The transmission of the IDT resonator structure is presented in Fig. 6 (a) and the results demonstrate a resonance of almost 41 GHz in a very good agreement with the simulation results. The transmission of IDT resonator structure covered with MWCNT and the DNA-MWCNTs composite are displayed in Fig. 6 (b).The results demonstrate a shift in frequency in comparison with the response of IDT resonator structure respectively in the left side for the IDT resonator structure covered with MWCNTs and in the right side for the IDT covered with DNA-MWCNTs composite. We can see that the microwave signatures of the two compositions are quite different. The DNA signature is expressed by a distinct decrease of amplitude up to 20 GHz. Fig. 7 shows the corresponding phase for the two distinct depositions.

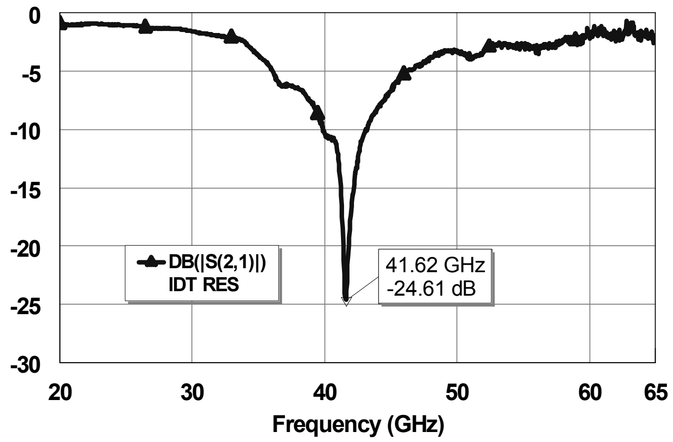

a)

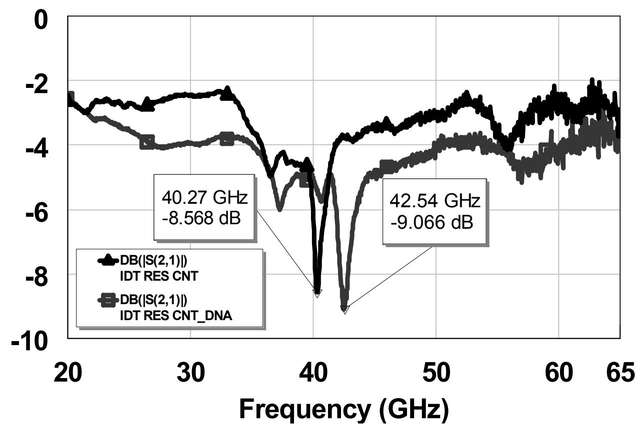

b)

Fig. 6. S_{21} parameters for (a) IDT resonator structure, (b) IDT resonator structure covered with MWCNT and IDT resonator structure covered with DNA - MWCNT composite.

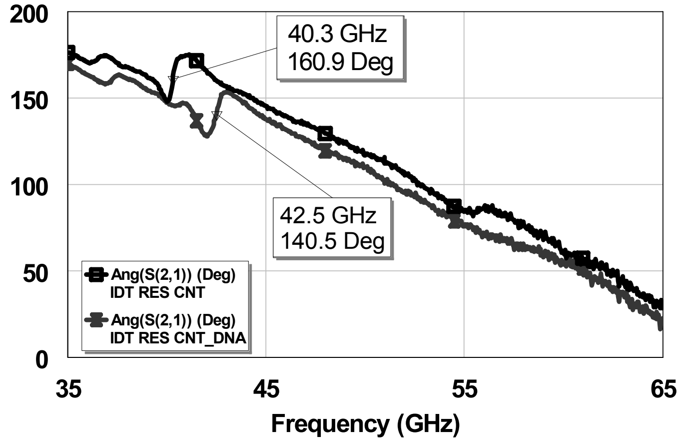

Fig. 7. The phase of the IDT resonator structure covered by MWCNTs and by the DNA- MWCNT composite.

The most interesting sensing parameter is the phase, which is shifted with 20 degrees in the range of resonance frequency for both structures (Fig. 7) and decrease at higher frequencies. The behavior in microwave range of MWCNTs and the DNA-MWCNTs composite IDT resonator structures can be explain by the differences in the microwave effective permittivity which is calculated as around 2 for MWCNTs and 11-58 for DNA-MWCNTs composite [4]. This is the reason why such a large phase shift occurs in Fig. 7 for the composite DNA-MWCNTs in contrast to the MWCNTs deposition. Repeated measurements over an interval of several days (not shown here) demonstrated that the electromagnetic responses of both the MWCNTs and the DNA-MWCNTs composite are stable in time.

5. Conclusion

In conclusion, we demonstrated using an IDT resonator structure covered by MWCNTs a detection method of DNA for a high frequency. The MWCNTs plays a key role in this sensitive detection procedure due to its low effective permittivity in microwaves, which contrasts the high permittivity of the DNA in the same frequency region. Instead of the decrease in quality factor of CNTs based resonator, the results are very important for the DNA sensing devices in high frequencies domain.

Acknowledgement. The authors Alina Cismaru, Antonio Radoi and Mihaela Carp acknowledge the support of the Sectorial Operational Programme Human Resource Development (SOPHRD) under the contract number POSDRU/89/1.5/S/63700.

References

[1] M. DRAGOMAN and D. DRAGOMAN, *Nanoelectronics Principles and Devices*, 2nd edition, Chap. 1, Artech House, Boston, 2009.

[2] M. DRAGOMAN, K. GRENIER, D. DUBUC, L. BARY, R. PLANA, E. FOURN, E. FLAHAUT, *High-Q microwave resonator based on millions of nanotube cantilevers*, Journal of Applied Physics*,* **101**, 106103, 2007.

[3] G. GRUNER, *Carbon nanotube transistors for biosensing applications*, Anal. Bioanal. Chem **384**, pp. 322–325, 2006.

[4] R. HÖLZEL, *Dielectric and dielectrophoretic properties of DNA*, IET Nanobiotechnol. **3**, pp. 28–45, 2009.

[5] C. WICHAIDIT, J.R. PECK, Z. LIN, R.J. HAMERS, S. HAGNESS and D.W. van der WEIDE, *Resonant slot antenna as transducers of DNA hybridization; acomutational feasibility study,* International Microwave Symposium Digest, pp. 163–166, May 20-25, Phoenix, USA, 2001.

Design of RF Feedthroughs in Zero-Level Packaging for RF MEMS Implementing TSVs

Hamza El GANNUDI[1], Vladimir CHERMAN[2], Paola FARINELLI[1], Nga P. PHAM[2], Lieve BOGAERTS[2], Harrie A.C. TILMANS[2], Roberto SORRENTINO[1]

[1]University of Perugia, Dept. of Electronic and Information Engineering, Via G. Duranti, 93, 06125 Perugia, Italy
E-mail: hamza.ghannudi@diei.unipg.it

[2]IMEC, Kapeldreef 75, B-3001 Leuven, Belgium
E-mail: pham@imec.be

Abstract. This paper reports on the design, manufacturing and RF characterization of a zero-level packaging for RF-MEMS devices implementing TSVs (Through-Silicon Via's) and metal bonding. Coplanar interconnection feedthroughs have been modelled and designed for low loss and wideband RF applications. The coplanar slot width of both sides in the vertical interconnection via's pads have been enlarged and reshaped to compensate for the excessive shunt capacitance. Compensated packaged CPW lines have been manufactured and measured in the 0-40GHz frequency band. A significant improvement in terms of RF loss and frequency bandwidth have been obtained thanks to the compensation procedure. A comparison between simulated and measured data up to 40 GHz are presented and discussed.

1. Introduction

Radio Frequency Micro-Electro-Mechanical System (RF-MEMS) devices have demonstrated great potential for applications at millimetre-wave frequencies because of several advantages such as high signal linearity, low insertion loss, and power saving [1]. However, in order to protect its movable friable parts during its entire lifetime, the RF MEMS device needs to be sealed into a hermetic cavity. Several different technologies exist in order to create hermetic cavities [2] and the most of them depends on several factors such as process temperature, device requirements, costs etc,. One of the main approach exists for 0-level packaging is the ―"chip capping". It can be done as die-to-die (D2D) capping, as a die-to-wafer (D2W) capping, or as a wafer-to-wafer (W2W) capping. A capping technology tolerating a certain level of wafer topology is needed. Since the 0-level package defines the first interface of the RF MEMS device to the outside world, it is clear that the RF design of the package is very important.

The package should provide a good electrical contact for RF signals with the higher level of the system and has a low impact on the RF characterization of the RF structures. The use of low-loss high resistivity cap materials (and MEMS substrate materials) and cap with sufficient cavity height will minimize the degradation influence of the presence of cap [3]. The RF signal feedthrough or transition is one of the promising schemes at 0-level package to serve the RF MEMS devices for wideband interconnection applications [4] . One of the possible implementations for the RF feedthroughs is Vertical via's, implemented either in the MEMS substrate [5,6] or in the Cap [7]. These present a more compact solution (smaller footprint) than the horizontal feedthrough designs, but, the process is more complex as through-wafer hole etching is required. Another advantage of vertical via's is the readiness for 3D implementation.

In this paper, a 0-level package solution based on chip capping is presented. All RF feedthroughs interconnections including Cu-coated through-silicon via's (TSVs) are electromagnetically designed and optimized in order to improve the RF performance of overall structure.

2. Fabrication Process

Within the EU-FP7 project MEMSPACK, a Zero level packaging for RF MEMS devices implementing TSVs and metal bonding is realized using die-to-die bonding process (D2D).

The process flows for the MEMS and cap wafers are manufactured at IMEC (*Interuniversity MicroElectronics Center*). The MEMS package consists of two parts: the MEMS substrate and the CAP. Both are made of high resistivity Si wafers using the 0.35µm CMOS technology adjusted to be compatible with the RF design rules and the flip-chip assembly. This adjustment includes the optimization of the Cu-oxide damascene technology, thicker metal lines and the additional surface passivation layers between the Si and the backend. The CAP wafer was further thinned down to the thickness of 100µm. The thinning step was followed by the etching of the through silicon vias (TSVs) 70µm in diameter. The 2µm thick polymer was then deposited from the back side of the CAP creating the DC and RF isolation for the 5µm thick electroplated copper. As the last step before the assembly the 3µm thick Sn was electroplated to ensure the formation of the reliable solder joints. The CAP and the MEMS dies were then assembled together using the die-to-die (D2D) flip-chip alignment and bonding. The cross-section of the complete assembly is shown in Fig.1 More details on fabrication process including: MEMS substrate, bonding and thining, TSV etching, dielectric patterning, TSV metallization and CuSn/Cu bonding are presented in [8].

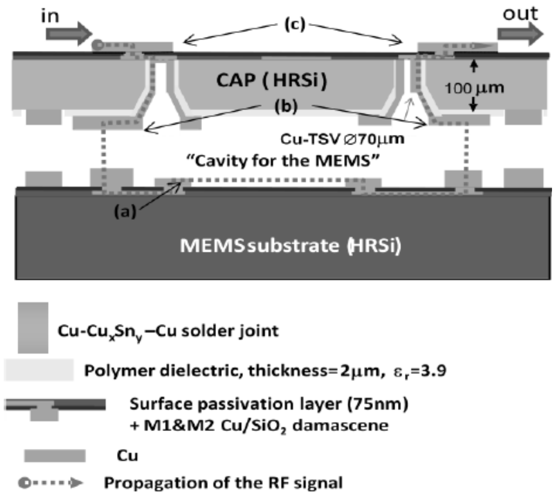

Fig. 1. The cross-section of the hermetic chip MEMS package. The dotted line represents the path for the propagating RF signal.

The blue dotted line in Fig.1 schematically shows the propagation path for the RF signal. The 50Ohm coplanar waveguide (CPW) is patterned on metal of the MEMS die (not shown) and is used to provide the connection between the input and output ports inside the package. The RF signal propagates from the CPW access pad on the top surface of the cap (as show in Fig. 2) through the Cu TSV connected to the short CPW patterned on the back surface of the CAP die. It then continues through the solder joint down to the MEMS die where it goes along the 50 Ohm CPW (which can be replaced by a MEMS in the real application) and then up to the CAP die and to the output RF terminal.

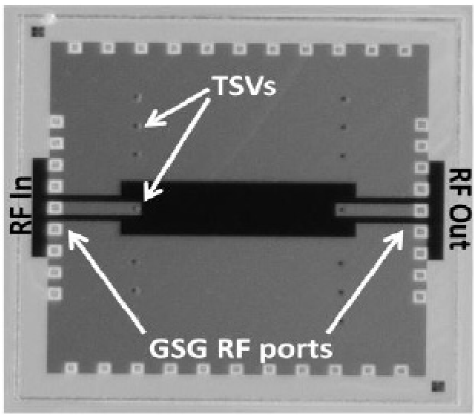

Fig. 9. The top view of the MEMS package with 150μm pitch GWG RF pads.

3. RF Feedthroughs Interconnection Design and Optimization

The most critical part for electrical RF performance is the RF feedthroughs interconnections between layers. In this package, they are based on coplanar-to-coplanar waveguide (CPW-to-CPW) line transitions.
The RF feedthroughs from the MEMS substrate to the RF pads on top of cap consist of the series of three different CPW lines connected through vertical interconnection and Cu TSV. Fig.3 shows the three different CPW lines indicated as (a), (b) and (c) in Fig.1.

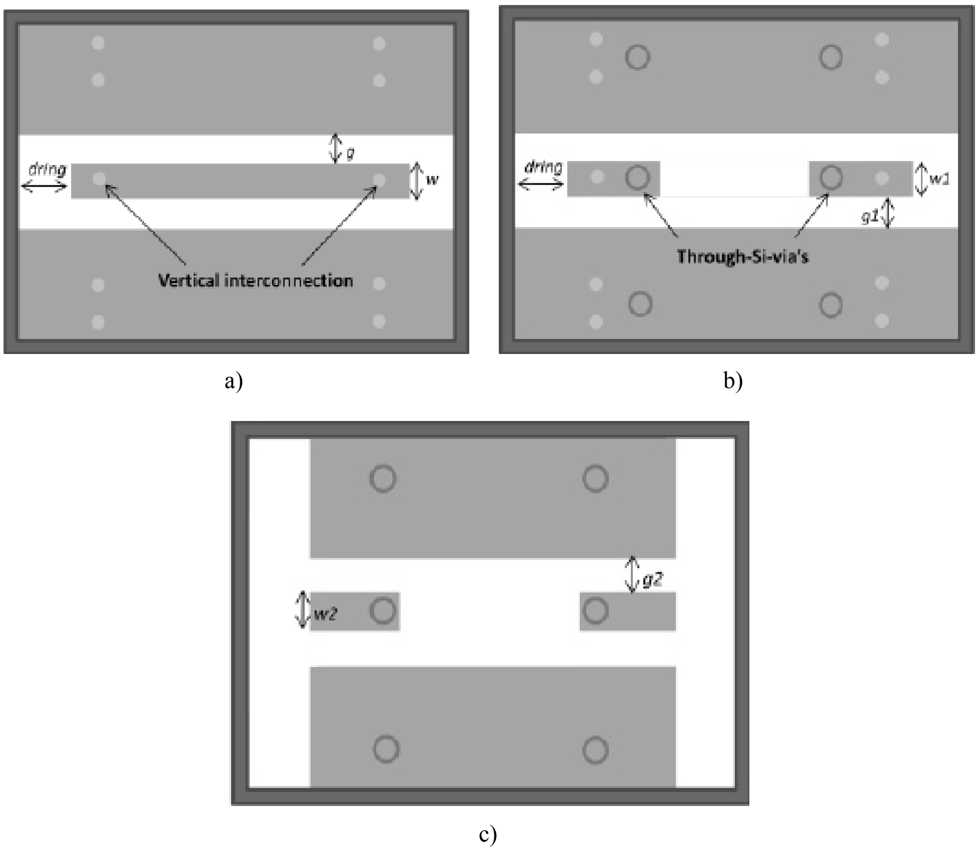

Fig. 3. The three CPW lines with original dimensions before optimization.

A full wave electromagnetic analysis has been performed to study the effect of these transitions on the RF performance, in terms of return and insertion losses. First simple straight CPW-CPW interconnections as indicated in Fig. 3 have been simulated. The dimensions of the three CPW lines are summarized in Table. 1

Table 1. Dimensions of CPW lines

Parameter	Size	Parameter	Size
w	90 µm	*w1*	160 µm
g	50 µm	*g2*	70 µm
dring	100 µm	*w2*	90 µm
Rw (width of ring)	50 µm	*g2*	45 µm

All simulations have been performed using the Ansoft HFSS software. Fig.4 shows the RF performance for these transitions which is significantly deteriorated by the vertical interconnections. Return loss better than 14 dB and insertion loss better than 0.7 dB up to 20 GHz have been obtained.

The basic effects at the transitions of vertical interconnections can be represented as a series reactance. This reactance results from the superposition of capacitive and inductive effects. The capacitive part is caused by dielectric loading at the transition due to the silicon substrate. The inductive contribution is due to the change in current density distribution and direction when going from layer to another layer.

The parameters affecting the interconnection performance are:

• Via diameter.
• Via height (*i.e.* substrate thickness)
• Via pad area (length and width).
• CPW slot width in correspondence of transitions.

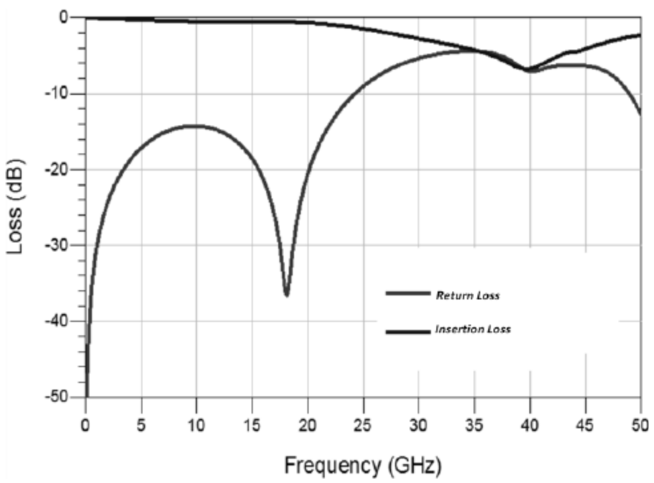

Fig. 4. The three CPW lines with original dimensions before optimization.

The via diameter and height are fixed by technology, the via pad area has been taken as small as possible. We have concentrated on the forth parameter.

In order to improve the RF performance, the basic idea is to compensate the excessive shunt capacitance at the transition by redesigning and adding an inductive section in correspondence of the vertical via. This can be done by locally enlarging the coplanar slot width of the CPW line of both sides in the vertical interconnection pad region as shown in Fig. 5.

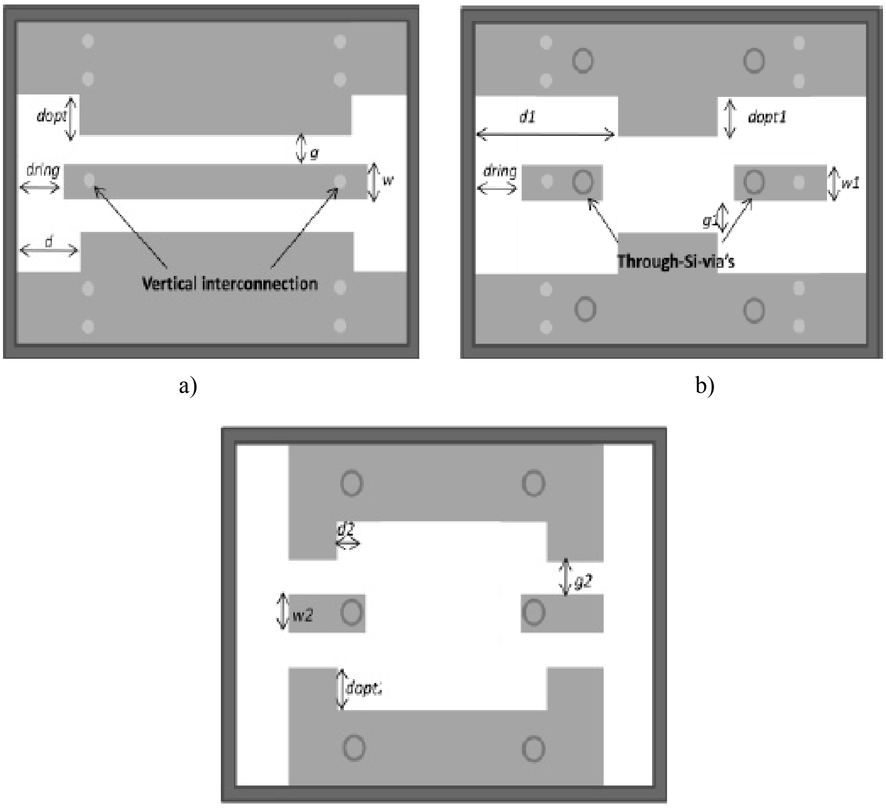

a) b) c)

Fig. 5. The three CPW lines dimensions after optimization.

The compensation has been performed by fixing *dring, d, d1, d2* and varying the distances called *dopt, dopt1,dopt2* from 60 µm to 150 µm. The new dimensions for the compensation steps are summarized in Table. 2

Table 2. Dimensions of redesigned parameters

Parameter	Size	Parameter	Size
d	90 µm	*dopt*	60, 90, 120, 140, 150 µm
d1	50 µm	*dopt 1*	60, 90, 120, 150µm
d2	100 µm	*dopt 2*	60, 90, 120 µm

A parametric electromagnetic simulation using Ansoft HFSS is run in order to find the values of *dopt, dopt1, dopt2* which compensate the excessive shunt capacitance and give better RF performance.

The corresponding results are plotted in Fig. 6 and Fig. 7. It can be noted that the increase of *dopt, dopt1, dopt2* leads to an improvement in RF performance.

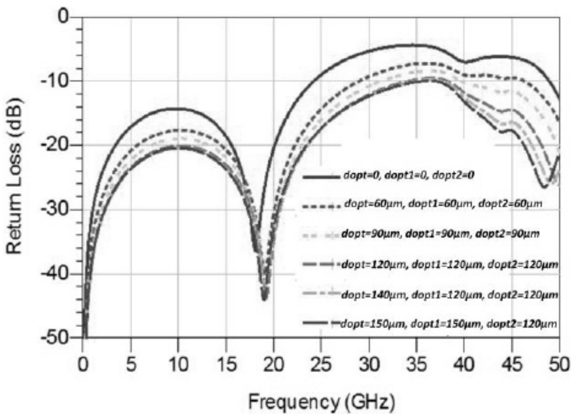

Fig. 6. The simulated Return loss of the compensated structure.

The best return and insertion loss have been obtained for *dopt*=140µm, *dopt1*=120µm, *dopt2*=120µm (green curve). Return loss better than 20 dB and insertion loss better than 0.6 dB from Dc up to 20 GHz have been achieved.

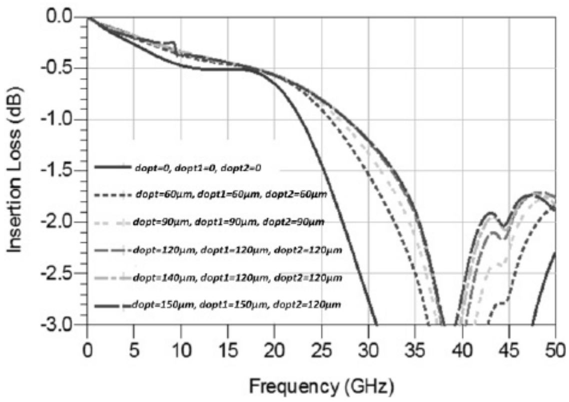

Fig. 7. The simulated Insertion loss of the compensated structure.

Finally, the comparison between the simulated and the measured RF performance of the package in the frequency range of 100MHz-40GHz is shown in Fig. 8 and Fig. 9.

Figure 8 shows that the return loss of both have similar slope but with discrepancy at frequencies less than 20 GHz. The acceptable magnitude of the return loss (better than15dB) indicates that the actual wave impedance of the line is close to the target value in a wide frequency range and that the precision of the flip-chip assembly is accurate enough.

However, a high insertion loss (more than 3.5 dB), indicates the presence of a source of an extra RF loss in the interconnects of the package.

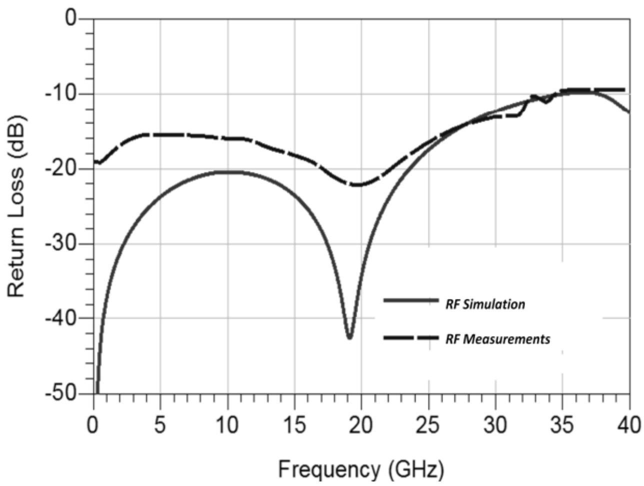

Fig. 8. Comparison between simulated and measured Return loss for the compensated structure.

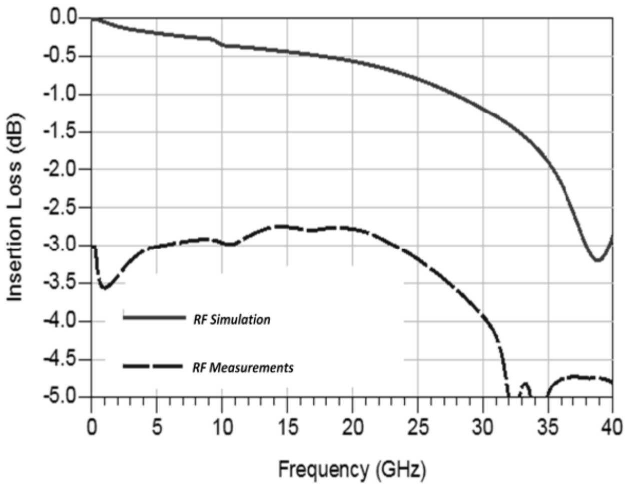

Fig. 9. Comparison between simulated and measured Insertion loss for the compensated structure.

Such abnormal frequency behavior is, however, often reported for coplanar waveguides patterned on a Si substrate [9].

The magnitude of the RF loss in the frequency independent plateau can vary with the doping level of Si and with the surface passivation technique being utilized. Thus, the relatively high level of insertion loss reported in this work may be attributed to the lack of the passivation of the bottom surface (the side from which the TSV are etched) of the HRSi Cap. By minimizing the length of the interconnects (by design) on the Si surfaces, which cannot be passivated, or, by tuning the technology, the insertion loss of the 1-2mm package can be lowered to acceptable values of 0.5-0.7dB.

4. Conclusion

This paper has presented the RF design, manufacturing and characterization of a zero-level packaging for RF MEMS devices implementing TSVs and metal bonding. The CPW to CPW line transitions have been redesigned and optimized in order to compensate the excessive shunt capacitance and improve the RF performance. A simulated return loss better than 20 dB and insertion loss better than 0.6 dB up to 20 GHz have been achieved. A disagreement between measured and simulated loss has been noted due to, most likely, the lack of the passivation of the bottom surface (the side from which the TSV are etched) of the HRSi Cap. The improvement of technology will lead to an acceptable measured loss similar to the simulated one.

Acknowledgments. The authors wish to thank Lieve Bogaerts and Roelof Jansen (IMEC) for helping with the processing.

This work was financially supported by the EC FP7 project MEMSPACK (www.memspack.eu), under grant agreement nr. 223882, a collaboration between IMEC, VTT, FhG-ISiT, Univ. of Perugia, FBK institute, CNRS-IEMN, and MEMS TC. The help and support given by the other partners of the project are greatly acknowledged.

References

[1] G.M. REBEIZ, J.B. MULDAVIN, *RF MEMS switches and swith circuits*, IEEE Microwave Magazine, **2**(4), pp. 59–71, DC. 2001.

[2] R. PELZER, H. KIRCHBERGER, P. KETNNER, *Wafer-to-Wafer Bonding Techniques: From MEMS Packaging to IC Integration Applications*, Proc 6th International Conference on Electronic Packaging Technology, pp. 508–513.C, August 2005

[3] A. JOURDAIN, X. ROTTENBERG, G. CARCHON and H.A.C. TILMANS, *Optimization of 0-level packaging for RF-MEMS devices*, proc. Transducers'03, pp. 1915–1918. Boston, USA, June 8-12, 2003.

[4] H.J. De Los SANTOS, G. FISCHER, F.A.C. TILMANS, J.T.M. van BEEK, *RF MEMS for ubiquitous wireless connectivity. Part II. Application*, IEEE Microwave Magazine, **5**(4), pp. 50–56 Des 2004.

[5] M. FUJII, I. KIMURA, T. SATOH and K. IMANAKA, *RF MEMS switch with wafer level package utilizing frit glass bonding*, proc. 32nd European Microwave Conference EUMC2002, **1**, pp. 279–281, Milan, Italy, 23-27 September 2002.

[6] Li-Han HSU, Wei-Cheng WU, Chang Edward YI, Zirath HERBERT, Yun-Chi WU, Chin-Te WANG and Ching-Ting LEE, *Design and fabrication of 0/1-level RF-via interconnect for RF-MEMS packaging applications*, IEEE Trans. on Adv. Packaging, **33**(1), pp. 30–36, Feb. 2010.

[7] C. FERRANDON, F. GRECO, E. LAGOUTTE, P. DESCOURS, G. ENYEDY, M. PELLAT, C. GILLOT, P. REY, D. MERCIER, M. CUEFF, X. BAILLIN, F. PERRUCHOT, N. SILLON, L.J. LIU, S. PACHECO, M. MILLER, *Hermetic wafer-level packaging development for RF MEMS switch*, proc. Electronics System Integration Technology Conference ESTC2010, , Berlin, Germany, September 13-16, 2010.

[8] Nga P. PHAM, Vladimir CHERMAN, Bart VANDEVELDE, Paresh LIMAYE, Nina TUTUNJYAN, Roelof JANSEN, Nele Van HOOVELS, Deniz S. TEZCAN, Philippe SOUSSAN, Eric Beyne and Harrie A.C. Tilmans, *Zero-level packaging for (RF-)MEMS implementing TSVs and metal bonding*, submitted and accepted for the Electronic Components and Technology Conference ECTC2011, 31 May-3 Jun 2011, Florida, USA.

[9] B. RONG, J.N. BURGHARTZ, L.K. NANVER, B. REJAEI, M. van der ZWAN, *Surface-passivated high-resistivity silicon substrates for RFICs*, IEEE El. Dev. Lett., **25**(4), pp. 176–178, April 2004.

Material Properties Characterization of BiCMOS BEOL Metal Stacks for RF-MEMS Applications

M. WIETSTRUCK[1], M. KAYNAK[1], W. ZHANG[1], D. WOLANSKY[1], S. KURTH[2], B. ERLER[3], B. TILLACK[1,4]

[1]IHP, Im Technologiepark 25, 15236 Frankfurt (Oder), Germany
Tel: (+49) 3355625 609,
Email: wietstruck@ihp-microelectronics.com

[2]Fraunhofer ENAS, Technologie-Campus 3, 09126 Chemnitz, Germany

[3]Polytec GmbH, Polytec Platz 1, 76337 Waldbronn, Germany

[4]Technische Universität Berlin, HFT4, Einsteinufer 25, 10587 Berlin, Germany

Abstract. The mechanical material parameters of complex metal layer stacks embedded inside a BiCMOS process have been analyzed. Finite-Element-Method simulations (FEM) with a combination of statistical calculation methods have been used to accurately determine the material properties. The Young's modulus of AlCu and TiN have been found to be 65 GPa and 410 GPa. The residual stress values have been extracted as -514 MPa (compressive), 494 MPa (tensile) and -964 MPa (compressive) for the TiN Top-layer, AlCu and the TiN Bottom-layer which is in good agreement to in-line wafer curvature measurement. Intrinsic stress was found to play an important role for the reason that it partly compensates temperature-induced stress and offers a reliable RF-MEMS switch operation. The extracted material parameters are very useful to perform accurate FEM simulations and help to reduce the design/modeling time of new BiCMOS embedded MEMS components.

Index Terms: FEM analysis, material characterization, residual stress, RF-MEMS switch, monolithic integration.

1. Introduction

The knowledge of mechanical material parameters is mandatory for the development of MEMS due to their influence on device performance and reliability [1]. One of the most important MEMS components for RF applications are electromechanical switches [2].

Electromechanical switches are considered as a key component for multi-band circuits due to their low insertion loss, high isolation and low power consumption [3, 4]. Recently a BiCMOS embedded RF-MEMS switch was demonstrated with an excellent performance and a very good reliability [5, 6]. The specific switch consists of electrodes in Metal 1, the signal line in Metal 2 and a TiN/AlCu/TiN stack in Metal 3 which is used as a movable membrane (Fig. 1).

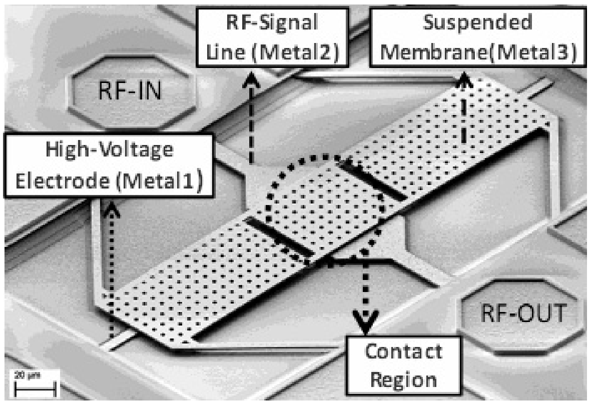

Fig. 1. SEM of the BiCMOS embedded RF-MEMS switch.

For a cost-efficient development and fabrication, the mechanical and electrical performance has to be simulated/modeled with accurate material parameters which strongly depend on deposition conditions [7], determine the stiffness of the system and therefore define the actuation voltage, switching time and reliability which need to be optimized before fabrication. In this work we have demonstrated the characterization of a complex metal layer stack of a BiCMOS BEOL metallization based on optical measurements and FEM simulations. The developed method provides mechanical material properties of the suspended Metal 3 layer and is very promising to perform accurate mechanical simulations of MEMS structures.

2. Material Parameter Estimation

Different material characterization methods like mechanical resonance, pull-down voltage and load-deflection method have been proposed in literature to estimate mechanical material properties [8, 9]. In this work, the determination of the specific mechanical material properties is based on mechanical resonance and load-deflection method combined with FEM simulations and statistical methods (Fig. 2).

The mechanical resonance frequency or load-dependent deflection of a mechanical system strongly depends on the material parameters. These two main properties of the specific test structures are simulated using CoventorWare ®. A multivariate linear regression (MLI) is used to determine a dependency between measurement value and the important material parameters. The “coefficient-of-determination” shows if the linear regression is sufficient or a higher-order polynomial function is required. The method is resulting in different sets of material parameters which show the lowest deviation to measurement results. The shown method is universal for different types of static and dynamic behavior and can be adapted to several applications.

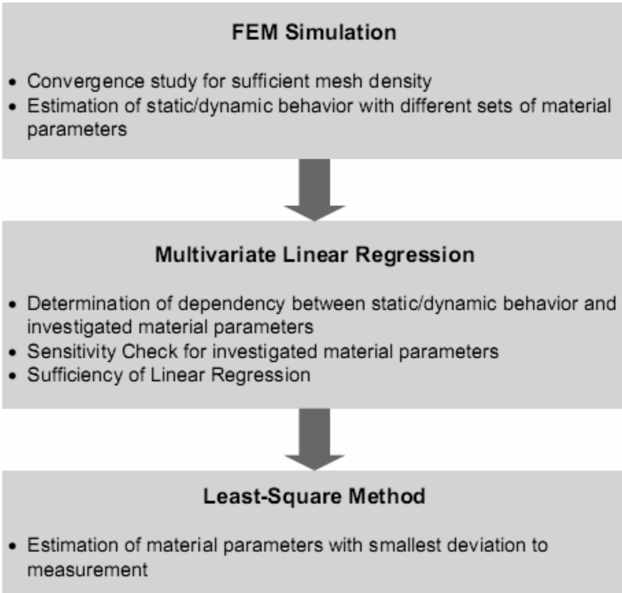

Fig. 2. Material parameter estimation method.

3. Experimental Results

The movable part of the RF-MEMS switch is realized using the Metal 3 layer of the BiCMOS BEOL stack. Metal 3 consists of three different layers: TiN/AlCu/TiN. TiN layers are used as a barrier layer between AlCu and the BEOL oxide whereas AlCu (99.5% Al) is used as the main conductive part of Metal 3. Typically, the TiN layer has a thickness of ~200 nm while the AlCu layer has a thickness of ~700 nm. The mechanics are mainly dominated by the Young's modulus of TiN, AlCu and the residual stresses of these layers. Residual stress is a combination of temperature-induced stress and intrinsic stress [10]. Temperature-induced stress is a result of cooling down process from deposition temperature (~500K) to room temperature due to the different thermal expansion coefficients of AlCu and TiN. Intrinsic stress is caused by crystallographic defects, grain boundaries and further deposition effects [11]. The material parameters are strongly affected by the type of deposition and the deposition conditions like temperature and pressure. The estimation of Young's modulus and residual stress is done with different types of structures and the aforementioned estimation method.

A. Determination of Young's modulus

To determine the Young's modulus, clamped beams with different lengths and widths have been fabricated and measured (Fig. 3).

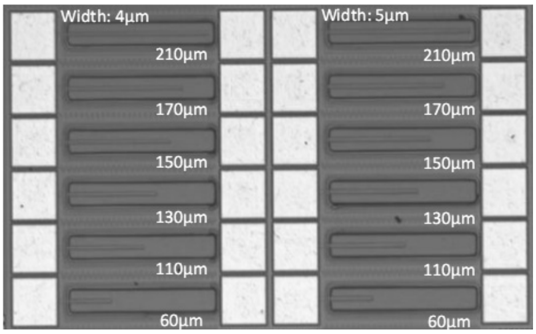

Fig. 3. Clamped beams for estimation of Young's modulus.

The frequency-response-function (FRF) of simple clamped beams depends on the Young's modulus. The first eigenfrequency can be calculated by (1) and shows a dependency on the length, the thickness, the material density and the Young's modulus E.

$$f_r = \frac{1}{2\pi \cdot l^2} \cdot \sqrt{\frac{4 \cdot E \cdot t^2}{\rho}} \tag{1}$$

The geometry was investigated by Focused-Ion Beam Milling (FIB) to consider process-specific characteristics like under-etching of the cavity mask (lateral etch of SiO_2) and unwanted etching of AlCu to take these effects into account during FEM simulation (Fig. 4).

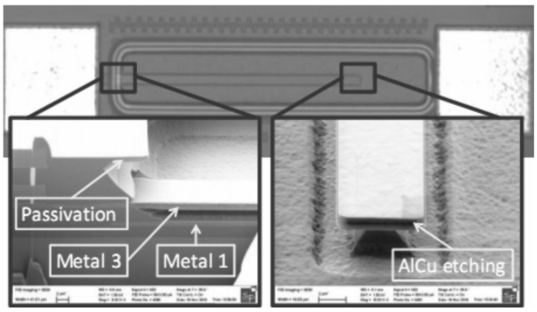

Fig. 4. FIB analysis of clamped beam.

The MLI has shown that the FRF is independent from residual stress and therefore it is only defined by geometry and the effective Young's modulus of the metal stack. The FRF was detected by electrostatic actuation with a broadband signal and observing the mechanical response with the Laser-Doppler Vibrometer (LDV) MSA-500 from Polytec®. The FRF of a 210 µm beam is shown in Fig. 5. It provides 6 detectable eigenfrequencies in the maximum frequency range of 2.5 MHz.

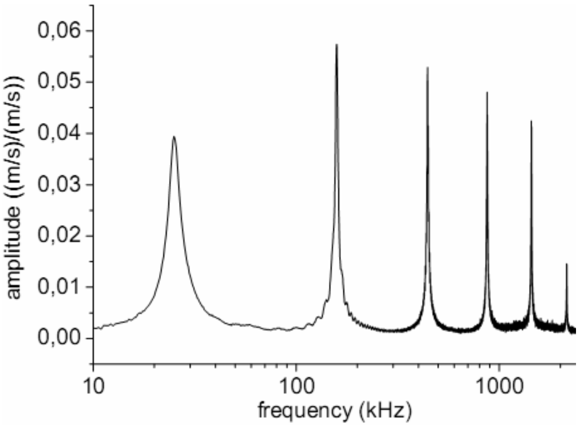

Fig. 5. Frequency-response-function of 210 µm beam.

The "coefficient-of-determination" is higher than 0.998 for every eigenfrequency and therefore the linear type of multivariate regression is suitable. The most accurate result of the least-square method with lowest deviation tomeasurement is shown in Table 1.

Table 1. Results for determination of Young's modulus

E_{AlCu}	E_{TiN}	Maximum deviation $f_{1\text{-}6}$
65 GPa	410 GPa	3.0%

The Young's modulus of 65 GPa for AlCu and 410 GPa for TiN are in a very good agreement with literature [12, 13] and the simulated FRF with the estimated material properties shows a small deviation of 3% compared to the measured FRF. For further analysis of residual stress, the estimated Young's moduli are applied to RF-MEMS switch structure to analyze the residual stress characteristics of the AlCu and TiN layers.

B. Determination of Residual Stress

Residual stress in suspended structures results in an up or down bended membrane and strongly influences the performance of the switch. Residual stress is not only limiting the reliability performance by affecting the restoring force and therefore the risk for stiction, but also results in poor electrical and RF performance.

By the help of this analysis, optimal switch structures can be selected in design-level. This helps to decrease the design optimization time and to improve the yield of the process.

To perform the residual stress analysis, the surface topology of the RF-MEMS switch has been observed using White-Light-Interferometer (WLI) shown in Fig. 6.

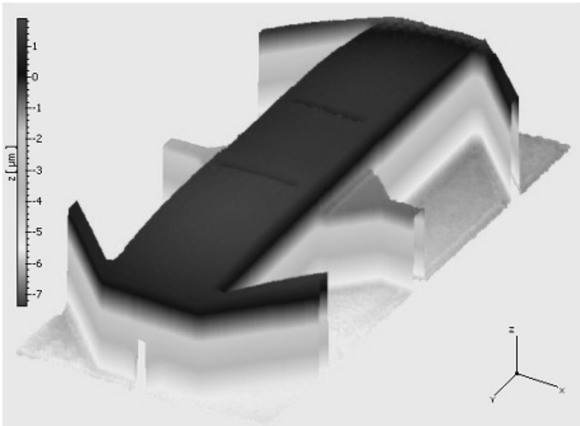

Fig. 6. WLI of RF-MEMS switch.

The aforementioned calculation method is used to estimate the residual stress. An initial deflection of the suspended membrane is achieved by adding residual stress to the different layers. Different tensile and compressive stress cases have been applied and the surface topology was extracted along the black line shown in Fig. 7.

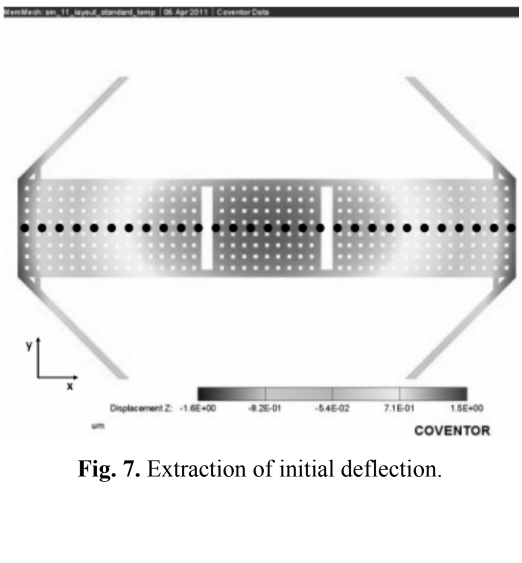

Fig. 7. Extraction of initial deflection.

The MLI shows a high sensitivity to residual stress but it has to be considered that the “coefficient-of-determination” varies for different locations in x-direction. Only points with a high “coefficient-of-determination” have been taken into account. The most accurate result of the least-square method is shown in Table 2. The results are in good agreement to in-line stress measurements using wafer curvature method. Characterization of stand-alone layers was only possible for the Bottom TiN and AlCu layers.

Table 2. Results of residual stress for different layer

Layer	TiN-Top [MPa]	AlCu [MPa]	TiN-Bottom [MPa]
Calculation	-514 (comp.)	494 (tensile)	-964 (comp.)
Wafer Curvature	---	432 (tensile)	-860 (comp.)

The initial deflection of the switch has been simulated with the resultin residual stress and shows an excellent agreement to the real surface topology of the investigated RF-MEMS switch (Fig. 8). The zero-level of initial deflection shows the position of the clamped anchors.

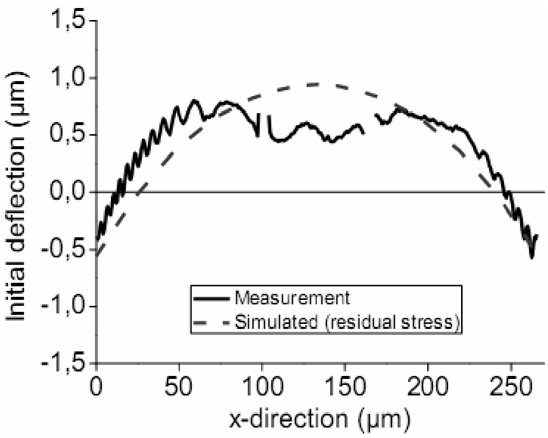

Fig. 8. Initial deflection due to residual stress.

In fact, the initial deflection is caused by two effects: temperature-induced stress and intrinsic stress. To distinguish between these two effects, firstly the temperature-induced stress is simulated by the thermal expansion coefficients taken from [14, 15] and a constant zero-stress temperature option which is provided by CoventorWare®. The initial deflection of the switch after applying the temperature-induced stress is shown in Fig. 9.

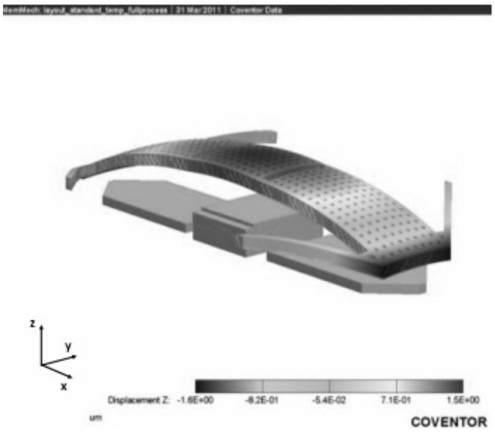

Fig. 9. Initial deflection due to temperature-induced stress.

As can be seen from Fig. 9, the center of the suspended membrane is up-bended compared to the anchors whereas the edges are strongly down-bended. Temperature-induced stress leads to a deflection status higher than measured which shows that intrinsic stress partly compensates the temperature-induced stress and has a primary importance. Without any compensating intrinsic stress, the distance between the grounded membrane in Metal 3 and the high-voltage electrodes in Metal 1 is about 1.5μm which increases the risk for a short between Metal 1 and Metal 3.

The estimation of stress compensating intrinsic stress is achieved by adding intrinsic compressive and tensile stress combinations to the different layers. The initial deflection of the switch has been simulated with the resulting temperature-induced stress and intrinsic stress and shows again a good accuracy to the real surface topology of the switch (Fig. 10).

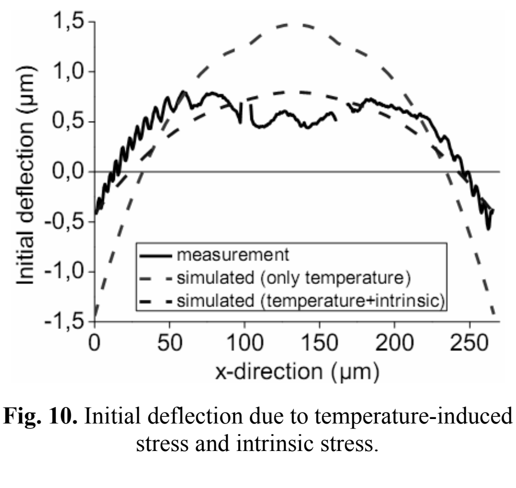

Fig. 10. Initial deflection due to temperature-induced stress and intrinsic stress.

The estimated intrinsic stress parameters are shown in Table 3. The stress compensating intrinsic stress has a crucial importance to prevent from device failure.

Table 3. Results for determination of intrinsic stress

Layer	TiN-Top [MPa]	AlCu [MPa]	TiN-Bottom [MPa]
Calculation	-1240 (comp.)	-240 (comp.)	-1460 (comp.)

4. Conclusion

The mechanical material properties of a complex three-layer metal stack have been characterized using the FRF of clamped beams and the surface topology of current RF-MEMS switch structure. The Young's moduli of AlCu and TiN have been found to be 65 GPa and 410 GPa which are in good agreement with literature. The residual stress values have been extracted as -514 MPa (compressive), 494 MPa (tensile) and -964 MPa (compressive) for the TiN Top-layer, AlCu and the TiN Bottom-layer. Intrinsic stress partly compensates temperature-induced stress and therefore plays an important role by enabling a stable and reliable RF-MEMS switch operation.

The developed technique can be applied for different process conditions and provide precise material properties which help the modeling of various MEMS structures. Furthermore, understanding the stress non-uniformity over the wafer using the developed technique helps to enhance the yield of the MEMS process.

Acknowledgement. The authors thank to the team of the IHP pilot line for excellent support. This work was supported by the European Commission (contract no. 257335-FLEXWIN) and BMBF (contract no. 03IS2011-NANETT "Nanosystemintegration").

References

[1] J. GASPAR, *et al*, *Mechanical Characterization of CMOS Metal Layers*, IEEE 2009.
[2] J. WALRAVEN, *Introduction to Applications and Industries for Microelectromechanical Systems (MEMS)*, IEEE 2003.
[3] G. REBEIZ, *et al*, *RF MEMS Switches and Switch Circuits*, IEEE 2001.
[4] E. BROWN, *RF-MEMS Switches for Reconfigurable Integrated Circuits*, Antenna IEEE 1998.
[5] M. KAYNAK, *et al*, *BEOL Embedded RF-MEMS Switch for mm-Wave Applications*, IEDM 2009.
[6] M. KAYNAK, *et al*, *Characterization of an Embedded RF-MEMS Switch*, SiRF 2010.
[7] K. SATO, *Characterization of MEMS Materials: Measurement of Etching Properties and Mechanical Strength*, IEEE 1996.
[8] X.Y. YE, *et al, Measurement of Young's Modulus and Residual Stress of Micromembranes*, IEEE 1996.

[9] G. Yaralioglu, *et al*, *Residual Stress and Young's Modulus Measurement of Capacitive Micromachined Ultrasonic Transducer Membranes*, IEEE 2001.
[10] S. Chen, *et al*, *A New in Situ Residual Stress Measurement Method for a MEMS Thin Fixed-Fixed Beam Structure*, IEEE 2002.
[11] C. Hollauer, *Modeling of Thermal Oxidation and Stress Effects*, Dissertation, Fakultät für Elektrotechnik und Informationstechnik, Technische Universität Wien,2007.
[12] M. Pritschow, *Titannitrid- und Titan-Schichten für die Nano-Elektromechanik*, Fakultät Maschinenbau, Universität Stuttgart, 2007
[13] F. Macionczyk, *et al*, *Tensile Testing of AlCu thin films on polyimide foils*, Journal of Applied Physics 1999.
[14] J. Lee, *et al*, *Finite Element Simulation of a Stress History During the Manufacturing Process of Thin Film Stacks in VLSI Structures*, IEEE 1998.
[15] D. Dobkin, *CVD of TiN and other barrier metals*, enigma-consulting.com.

Charge Trap Investigation Methodology on RF-MEMS Switches

M. BARBATO[1], V. GILIBERTO[1], A. MASSENZ[1], F. Di MAGGIO[3], M. DISPENZA[4], P. FARINELLI[2], B. MARGESIN[5], E. CARPENTIERI[6], U. D'ELIA[6], I. POMONA[3], M. TULUI[7], F. CASINI[2], R. SORRENTINO[2], E. ZANONI[1], G. MENEGHESSO[1]

[1]University of Padova, Dept. of Information Engineering and IUNET, via Gradenigo 6B - 35131, Padova, Italy
E-mail: gaudenzio.meneghesso@dei.unipd.it
[2]University of Perugia, DIEI, Via G. Duranti 93, 06125 Perugia, Italy
[3]Selex Communications Spa, Via Sidney Sonnino, 6 - 95045 Misterbianco (CT), Italy
[4]Selex Sistemi Integrati S.P.A. Via Tiburtina 1231 00100 Roma, Italy
[5]MEMSRaD Research Unit, FBK-irst, Via Somarive 14, 38050 Trento, Italy
[6] MBDA Italia SPA, Via Tiburtina Km.12400 00131 Roma, Italy
[7]Centro Sviluppo Materiali SpA, via di Castel Romano, 100 -00128 Roma, Italy

Abstract. We hereby discuss effects and consequences of using certain measurements approaches on the charge trap analysis of RF-MEMS switches during cycling tests. We analyze how measurements are affected when the shape of the pulse changes, when the cycling frequency decrease and when measurements are carried out as a function of temperature. The trends here presented must to be taken into account when devices, that suffer of severe charge trapping phenomena, like those used in the following experiments, are considered. The real goal in fact, is to fully characterize the real performances of the devices separating the effects that different measurements analysis have on the device itself.

1. Introduction

RF-MEMS switches combine excellence electrical responses such as high isolation, ultra low-losses and high liner response with the well known advantages provided by the solid state fabrication processes, like reduced size, power consumption and costs of high volume products.

These devices are nowadays among the most promising technologies for terrestrial and satellite telecommunication systems because of their advantages, even though some issues, especially related with reliability and packaging [1], have not been resolved yet.

As regards reliability aspects both mechanical and electrical issues as well as semiconductor phenomena are often present leading, sometimes, to unreliable devices especially for high requirements applications like those related with space and aerospace market. In particular contact degradation [2], charge trapping phenomena [3], elastic/plastic deformations, fractures and structural elements stresses can be named. For the scope of our work, it has to be underlined that charge trapping issues appeared to be the dominant effect on devices. Charge trapping, i.e. the physical effect that traps charge carriers usually into the oxide layers, heavily modifies both electrical and mechanical properties of devices until charges are in somehow released. This usually causes an apparent early grave of devices. The necessity of fully characterize RF-MEMS on all their aspects requires several analysis approaches such as measurements at different frequencies, analysis carried out as a function of temperature as well as cycling tests [4] with different pulse shapes. Charge trapping phenomena though, combined with the effects induced by these methods, might lead to unclear or even counterintuitive results since different aspects combine together in a common outcome.

The aim of this work is to explain the role of each measurements aspects involved and, therefore, to separate charge trapping effects from those caused by different measurements approaches. In such a way we aim to a better understand the actual performances of devices measured, which is always the ultimate goal.

In particular, the effect of different pulse shapes, different plate temperature and, eventually, the effect of different frequencies are considered. For each of these aspects we provide experimental results and their interpretation.

When measuring devices that considerably suffer of charge trapping issues, the reader should take into account results proposed in this work in order to better understand how the effect of these analysis methods overlaps with trapped charges.

2. Technology Process and Measurement Setup

The devices have been fabricated at FBK by employing a well established process for RF-MEMS switches based on surface micromachining techniques combined to standard CMOS technology processing steps. The schematic flow of the 8 mask process is shown in Figure 1.

Initially on the p-type 5 kΩ silicon substrates a 1000 nm thick thermal oxide is grown. Next a 630 nm thick polysilicon layer is deposited, slightly doped by ion implantation and defined by photolithography and etching. In the next step a multi layer metallization of Ti/TiN/Al/Ti/Ti is deposited by sputtering for a total thickness of 630 nm in order to equal the thickness of the polysilicon layer. In turns, this metal layer is protected with 100 nm of a low temperature oxide obtained by

Low Pressure Chemical Vapor Deposition (LPCVD) from silane. At this point a 3 μm thick photoresist layer is deposited. After the evaporation of a 25 nm thick gold layer (with an 3 nm thick chromium film as adhesion layer underneath) in a first galvanic process a 1.8 μm thick gold layer is deposited in areas defined by photoresist. With a second galvanic process an approximately 4 μm thick gold layer is deposited, again defined by photoresist.

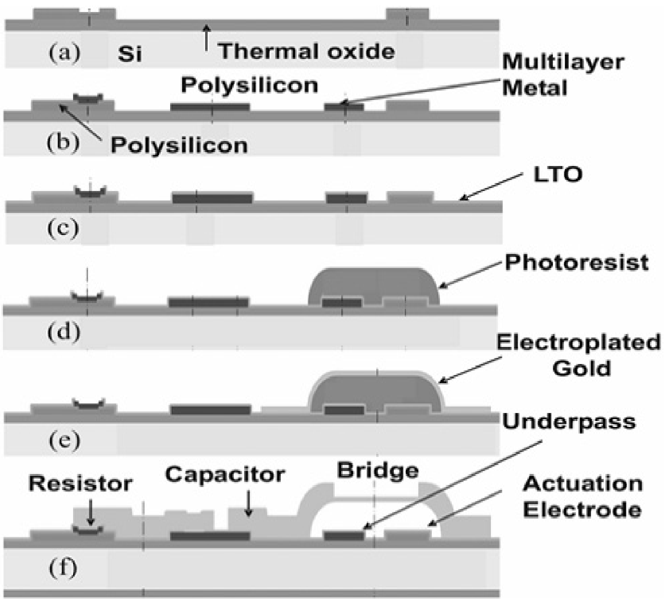

Fig. 1. Micromachining techniques description: 8 mask process from silicon substrate to gold membrane.

Ohmic series switches have been fabricated and in Figure 2 we report S_{21} versus bias voltage taken from a typical device that clearly shows low losses and high isolation. It must be stressed that all the measurements carried out in this work, have been carried out on wafer level in air, at controlled temperature, but not in nitrogen atmosphere. This is clearly the reason for the relatively low lifetime obtained in these test (as it will be shown later). The aim of this work, however, was to study the charge trapping mechanisms, in the devices and not the lifetime evaluation.

The actuation voltage is about 20 V while the release voltage is close to 16 V. The DC bias voltage used in cycling tests has been chosen at 40 V in order to obtain a good actuation of the device. The setup used in our experiments consists of a vector network analyzer used to monitor S-parameters, a waveform generator and a pulse generator used to generate the actuation waveform during cycling and a source meter used during DC characterization.

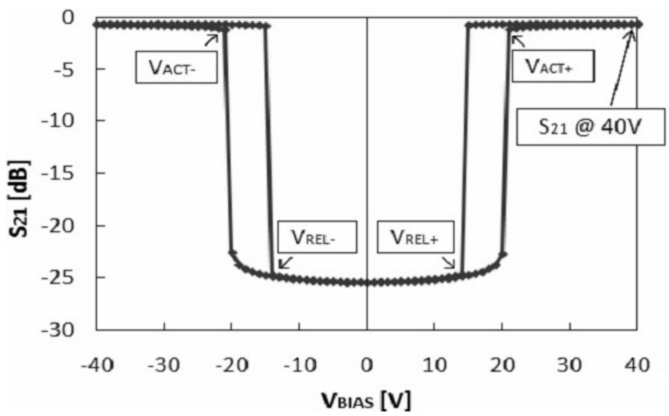

Fig. 2. S_{21} parameter vs. bias voltage for a typical device.

3. Analysis Methods and Their Effects

A. The effect of the pulse shape

Three different cycling pulse shapes, shown in the inset of Figure 4, have been used and compared in terms of their effect on the measurements. It is hereby shown that, by using different shapes for the cycling pulse, more or less charge is trapped [5].

First of all, we notice that degradation of scattering parameters can be mainly attributed to the charge trapping phenomena, since no significant permanent degradation has been measured once trapped charges was released.

To highlight the charge trapping phenomena in these devices (leading to a recoverable degradation), a cycling test has been carried out by setting the DC bias voltage below the actuation voltage, see Figure 3.

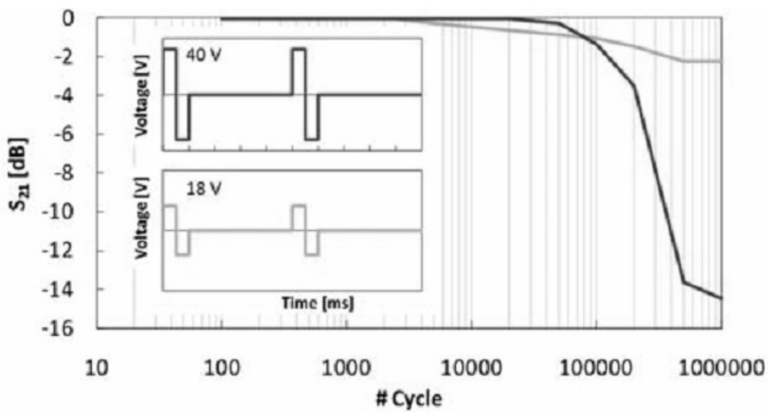

Fig. 3. S_{21} parameter vs. number of cycles with a bias voltage set above and below the actual device actuation voltage.

In such a way, in fact, the bias voltage was slightly less than the one required to lift the bridge down, but strong enough to create a significant electric field and hence charge trapping, in the MEMS structure. As see in Figure 3 a slight (but relevant) S21 degradation is observed, also when cycling the MEMS below the actuation voltage (orange curve, with VSTRESS = 18V). Since no mechanical contact degradation can happen in this experiment, this is an indirect confirmation that charge trapping is present in these devices.

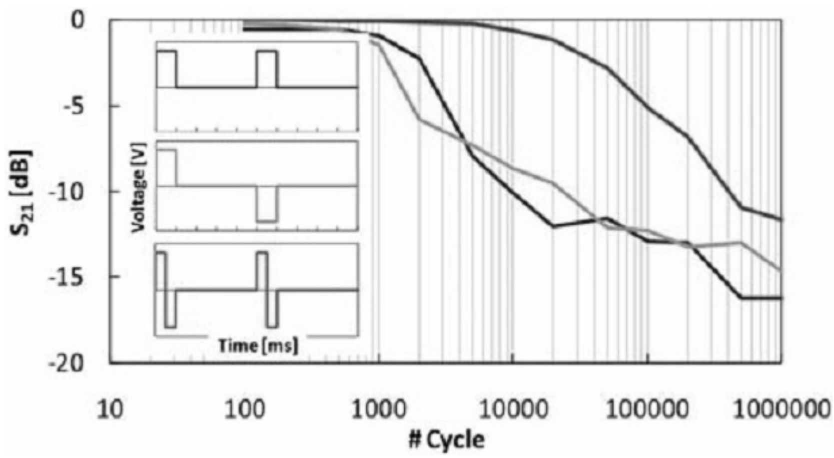

Fig. 4. Average S_{21} parameter vs. number of cycles of the same device cycled with different pulse shapes. The S_{21} parameter values are taken at 40 V.

Once we proved that charge trapping issues affects these devices during cycling tests, we investigated how different pulse shapes affect the behavior. Figure 4, shown the degradation of the S_{21} parameter during cycling in three representative series ohmic switches, driven with different pulses. The RF-MEMS switches, cycled with unipolar and alternating bipolar pulses (blue and green curves), show large S_{21} degradation after only 103 cycles. The dual-polarity pulse shape within the same period (the red curve in Figure 4), shows an improvement of the sustainable cycles (up to about 0.1 Million Cycles).

This is a clear indication that these dual polarity pulses (within the same period) largely mitigate charge trapping effects with respect to the other pulses. Another possible reason for the larger lifetime, induced by these bipolar pulses, could be related to a certain attenuation of the strength with which the contacts collapse one on the others, leading to a lower mechanical degradation.

The different effect caused by the double pulse within the same period and the one in which positive and negative bias alternates to each other, is still under investigation. However we have to point out that the inversion of polarity in the former pulse is fast enough so that the cantilever membrane does not have time to detach while the electric field inversion mitigate the trapped charge. At least three devices, with identical design and taken from different wafer area have been cycled and averaged for each pulse shape. In conclusion we have just shown that, by using different pulse shape, we can mitigate charge trapping on the device and by knowing these effects we can largely improve the lifetime of these RF-MEMS switches.

B. Effect of the temperature

Having proved that these devices suffer from severe charge trapping issues, during cycling tests, we wanted to investigate the effect of temperature. By the means of a thermal chuck we have tested "on-wafer" devices at different temperatures (from ambient to +70°C). The energy provided in such a way was expected to be partially transferred to charges in those midway energy levels that trap electrons, allowing in such a way their releasing. Surprisingly, we have actually measured a worsening of the scattering parameters, when testing the RF-MEMS at higher temperature, as shown in Figure 5.

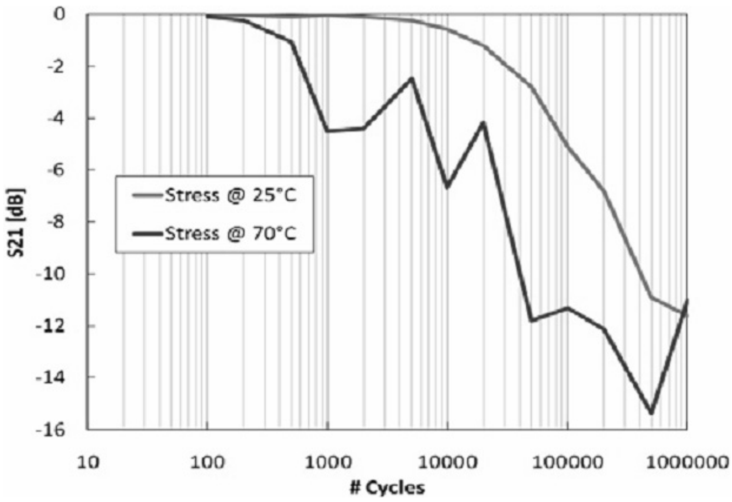

Fig. 5. Average S_{21} parameter vs. number of cycles of the same device cycled at different temperatures. The higher the temperature, the faster a switch is damaged. The S_{11} parameter, shows the same behavior.

This result can be explained as follow. Since the pulse shape used in our tests was the dual polarity one within the same period (third in Figure 3), trapped charges effects was already largely reduced thanks to the adopted dual polarity pulse shaping. Also we observed that the degradation observed in the RF-MEMS using the dual polarity pulse, is non-recoverable. This suggests us that the degradation in this case is related to the mechanical deformation of the switch. As a consequence, by increasing the temperature, device became more prone to plastic deformation and this can explain the lower lifetime of the switches at high temperatures [6].

C. Effect of frequency

We also confirmed that the choice of the cycling frequency (using unipolar pulses) can affect the charge trapping phenomena. As shown in Figure 6, in fact, a lower cycling frequency seems to reduce the lifetime of a device in terms of number of cycles by trapping more charges, compared to the one of an identical device that switches faster.

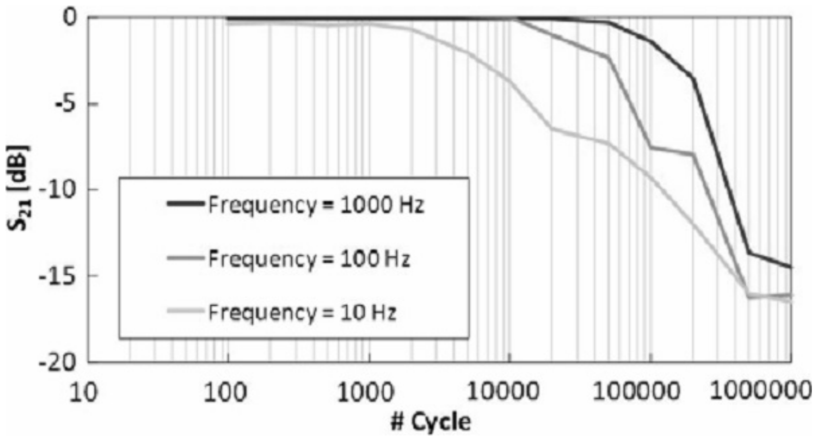

Fig. 6. Cycling tests performed at different frequencies. The charge trapping effect appears stronger at lower frequency than the one at higher frequency.

However, as shown in Figure 7, the actual lifetime of a device switched at lower frequency, is much longer that these used at higher frequency. The fact that scattering parameters degradation is much faster at lower frequency (in Figure 6) can be motivated as follow. Even though the duty cycle is kept at a constant value of 0.2, the stress voltage, and therefore the electric field, is applied for a longer time at a lower frequency. As a consequence, more charge is trapped and therefore the number of cycles tends to be smaller. Figure 6 and Figure 7 differs from each other for the horizontal axis expressed in number of cycle and time domain respectively.

From Figure 7 we can see that considering the same actuation time (i.e. the time in which the MEMS remain actuated) the device cycled at a higher frequency is subjected to a major number of impacts and hence the contact degradation occurs earlier than a device cycled at lower frequency.

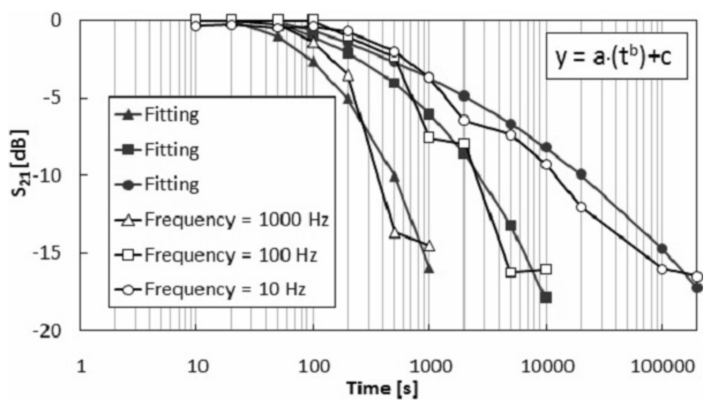

Fig. 7. Cycling tests performed at different frequencies. The picture show that at parity of actuation time in one period (duty cycle = 0.2) higher frequency due to a degradation of contact.

It is interesting to note that the slope of the S21 in Figure 7, can be considered as a degradation rate, and hence as a factor to evaluate the robustness of RF-MEMS: the faster the slope is, the easier and faster is the contact degradation. Power law curves (1) and stretched exponential law (2) were used to fit experimental data obtaining good results (see Figure 7 and Figure 8) like in [7] and [8].

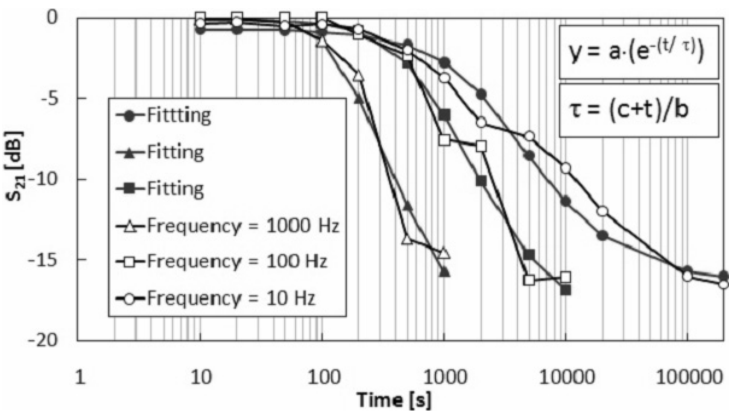

Fig. 8. Cycling tests performed at different frequencies. The picture show the fitting using stretched exponential law.

$$y = a \cdot (t)^b + c \tag{1}$$

$$\begin{aligned} y &= a \cdot e^{-(t/\tau)} \\ \tau &= (c+t)/b \end{aligned} \tag{2}$$

The fitting parameters are shown in Table 1 for power law and in table II for stretched exponential law.

Table 1. Parameters used for fitting (power law).

	a	b	c
F = 1000 Hz	-0.3725	0.5639	2.36
F = 100 Hz	-0.6506	0.3747	2.65
F = 10 Hz	-3.499	0.1568	5.98

Table 2. Parameters used for fitting (exponential law).

	a	b	c
F = 1000 Hz	-1.7E-07	-18.67	17
F = 100 Hz	-0.07	-5.61	265
F = 10 Hz	-0.7	-3.15	1301

4. Conclusion

We discussed three different analysis methods and their effect on the RF-MEMS characterization. In particular we have shown how the pulse shape affects charge trapping phenomena. We have also shown that the effect of the temperature, associated with a specific cycling pulse, might only worsen the scattering parameters degradation instead of improving them.

Eventually, we proved that also different frequencies affect the results of cycles lifetime of a RF MEMS. These approaches and results here should be considered whenever RF-MEMS switches, especially those that suffer of charge trapping phenomena, are studied. Our approach allows users to focus on the final goal, which is to discover the actual performance of devices analyzed.

By knowing the effect that a measurement set-up induces in the MEMS performances, it is then possible to separate the induced parasitic behavior form the real device response. As already mentioned, the relatively low cycling robustness is a consequence of the measurements carried out on uncapped devices.

Acknowledgement. This work was partially supported by Finmeccanica under the project CONFIRM, and by ENIAC project END “Models, Solutions, Methods and Tools for Energy-Aware Design”. The END project has received funding from the ENIAC Joint Undertaking under grant agreement n° 120214 and from the national programmes/funding authorities of Belgium, Greece, Italy, and Slovakia.

References

[1] Tai-Ran HSU, *Reliability in MEMS packaging*, 44th Annual International Reliability Physics Symposium, San Jose, IEEE, 2006.

[2] Daniel HYMAN and Mehran MEHREGANY, *Contact Physics of Gold Microcontacts for MEMS Switches*, Trans. On components and packaging technology, IEEE, **22**(3), 1999.
[3] Zhen PENG, *et al*., *Dielectric Charging of RF MEMS Capacitive Switches under Bipolar Control-Voltage Waveforms*, Microwave Symposium, IEEE, 2007.
[4] A. TAZZOLI, V. PERETTI, R. GADDI, A. GNUDI, E. ZANONI, G. MENEGHESSO, *Reliability Issues in RF MEMS Switches Submitted To Cycling And ESD Test*, 44th Annual., IEEE International Proceedings, Reliability Physics Symposium, 2006.
[5] C. PALEGO, F. SOLAZZI, S. HALDER, J.C.M. HWANG, P. FARINELLI, R. SORRENTINO, A. FAES, V. MULLONI, B. MARGESIN, *Effect of substrate on temperature range and power capacity of RF MEMS capacitive switches*, Microwave Conference (EuMC), 2010.
[6] A. TAZZOLI, M. BARBATO, F. MATTIUZZO, V. RITROVATO, G. MENEGHESSO, *Study of the Actuation Speed, Bounces Occurrences, and Contact Reliability of Ohmic RF-MEMS Switches*, ESREF 2010 European Symposium on Reliability of Electron Devices, Failure Physics and Analysis.
[7] D. MARDIVIRIN, *et al*., *Charging in Dielectricless Capacitive RF-MEMS Switches*, IEEE Transactions on Microwave Theory and Techniques, vol. 57, no. 1, Jan. 2009, pp. 231-236.
[8] G.J. PAPAIOANNOU, M. EXARCHOS, V. THEONAS, G. WANG, J. PAPAPOLYMEROU, *On the dielectric polarization effects in capacitive RF-MEMS switches*, Microwave Symposium Digest, IEEE MTT-S International. 12-17 June 2005.

Dielectric Charging in Capacitive RF MEMS Switches: The Effect of Dielectric Film Leakage

N. TAVASOLIAN[1], M. KOUTSOURELI[2], G. PAPAIOANNOU[2], J. PAPAPOLYMEROU[1]

[1]School of ECE, Georgia Institute of Technology,
85 fifth Street NW, Atlanta, GA, 30332, USA
[2]University of Athens, Physics Department, Solid State Physics Section,
15784 Athens, Greece

Radio frequency (RF) micro-electromechanical systems (MEMS) switches are one of the most promising applications of the RF MEMS technology. However, reliability issues still limit their application in wireless and communication systems. In capacitive MEMS switches, the most important reliability problem is charging of the dielectric [1]-[2]. In the case of silicon nitride MEMS switches, significant effort has been made to identify the dependence of dielectric charging on film thickness and deposition temperature [3]-[6]. The objective of these efforts has been to determine the most favorable deposition conditions to induce minimum dielectric charging in silicon nitride capacitive switches. Extending on our previous studies, in this work we focus on PECVD silicon nitride films deposited at the same temperature but with different nitrogen to silicon concentration ratios, and try to determine the dependence of dielectric charging on the silicon content hence the dielectric material conductivity. The goal is to address the uncertainty of whether the implementation of a leaky dielectric would reduce the charging effects in capacitive MEMS switches. Both RF MEMS switches and metal-insulator-metal (MIM) capacitors with silicon nitride films deposited at 150ºC and 250ºC are considered for this study.

Fig. 1 shows the stoicbiometry of the silicon nitride films used. The films are deposited at 150ºC and 250ºC with different gas flow ratios. The straight lines are drawn to show the stoichiometry trend. The TSDC spectra for the 150ºC Silicon nitride MIMs, inset of Fig. 2, were found to depend strongly on the film composition. In the case of sample A ([NH3]/[SiH4]= 1.33%), the current level at high temperatures (>380K) is almost two orders of magnitude larger than those of samples B ([NH3]/[SiH4]=2%) and C ([NH3]/[SiH4]=4%), indicating a significantly larger stored charge. Moreover, the envelope of the TSDC current in the high temperature region reveals activation energy of 0.45eV for sample A material decreasing to 0.20eV for sample C.

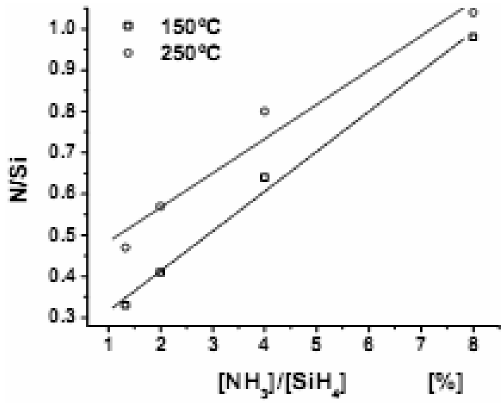

Fig. 1. Stoichiometry vs. gas flow ratio for 150ºC and 250ºC PECVD silicon nitride.

This behavior suggests that for sample A, a larger amount of charge is trapped in deep traps compared to sample C. This becomes obvious in the plot of the temperature dependence of charge measured in the external circuit Qext, which is calculated by integrating the TSDC spectra over temperature. Furthermore, Fig. 2 reveals that in the low temperature range (<350K), the values of TSDC charge do not differ significantly and are characterized by almost the same activation energy. A significant difference arises above 350K, where much deeper defects are activated in sample A leading to much larger charge trapping.

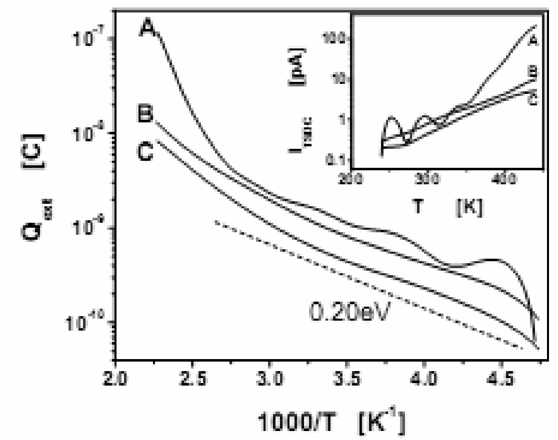

Fig. 2. Temperature dependence of stored charge measured in the external circuit. The inset shows the TSDC spectra. The films were deposited at 150ºC. Samples A, B, and C correspond to [NH3]/[SiH4] of 1.33%, 2%, and 4% respectively.

The total charge stored in the 150ºC silicon nitride MIMs were compared to the 250ºC ones for the three gas flow ratios mentioned above (Fig. 3). The total charge is calculated for all materials by integrating the TSDC spectra from 200K to 500K.

The total charge stored in the 250ºC silicon nitride is higher than the 150ºC one for all flow ratios.

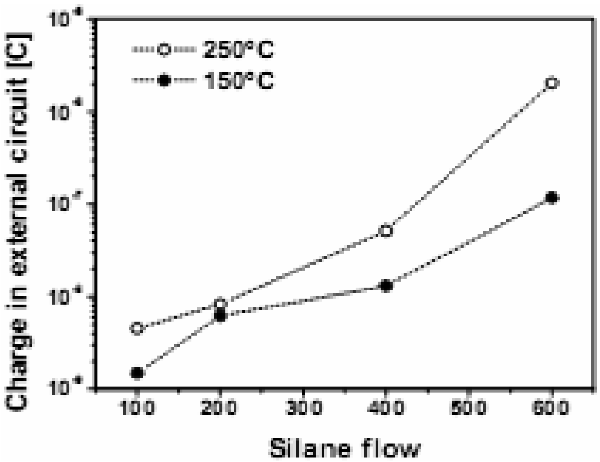

Fig. 3. Dependence of the total stored charge measured in the external circuit on silane flow for the 150ºC and 250ºC silicon nitride material.

The charging in MEMS switches can be monitored through the shift of bias for minimum capacitance (Vm). The bias for minimum capacitance (Vm) of sample A was found to shift rapidly with temperature from +12.6 volts at 300K to -5 volts at 380K (Fig. 4). On the other hand, Vm for sample C shifted only from -1.2 volts at 300K to -0.9 volts at 380K. The calculated activation energies were found to be 0.31eV, 0.22eV and 0.11eV for samples A, B, and C respectively, being in reasonable agreement with the ones obtained from TSDC assessment.

In summary, a systematic investigation was performed to relate the electrical properties of the silicon nitride insulating film of MEMS capacitive switches with the monitored dielectric charging. The investigation was focused on silicon-rich PECVD silicon nitride, which deviates significantly from the ideal material stoichiometry. Both assessment methods, the TSDC assessment in MIM capacitors and monitoring the shift of bias for capacitance minimum in MEMS switches revealed that charging increases when the silicon content increases in spite of the increasing leakage current. This is attributed to the formation of silicon nanoclusters, where potential barriers retain the trapped charges in the potential wells, as well as the generation of trapping sites by unsaturated bonds, etc. Taking all these into account, we are led to the conclusion that silicon nitride films that are closer to stoichiometry seem to be more promising materials for reliable switches. Since in such highly resistive materials the injected charges require a large time to be collected by the bottom electrode, investigation is in progress for the determination of optimum solution.

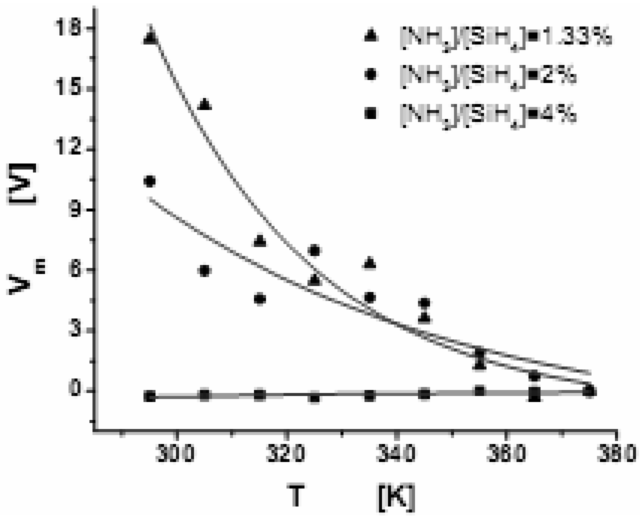

Fig. 4. Temperature dependence of Vm for 150ºC silicon nitride MEMS switches. $[NH_3]/[SiH_4]$ flow ratios of 1.33%, 2%, and 4% are used.

References

[1] J. WIBBELER, G. PFEIFER and M. HIETSCHOLD, Sensors and Actuators, **A 71**, pp. 74-80, 1998.

[2] G.M. REBEIZ, *RF MEMS. Theory, Design and Technology*, pp. 185-192, Hoboken, New Jersey: J. Wiley & Sons, 2003.

[3] M. LAMHAMDI, P. PONS, U. ZAGHLOUL, L. BOUDOU, F. COCCETTI, J. GUASTAVINO, Y. SEGUI, G. PAPAIOANNOU, R. PLANA, Microelectronics Reliability **48**, 1248, 2008.

[4] U. ZAGHLOUL, G. PAPAIOANNOU, F. COCCETTI, P. PONS, R. PLANA, Microelectronics Reliability **49**, 1309, 2009.

[5] R. DAIGLER, E. PAPANDREOU, M. KOUTSOURELI, G. PAPAIOANNOU, J. PAPAPOLYMEROU, Microelectronic Engineering **86**, 404, 2009.

[6] N. TAVASSOLIAN, M. KOUTSOURELI, E. PAPANDREOU, G. PAPAIOANNOU, B. LACROIX, Z. LIU, J. PAPAPOLYMEROU, IEEE Transactions on Microwave Theory and Techniques **57**, 3518, 2009.

Low-Temperature Photosesitive Film-Type Permx Polymer Zero-Level Packaging Technique for RF Applications

Seonho SEOK, Janggil KIM, Nathalie ROLLAND, Paul-Alain ROLLAND

IEMN/IRCICA CNRS 8520 Cité Scientifique-Avenue Poincare BP 60069
59652 Villeneuve d'Ascq Cedex, France

Abstract. This paper presents a film type PerMX polymer-based low temperature zero-level packaging technique for RF devices. PerMX polymer capping technique was developed in two different types that are PerMX ring and PerMX membrane, SU8 ring and PerMX membrane. The height of the implemented cap is 100 µm having 50 µm thick sealing ring and 50 µm thick membrane and the implemented dimensions are 1.4×1.1 mm^2, 2.1×2.1 mm2 and 5.1×5.1 mm^2. The electrical characterization of microstrip line on PerMX is also presented. Also, the effect of the PerMX package on coplanar was found to be negligible insertion loss change of the packaged transmission line while its return loss is better than 20 dB at the measured frequency range.

Index Terms: Packaging, Polymer, PerMX, RF.

1. Introduction

MEMS packaging is considered as an essential technology because MEMS contains movable fragile parts such as membrane or spring. One big approach for wafer-scale zero-level package is an adhesive-bonding of a cover wafer that contains cavities on its surface over a wafer containing active devices. As a capping material, pyrex glass and silicon have been mainly chosen because of their manufacturability [1, 2]. For RF devices packaging, a relatively high cavity should be considered to minimize the effect of packaging material to the packaged devices. Hence, additional processes like glass wet-etching and deep Si etching are needed.

Polymer cap packaging technique is being attractive due to its small size capability, enhanced manufacturability compared with the conventional packaging techniques. Furthermore, it has negligible effect on the package RF devices owing to its low dielectric constant. SU8 [3] or BCB [4] polymers have been implemented as a packaging cap. In general, the polymer capping has been realized by sacrificial etching [3] or polymer cap transfer technique [5]. We reported BCB cap transfer packaging technique that uses BCB caps bonding at 250 °C. It could be a significant problem for some RF MEMS devices.

In this paper, low-temperature packaging technique based on the film type PerMX polymer is presented. It is first noted that micropstrip line on PerMX has insertion loss of 0.1 dB/mm at 10 GHz and return loss of less than 15 dB up to 70 GHz as shown in Fig. 1. Also, the influence of the PerMX cap on the packaged device will be presented.

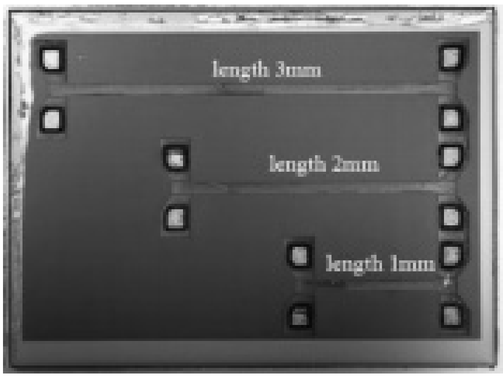

a)

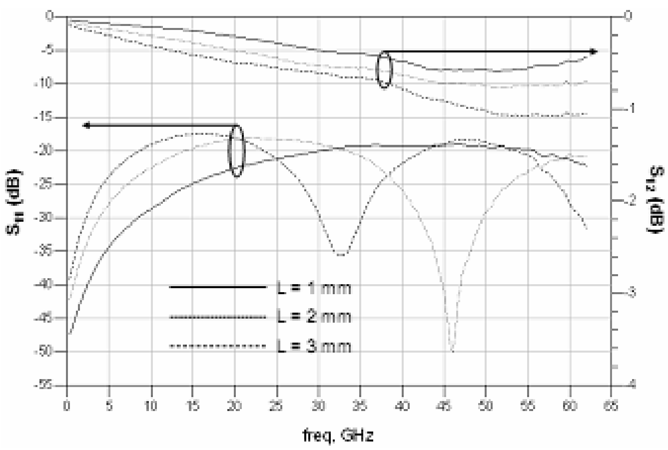

b)

Fig. 1. Microstrip line on PerMX (a) and measured S-parameters (b).

2. PerMX Packaging

The basic PerMX packaging process is shown in Fig. 2; (a) PerMX sealing ring patterning (b) Lamination PerMX film on the patterned sealing ring (c) Exposure and PEB (Post-Expose Bake) (d) Development and hard bake. It should be noted that at step (a), the PerMX ring can be replaced by other polymers such as

SU8 or BCB that are often used for microwave devices and packaging. The thickness of PerMx at step (a) and (b) is 50 µm. The process condition of PerMX is presented in Table 1. PerMX sheet is first laminated on a substrate at 65°C and then it is soft-baked at 95°C for 4 minutes. The PerMX is patterned by a conventional photolithography process.

Exposure energy was 400 mJ and it is developed using PGMEA after 10 minutes PEB. Finally, it is hard-baked for 30 minutes. The maximum process temperature is 150°C.

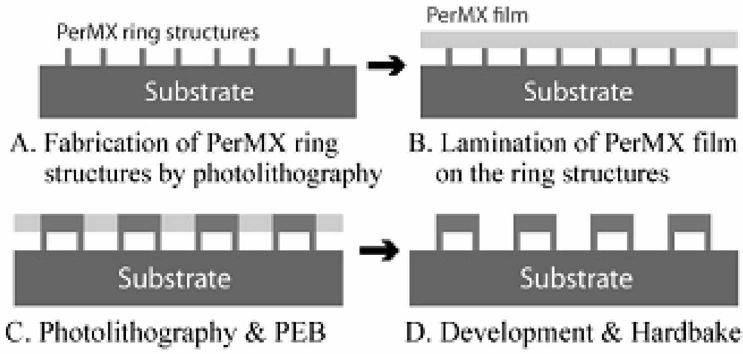

Fig. 2. PerMX packaging process.

Table 1. PerMX 3050 process conditions

Step	Conditions
Lamination	Hot roll @ 65°C
Soft bake	4 minutes @ 95°C
Expose	400 mJ
PEB	10 minutes @ 60°C
Develop	PGMEA, 5 minutes
Hard bake	30 minutes @ 150°C

Fig. 3 shows the result of wafer-level PerMX packaging using 3 inches Si substrate. The sizes of test packaging caps are 1.4 × 1.1 mm^2, 2.1×2.1 mm^2, and 5.1×5.1 mm^2. As seen in Fig. 3, some of the largest ones were not successfully implementedbecause of the high aspect ratio of the membrane. Themeasured profiles of the PerMX caps are shown in Fig. 4. Theheight of the caps was 100 µm because both sealing ring and membrane were 50 µm. The maximum deflection of the PerMX cap was approximately 6.2 µm for 5.1×5.1 mm^2 at itscenter due to the residual stress effect. It should be noted that the deflection should be considered at the design step becauseit could affect the performance of the packaged device. It willbe mentioned later at discussion section.

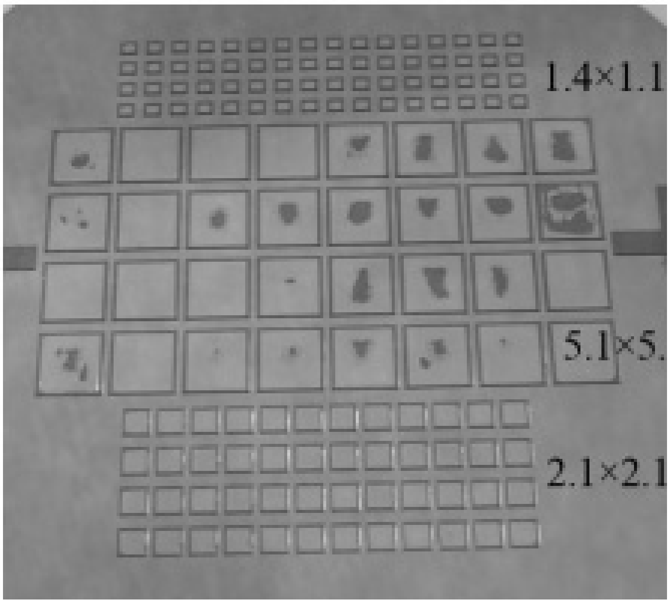

a)

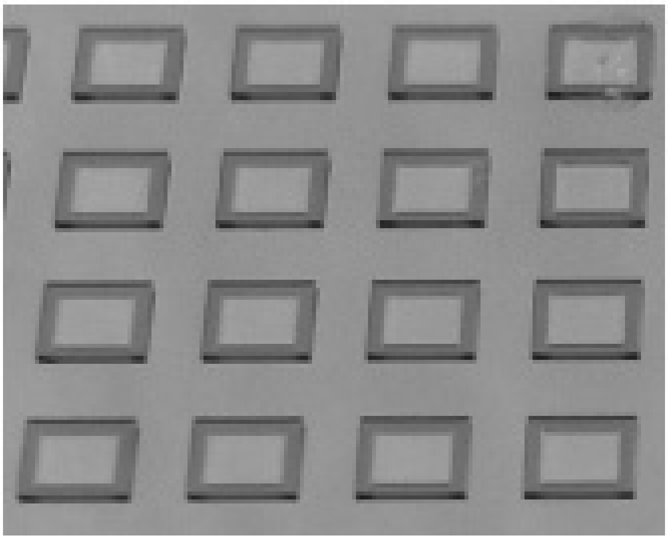

b)

Fig. 3. PerMX packaging results; (a) whole wafer (b) the smallest size PerMX caps.

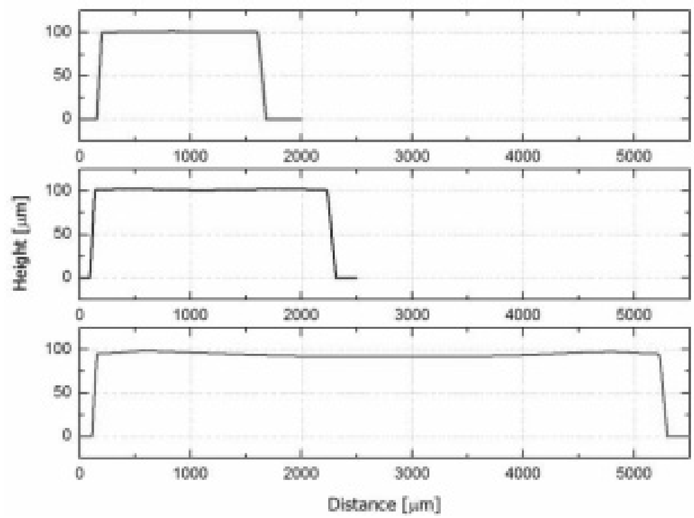

Fig. 4. Measured PerMX cap profiles.

3. RF Measurement and Discussion

To estimate the PerMX packaging effect on transmission line, a 50 Ω coplanar on HRS (High Resistivity Silicon) was measured before and after packaging. Fig. 5 shows the PerMX packaged test coplanar line. The insertion loss change was negligible up to 67 GHz while the return loss is better than 20 dB at the whole range as shown in Fig. 6. It is noted that the proposed PerMX packaging has a competent RF performance with our earlier BCB film one although it has slightly poor material properties as mentioned earlier. It resulted from its bigger cavity depth that is one of the critical parameter of packaging influence that will be investigated later.

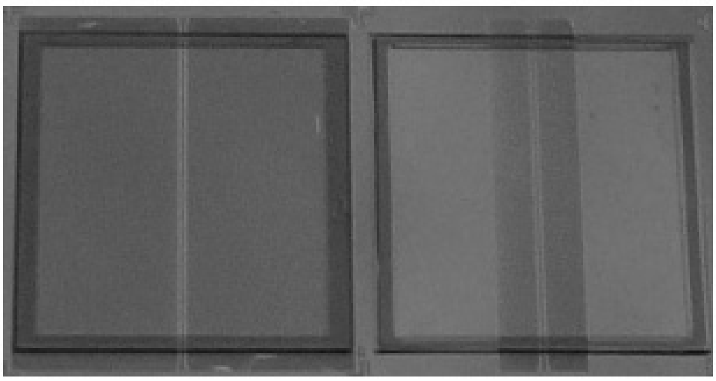

Fig. 5. PerMX polymer capped CPW.

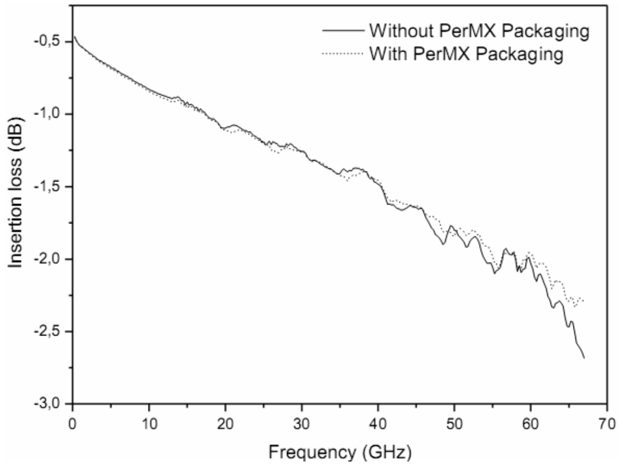

a) Insertion loss S12

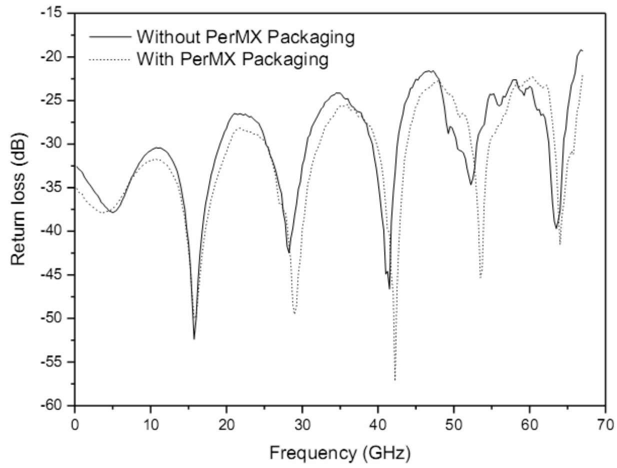

b) Return loss S22

Fig. 6. Measured S-parameter before and after PerMX packaging.

From here, the influence of the packaging cap materials will be investigated in terms of characteristic impedance Z_c and effective dielectric constant ε_{reff} of the packaged CPW. For comparison, Si capping and PerMX capping were chosen for a 50 ohm coplanar line packaging. The dielectric constants are 12 for Si and 3 for PerMX respectively. It is assumed that the I/O interfaces at bonding area are suitably designed to be 50 ohm. The packaging cap thicknesses are determined to be 100 µm and 50 µm for Si and PerMX due to technological constraints. Also, analytical expression from conformal mapping method that assumes a quasi-TEM mode of propagation along the line will be applied to find Z_c and ε_{reff} of the packaged CPW. Additionally, the partial capacitance technique in which the line capacitance of CPW is presented as a sum of partial capacitances is applied [6]. Fig. 7 shows the characteristic impedance and effective dielectric constant of unpackaged and packaged coplanar line. The unpackaged coplanar has characteristic impedance of 50.3 Ω and effective dielectric constant of 6.4537. Silicon capping makes the uncapped CPW impedance 40.5 Ω at 10 μm cavity depth and 46.4 Ω at 50 μm one, while PerMX capping has 48.7 Ω and 50.3 Ω at each depth. It is noted that silicon cap must have high cavity depth to minimize its influence on the packaged device due to its relatively high dielectric constant. It needs more than 50 μm cavity depth to reach the impedance of the unpackaged coplanar line. Also, it can be said that Si cap and PerMX cap result in impedance change per cavity depth of 0.1475 Ω/μm and 0.04 Ω/μm respectively. As seen in Fig. 8, the effective dielectric constant of Si capped CPW is higher than that of PerMX capped one; Si packaged CPW has 9.9603 at 10 μm cavity height and 7.5914 at 50 μm one and PerMX packaging one has 6.8844 and 6.4537 at the same cavity heights.

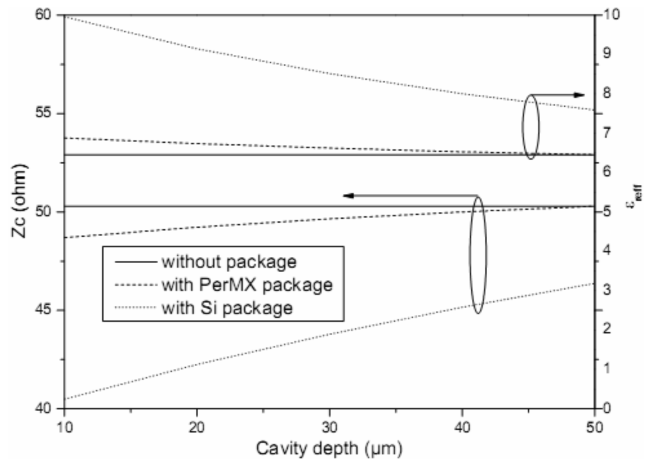

Fig. 7. Characteristic impedance and effective dielectric constant of unpackaged and packaged coplanar line.

4. Conclusion

A low-temperature PerMX film-type polymer zero-level packaging technique has been proposed. The electrical parameters of PerMX were extracted from the measured S-parameter of microstrip line. PerMX showed slightly higher loss tangent than BCB, while the effective dielectric constant of these two materials had almost same value of 2.4. Polymer capping is attracting an increasing interest because its negligible package influence on the packaged devices. For this purpose, the polymer packaging caps are manufactured by the release of SU8 cap and wafer-level transfer of BCB cap. The technological difficulties of the methods were overcome by laminating PerMX film on the packaged device at low temperature. Therefore, the film type PerMX can provide more efficient approach for polymer thin-film packaging. The developed package was applied to CPW line on a Si substrate to evaluate its influence. The measured results of PerMX film packaged CPW lines have shown that the insertion loss change was negligible up to 67 GHz while the return loss is better than 20 dB at the whole range. In addition, analytical calculation based on partial capacitance technique was presented to theoretically show the effect of the packaging material to the packaged coplanar line. It is clearly proven that the polymer cap has better performance than the conventional ones thanks to its low dielectric constant. Finally, it can be said that the proposed PerMX polymer film packaging technique can be an excellent candidate for RF devices.

Acknowledgement. The authors wish to acknowledge the technical staffs of IEMN. This work was supported by European funding FEDER (Fonds Europeen de DEveloppement Regional).

References

[1] J. OBERHAMMER, F. NIKLAUS AND G. STEMME, *Sealing of adhesive bonded devices on wafer level*, Sensors and Actuators A: Physical, **110**(1-3), pp. 407–412, 2004.

[2] A. POLYAKOV, P.M. MENDES, S.M. SIANGA, M. BARTEK, B. REJAEI, J.H. CORREIA and J.N. BURGHARTZ, *Processibility and electrical characteristics of glass substrates for RF wafer-level chip-scale packages*, IEEE Electronic Components and Technology Conference, pp. 875–880, 2003.

[3] I. ZINE-El-ABIDINE, and M. OKONIEWSKI, *A Low-Temperature SU-8 Based Wafer-Level Hermetic Packaging for MEMS Devices*, IEEE Trans. Advanced Packaging, **32**(2), pp. 448–452, May 2009.

[4] S. SEOK, N. ROLLAND and P.-A. ROLLAND, *Packaging methodology for RF devices using a BCB membrane transfer technique*, Journal of Micromechanics and Microengineering, **16**(11), pp. 2384–2388., Nov. 2006.

[5] J. KIM, S. SEOK, N. ROLLAND, P.-A. ROLLAND, *A Novel Wafer Level Bonding/Debonding Technique Using an Anti-adhesion Layer for Polymer-based 0-level Packaging of RF device*, The 60th Electronic Components and Technology Conference (ECTC 2010), pp. 323–328, June 2010.

[6] Z. WAND and Z. LIU, *An Analytical Method for Optimization of RF MEMS Wafer Level Packaging with CPW Detuning Consideration*, Progress In Electromagnetics Research Symposium Proceedings, pp. 479–483, Moscow, Russia, August 18-21, 2009.

Controllable Artificial Micro-Transmission Lines

Julien PERRUISSEAU-CARRIER[1], Frédéric BONGARD[2]

[1]Ecole Polytechnique Fédérale de Lausanne (EPFL), CH-1015 Lausanne, Switzerland
E-mail: julien.perruisseau-carrier@epfl.ch

[2]JAST SA, Scientific Park of the Ecole Polytechnique Fédérale de Lausanne
CH-1015 Lausanne, Switzerland.

1. Introduction

The composite right/left-handed transmission line (CRLH-TL) metamaterial has recently drawn exceptional interest [1, 2]. For instance, various 1-dimensional devices based on this principle have been demonstrated, such as leaky-wave antennas [3] and phase shifters used for instance in series feed networks of antenna arrays [4] or compact dual-band couplers [5]. However, most of these demonstrations were made at rather low frequency (below 5-10 GHz) or without reconfiguration capability, which is nevertheless of tremendous interest for, *e.g.*, beam-scanning in leaky-wave antennas, frequency reconfiguration of zero-phase shift transmission lines, etc.

In view of these observations a first goal we have been pursuing was to implement CRLH-TLs using micromachining techniques, both for miniaturization purpose and to extend the frequency range of application of such structures up to millimeter waves. Based on these first CRLH-TL micromachined implementations, the design of MEMS-based CRLH-TLs was then considered in order to achieve, in addition to the aforementioned benefits of micromachined technology, the possibility of dynamic reconfiguration in the various CRLH-TL applications.

MEMS technology was selected here since it allowed radically challenging the performances of some reconfigurable microwave devices in terms of insertion loss, drive power, monolithic integration and, in the case of industrial production, cost. However, it is worth mentioning that different groups have investigated other means of implementing reconfigurable TL-based metamaterial devices, such as for instance the varactor-based CRLH-TLs of [6] and [7], or the ferroelectric device of [8]. Implementations using active elements are also of significant interest and have been studied in [9]. Finally, [10] studied a MEMS-reconfigurable metamaterial, but based on the split-ring resonator loaded TL approach and is thus mainly applicable to filtering applications due to its narrower band behavior.

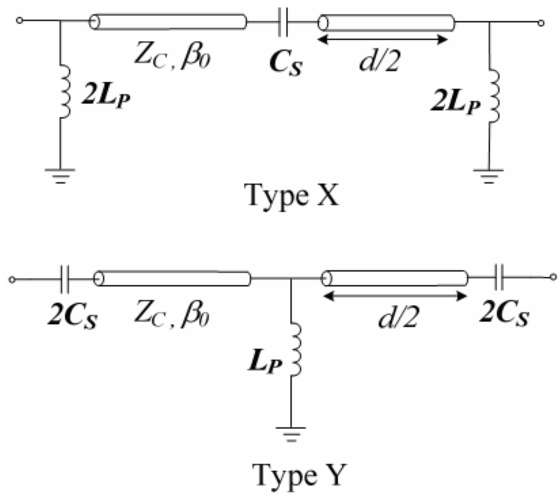

Fig. 1. circuit models of the conventional 1-D CRLH-TL unit cells.

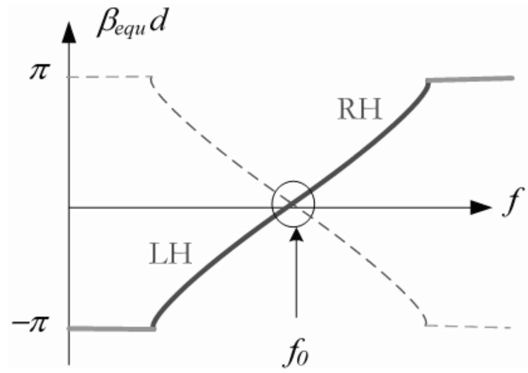

Fig. 2. Dispersion diagram of a balanced conventional CRLH-TL.

2. Microfabricated Conventional CRLH-TL Topologies

In this section we review some fundamentals of micromachined CRLH-TLs and results previously achieved based on the ‘conventional’ CRLH-TL unit cells shown in Fig. 1. After this brief review Section 3 will present the latest results based on the so–called ‘lattice network’ CRLH-TL unit cell.

It is well known that CRLH-TLs exhibit a left-handed (LH) band at low frequencies and a right-handed (RH) band at high frequencies, with a possible seamless transition between the two bands (‘balanced’ case) [1, 2], as symbolically depicted in Fig. 2. In [11, 12], we have shown that the theory previously developed for such CLRH-TL had to be revisited in the case of micromachined design, since assumptions previously employed are not valid for the range of achievable low-loss L and C loading elements in microfabrication processes. Based on this theory and the corresponding design formulas summarized in Fig. 3, fixed micromachined CRLH-TLs with transition frequency at 17.5 GHz were successfully designed and measured both on silicon and on quartz wafer [11, 12]. In addition, the new theory showed that it is possible to implement very high or low characteristic impedance artificial transmission line, as presented in [13].

In a logical next step, reconfiguration capability was implemented using a MEMS process. The initial demonstration was made in [14] (device shown in Fig. 4), which constituted to the best of our knowledge the first MEMS-reconfigurable metamaterial structure ever presented. Design and performance were then significantly improved in [15, 16].

	Effect. homog. medium	General case
Balanced condition	$Z_{C,eff} = \sqrt{L_P/C_S}$	$Z_C = \sqrt{L_P/C_S}$
TL length for 0° $\omega_0 = 2\pi f_0$	$\tau_{eff} = \frac{1}{\sqrt{4L_P C_S \omega_0^2}}$	$\tau = \frac{1}{2\omega_0}\text{arcos}\left(\frac{4L_P C_S \omega_0^2 - 1}{4L_P C_S \omega_0^2 + 1}\right)$
Impedance at f_0	$Z_{equ,X,eff}(f_0) = \sqrt{\frac{L_P}{C_S}}$	$Z_{equ,X}(f_0) = \frac{2L_P\omega_0}{\sqrt{4C_S L_P \omega_0^2 + 1}}$
	$Z_{equ,Y,eff}(f_0) = \sqrt{\frac{L_P}{C_S}}$	$Z_{equ,Y}(f_0) = \frac{\sqrt{4C_S L_P \omega_0^2 + 1}}{2C_S\omega_0}$

Fig. 3. Basic design equations for micromachined CRLH-TL.

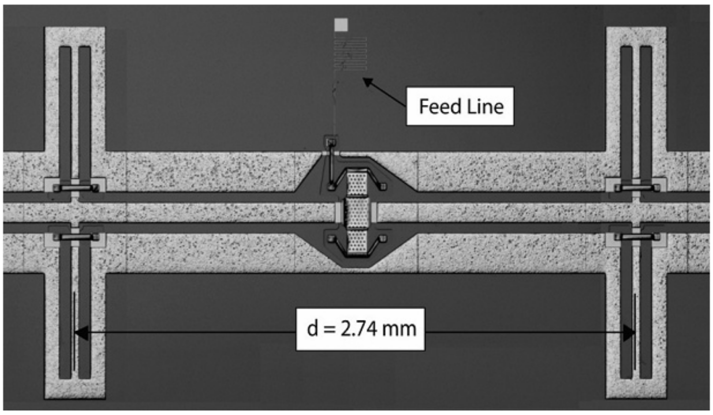

Fig. 4. The first MEMS-reconfigurable CRLH-TL designed, presented in [14].

3. Lattice-Network CRLH-TLs

A. Introduction

The conventional 'balanced' CRLH-TL implementations presented in the previous section [1, 2, 11, 12, 16-18] globally exhibit a band-pass behaviour, with stopbands below the LH band and above the RH band. However, a novel topology of CRLH-TL based on a lattice circuit has recently been proposed by the authors in [19]. Compared to its conventional counterpart, this 'lattice network' CRLH-TL circuit, shown in Fig. 5, exhibits an all-pass behavior and a frequency-independent Bloch impedance [19]. This results in an ultra-broad band that extends from DC (where the unit cell circuit reduces to the swapping of the TL conductors), to a higher frequency limited by the self-resonance of the L and C elements.

Therefore the logical next step in our work was to implement the new 'lattice network' in micromachining and MEMS technology for integration and much higher operation frequency, as described in the remainder of this section.

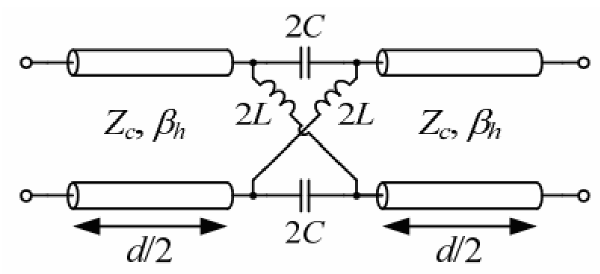

Fig. 5. 'Lattice network' CRLH-TL unit cell.

B. Design of the 'Lattice Network' on a CpwPW Host

The difficulty in implementing the 'lattice network' in micromachining technology relates to the particular nature of the circuit model of Fig. 5. Indeed, the two shunt inductors cross each-other, making its implementation particularly difficult in monolayer unbalanced host TLs. As a result, a mean to successfully implement the lattice unit cell circuit in a pseudo-monolayer planar technology was devised. Here a coplanar waveguide (CPW) host was selected as it allows simple on-wafer probe measurements while allowing implementing the lattice network circuit as explained next.

Since series capacitances must be implemented in both conductors of the TL (in contrast with conventional CLRH-TL unit cells), the ground conductors of the host CPW must be of finite width, and the required capacitances are realized by interdigited capacitors [see Fig. 6]. A more complex issue is the implementation of the crossed inductors. The solution devised here was to implement each of the inductances in a different slot of the CPW, as can be seen in Fig. 6. The excitation of odd CPW modes is then prevented by the use of the bridges shown in green in Fig. 6. Here, the devices were fabricated on a general MEMS process readily including a suspended metal layer, thus this layer was used to implement the bridges; however the lattice network could equally be produced using a fully monolayer process and wirebonds for the bridges, as done with conventional CRLH unit cells in [12]. The structure was optimized for a transition frequency of 20 GHz and a Bloch impedance of 50 Ω. Particular care was taken to lower the parasitics limiting the highest operation frequency (here about 35 GHz).

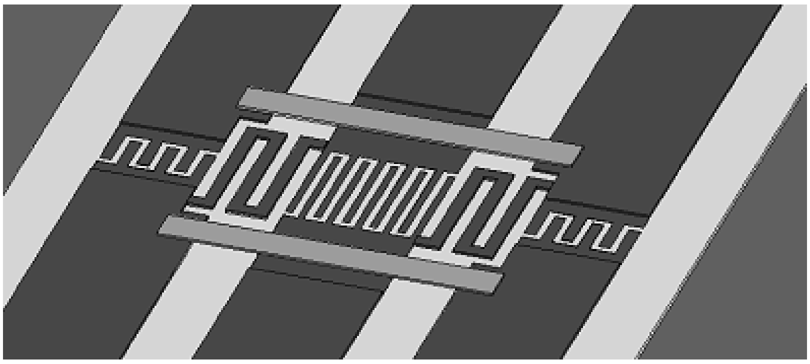

Fig. 6. Layout of the 'lattice network' CRLH-TL unit cell implemented in a CPW host TL. The total CPW width including GP conductors is 600um.

C. Fixed 'Lattice Network' Results

The layout of the designed lattice cell is shown in Fig. 6. The measurements were carried out using an on-wafer TRL calibration, which allows the arbitrary location of the reference planes along the CPW. Since a TRL calibration requires an on-wafer 'line' standard whose length increases with the lower measurable frequency, the lower bound of the measurement range was limited to 5 GHz.

Fig. 7 and Fig. 8 show measured results in terms of the unit cell's Bloch wave equivalents (which are uniquely related to the S-parameters of any finite number of cascaded cells [12]). These measurements confirm the expected theoretical properties of the 'lattice network'. First, ultra broadband matching is observed since the Bloch wave impedance is constant with frequency on the whole measured bandwidth, except for some amplitude-limited oscillations. In terms of S-parameters this corresponds to a return loss better than 10 dB in the whole 5-34 GHz band. Second, the dispersion diagram shown in Fig. 7 is linear on the whole band, with a seamless transition between LH and RH bands at the targeted frequency f0 = 20 GHz.

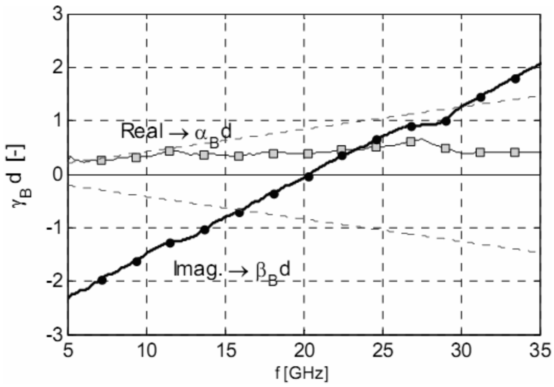

Fig. 7. Measured Bloch wave propagation constant of the 'lattice network' CRLH-TL (the dashed line represents the so-called 'light line').

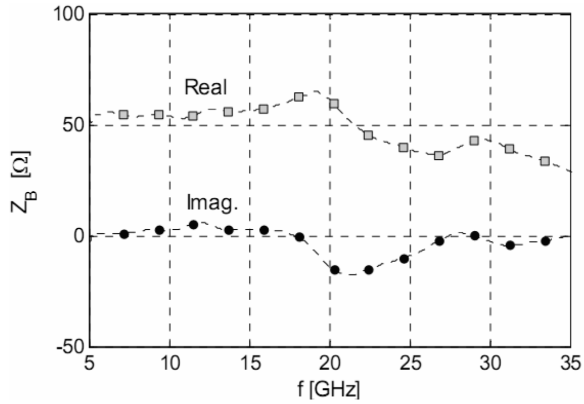

Fig. 8. Measured Bloch wave impedance of the 'lattice network' CRLH-TL.

D. MEMS-Reconfigurable Unit Cells and Series Dividers

Reconfigurable implementations of the 'lattice network' CRLH TL were also designed. Here, and by contrast with devices based on the conventional unit cells, reconfiguration is achieved by altering the RH section of the structure. In other words, while the 'lattice network' itself remains fixed, the host CPW is made controllable. This control of the CPW can be achieved using the well-down distributed MEMS transmission line (DMTL) approach, namely, a variable capacitive loading the transmission line affecting its propagation constant. Fig. 9 shows one of the devices designed following this approach. The 'lattice network' is clearly visible in the center of the cell. On each side a 2-bit short DMTL section is implemented. Each section embeds three identical shunt variable capacitors, one of which is controlled by the low-weight bit and the other two by the strong-weight one.

Corresponding S-parameter results in the four states of the device are presented in Fig. 10. The transition frequency (namely where the phase shift is zero) can be reconfigured from about 12 GHz to 13.5 GHz in equal steps. The matching is better than about -14 dB in this range and insertion loss is better than 1 dB.

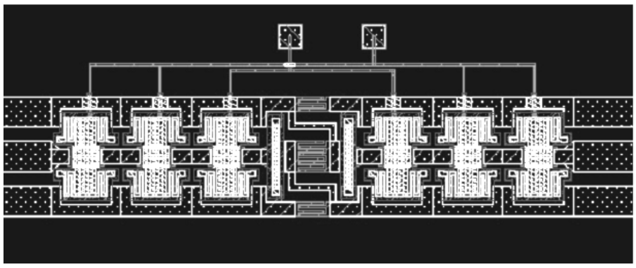

Fig. 9. 2-bit MEMS-reconfigurable 'lattice network' CRLH-TL unit cell.

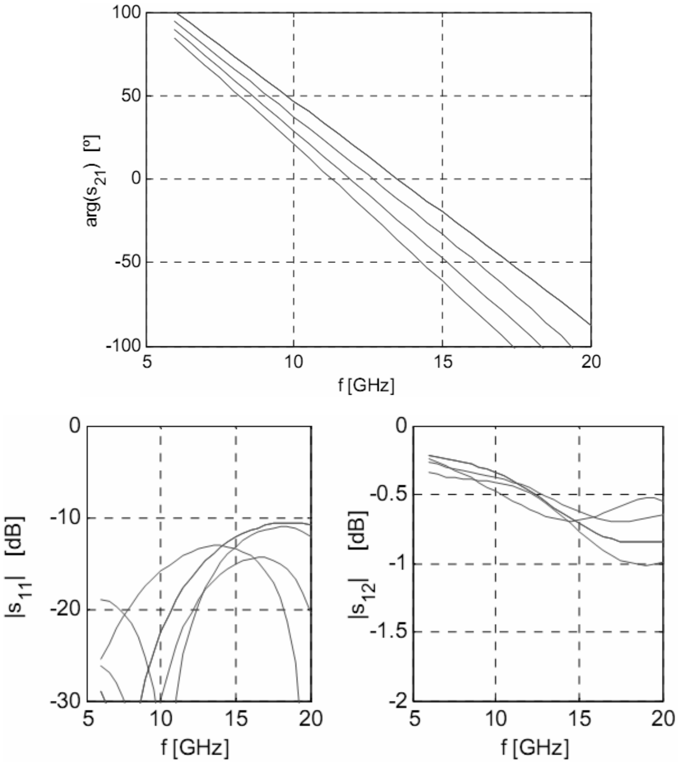

Fig. 10. Simulated S-parameters in the four states of the 2-bit reconfigurable 'lattice network' CRLH-TL unit cell.

Finally, series power dividers were also designed using the 'lattice network' CRLH-TL unit cell. The interest in using the CRLH-TL structure in such dividers is to obtain the same relative phase at all output ports of the divider without the need for large 360º conventional transmission lines [1, 2]. Fig. 11 presents the S-parameters achieved for a 3-output divider. At 10.5 GHz, all output ports present the same relative insertion phase and very similar magnitudes, demonstrating the concept.

The devices presented in this subsection were, by contrast with the fixed cell of Section 3.C, not successfully fabricated and thus no experimental validation could be made.

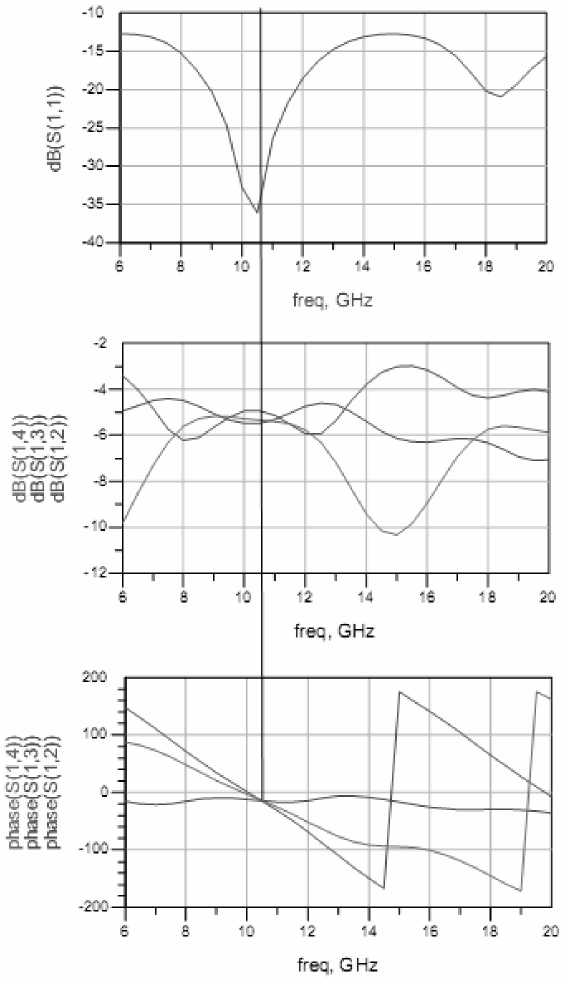

Fig. 11. Simulated S-parameters of a series power divider using the 'lattice network' CRLH-TL unit cell.

Acknowledgement. The authors would like to thank the different persons having contributed to the fabrication of the devices referenced and presented in this paper. In particular, Montserrat Fernandez-Bolaños and Adrian M. Ionescu at EPFL for introducing the lattice unit cells in one of their fabrication runs.

References

[1] C. CALOZ and T. ITOH, Electromagnetic Metamaterials, Transmission Line Theory and Microwave Applications, Hoboken, NJ: Wiley-IEEE Press, 2006.

[2] G.V. ELEFTHERIADES and K.G. BALMAIN, Negative-Refraction Metamaterials: Fundamental Principles and Applications., Hoboken, NJ: Wiley-IEEE Press, 2005.

[3] A. GRBIC and G.V. ELEFTHERIADES, *Experimental verification of backward-wave radiation from a negative refractive index metamaterial*, J. Appl. Phys., **92**, pp. 5930–5935, Nov. 2002.

[4] M.A. ANTONIADES and G.V. ELEFTHERIADES, *Compact linear lead/lag metamaterial phase shifters for broadband applications*, IEEE Antennas Wireless Propagat. Lett., **2**, pp. 103–106, 2003.

[5] I.-H. LIN, M. DEVINCENTIS, C. CALOZ and T. ITOH, *Arbitrary dual-band components using composite right/left-handed transmission lines*, IEEE Trans. Microw. Theory Tech., **52**, pp. 1142–1149 April 2004.

[6] S. LIM, C. CALOZ and T. ITOH, *Electronically scanned composite right/left handed microstrip leaky-wave antenna*, IEEE Microw. Wireless Compon. Lett., **14**, pp. 277–279, June 2004.

[7] C. DAMM, J. FREESE, M. SCHUSSLER and R.A. JAKOBY, *Electrically Controllable Artificial Transmission Line Transformer for Matching Purposes*, IEEE Trans. Microw. Theory Tech., **55**, pp. 1348–1354, 2007.

[8] G. HOUZET, A. MARTEAU, G. VELU, E. LHEURETTE, L. BURGNIES, J.C. CARRUR and D. LIPPENS, *Voltage-controlled composite metamaterials via the loaded transmission line approach*, Metamaterials, pp. 48-51, Rome, Italy, 2007.

[9] M.A.Y. ABDALLA, K. PHANG and G.V. ELEFTHERIADES, *Printed and Integrated CMOS Positive/Negative Refractive-Index Phase Shifters Using Tunable Active Inductors*, IEEE Trans. Microw. Theory Tech., *55*, pp. 1611–1623, 2007.

[10] I. Gil, F. MARTIN, X. ROTTENBERG and W.D. RAEDT, *Tunable stop-band filter at Q-band based on RF-MEMS metamaterials*, Electron. Lett., **43**, pp. 623–624 May 2005.

[11] J. PERRUISSEAU-CARRIER and A.K. SKRIVERVIK, *Composite Right/Left Handed Transmission Line Metamaterial Phase Shifters (MPS) in MMIC Technology*, IEEE Trans. Microw. Theory Tech., **54**, pp. 1582–1589, April 2006.

[12] J. PERRUISSEAU-CARRIER and A.K. SKRIVERVIK, *Bloch Wave Approach to the Design of Optimally Matched Non-Effective Medium Composite Right/Left Handed Transmission Lines*," Proc. IET Microw., Antennas Propag., **1**, pp. 50–55, Feb. 2007.

[13] J. PERRUISSEAU-CARRIER and A. SKRIVERVIK, *Design of Wideband High and Low Impedance Meta-Transmission Lines*, Microw. and Optical Tech. Lett., **49**, pp. 1926–1929, August 2007.

[14] J. PERRUISSEAU-CARRIER, T. LISEC and A.K. SKRIVERVIK, *Circuit Model and Design of Silicon-Integrated CRLH-TLs Analogically Controlled by MEMS*, Microw. and Optical Tech. Lett., **48**, pp. 2496–2499, Dec 2006.

[15] J. PERRUISSEAU-CARRIER, T. LISEC and A.K. SKRIVERVIK, *Analog and Digital MEMS-Variable Composite Right/Left Handed Transmission Lines*, ANTEM, International Symposium on Antenna Technology and Applied Electromagnetics and URSI/CNC Canadian Radio Sciences Conference, Montréal, Canada, 2006.

[16] J. PERRUISSEAU-CARRIER, K. TOPALLI and T. AKIN, *Low-loss Ku-band Artificial Transmission Line with MEMS Tuning Capability*, IEEE Microw. Wireless Compon. Lett., **19**, pp. 377–379, June 2009.

[17] M.A.Y. ABDALLA, K. PHANG and G.V. ELEFTHERIADES, *A 0.13-μ m CMOS Phase Shifter Using Tunable Positive/Negative Refractive Index Transmission Lines*, IEEE Microw. Wireless Compon. Lett., **16**, pp. 705–707, Dec. 2006.

[18] S.K. PODILCHAK, BRIAN M. FRANK, A. FREUNDORFER and Y.M.M. ANTAR, *Composite Right/Left Handed Artificial Transmission Line Structures in CMOS for Controlled Insertion Phase at 30 GHz*, Int. Journal of RF and Microw. Computer-Aided Engineering, **19**, pp. 163–169, March 2009.

[19] F. BONGARD, J. PERRUISSEAU-CARRIER and J.R. MOSIG, *Enhanced CRLH Transmission Line Performances Using a Lattice Network Unit Cell*, IEEE Microw. Wireless Compon. Lett. **19**, pp. 431–433, July 2009.

MEMS and Combined MEMS/LC Technology for mm-wave Electronic Scanning Reflectarrays

Simone MONTORI[1], Carsten FRITZSCH[2], Elisa CHIUPPESI[1], Paola FARINELLI[1], Luca MARCACCIOLI[1], Flavio GIACOMOZZI[3], Roberto SORRENTINO[1], Rolf JACOBY[2]

[1]Dept of Electronic and Information Engineering, University of Perugia, Italy

[2]Technische Universitat Darmstadt, Germany

[3]Fondazione Bruno Kessler, Trento, Italy

Abstract. This paper presents the most recent advances within ARASCOM project (MEMS & Liquid Crystal based' Agile Reflectarray Antennas for Security & COMmunication). One of the objectives of the project is the exploitation of MEMS and Liquid Crystal (LC) technology in mm-wave electronic scanning reflectarrays. In particular two solutions have been investigated: a MEMS-only approach, where the switches are used to obtain reconfigurable elementary cells with 1-bit of phase resolution - an efficient method applicable in large antennas; and a LC/MEMS combined solution, where the LCs provide a continuous phase-shift up to 180° and a MEMS is used to add another 180° when necessary. Preliminary results validate the proposed approach and give indications for future steps.

1. Introduction

Nowadays there are some emerging applications that would receive a significant benefit from the availability of low-cost mm-waves electronic beam scanning antennas, such as imaging and remote sensing. In such applications the electronic reconfigurability is a fundamental requirement if a reliable and real-time system (such as mm-wave imaging cameras) is to be obtained. However antennas with electronic beam scanning are very complex and costly to realize, especially at mm-waves.

In such a framework, reflectarray antennas represent a very attractive solution, since the quasi-optical feeding eliminates the loss and the parasitic effects associated with conventional RF distribution networks (e.g. phased arrays). In reflectarrays the reconfigurability of radiation pattern is obtained at element level, by varying the phases reflected by the radiating elements (i.e. by the elementary cells) [1-4].

A programme has been launched within the 7th Framework Program funded by the European Commission for the investigation of "MEMS & Liquid Crystal based Agile Reflectarray Antennas for Security & COMmunication" (ARASCOM) [5].

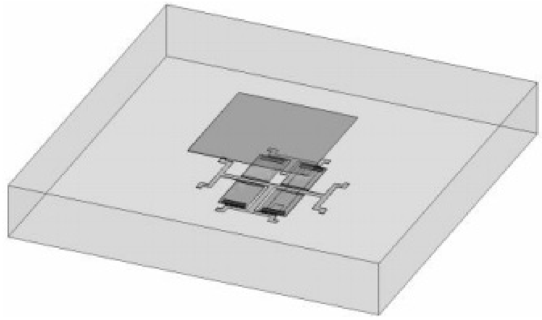

a)

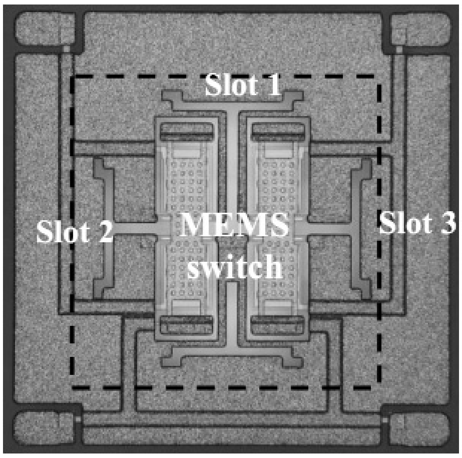

b)

Fig. 1. Sketch of the elementary cell and picture of the phase shifting layer. Dotted line indicates the square patch located on the radiating side of the cell.

One of the major aims is the development of a 77 GHz electronic steerable reflectarray for imaging and security applications. Two solutions have been investigated: the first one is a pure MEMS solution based on the concept of 1-bit scanning antennas. In [6-7] it has been demonstrated that the beam of very large arrays can be steered by using just 1-bit phase shifters, with a loss of only 3 dB directivity and virtually no loss of pointing angle accuracy. This solution is simple yet very effective, and has proved to work in a 16x16 sample board where MEMS have been substituted by short/open connections [8-9]. Meantime the MEMS switching cells have been manufactured and tested, and are ready to be assembled in a first prototype.

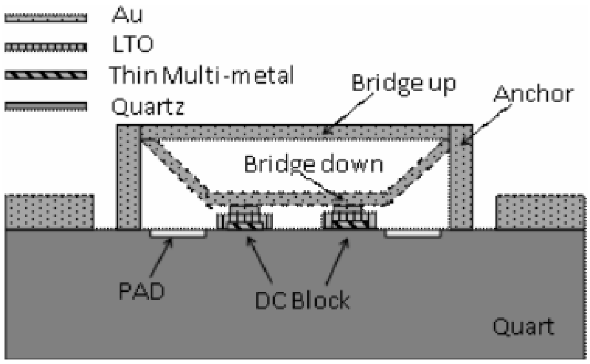

Fig. 2. Schematic side view of the slot line MEMS switch.

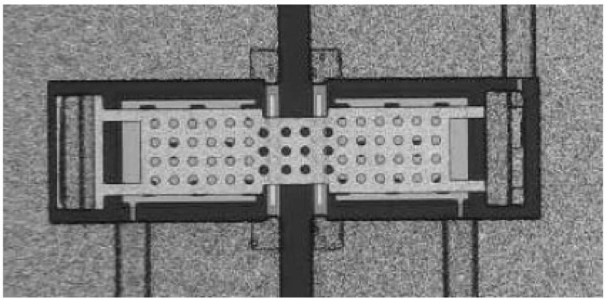

Fig. 3. Photo of SLO switch.

The second solution is based on a combination of LC and MEMS technology. LC, mainly known from display applications, can be used as tunable dielectric layer in structures similar to parallel plate capacitors [10]. By applying a tuning voltage the alignment of the anisotropic LC molecules can be controlled, therefore it is possible to change the effective permittivity of the material. The tuning process works continuously, hence analogue tunable phase shifters can be realized.

The phase shifter presented in this paper is based on a novel technology, which is compatible with a RF-MEMS process. The integration of tunable LC and MEMS components is possible and allows combining the advantages of both technologies, analogue tuning for LC part as well as a low loss design for the MEMS.

A description for both solutions is reported and future developments are discussed.

2. MEMS Slot-Line Solution

The elementary cell developed is depicted in. It is made by a square patch antenna realized on the top layer of a thin quartz substrate (h=300 μm). The patch is slot coupled to the 1-bit phase shifting circuit realized in slot-line technology on the backside of the quartz substrate. Two MEMS switches are placed on the slot-line layer (or phase-shifting layer), consisting of 3 lines connected in T configuration; each line is terminated with an U-shaped slot, so as to be coupled to one of the two linear polarizations that can be radiated by the patch. A fourth dummy slot (not connected) is used to make the layout symmetrical so that the radiation diagram of the elementary cell is identical for both polarizations.

The elementary cell is electronically reconfigured to provide 1-bit of phase resolution (0°/180°). A couple of MEMS switches are integrated in the phase-shifting layer; the MEMS bridges are anchored at the substrate and short-circuit the two metal planes when pulled down. The control of the cell is obtained by activating the switches so as to obtain a SPDT that alternatively connects slot 1 with slot 2 or slot 3. Observe that in order to independently activate each MEMS the actuation pads needs to be electrically separated from the slot-line ground.

When a linearly polarized field, either vertical or horizontal, illuminates the elementary cell theorthogonal polarization is back radiated, independently of the cell state. However, since line 2 and line 3 feed the patch at opposite edges, in the two cases the reflected field has opposite signs, equivalent to 180° phase difference, independent of frequency.

3. MEMS Slot-Line Switch Design & Manufacturing

The MEMS shunt ohmic switch has been designed in slot-line technology on 300μm Quartz substrate. The switch consists of a 410μm × 90 μm thick gold membrane clamped on the substrate at both extremities and 3μm suspended above a 32μm wide slot line. Two windows have been etched away from the slot metallization in order to accommodate the bridge anchors as well as the lateral activation electrodes as shown in Fig. 6. When the switch is in the up position (OFF STATE) the signal can flow along the transmission line; on the contrary when it is activated (ON STATE) it short-circuits the two metallic planes at the two contact points shown in Fig. 2. In order to keep separated the DC and RF signals, two DC-blocks have been integrated in series with the switch contacts, providing a capacitive short circuit at 76.5GHz. Thick Silicon oxide (600nm thick LTO - Low Temperature Oxide) has been used as a dielectric for the MIM capacitors in order to guarantee no break down up to high polarization voltages (>100V).

In order to mitigate dielectric charging phenomena, the dielectric has been removed from the surface of the activation pads. Mechanical stoppers have been patterned in the pads to prevent the contact between the down-state bridge and the dielectric-less pads.

The slot line 76.5 GHz MEMS switches and the MEMS-based radiating cell unit have been monolithically manufactured on 300µm thick Quartz substrate (4") by using the 8 mask FBK RF MEMS process. A photo of the manufactured test switch is presented in Fig. 3.

DC measurement have been performed in order to characterize the behavior of the slot-line switches. The measurement set up consists of a Agilent 4156c Parameter Analyzer and 4284A LCR Meter. The variation of the capacitance between the grounded metal underpass and the bridge is recorded for increased positive bias voltage as shown in Fig 4. Actuation and de-actuation voltages of about 65V and 50V have been recorded. The monitoring of the pull-in and pull-out voltage under repeated and long term actuation show low charging effect thanks to the dielectric-less electrodes. Reliability tests are on-going.

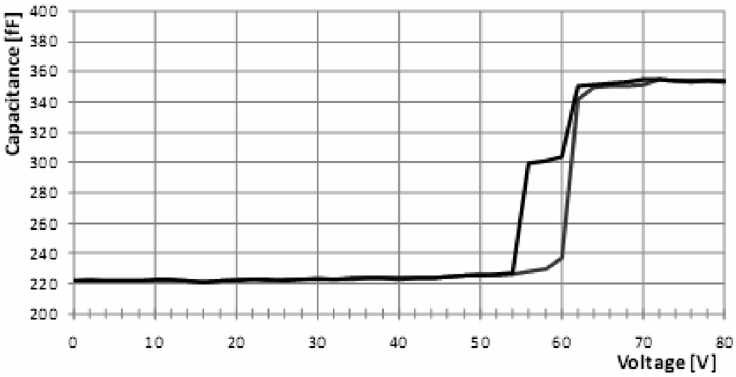

Fig. 4. CV measure of a switch.

4. LC/MEMS Solution

The combined LC and MEMS device is realized in a reflection type phase shifter (Fig. 5), where a 0…90° continuously tunable LC based phase shifter is terminated by a 0°/180° MEMS phase shifter.

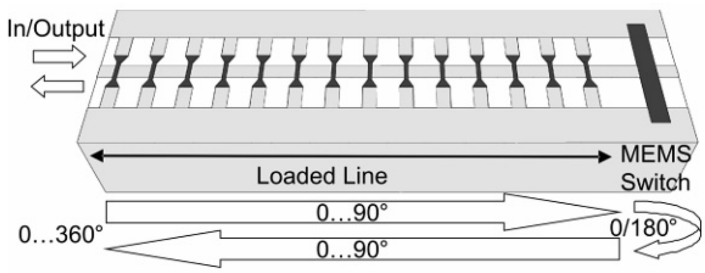

Fig. 5. LC MEMS combined reflection type phase shifter.

The incoming wave travels through the LC phase shifter, is delayed up to 90°, gets reflected at the MEMS phase shifter with 0° or 180° and is delayed on the way back by up to another 90°. Hence, the complete phase range of 360° can be tuned continuously.

In order to test and optimize the design process as well as the fabrication technology, a large number of variations of separate MEMS and LC parts as well as the combination have been fabricated and measured.

A photograph of the loaded line is shown in Fig. 6. The line consists of 14 unit cells, depicted in Fig. 7. Each of them contains a varactor, formed by a suspended MEMS bridge spanning over the inner conductor of the CPW line. The cavity between the MEMS bridge and the conductor is around 1.6 µm height. Filling of the LC cavity is performed with a micropipette, as a small drop of LC is placed close to the MEMS bridge and pulled underneath the bridge by capillary forces.

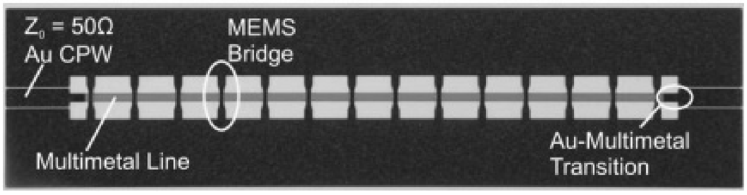

Fig. 6. Photograph of loaded line.

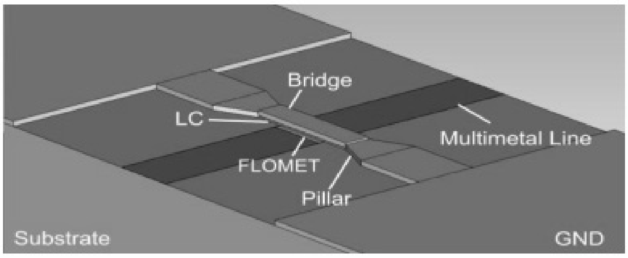

Fig. 7. LC based varactor.

The fabrication process is compatible with the RF MEMS process described in previous section. The structure is biased by applying a bias voltage between the inner conductor and the outer ground planes through the CPW measurement probes. By sweeping the bias voltage from 0V to 30 V, the differential phase delay can be set to values from 0 to 90° (Fig. 8).

The input matching of the LC loaded line phase shifter is below -15 dB for the frequency range from 65 to 97 GHz. The insertion loss is measured to be 2.4 dB at 76 GHz.

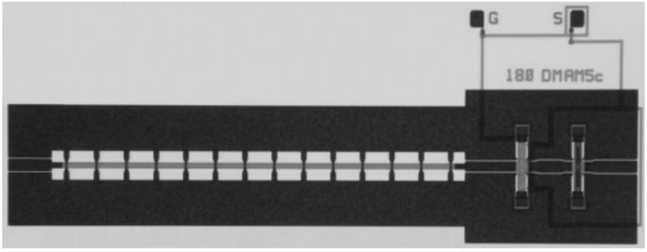

Fig. 8. Combined MEMS and LC phase shifter.

The complete combined LC/MEMS phase shifter is shown in Fig. 9. The MEMS is connected to the loaded line at the right side. Measurements of the 0/180° MEMS reflection-type phase shifter alone (not connected to the LC loaded line) have shown a differential phase shift of 198°.

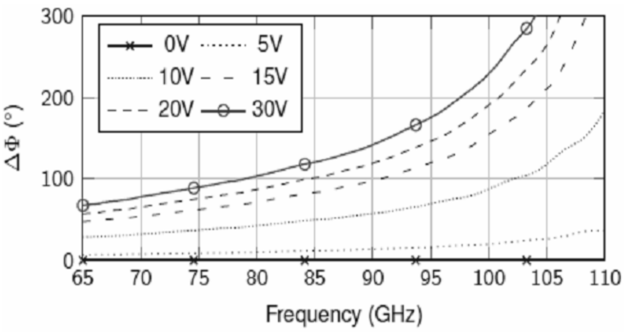

Fig. 9. Measured differential phase shift.

During the filling process of the combined phase shifter, it was observed that the LC is not only being pulled underneath the nearest MEMS bridge, but it also creeps along the CPW line towards the MEMS switch. The switch is therefore filled accidently by LC as well, measurements have shown that the phase shift of the MEMS termination is graduated to around 30°.

To overcome this problem, current work includes experiments on a barrier that will prevent the LC from flooding the MEMS switch as well as a capping solution for the MEMS.

5. Conclusions

Recent advances on reconfigurable reflectarrays operating at 77GHz investigated within the ARASCOM project are presented in this paper. Two approaches are proposed: the first one is suitable for very large reflectarrays and it is based on a MEMS elementary cell with 1 bit of phase resolution. The second approach uses analogue phase shifters obtained with a combined use of RF-MEMS and LC technology. Preliminary results are very promising; a first full working reflectarray is scheduled by September 2011.

Acknowledgment. This work has been performed in the frame of the ARASCOM project supported by the 7th European ramework program, contract no. 222620.

References

[1] John P. GIANVITTORIO, *et al*., *Reconfigurable patch antennas for steerable reflectarray applications*, IEEE Transactions On Antennas And Propagation, **54**(5), May 2006.

[2] E. CARRASCO, M. BARBA and J.A. ENCINAR, *Reflectarray Element Based on Aperture-Coupled Patches With Slots and Lines of Variable Length*, IEEE Transactions on Antennas and Propagation, **55**(3), Match 2007.

[3] M. RIEL, J.-J. LAURIN, *Design of an Electronically Beam Scanning Reflectarray Using Aperture-Coupled Elements*, IEEE Trans. on Antennas and Propagat., **55**(5), pp. 1260–1266, May 2007.

[4] J.H. SCHAFFNER, D.F. SIEVENPIPER, R.Y. LOO, J.J. LEE, S.W.L. RAYTHEON, *A Wideband Beam Switching Antenna Using RF MEMS Switches*, 2001 AP-S Int.l Symposium Digest C.C. Cheng, A. Abbaspour-Tamijani, *Study of 2-bit Antenna-Filter-Antenna Elements for Reconfigurable Millimeter-Wave Lens Arrays*, IEEE Trans. on Microwave Theory and Techniques, **54**(12), December 2009.

[5] www.arascom.eu

[6] S. EBADI, R. VINCENTI GATTI and R. SORRENTINO, *Linear Reflectarray Antenna Design Using 1-bit Digital Phase Shifters*, 3rd European Conference on Antennas and Propagation, EuCAP Berlin, Germany, March 2009.

[7] S. EBADI, R. VINCENTI GATTI, L. MARCACCIOLI, R. SORRENTINO, *Near Field Focusing in Large Reflectarray Antennas Using 1-bit Digital Phase Shifters*, EUMC 2009, Rome.

[8] S. MONTORI, C. FRITZSCH, L. MARCACCIOLI, R.V. GATTI, R. JAKOBY, R. SORRENTINO, *Design and measurements of a 1-bit reconfigurable elementary cell for large electronic steerable reflectarrays*, EuMC2010 Paris.

[9] L. MARCACCIOLI, S. MONTORI, R. VINCENTI GATTI, E. CHIUPPESI, P. FARINELLI, R. SORRENTINO, R. VINCENTI GATTI, L. MARCACCIOLI, *RF MEMS-Reconfigurable Architectures for Very Large Reflectarray Antennas*, APMC 2009, 7-10 Dec 2009.

[10] F. GOELDEN, A. GAEBLER, S. MUELLER, A. LAPANIK, W. HAASE and R. JAKOBY, *Liquid-crystal varactors with fast switching times for microwave applications*, Electronics Letters, **44**, pp. 480–481, 2008.

Silicon Supported Millimeter Wave CRLH Antenna Microprocessed by Laser Ablation

Alina-Cristina BUNEA[1], Florea CRACIUNOIU[1], Marian ZAMFIRESCU[2], Razvan DABU[2], Gheorghe SAJIN[1]

[1]National Institute for Research and Development in Microtechnologies, IMT Bucharest, Str. Erou Iancu Nicolae 126A, 077190 Bucharest, Romania
Phone: +40-21-269 0775

[2]National Institute for Laser, Plasma and Radiation Physics, Atomistilor 409, PO Box MG-36, 077125 Magurele, Bucharest, Romania
Phone: +40-21-457 5066

Abstract. The paper presents a zeroth order resonance CRLH CPW antenna on high resistivity silicon substrate for millimetric wave frequency range (28 GHz). As technological approach, the laser ablation was preferred due to better results in device microprocessing compared to classic photolithographic processes. Experimental results show RL < -25 dB / 28.6 GHz, the -3 dB beamwidth of the radiation lobe of approx. 370 and the gain 2.99 dBi / 28.6 GHz. It is, according to the authors' knowledge, the first report concerning the design, fabrication and full characterization of a CRLH antenna on silicon substrate intended to work integrated in a more complex mm-wave circuit.

1. Introduction

A possibility to obtain transmission media having metamaterial (MM) characteristics is to develop particular artificial transmission lines. If the artificial transmission line is realized by using cascaded cells of interdigital capacitors and parallel connected short-ended microstrip line inductors, CRLH (Composite Right/Left-Handed) transmission lines are obtained [1]. The CRLH TL cell is the key to a new class of devices such as coupled-line directional couplers [2], filters and resonators, [3]–[5] and various types of antennas [6]–[13]. Concerning the domain of antennas made on the basis of MMs, a lot of contributions were produced, some of the more recent being [10, 11, 12]. For the near future, this kind of circuits should be fabricated on semiconductor substrate due to the need to monolithically integrate a more complex circuit. To integrate these circuits together with other passive or active devices, they must be designed using coplanar waveguide (CPW) configurations. In this paper, the design, fabrication process and measurements of a CRLH TL CPW zeroth-order resonant antenna on silicon substrate for millimeter wave frequency range (28 GHz) are presented.

2. Constructive Data and Simulation

A CPW CRLH zeroth-order resonant antenna at the frequency f = 28 GHz was designed, fabricated and electrically characterized. It consisted of three resonant CRLH cells processed on a high resistivity silicon wafer.

The conditions and mathematical relations for the design are presented in literature [1], [13] and will not be presented here. The CRLH circuit was designed to be balanced, with the series resonance frequency equal to the shunt resonance frequency. The components of the elementary CRLH cell used in the antenna construction are presented in Fig. 1.

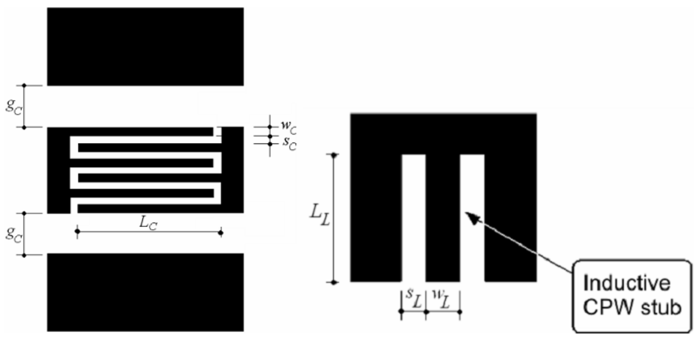

Fig. 1. Components of the CRLH elementary cell that is used in antenna construction: interdigital capacitor and inductive CPW stub.

The dimensions obtained for these components are the following: L_L = 212 µm; w_L = 42 µm; s_L =10 µm, for the inductive stub; L_c= 250 µm; w_c = 5 µm; s_c = 10 µm; g_c =65 µm and number of digits: 10, for the interdigitated capacitors.

The antenna input is made of an access line with 3400 µm length and the geometry computed to match the 50 µ characteristic impedance of the measuring system. This geometry allows the mounting of the antenna structure on a dedicated test fixture for the measurement of the radiation characteristic and of the gain.

3. Technology

The antenna structures were processed on a high resistivity (5 kΩcm) silicon substrate with 500 µm thickness and permittivity $\varepsilon_{r\cdot Si}$ = 11.9. On this silicon wafer a layer of 1 µm SiO_2 with permittivity $\varepsilon r.SiO_2$ = 4.7 was grown through thermal oxidation. A 0.4 µm Au / 500 Å Cr metallization was obtained by evaporation on the surface of the silicon wafer. The processing technology applied to obtain the antenna structure consists of two steps. In the first step, the Au/Cr metallization is removed from the large areas of the structure by standard wet photolithography. In the second step, the fine details of the interdigital capacitor are processed by laser ablation. This two step process is necessary because the removal of metallization from the large areas by laser ablation is a difficult task.

A direct laser writing (DLW) method was used to microprocess the Au/Cr layers deposited on silicon. The samples were laser ablated by tightly focusing a femtosecond laser with 200 fs pulse duration, 775 nm wavelength, tens of nJ pulse energy, and 2-kHz repetition rate. The 2D structures were generated according to a computer controlled algorithm by precisely translating the sample with resolution below 1μm.

The active part of the future antenna structure following the first microprocessing step is presented in Fig.3 (a). The grounded lines forming the inductive stubs and the areas where the interdigital capacitors will be created by laser ablation can be observed. The same area, after the capacitor was microprocessed by laser ablation, is presented in Fig.3 (b).

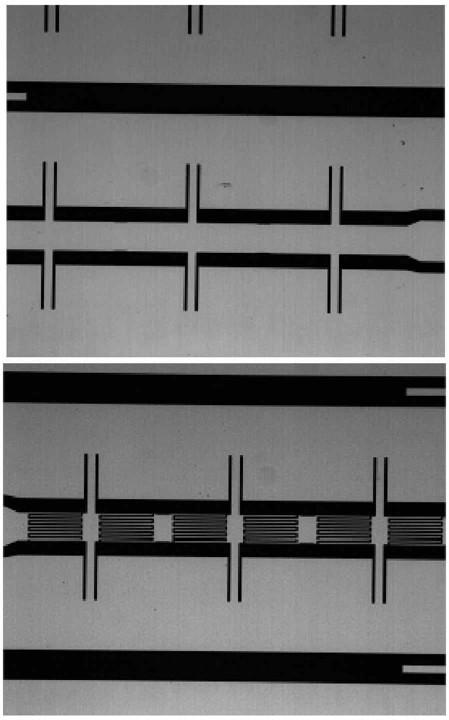

Fig. 3. Optical microscopy photos showing the active part of the CRLH antenna after the first step (a) and after the second step (b) of the technological approach.

After on wafer measurements of the S11 parameter, the silicon wafer was cut with a diamond abrasive cutting-off wheel tool, thus obtaining separate antenna chips. These discrete structures were mounted on dedicated test fixtures in order to measure directivity characteristics and antenna gain.

Two such separate CRLH antennas mounted on the test fixtures are presented in Fig. 4.

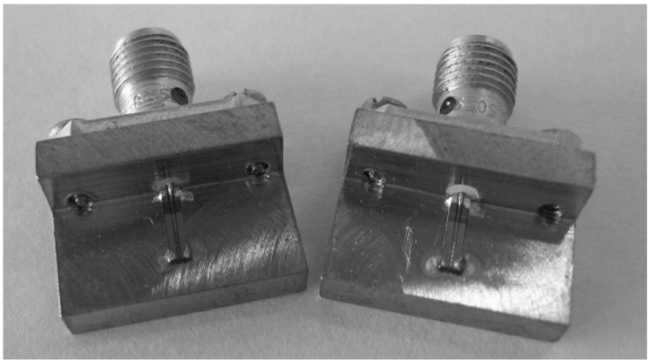

Fig.4. Two discrete CRLH antenna structures mounted on the test fixture.

4. Measurements and Experimental Results

A. Return loss

The S_{11} parameter was measured on wafer using a 37397D vector network analyzer from Anritsu, equipped with PM5 set-up from Süss Microtec. The results for two CRLH antenna samples are presented in Fig.5.

Fig. 5 shows that for two CRLH antenna structures (antenna #1 and antenna #2) the reflection losses (maximum absolute values) are, respectively, -27.05 dB / 28.78 GHz and -25.79 dB / 28.22 GHz. The frequency is slightly higher than the simulated one but the reflection losses are substantially smaller.

In order to obtain the radiation characteristic, the received power was measured for various angles. A CRLH antenna was used as emitting device and a Millitech SGH-28 horn antenna as receiving device connected to the spectrum analyzer. The frequency used was 28.7 GHz where the antenna return losses have a minimum. The measured power at reception was averaged over 50 measurements. The measurements of the radiation pattern were made both in transverse and longitudinal antenna planes.

The measurements were made using a frequency generator Agilent E8257D PSG, a spectrum analyzer Anritsu MS2668C and a measuring setup with the CRLH antenna as emitting device having the possibility to rotate both in transversal and in longitudinal planes.

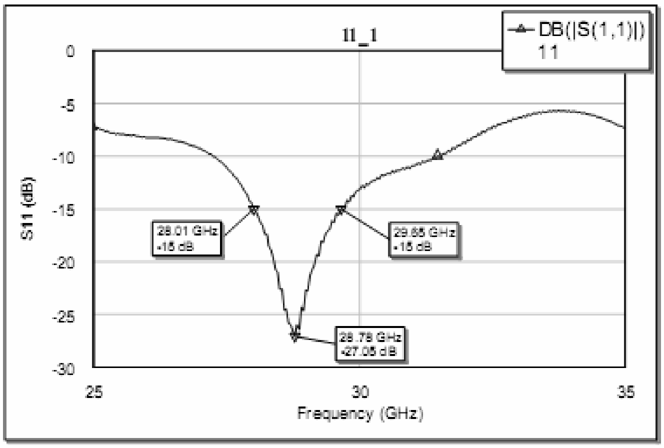

Antena #1

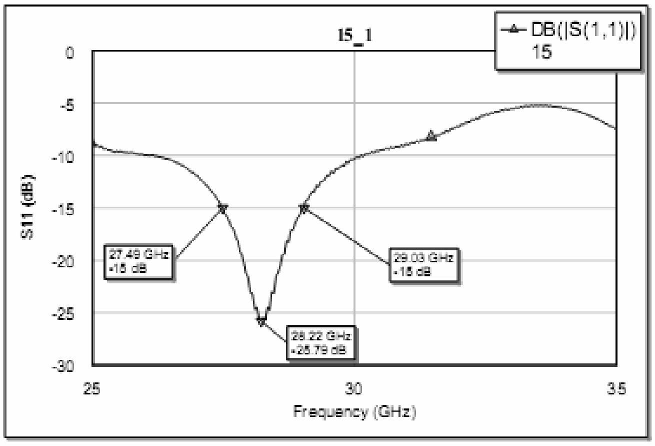

Antena #2

Fig. 5. Return loss of CRLH antennas for a frequency sweep between 25 GHz ... 35 GHz

B. Radiation characteristic in transversal plane (θ)

The radiation characteristics in the transversal plane (θ) for two CRLH antenna structures are shown in Fig. 6 where the received powers at different angles were rated to the maximum power value even if it happens at an angle slightly different of $\theta = 0^0$. According to Fig.6, the -3 dB beamwidth of the radiation characteristic extends approx. between +210 ÷ -160 for antenna #1 and approx. between $+20^0$ ... -18^0 for antenna #2.

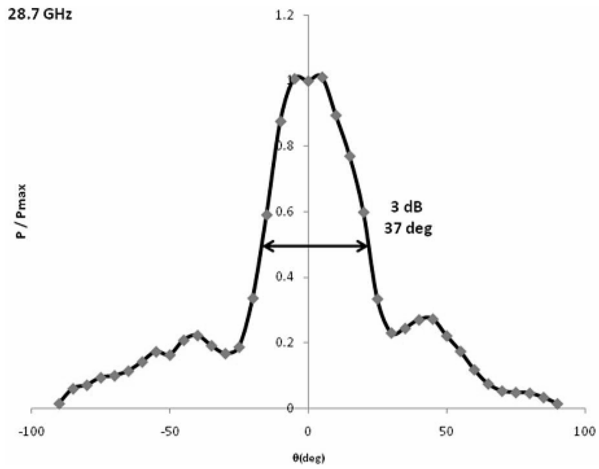

Antena # 1

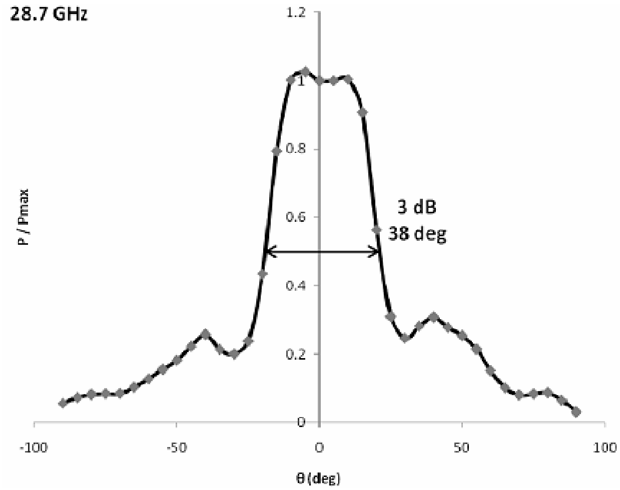

Antena # 2

Fig. 6. Radiation characteristic in transversal plane (θ) for two samples of CRLH antenna structures.

C. Radiation characteristic in longitudinal plane (φ)

In order to complete the characterization of the antenna's radiation capability, measurements were also made in the longitudinal antenna plane (φ). In this respect, the measuring setup was slightly modified and the measuring angle was in forward direction. The frequency was, also, 28.7 GHz and the measurement technique was the same as for the radiation characteristic in the transversal plane (θ) previously presented. The positive direction for the angle (φ) is toward end of the CRLH antenna.

The experimental results are shown in Fig.7 where the radiated powers at different angles in the (φ) plane for the two CRLH antenna samples (antenna #1 and antenna #2) were plotted. The domain of variation of the φ angle was between $-90^0 \div +90^0$. All the received power values were rated to the maximum value in this variation range.

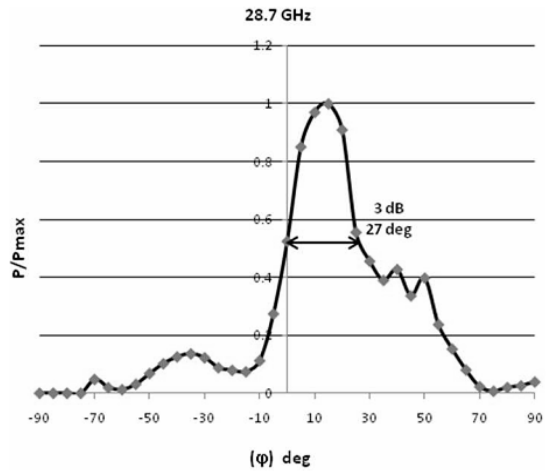

Antena # 1

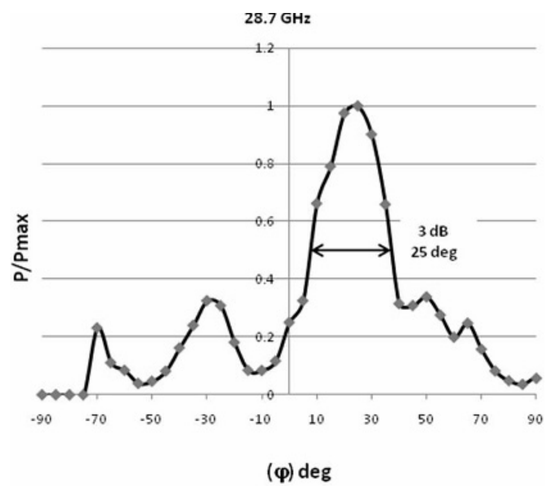

Antena # 2

Fig.7. Radiation characteristic in longitudinal plane (φ) for two samples of CRLH antenna structures.

As shown in Fig.7, the maximum radiated power occurs at an angle φ ≅ +140 for antenna #1 and φ ≅ +240 for antenna #2. The width of the radiation lobe in the longitudinal direction of the antenna is approx. 250 for antenna #1 and approx. 270 for antenna #2.

D. Antenna gain

The antenna gain was computed using the De Friis relation for two identical antennas (1):

$$\frac{P_r}{P_t} = G_i^2 \left(\frac{\lambda}{4\pi R} \right)^2 \tag{1}$$

where: P_t = power transmitted by the emitting antenna, P_r = power at the receiving antenna, G_i = antenna gain with respect to isotropic; λ = wavelength, R = distance between emitting and receiving antenna (in the same units as wavelength). In this situation the emitting and the receiving antennas are identical so that the gains with respect to isotropic of both devices are the same, (G_i) The gain in dBi is expressed by:

$$G(dBi) = 10\log_{10}\left(\frac{4\pi R}{\lambda} \sqrt{\frac{P_r}{P_t}} \right) \tag{2}$$

The antenna gain was evaluated in the frequency domain 28 GHz ... 29 GHz and the obtained data are the following: λ = 10,7 mm/f = 28 GHz, R = 100 mm, power at the emitting antenna: Pt = 0,45 mW, power at the receiving antenna Pr = 1.29E-04 mW.

The antenna gain was computed with (2) at different frequencies in the 28 GHz ... 29 GHz frequency band. The results show the following gain values G = 2,12 dBi / 28 GHz for and G = 2.62 dBi / 29 GHz with a maximum value G = 2,99 dBi / 28.6 GHz. It was observed that the value of G is approx. constant in the 28 GHz ... 29 GHz frequency band.

5. Conclusions

A zeroth-order resonant wave millimeter wave CRLH CPW antenna on silicon substrate was proposed. The silicon substrate and the CPW transmission lines were chosen for the future antenna integration in a more complex monolithically integrated circuit. The antenna was fabricated and the electrical parameters (on-wafer measured return loss, the radiation characteristic and the gain) were measured for two antenna samples obtained in the same technological run.

The measured return-loss: -27.05 dB / 28.78 GHz and -25.79 dB / 28.22 GHz shows a very good matching of the obtained devices. The slightly higher value for the working frequency is due to a technological overetching of the interdigital capacitors metallization. Due to that, the interdigital space increases, the capacity decreases and the working frequency may be higher than designed.

The 3 dB beamwidth of radiation lobe is approx. 37^0 for one of the CRLH antenna samples and approx. 38^0 for the other one.

Concerning the gain, the values computed from the measured data give G = 2,12 dBi / 28 GHz and G = 2.62 dBi / 29 GHz with a maximum G = 2,99 dBi / 28.6 GHz.

There is a frequency difference of approx. 0,5 GHz ÷ 0,7 GHz between S11 measurements (see Fig. 5) and adiation characteristic (see Fig. 6 and Fig. 7) and gain measurement. These differences are due to the fact that the S_{11} parameter of the CRLH antenna structures was measured on-wafer and the gain and the radiation characteristic were evaluated with the antenna structures mounted on the test fixture. The mechanics and the antenna structure contacting to the test fixture connector generate this slight frequency displacement.

References

[1] C. CALOZ, T. ITOH, *Electromagnetic metamaterials: transmission line theory and microwave applications*, John Wiley & Sons, Inc., 2006.

[2] C. Caloz, A. SANADA, T. ITOH, *A novel composite right-/left-handed coupled-line directional coupler with arbitrary coupling level and broad bandwidth*, IEEE Trans. on Microwave Theory and Techniques, **52**(3), pp. 980–992, March 2004.

[3] I. VENDIK, D. KHOLODNYAK, P. KAPITANOVA, K. ZEMLYAKOV, *Multiband tuneable microwave resonators and filters on a combination of right/left-handed transmission line sections*, Proc. of the 3rd International Congress on Advanced Electromagnetic Materials in Microwaves and Optics, METAMATERIALS, pp. 181–183., London, UK, 30th Aug. – 04th Sept. 2009.

[4] Jian-Qiang GONG, Qing-Xin CHU, *Miniaturized Microstrip Bandpass Filter Using Coupled SCRLH Zeroth-Order Resonators*, Proc. of the European Microwave Conference, EuMC, EuMW, pp. 370–373, Rome, Italy, 28 Sept. 02 Oct. 2009.

[5] R.H. GESCHKE, B. JOKANOVIC, P. MEYER, *Compact Triple-Band Resonators Using Multiple Split-Ring Resonators*, Proceedings of the European Microwave Conference, EuMC, EuMW, pp. 366–369, Rome, Italy, 28 Sept. 02 Oct. 2009.

[6] A. SANADA, M. KIMURA, I. AWAI, S. CALOZ, T. ITOH, *A planar zeroth-order resonator antenna using a left-handed transmission line*, Proc. of the 34th European Microwave Conference, pp. 1341–1344, Amsterdam, 2004.

[7] Cheng-Chi YU, *et al.*, *A compact antenna based on metamaterial for WiMAX*, Proc. of Asia-Pacific Microwave Conference, Paper J2-05, Hong Kong, 2008.

[8] Seongmin PYO, *et al.*, *A metamaterial-based symmetrical periodic antenna with effiency enhancement*, Proc. of Asia-Pacific Microwave Conference, Paper A3-49, Hong Kong, 2008.

[9] Chen-Jung LEE, Maha ACHOUR, Ajay GUMMALLA, *Compact metamaterial high isolation MIMO antenna subsystem*, Proc. of Asia-Pacific Microwave Conference, Paper A2-27, Hong Kong, 2008.

[10] Richard W. ZIOLKOWSKI, Peng JIN, Chia-Ching LIN, *Electrically Small Metamaterial-Inspired Antennas: The Next Generation*, Proc. of the 3rd International Congress on Advanced Electromagnetic Materials in Microwaves and Optics, METAMATERIALS, pp. 44–46, London, UK, 30th Aug. – 04th Sept. 2009.

[11] A.A. BASHARIN, N.P. BALABUKHA, *The Radiation of Antennas Based on Metamaterial Waveguides*, Proc. of the 3rd International Congress on Advanced Electromagnetic Materials in Microwaves and Optics, METAMATERIALS, pp. 224–226, London, UK, 30th Aug. – 04th Sept. 2009.

[12] S. EGGERMONT, R. PLATTEBORZE, I. HUYNEN, *Analysis of Radiation in a Metamaterial Leaky Wave Antenna Based on Complementary Split Ring Resonator*, Proc. of the 3rd International Congress on Advanced Electromagnetic Materials in Microwaves and Optics, METAMATERIALS, pp. 102–104., London, UK, 30th Aug. – 04th Sept. 2009.

[13] G. SAJIN, S. SIMION, F. CRACIUNOIU, R. MARCELLI, *Silicon supported microwave zeroth-order resonance antenna on metamaterial approach*, Proceedings of the 2007 Asia-Pacific Microwave Conference, APMC, pp. 221–224., Bangkok, Thailanda, 11–14 Dec.2007.

Frequency-Reconfigurable E-Plane Filters Using MEMS Switches

Luca PELLICCIA, Paola FARINELLI, Roberto SORRENTINO

University of Perugia, DIEI, Via G. Duranti 93, 06125 Perugia, ITALY
Phone: +39-075-585-3658
E-mail:{luca.pelliccia, paola.farinelli, roberto.sorrentino}@diei.unipg.it

Abstract. In this paper a new concept for the design of reconfigurable bandpass filters showing very high unloaded Q-factor is presented. The new solution uses rectangular waveguide resonators loaded with a reconfigurable E-plane circuit. Ohmic MEMS switches are placed around E-plane metal strips so as to modify the TE_{101} mode resonant frequency, thus changing the central frequency of the filters. Unloaded Q-factors over 1000 and tuning ranges up to 10% can be achieved. Preliminary measurements of a 3rd order bandpass hardwired filter at 10 GHz show 625 MHz frequency shift (6.25%) with unloaded Q-factors above 1000. The final version of the filter using actual RF MEMS is presently under fabrication at FBK.

1. Introduction

Tunable and reconfigurable bandpass filters will be key elements in future telecommunication systems both for satellite and terrestrial applications. Size and weight of tunable and multi-standard satellite front-ends will be reduced and innovative programmable and reconfigurable RF-systems will be developed and realised, if efficient and reliable solutions for electronically tunable filters are found. High unloaded Q-factor (>500), wide tuning range (5-10%) and low manufacturing cost should be provided.

Magnetically tunable filters show high Q-factors but they are bulky and consume a considerable amount of DC power [1]. Planar tunable filters using MEMS or varactors allow for an easy implementation but provide low Q-factors (<300) [2]. Evanescent-mode cavities [3], dielectric-loaded resonators [4] and ridged waveguide resonators [5] achieve higher unloaded Q-factors (>500) but they require complex MEMS arrangement.

The use of ohmic cantilever RF-MEMS switches for the realisation of very high-Q (up to 1000) bandpass reconfigurable filters has been proposed by the authors of the present paper in [6] and [7], where an accurate review of the reconfigurable and tunable filter state of the art is also described. A similar concept yielding very high Q-factors has been implemented in E-plane bandpass filters with a reconfigurable bandwidth [8].

Magnetically tunable E-plane filters [9] and tunable E-plane filters using both varactors and capacitive MEMS [10][11] have been developed in last decades yielding significant central frequency tunings with Q-factors up to 500. A new concept of reconfigurable bandpass filters leading to very high Q-factors (>1000) is proposed in this paper. The filter is based on rectangular waveguide resonator loaded with an E-plane metal strip on a low-loss substrate [12]. Ohmic RF MEMS switches are used to modify the length of the metal strip so as to change the resonant frequency of the dominant the TE101 mode thus the filter passband frequency.

To illustrate and validate the proposed tuning principle, a 3rd order bandpass filter at 10 GHz has been designed and fabricated using equivalent hardwired connections emulating the MEMS states.

2. New Tuning Principle

The resonator depicted in Fig. 1 consists of a waveguide section comprised by two E-plane septa of length *d*. The latter determines the input/output (inductive) coupling, while the distance *l* between the septa determines the resonant frequency of the TE_{101} mode. An additional E-plane conductive strip between the septa is used to lower the resonant frequency of the TE_{101} mode. Thin longitudinal lines, each being interrupted in the middle by a MEMS switch, connect both ends of the central strip to the coupling septa. In the following the structure in Fig. 1 is called strip-loaded E-plane resonator.

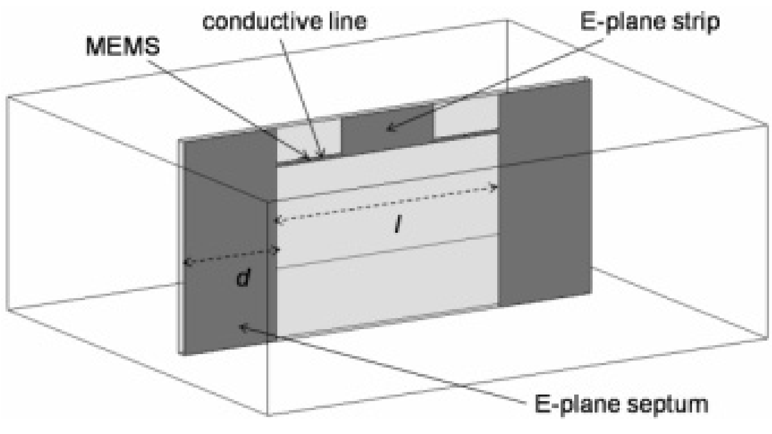

Fig. 1. MEMS-based reconfigurable strip-loaded E-plane resonator.

The MEMS switches can be realised as ohmic cantilever switches. As is well known, in the on-state the switch is closed and can be modelled as a very low series resistance (R_{on}), while in the off-state the switch is open and can be modelled as a low series capacitance (C_{off}) [13].

The tuning principle of the strip-loaded E-plane resonator is as follows. When both MEMS are closed, the electric field in the longitudinal plane is confined below the conducting lines, while when the MEMS are open, the electric field goes through the conducting lines. As a result, the resonant frequency is lowered by switching the MEMS off. The amount of the frequency shift can be controlled by suitably choosing the geometry of the E-plane printed circuit.

3. Reconfigurable Resonator Design

As an example, the practical design of a MEMS-reconfigurable resonator operating in the X band (centre frequency is 10 GHz) is illustrated in this section. The full-wave HFSS ® model is shown in Fig. 2a.

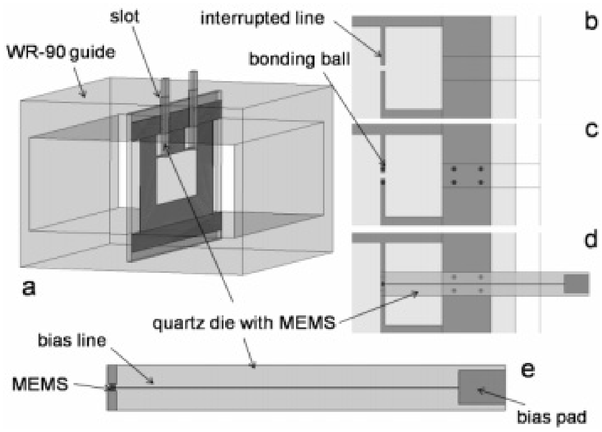

Fig. 2. MEMS-reconfigurable strip-loaded E-plane resonator (a), flip-chip mounting of the MEMS quartz die (b) (c) (d), MEMS quartz die (e).

The E-plane circuit pattern is realised on a 500µm thick quartz substrate (ε_r = 3.78; tanδ = $1 \cdot 10^{-4}$). The longitudinal lines are 200µm width (Fig. 2b). The cantilever MEMS are realised on 500µm thick quartz dies and mounted at the centres of the longitudinal lines using flip-chip technology (Fig. 2c and 2d). Small gold bonding balls (typically 200µm diameter) are employed both to solder the MEMS interfaces to the lines and to support the quartz dies on the substrate. Quartz is preferred to silicon because of its lower εr and tanδ. As shown in Fig. 2a, the thin quartz dies protrude beyond the waveguide broad wall in order to allow the connection of the MEMS bias lines (Fig. 2e). The slots opened in the waveguide broad wall are thin enough not to interrupt the flowing currents, thus preventing or minimising undesired radiation.

Series ohmic cantilever MEMS switches have been considered. They consists of 110 µm wide and 170 µm long gold beams suspended above an interrupted microstrip line. Similar designs previously manufactured by FBK, Trento Italy, showed an on-state resistance R_{on}=0.9 Ω and an off-state capacitance C_{off} =10 fF. The 10 µm wide bias lines are realised in high resistivity polysilicon [2], [13].

The structure has been carefully modelled by HFSS ® including the bias lines, the lossy substrates, the actual material conductivity as well as any undesired radiation through the thin slots. Fig. 3 shows the simulated scattering parameter $|s_{21}|$ for both MEMS states.

As can be seen, the off-state response is down shifted by 650MHz (6.5%) with respect to the on-state. The input/output coupling (K_{s1}) in the on-state is 0.1, whereas it is 10% lower in the off-state. The total unloaded Q-factor is 1430 and 1590 for the on- and off-state respectively.

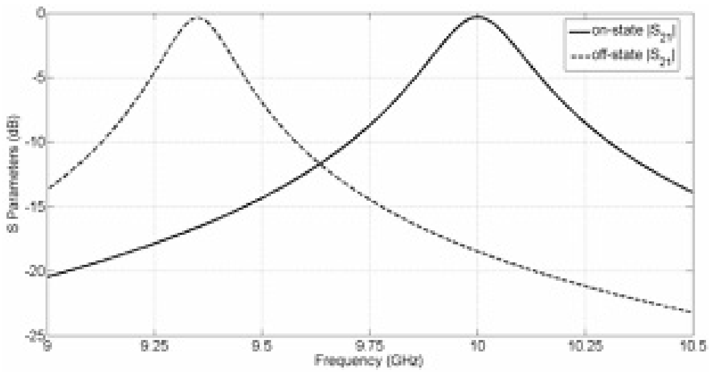

Fig. 3. Simulated $|s_{21}|$ (Ansoft HFSS) of the X-band reconfigurable strip-loaded E-plane resonator of Fig. 4: on-state MEMS (solid blue line); off-state MEMS (dashed red line).

According to HFSS ® simulations, frequency shifts up to 10% are obtained maintaining the unloaded Q-factors above 1000 for both MEMS states.

4. Preliminary Measurements and Future Work

In order to validate the proposed approach, a 10 GHz 3rd order filter has been designed manufactured and tested. Photographs of the disassembled structure are shown in Fig. 4.

The ohmic MEMS switches have been replaced by hardwired connections, *i.e.* open- or short-circuits, which emulate the two MEMS states: a 100 µm thick continuous copper line is used for the on-state MEMS, whereas a 100 µm gap in the lines is used for the off-state MEMS.

The two hardwired configurations (on- and off-state) are alternatively assembled in the waveguide (Fig. 4). The substrate is Arlon DiClad 880 (ε_r = 2.17; tanδ = $1 \cdot 10^{-3}$).

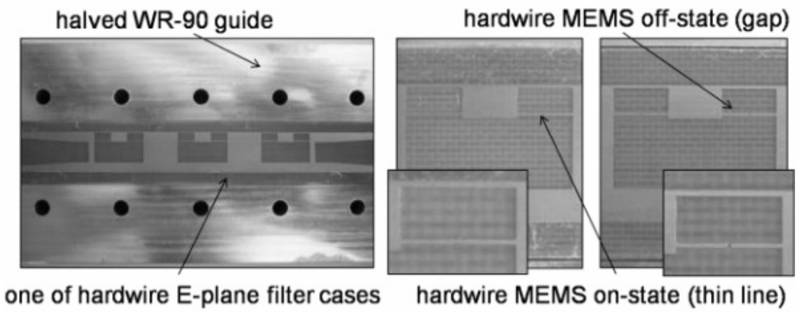

Fig. 4. Photographs of the 10 GHz.3rd order reconfigurable bandpass filter employing hardwired connections.

The simulated and measured insertion loss and return loss of the band-pass filter in the two configurations are shown in Fig. 5 and 6 respectively.

A frequency shift of 625 MHz (6.25%) has been measured; this value fits well with the 650 MHz simulated frequency shift. The measured insertion losses at centre frequency are 0.30 dB and 0.31 dB for the on- and off-state respectively (Fig. 5). The measured 25 dB equiripple relative bandwidths are 3% and 2.8% (Fig. 6), corresponding to measured unloaded Q-factors of 1050 and 1100 respectively.

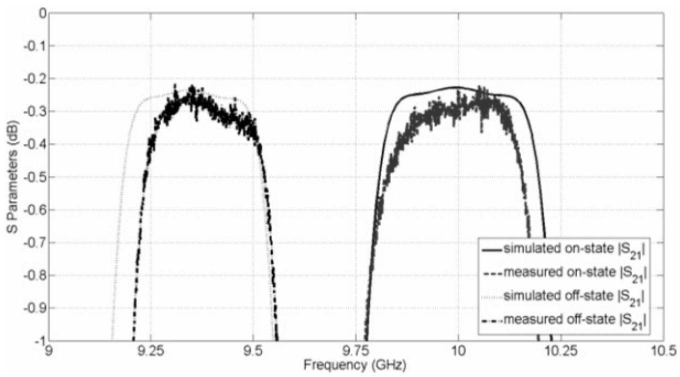

Fig. 5. Simulated and measured $|s_{21}|$ of the 3rd order hardwired filter prototype on-state MEMS (simulated $|s_{21}|$ solid blue line, measured $|s_{21}|$ dashed red line); off-state MEMS (simulated $|s_{21}|$ dotted green line, measured |s21| dot-dashed black line).

The simulated unloaded Q-factor is 1400 and 1450 for the on- and off-states respectively, so the corresponding measured values are roughly 25% lower for both states. This is to be ascribed to a loose contact between the printed circuit and the waveguide wall.

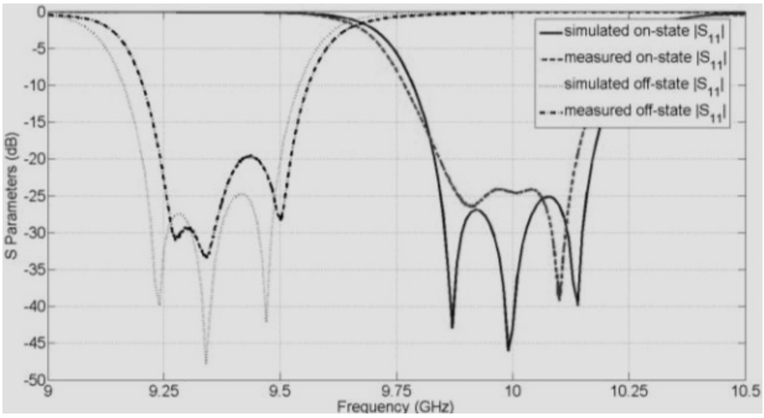

Fig. 6. Simulated and measured $|s_{11}|$ of the 3rd order hardwired filter prototype: on-state MEMS (simulated $|s_{11}|$ solid blue line, measured $|s_{11}|$ dashed red line); off-state MEMS (simulated $|s_{11}|$ dotted green line, measured |s11| dot-dashed black line).

A 6.5% shrink of the relative bandwidth in the off-state is observed compared to the on-state, because of small variations of the filter couplings. The measurements are very promising both in terms of unloaded Q-factor and bandwidth robustness especially when compared to other tunable filter realizations presented in the literature [5][6].

A 3rd order E-plane reconfigurable filter at 10 GHz employing real ohmic cantilever MEMS switches is being manufactured by FBK (Fondazione Bruno Kessler) using an established eight-mask surface micro-machining process on 500μm thick quartz substrate [2][13].

5. Conclusion

A new concept has been proposed for high-Q MEMS-based reconfigurable bandpass filters. A waveguide resonator is employed consisting of a rectangular waveguide section comprised between two metallic E-plane septa and loaded with an E-plane conductive strip.

The strip is connected to both septa by conducting lines that can be switched on and off by RF-MEMS. Therefore, the TE_{101} mode resonant frequency can be changed depending on the MEMS state. The proposed tuning principle provides a frequency tuning up to 10% and unloaded Q-factors above 1000.

The tuning concept has been validated by fabricating and measuring a 10 GHz 3rd order bandpass filter where MEMS switches have been replaced by hardwired connections. A 6.25% frequency shift and unloaded Q-factors above 1050 have been measured in agreement with the HFSS simulations. Return loss variation due to the tuning is negligible, while a little relative bandwidth change occurs (6.5%).

The final version of the filter using actual RF MEMS is presently under fabrication at FBK.

References

[1] J. UHER and W.J.R. HOEFER, *Tunable Microwave and Millimeter-wave Band Pass Filters*, IEEE Trans. Microwave Theory & Tech.. **39(**4), pp. 643–653, April 1991.

[2] A. OCERA, P. FARINELLI, P. MEZZANOTTE, R. SORRENTINO, B. MARGESIN, F. GIACOMOZZI, *A Novel MEMS-Tunable Hairpin Line Filter on Silicon Substrate*, 36th EuMC, Manchester Sept. 2006.

[3] Sang-June PARK, Isak REINES, Chirag PATEL, and Gabriel REBEIZ, *High-Q RF-MEMS 4-6 GHz Tunable Evanescent-Mode Cavity Filter*, IEEE MTT-S Int. Microwave Symp. Dig., Proceedings of workshop WFD, pp. 1145–1148, 7-12 June 2009.

[4] D.W. WINTER and R.R. MANSOUR, *Tunable Dielectric Resonator Bandpass Filter with Embedded MEMS Tuning Elements*, IEEE Trans. Microwave Theory & Tech. **55(**1), pp. 154–159, January 2007.

[5] R. STEFANINI, M. CHATRAS, A. POTHIER, J.C. ORLIANGES, P. BLONDY, *High Q Tunable Cavity using Dielectric Less RF-MEMS Varactors*, Proceedings of the 39th EuMC, pp. 1744–1747, Rome, 29 September – 1 October 2009.

[6] L. PELLICCIA, S. BASTIOLI, F. CASINI, R. SORRENTINO, *High-Q MEMS-Reconfigurable Waveguide Filters*, Proceeding of 40th EuMC, Paris, September - October 2010.

[7] L. PELLICCIA, S. BASTIOLI, F. CASINI, P. FARINELLI, R. SORRENTINO, *High-Q Reconfigurable Waveguide Filters using Cantilever MEMS Switches*, Proceeding of the 11th International Symposium on RF MEMS and RF Microsystems, Otranto, Italy, 28th – 30th June 2010.

[8] L. PELLICCIA, R. SORRENTINO, *High-Q MEMS-based Bandwidth-Reconfigurable E-plane Filters*, Proceeding of the APMC 2010, Yokohama, Japan, December 2010.

[9] J. UHER, J. BORNEMANN, F. ARNDT, *Magnetically Tunable Rectangular Waveguide E-Plane Integrated Circuit Filters*, IEEE Trans. Microwave Theory & Tech. **36**(6), pp. 1014–1022, June 1988.

[10] Jian XU, Xiao-Peng LIANG, K. SHAMSAIFAR, *Full Wave Analysis and Design of RF Tunable Filters*, Microwave Symposium Digest, 2001 IEEE MTT-S International **3**, pp. 1449–1452, May 2001.

[11] D. SCARBROUGH, C. GOLDSMITH, J. PAPAPOLYMEROU, and Yuan LiI, *Miniature Microwave RF MEMS Tunable Waveguide Filter*, EuMC, pp. 1860–1863. Oct. 2009.

[12] L. PELLICCIA, P. FARINELLI, R. SORRENTINO, *MEMS-based High-Q Reconfigurable E-plane Filters*”, Submitted to the 41st EuMC, Manchester, October 2011.

[13] P. FARINELLI, F. GIACOMOZZI, G. MANNOCCHI, R. MARCELLI, B. MARGESIN, P. MEZZANOTTE, S. DI NARDO, P. RUSSER, R. SORRENTINO, F. VITULLI, L. VIETZORRECK, *RF-MEMS SPDT Switch on Silicon Substrate for Space Application*, Silicon Monolithic Integrated Circuits in RF Systems, Digest of Papers, Topical Meeting, pp. 151–154, 8-10 Sept. 2004.

5-bit MEMS Phase Shifter

F. CASINI[1], P. FARINELLI[1], E. CHIUPPESI[1], Giuseppe RESTA[2], Francesco SOLAZZI[2], Sabrina COLPO[2], F. Di MAGGIO[3], I. POMONA[3]

[1]RF Microtech, Via Mascagni, 11 - I-06125 Perugia, Italy

[2]MEMSRaD Research Unit, FBK-irst, Via Sommarive 18, 38050 Povo, Trento, Italy

[3]Selex Communications Spa, Via Sidney Sonnino, 6 - 95045 Misterbianco (CT), Italy

E-mail: farinelli@rfmicrotech.com

Abstract

This work presents the latest progresses on the CONFIRM "reCONFIrable circuits by Rf Mems" project. Previously the design of three different typologies of 5-bit MEMS phase shifters at 20.7GHz was developed and the most promising design options were identified and selected [1]. In this paper we present the design, manufacturing and RF tests of three 5-bit K-band MEMS phase shifters based on similar architectures but working in different frequency bands, namely 20.7GHz, 30.5GHz and 35GHz. The phase shifters are intended to be used in Phased Array Antennas for SOTM Terminals and ESA (Electronically Scanned Antenna) seekers, in both the transmitting and receiving channels [2-8].

A hybrid architecture has been developed: for the first two prototypes (20.7 GHz and 30Ghz) a switched line topology has been chosen to realize the first four bits, 180°, 90°, 45° and 22.5°. On the other hand the fifth bit, 11.25°, is based on a loaded line topology, which is convenient for this bit since a small phase shift is required. In the 35GHz device both 22.5°and 11.25° bits are realized in loaded line topology since this turned to be more convenient at high frequencies.

All phase shifters are based on series ohmic cantilever switches. The suspended membrane of the switch has a size of 110μm × 170μm and an air gap of 2.7μm (Fig. 1). In the OFF state the switch introduces a very low series capacitance (10fF) given by the interface area between the suspended membrane and the signal line below underneath. On the contrary, in the actuated state the metal to metal contact introduces a series resistance RON, whose value is about 0.9Ω. The devices have been monolithically manufactured on 200μm thick HR Si substrate by using the eight-mask surface micro-machining process available at FBK [9]. The device single bits as well as the complete phase shifters have been measured on 5

different wafers in order to check their performance repeatability. Preliminary measurements show very promising results and high yield of the manufactured MEMS switch.

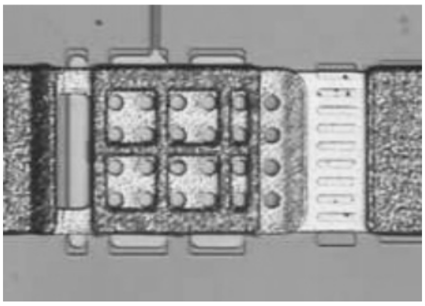

Fig. 1. MEMS ohmic cantilever switch used in the phase shifters.

The layout masks of the two prototypes are shown in Fig. 2. Excellent RF performances have been measured for the three devices, with an average insertion loss of 2, 2.5 and 2.7 for the 5-bit device at 20.7GHz, 30.5GHz and 35GHz respectively (Fig. 3).

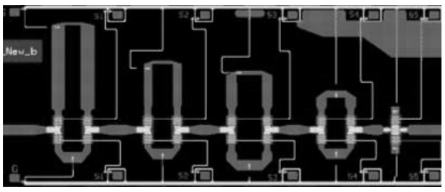

a)

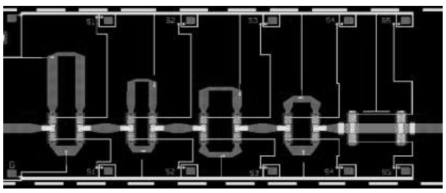

b)

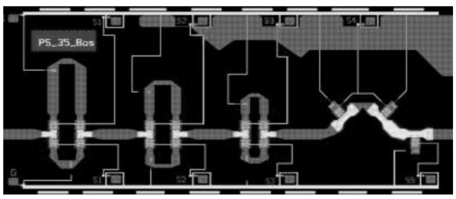

c)

Fig. 2. Layouts of the 5-bit K-band MEMS phase shifters.
(a) 20.7 GHz device (b) 30 GHz device (c) 35 GHz device.

Return loss better than 14 dB and average phase shift error lower than 2 degrees (for the single bits) has been obtained for all states. More data on the wafer uniformity will be presented in the final paper as well as RF test on the packaged devices.

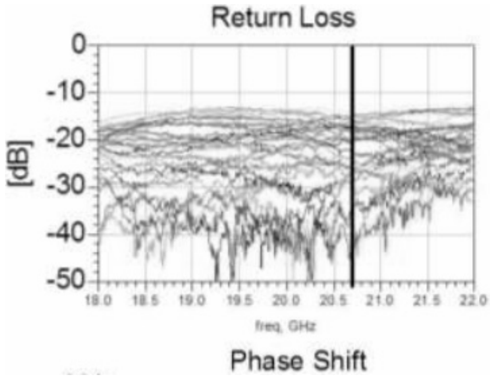

a)

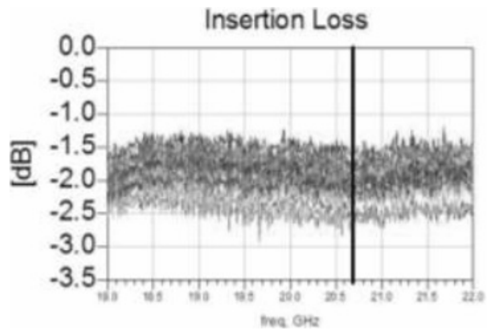

b)

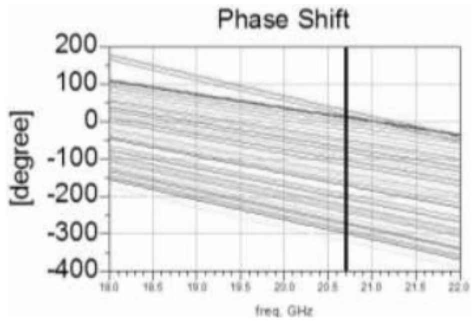

c)

Fig. 3. On-wafer measured performances of the 32 stated of the 20.7 GHz 5-bit MEMS phase shifter (a) Return loss (<14dB for all states) (b) Insertion Loss(=2dB in average, 1dB dispersion) (c) Phase shift (average error= 2degrees).

Acknowledgments. This work has been carried out and supported by the Finmeccanica Corporate Project CONFIRM, reCONFIrable circuits by RF MEMS", in collaboration with Selex-Communications, Selex-Sistemi Integrati, MBDA, Centro Sviluppo Materiali SpA, University of Padova and University of Perugia).

References

[1] P. FARINELLI, E. CHIUPPESI, F. DI MAGGIO, B. MARGESIN, S. COLPO, A. OCERA, M. RUSSO, I. POMONA, *Development of different K-band integrated MEMS phase shifters for satellite COTM terminals*, International Journal of Microwave and Wireless Technologies, **2**(3-4), pp. 263–271, 2010.

[2] Guimin XU, Huachun XU, Wei JIN, *Study on stabilization and tracking for SOTM*, Electronic Measurement & Instruments, ICEMI, 9th International Conference, pp.1-240–1-244, 16-19 Aug. 2009.

[3] R.S. WEXLER, D. HO, D.N. JONES, *Medium data rate (MDR) satellite communications (SATCOM) on the move (SOTM) prototype terminal for the army warfighters*, Military Communications Conference, MILCOM, IEEE, **3**, pp.1734–1739, 17-20 Oct. 2005.

[4] A.I. ZAGHLOUL, O. KILIC, *Antenna system solution for uninterrupted satellite-on-the-move (SOTM) communications*, Antennas and Propagation Society International Symposium, IEEE, **2**, pp. 353–356, 22-27 June 2003.

[5] Sanghyo LEE, Jae-Hyoung PARK, Jung-Mu KIM, Hong-Teuk KIM, Yong-Kweon KIM, Youngwoo KWON, *A compact low-loss reconfigurable monolithic low-pass filter using multiple-contact MEMS switches*, Microwave and Wireless Components Letters, IEEE, **14**(1), pp. 37–39, Jan. 2004.

[6] Erdil EMRE, Topalli KAGAN, Unlu MEHMET, Istanbulluoglu IPEK, Temocin Engin UFUK, Atasoy Halil IBRAHIM, Bayraktar OMER, Civi Ozlem AYDIN, Demir SIMSEK, Koc SENCER, Akin TAYFUN, *Reconfigurable slot antenna with fixed-fixed beam type RF MEMS capacitors*, Antennas and Propagation, EuCAP, First European Conference, pp. 1–5, 6-10 Nov. 2006

[7] K. TOPALLI, O.A. CIVI, S. DEMIR, S. KOC, T. AKIN, *A Monolithic Phased Array Using 3-bit Distributed RF MEMS Phase Shifters*, Microwave Theory and Techniques, IEEE Transactions, **56**(2), pp. 270–277, Feb. 2008.

[8] F. CASINI, F. DI MAGGIO, M. DISPENZA, P. FARINELLI, B. MARGESIN, E. CARPENTIERI, U. D'ELIA, R. VITIELLO, I. POMONA, A. TAZZOLI, G. MENEGHESSO, M. TULUI, R. SORRENTINO, *Design of mm-wave 5-bit phase shifters for Phased Array Antenna Systems*, MEMSWAVE, Otranto 29-30 June 2010.

[9] A. OCERA, P. FARINELLI, F. CHERUBINI, P. MEZZANOTTE, R. SORRENTINO, B. MARGESIN, F. GIACOMOZZI, *A MEMS-Reconfigurable Power Divider on High Resistivity Silicon Substrate*", IEEE MTT-S International Microwave Symposium, Honolulu, 3-8 June 2007.

[10] MARDIVIRIN, *et al*., *Charging in Dielectricless Capacitive RF-MEMS Switches*, IEEE Trans on Microwave Theory and Techniques, **57**(1), pp. 23 –236, Jan. 2009.

Improved Insertion Loss for a WR-3 Waveguide Using Fully Cross-Linked Two-layer SU8 Processing Technology

Maolong KE, Xiaobang SHANG, Yi WANG, Michael J. LANCASTER

School of Electrical, Electronic and Computing Engineering, University of Birmingham, Birmingham, B15 2TT, UK

Tel: 0121 4147965

Abstract. Fully cross-linked two-layer SU8 photoresist technology has been successfully developed and used to fabricate a WR-3 waveguide with two back-to-back right-angle bends at both ends. The resulting waveguide is within 0.01 db/mm of a precision machined waveguide, making the SU8 waveguide a very viable proposition for terahertz applications. The right angle bends are designed to facilitate accurate connection with external waveguides for measurement purpose. The insertion loss has shown significant improvement over previous results obtained using four separate SU8 layers. It is believed that elimination of localized air gaps between the fully cross-linked interface of two adjacent SU8 layers contributed to the improvement. The two-layer SU8 processing technology can be extended into multi-layer technology, which will greatly expand the scope of device applications. The technology is particularly useful in devices which consist of isolated regions or weakly joint parts, which is very difficult to fabricate using previously reported separate layer processing technique.

1. Introduction

There is a growing interest in fabricating high performance components at millimetre wave and submillimetre wave frequencies using micromachining technologies. Among many reported so far [1], thick layer SU8 photoresist technology has displayed some important advantages in terms of near vertical sidewalls (aspect ratio >30:1), as well as being relatively cheap to fabricate using standard photolithographic equipment; hence easily accessible to many. In contrast, other competing technologies, such as Si deep reactive ion etching (DRIE) [2] requires an expensive etching machine, while LIGA process [3] requires synchrotron radiation source. In fact, SU8 has been successfully employed by us to make many high frequency components, including WR-3 (220-325 GHz) waveguide, a filter and a slot antenna [4-6].

However, all the SU8 devices made so far are based on separate layers bonded/assembled together. Typically, for example, a waveguide device was split into 4 equally thick layers and all the layers were made in one mask processing. The layers were then released from Si substrate, metal coated and then bonded/assembled together. The drawback of this method is that it is quite difficult to completely avoid localized air gaps between the different layers because the SU8 surfaces are not perfectly flat. When two uneven surfaces come into contact, air gaps will form among the lower surface regions. As is well known, air gaps have deleterious effect on device performance, resulting in current leakage and higher loss.

In this paper, we report results of a 300 GHz waveguide device with two back to back right angle bends obtained through a new fabrication method. The paper is organized as follows: in the next section (2), device details are reported, which is followed by a detailed description of the fabrication method (3). Measurements and discussions will be given in Section 4, which is followed by conclusions in Section 5.

2. Device Details

In order to facilitate measurement of a 300 GHz rectangular waveguide device, two H-plane back to back right angle bends were designed as shown in Fig. 1. This allows for reliable and accurate interconnection with standard waveguide flanges. Fig. 1(b) and (c) shows the top view of layer 1 (and 4) and 2 (and 3). The waveguide is only about 16 mm long by 0.432 mm wide. Each layer is, however, 48 mm long by 24 mm wide in order to fully accommodate all the alignment pin holes as wells as holes for flange screws (more details are given later).

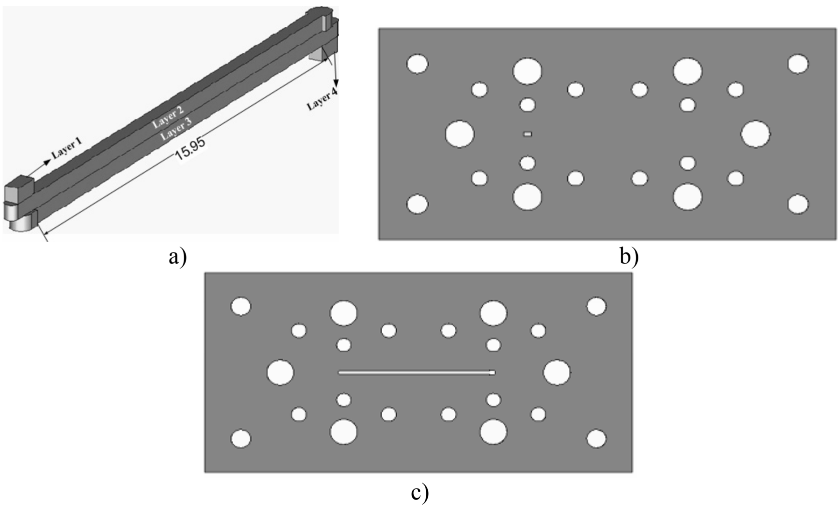

Fig. 1. (a) WR-3 waveguide structure with two right angle bends (unit mm), (b) top view of the first/fourth layer, (c) top view of the second/third layer.

3. Fabrications

Previously this device was fabricated using one mask photolithographic process, in which all four layers were printed onto one mask and processed together in one lithographic step. Each layer i is then individually silver coated and bonded/assembled described in [4]. The disadvantage of such a method is that localized air gaps may form after bonding due to the surface unevenness. These air gaps are likely to lead to increased insertion losses due to current leakage. In order to eliminate the air gaps, we have here developed two-layer SU8 processing technology. Instead of making four separate layers, two layers were processed together to form one half of the waveguide. The final device was formed by combining the two halves together. The fabrication details will be published elsewhere; however here is a brief outline of how it was achieved. Two masks were used instead of one. In mask 1 only the layer 1 and 4 were printed with alignment marks. In mask 2 the layer 2 and 3 printed along with the same alignment marks. Firstly, a 432 μm thick layer of SU8 was spun onto a Si substrate, pre-baked, UV exposed processed with mask 1 and post-baked. Then another 432 μm thick SU8 layer was added onto the top of the layer, pre-baked, UV exposed with mask 2 after careful alignment and post-baked again. During the second UV exposure, both the top and bottom layers were exposed together, hence the second post exposure bake will crosslink the two layers together to form one fully joined piece, hence eliminating the air gaps between the interface. Fig. 2 displays a photo of the processed SU8 device using this new technique where two layers were fully crosslinked together to form a half of the designed waveguide Finally the waveguide was formed by aligning and bonding the two halves together after silver coating.

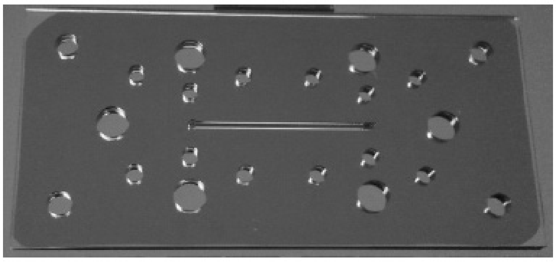

Fig. 2. A photo of the processed SU8 piece where two layers were fully cross-linked together to form a half of the said waveguide.

This method eliminates any air gaps between layer 1/2 and 3/4 interfaces, but it can still leave some air gaps between the middle interface (layer 2/3). However, since the waveguide was designed to split in the E-plane and little current is expected to cross the middle interface, any air gaps there are not expected to have large adverse effect on the device performance.

4. Measurements and discussions

During the measurement, the micromachined waveguide was sandwiched between two brass plates, as shown in Fig. 3. Standard waveguide flanges were inserted into the opening region on the clamping brass to connect directly with the micromachined waveguide circuits [4]. Screws on the flanges go straight through the micromachined waveguide onto nuts at the opposite plate. The alignment pins provide the accuracy to which the two halves are aligned, as well as the accuracy to which the device is aligned to the external flange. The screws are used to clamp the layers together as well as fixing the external flange to the micromachined waveguide. The length of waveguide excluding the bends is 15.95 mm, which is made sufficiently long to allow adequate separation between the flanges of measurement equipment to avoid overlapping of pins and screws from the other side. The measurements were carried out on an Agilent E8361A Network Analyzer with a WR-3 extension T/R module at test port 1 and a receive-only T module at test port 2. Enhanced response calibrations, which combine a one-port calibration and a response calibration were performed before measurements.

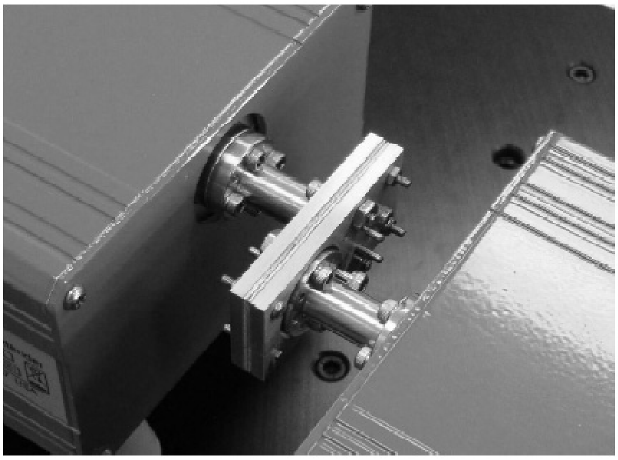

Fig. 3. A photograph of the testing setup.

Fig. 4(a) shows the measured S21 and S11 results from the two-layer waveguide device. The previously obtained results based on four single layers are also included for comparison. The improvement in insertion loss (S21) is significant over a wide frequency range from 220 to 300 GHz as shown in the enlargement Figure 4(b).

The average insertion loss is now only around 0.5dB using the newly developed SU8 two-layer process as compared to about 2.3 dB obtained previously through 4 separate layer process in the frequency range of 220 to 300 GHz. The new data represents a loss of only 0.03 dB/mm, which is comparable to the reported performance of around 0.02 dB/mm for the commercially CNC-machined and then gold plated WR-3 metal waveguide [7].

The return loss is very good for this frequency range being better than 10dB in the across the band. This is however worse than the previous results. We are currently trying to find out the reasons for it, but the most likely is dimensional accuracy. At above 300GHz frequency range, the S21 starts to deteriorate, which is possibly due to misalignment and higher mode effect. Currently, the alignment accuracy between layers 1/2 or 3/4 is around 15 μm, which, we believe can be further reduced through process optimization. The insertion loss results, to our best knowledge, are the lowest reported so far from any micromachining technologies.

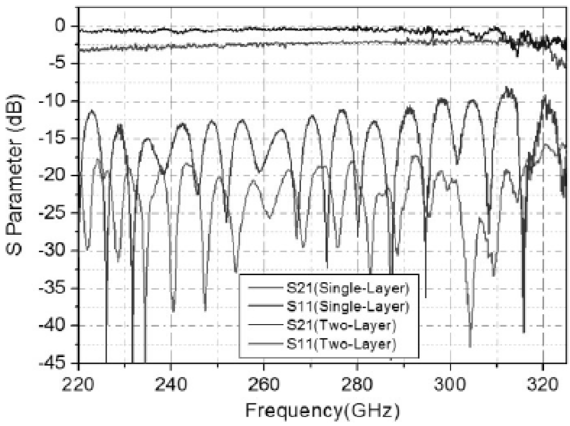

a)

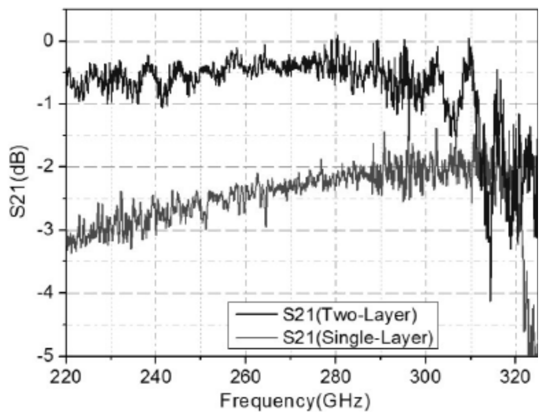

b)

Fig. 4. (a) Measured S21 and S11 results for WR-3 waveguide obtained with SU8 two-layer processing technique; (b) Measured S21 results for the fully linked two-layer processing technique as compared to the previous 4 separate layer processing technique.

5. Conclusions

A two-layer SU8 processing technique was developed and used to fabricate a WR-3 waveguide device with two back to back right angle bends. The insertion loss performance of the device is found to be greatly improved as compared to the previous method of using 4 separate layers. This is believed to be due to the elimination of localized air gaps because layers 1/2 and 3/4 were fully joined together through inter-layer crosslinking. The new processing technique is likely to expand the scope of device applications for thick SU8 photoresist micromachining technology.

Acknowledgements. The authors would like to thank Dr T. Jackson for useful discusions and Donna Holdom for her help during various stages of device processing. The work is supported by the U.K. Engineering and Physical Science Research Council (EPSRC).

References

[1] M.L. KE, Y. WANG, S WEI, K. JIANG, M.J. LANCASTER, *Precision Microfabrication of Millimetre-wave Components*, Proceedings of the 9th International Conference and Exhibition on laser metrology, machine tool, CMM and robotic performance, pp. 397–403, July, London, 2009.

[2] P. BLONDY, A.R. BROWN, D. CROS and G.M. REBEIZ, *Low loss micromachined filters for millimetre wave communication systems*, IEEE Transaction on Microwave Theory and Technique., **46**, pp. 2283–2288, 1988.

[3] Y.S. LIAO and Y.T. CHEN, P*recision fabrication of an arrayed micro-metal probe be the laser-LIGA process*, Journal of Micomechanics and Microengineering, **15**, pp. 2433–2440, 2005.

[4] X. SHANG, M.J. LANCASTER, M. KE, Y. WANG, *Measurements of Micromachined Submillimter Waveguide Circuits*, 76th ARFTG Microw. Measurement conf., pp. 1–4, Florida, USA, 2010.

[5] X. SHANG, M.L. KE, Y. WANG and M.J. LANCASTER, *A Micromachined WR-3 Waveguide Filter With Embedded Bends*, Electronics Letters, **47**(9), p. 545–547, 2011.

[6] Y. WANG, M.L. KE, M.J. LANCASTER, J. CHEN, *Micromachined 300GHz SU8 based slotted waveguide antenna*, to appear in IEEE Antennas and Wireless Components Letters, 2011.

[7] A.R. KERR, C. LITTON, G. PETENCIN, D. KOLLER and M. SHANNON, *Loss of Gold Plated Waveguides at 210- 280 GHz*, ALMA Memo 585, 2009.

A New Approach to Wafer Level Thin-Film Encapsulation for RF-MEMS

V. MULLONI[1], S. COLPO[1], H. El GHANNUDI[2],
F. GIACOMOZZI[1], B. MARGESIN

[1]Fondazione B. Kessler, Via Sommarive 18, 38123 Povo-Trento, Italy
Tel.: +39 0461 314432
[2]RF Microtech, via Mascagni, 11, Perugia, Italy

Abstract. The paper will discuss in detail a new fabrication process developed for the encapsulation of RF-MEMS switches. A shell covering the unreleased switch is created with two layers of PECVD silicon nitride patterned with holes and separated by an aluminum layer which is removed at the end of the shell fabrication sequence. The cavity beneath the shell is then made free burning by oxygen plasma the sacrificial photoresist spacer covering the switch.

The mechanical design of the shell and the optimization of the film parameters are reported and discussed. The shell is then covered with a sealing polymer that should not penetrate into the holes. In order to achieve this result a special design for the hole pattern is presented.

1. Introduction

One of the limits to full exploitation of the potentialities of RF-MEMS switches is the lack of a low-cost packaging system. The requirements of such a package are quite demanding: it must protect the switch from mechanical damage and contaminants, add minimal RF losses and maintain the performances of the switch or circuit. A suitable package should also be low cost, require little additional space and be easy to incorporate in the microwave integrated circuit. It must be hermetic, because MEMS RF components are particularly sensitive to contaminants and humidity, and for this reason the ideal package atmosphere is dry nitrogen or similar inert gases. The usual approach to packaging uses conventional techniques which results in high costs. On the other hand, wafer level packaging techniques include normally wafer bonding schemes and a sealing ring around the switch that increases the switch footprint, while the temperature sensitivity of these devices requires metal-based low temperature solders which can introduce high RF-losses.

In this contribution a thin-film encapsulation scheme is proposed as packaging methodology. This technique is low cost and has a high level of integrated circuit compatibility. Instead of bonding the MEMS wafer on a separate wafer with caps, an open cage-like structure is build around the switch. This is done exploiting standard wafer processing techniques and requires moderate temperatures (200-250°C) [1].

In this type of approach a sacrificial photoresist is deposited above the (unreleased) switch, and then covered with a dielectric to form the shells. Convenient holes are then etched on the dielectric in order to form a release channel. In similar approaches found in the literature [1]-[2], the sacrificial layer is then plasma etched and the cavity sealed with a convenient polymer. The final sealing is however the most critical part of the process because the encapsulant polymer viscosity, the diameter of the holes, the chemical affinity between polymer and cage and the mechanical stiffness of the cage itself play an important role in determining the yield of the process and the final performance of the packaged device. It is then important to find a hole design solution to reduce or prevent polymer wicking through the cage holes keeping in mind that the reduction of hole dimensions is limited by lithographic resolution. In this paper a particular solution to this problem is addressed, that in principle can avoid any wicking phenomena, and produce reliable polymer sealing without compromising the underlying switch functioning.

2. Encapsulation Design Concept

In this section a particular fabrication scheme is presented in order to build a better performing cage structure above the switching devices. The basic idea is to build the shell with two different layers of PECVD silicon nitride with a thin sacrificial layer of aluminum in between them. In all three layers holes are etched but with only a slight superposition between them. When finally the thin aluminum layer is removed, no direct superposition between holes of the two nitride layers is left. This allows the plasma removal of the sacrificial photoresist but inhibits the sealing polymer wicking through the cage holes. A process section for this particular scheme is presented in Fig. 1, while a top view of the holes 2D distribution is reported in Fig. 2. The shell shape is square or rectangular, with side dimensions varying from 500 to 1000 μm. The hole dimensions are 8×8 μm on the two nitride layers, and 6×6 μm on the sacrificial aluminum layer. The free cavity height is determined by the sacrificial spacer height, that is about 3 μm above the device, assuming negligible resist planarization.

In addition a detailed study of parameters influencing the stiffness of the cage material has been planned and performed in order to obtain a more robust shell, which can resist to the sealing polymer spinning process without collapsing on the bottom of the cavity and/or deteriorating the switch performances.

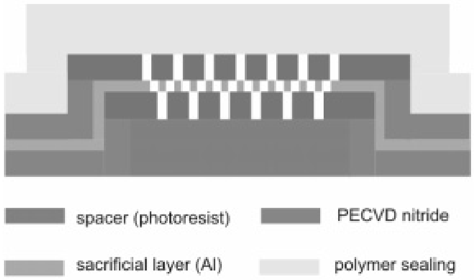

Fig. 1. Encapsulation process scheme.

Improvement of silicon nitride mechanical stiffness can be achieved by controlling its residual stress properties, because the bending spring constant of the shell is strongly depending on its residual stress value. This task involves an evaluation of the stress properties of the PECVD nitride building material as a function of its deposition parameters, and it is reported in detail in the next experimental section.

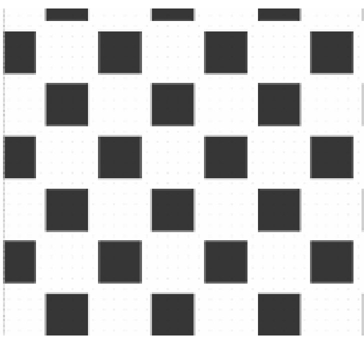

a)

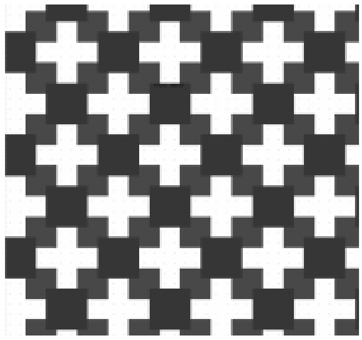

b)

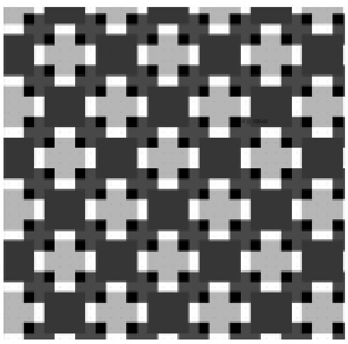

c)

Fig. 2. Bi-dimensional hole distribution in the different cage layers. a) First PECVD nitride layer. The red squares are the holes in this layer. b) Sacrificial aluminum layer. The pink squares are the holes in this layer. c) Second PECVD nitride layer. The green squares are the holes in this layer.

3. Experimental

The thin film encapsulating shells have been fabricated above structured wafers where the complete FBK switch fabrication process [3] has been performed, with exclusion of the final release process in oxygen plasma. The basic switch process includes 8 mask levels, and will not be reported here, while other 5 mask levels are required for the shells. Above the unreleased switches a 3-micron thick photoresist has been deposited, patterned and baked at 250°C, to define the cage dimensions and to act as shell sacrificial layer.

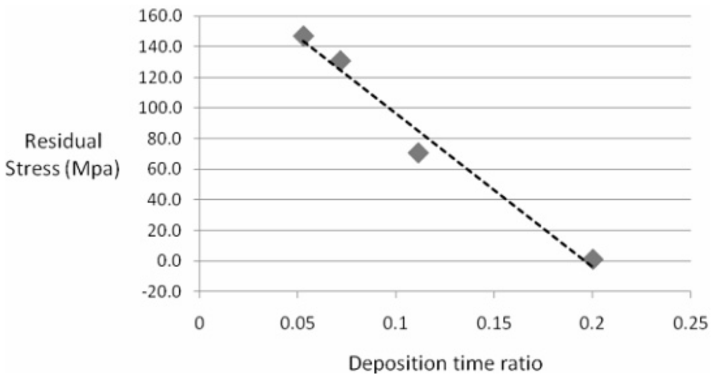

Fig. 3. Silicon Nitride multilayer residual stress variation as a function of deposition time ratio of two basic recipes with stress of -800 Mpa (recipe 1) and 580 MPa (recipe 2).

Preliminary characterization of PECVD silicon nitride residual stress has been obtained depositing at 200°C more than 100 alternating thin layers of silicon nitride having very different stress values. The stress values of the single recipes are -800 MPa (compressive) and 580 MPa (tensile), and are obtained varying the relative compositional parameters of the PECVD gases [4], together with the plasma frequency. Their relative thicknesses can be changed by varying the deposition times [4], and the variation of this parameter allows a continuous variation in average residual stress approximately from zero to 150 MPa as reported in Fig. 3. The residual stress values have been obtained on blank test wafers using the Stoney wafer curvature method.

The more convenient value for nitride stress have been estimated to be around 100-120 MPa (tensile). This value should increase mechanical stiffness but avoids the risk of cracking and should cause only limited deformation of the underlying silicon wafer.

After the characterization 1.5 µm of PECVD nitride with this stress value were deposited, patterned with holes and dry etched (Fig 3a). Then a 500 nm aluminum layer was deposited above the nitride layer, and again patterned with holes and wet etched (Fig. 3b).

A second PECVD nitride layer with the same thickness and deposition parameters of the first one was finally deposited, patterned and etched, as shown in Fig. 3c. From Fig. 3 it can be seen how the lithographic limitations affect the hole shape, but the resolution and the alignment are enough to ensure the correct superposition of the patterned holes. The hole opening on the nitride layers has been performed with some care, since the dry etching rate is sensibly lower in the hole structures than on large areas or blank wafers.

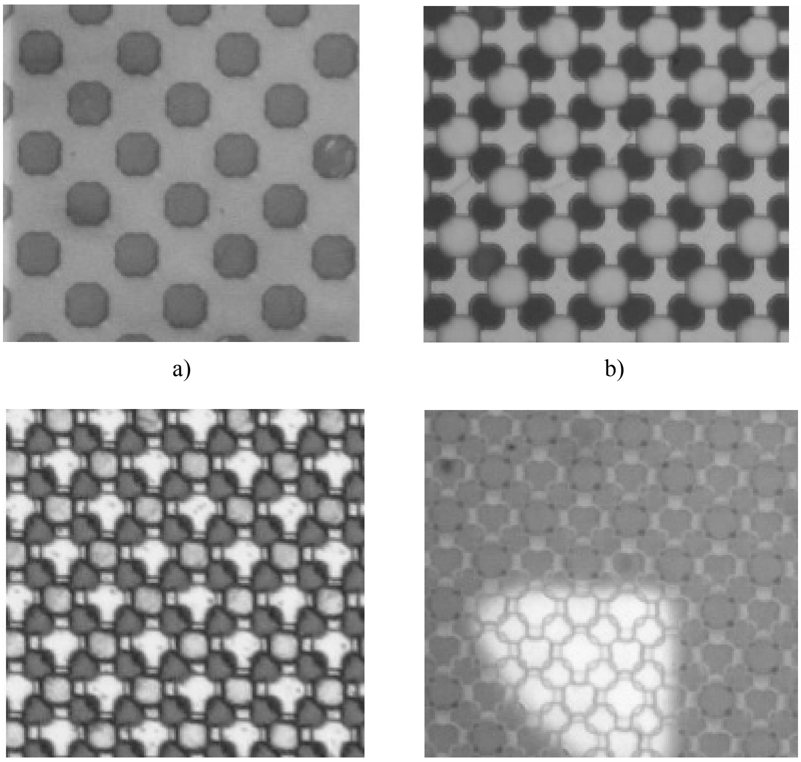

a) b) c) d)

Fig. 3. Pictures of holes distribution at different process stages: a) First PECVD nitride layer. b) Sacrificial aluminum layer. The dark areas are the holes in this layer. c) Second PECVD nitride layer. The holes in this layer are centered on the cyan crosses, while the light green squares correspond to the holes in the first nitride layer. d) Final released structure. The light area is an underlying aluminum pattern.

At this point the removal of the sacrificial aluminum layer has been performed by wet etch. This process step has the purpose to create a lateral release channel between the holes of the two nitride layers, since the two hole patterns are not overlapping.

Finally the burning of the shell sacrificial layer was performed, leaving free the underneath cavity. This is accomplished with a oxygen plasma asher, and the process is planned to be long enough to burn also the switch spacer and free the movable membrane. A detail of a released shell is reported in Fig. 3d, where it can be noted that the cage is completely transparent and the underlying structure is clearly visible. This last characteristic is even more evident looking at Fig. 4, where an entire (still unreleased) switch included in the nitride shell is reported in the picture.

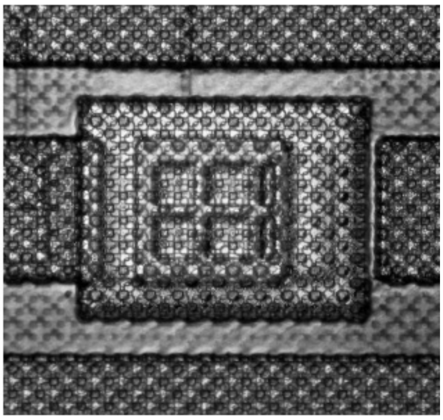

Fig. 4. Cantilever switch included in the nitride cage.

After release of the sacrificial photoresist the free cavity has been tested for its mechanical resistance to external loading by means of a mechanical profilometer equipped with a tip diameter of 2μm. An example of the results of these tests is shown in Fig. 5, where it can be noted that the mechanical resistance is quite good. In addition it has been found that deformations are completely reversible, that is no cracking or irreversible damage has been detected. The holes in the cage profiles are due to some misalignement between the holes and the tip scan.

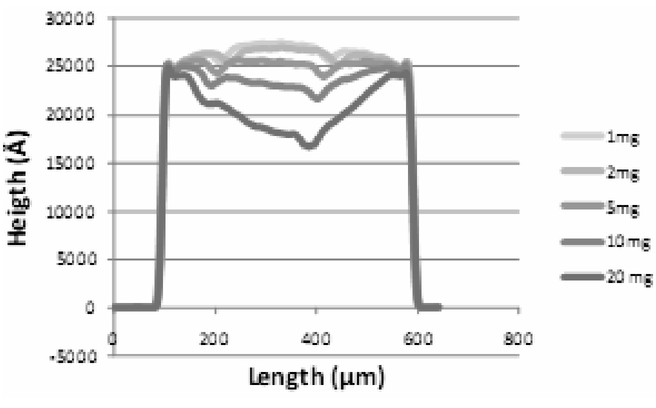

Fig. 5. Load test of a 500 μm wide released nitride shell.

At present, the final covering with a sealing polymer is still under development. Different options are currently under investigation, like polyimide, SU8 and BCB. From the mechanical and structural point of view, the modified cage structure is supposed to work as it was defined at design level. The specific polymer properties may however play an important role in determining the final outcome of this approach, because the capillary forces could allow the polymer to penetrate to some extent through the interstitial channels. In this case the nitride surface affinity and the sealing polymer surface tension may turn out to be important, and the polymer viscosity as well.

4. Conclusion

A new design approach to thin film encapsulation for RF-MEMS devices has been proposed. The main feature consists in the superposition of two different cover layers with holes not directly superimposed. The feasibility of this concept has been practically demonstrated building encapsulating nitride cages above FBK switch wafers.

The cages show good mechanical resistance and no damage of the underlying devices has been detected. The final details of this process and its full validation are still under development and testing.

Acknowledgement. This work has been partially supported by the ARASCOM project, 7th European framework programme, contract no. 222620.

References

[1] D.I. FOREHAND and C.L. GOLDSMITH, *Wafer Level Micropackaging of RF-MEMS Switches*, Proceedings of IPACK 2005, July 1-22 S, Francisco, CA, USA.

[2] K.D. LEEDY, R.E. STRAWSER, R. CORTEZ and J.L. EBEL, *Thin Film Encapsulated RF MEMS Switches*, J. Microelectromech. Syst. **16**, pp. 304–309, 2007.

[3] K.J. RANGRA, F. GIACOMOZZI, B. MARGESIN, L. LORENZELLI, V. MULLONI, C. COLLINI, R. MARCELLI and G. SONCINI, *Micromachined Low Actuation Voltage RF_MEMS capacitive switches, technology and characterization*, Proceedings of CAS 2004.

[4] A. PICCIOTTO, A. BAGOLINI, P. BELLUTTI, M. BOSCARDIN, *Influence of interfaces density and thermal processes on mechanical stress of PECVD silicon nitride*, Applied Surface Science **256**, pp. 251–255, 2009.

Improving Controllability in RF-MEMS Switches using Resistive Damping

M. SPASOS[1,2], N. CHARALAMPIDIS[1],
K. TSIAKMAKIS[1], R. NILAVALAN[2]

[1]ATEI of Thessaloniki, Greece
E-mail: spasos@el.teithe.gr

[2]Brunel University, London, United Kingdom

Abstract. An efficient way to control the impact velocity in order to achieve soft landing and fewer bouncing phenomena is the resistive damping. This control method is also referred as charge drive and presented for first time by Castaner and Senturia [1]. Under charge control the Pull-in phenomenon of the Constant Voltage controlled electrostatic actuators does not exist and if the current drive is ideal, any position across the gap is stable. The main reason for this behavior is that the electrostatic force applied is always attractive and independent of the remaining gap of the actuator. Charge drive control incorporating constant current sources is mostly preferred to extend the travel range of electrostatic micro-actuators [2], [3], [4], [5]. Nevertheless there are very few references in the literature about charge drive control on RF MEMS. Recently published work based on numerical simulations for capacitive RF-MEMS, [6] and [7] present a learning algorithm in order to reduce fabrication variability using resistive damping for the pull-down phase. Nevertheless none of them present any details on how to implement resistive damping and any results of such kind of applications. This work presents in detail the entire procedure in calculating the bias resistance of an RF-MEMS switch controlled under resistive damping.

Key words: charge drive control, RF-MEMS switch, resistive damping, bouncing, contact force.

1. The Significance of Resistive Damping

The controllability of a switch is the key factor to reduce wear by minimizing the impact velocity. Despite the sophisticated design, adopting special cantilever shapes for contributed actuation force as well as utilizing fringing fields by making use of protruded electrodes, controllability still remains a difficult task which requires great thought and mathematical calculations. In case of a very stiff device, like the one which has been fabricated and presented by Guo, McGruer and Adams [8], the actuation control under resistive damping is the only way to achieve controllability. Due to the small switching time as well as the high actuation voltage, it is not practical to implement a tailored control pulse. Experimental results have shown that time intervals smaller than 1μs and pulses with slew-rate greater than 200V/μs are necessary in order to shape a tailored pulse for this switch, as the switching time is about 1.24μs when a sharp actuation pulse of 83V is applied. Even for the case that this fast and high in voltage pulse can be generated, there are other subjects like overshooting that they will possibly render problematic the control of the switch.

To eliminate bouncing phenomena, during the release phase of the switch, when the cantilever is oscillating within mechanical resonance frequency, the R_bC_{el} product must be equal to the period of the resonance frequency [9].

Very stiff devices [8], present high mechanical resonance frequency and make them appropriate for this kind of control as the time constant RC, which has been calculated for the pull-down phase, is near the period of the mechanical resonance frequency. Consequently, significant improvement in both switching operation phases of the switch is achieved. Thus, control under resistive damping is the only practical solution for very fast RF-MEMS switches where switching time and period of the resonance frequency are of the same order.

2. Applying Resistive Damping to Improve Controllability

The ohmic RF-MEMS switch of Fig.1 has been evaluated under the Coventorware software package examining controllability with and without resistive damping.

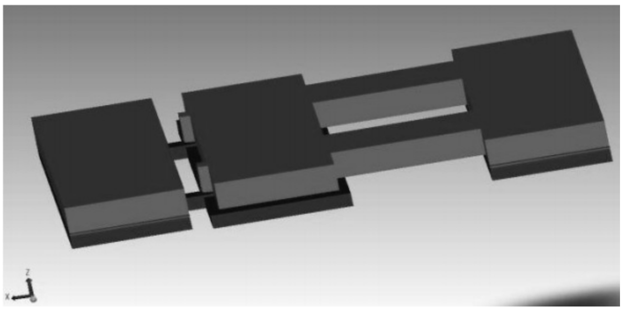

Fig. 1. The “NEU” ohmic RF MEMS Switch.

Initially, a transient analysis is performed under step pulse implementation with 83V amplitude, width p_w=48μs, rise time t_r=1μs and fall time t_f=1μs. The amplitude of 83V has been calculated in order to be high enough to ensure immunity to switch parameters uncertainty due to the tolerances of the fabrication process, and low enough to ensure plenty of room for RF signal.

The switching time obtained under the above pulse conditions was some 1.7μs for the OFF-ON transition and around 1.4μs for the OFF-ON transition, as shown in Fig. 2, the fastest ON and OFF switching time that can be achieved.

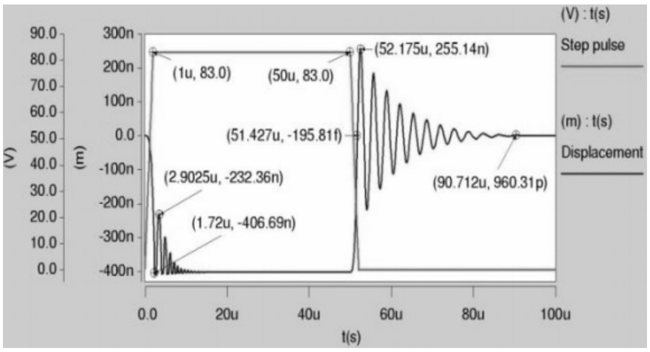

Fig. 2. Displacement under step pulse control mode.

The same figure illustrates the bouncing problems during the pull down (max. bounce=174μm) and release (max. bounce=255μm) phases. High settling times are observed also due to the stiffness of the cantilever (k≈1000 N/m), which are some 11μs for the pull down phase and roughly 39μs for the release-phase. In Fig. 3 other characteristics of the switch under step pulse implementation are illustrated, such as the contact area (11.566pm^2), the conductance per contact area (2.53S which corresponds to a resistance of 0.394Ω) and the contact force (99.3μN). Control difficulties are illustrated also as concerns the high initial contact force (almost 496μN) due to the high impact velocity (around 65.9cm/sec). In order to introduce resistive damping, a bias resistor is necessary to be calculated. Having calculated the capacitance within the electrode area (C_{el}=30fF) and with a pulse amplitude of 83V and rise time of t_r=1μs, the bias resistance can be calculated has been extracted.

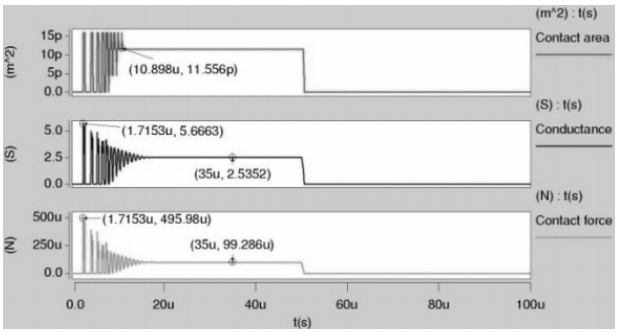

Fig. 3. Characteristics under step pulse control mode.

$$R_b\, C_{el} = t_r = 1\mu\text{m} => R_b \approx 33\text{M}\Omega \quad (1)$$

Figure 4 illustrates the characteristics of the switch under step pulse implementation with resistive damping. >

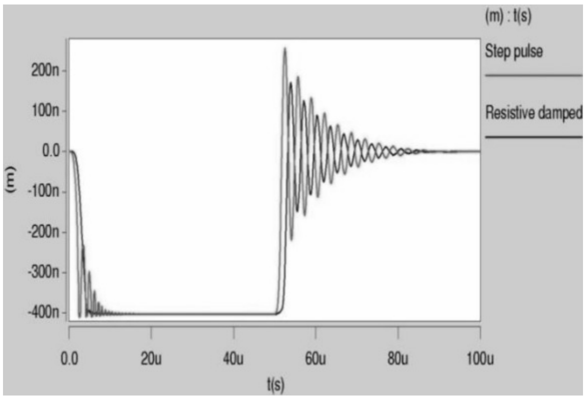

Fig. 4. Comparison between step pulse and resistive Damping modes.

The simulation results with R_b=33MΩ shown excellent response of the switch during the pull down phase as elimination of the bouncing phenomena is observed as well as dramatic reduction of the initial impact force (the high impact velocity has been reduced to 13.2 cm/sec from 65.9cm/sec), with only a small increase in the switching time (3.47μN from 1.72μN). During the release phase a significant reduction of the amplitude of bouncing is observed too (174nm instead of 255nm).

A comparison between step-pulse and step pulse with resistive damping actuation modes is presented in Fig. 5.

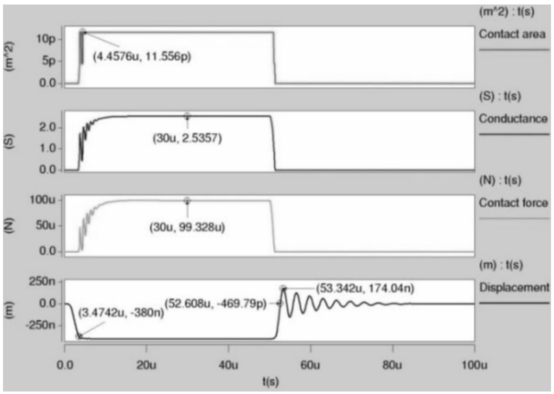

Fig. 5. Characteristics under resistive damping control.

It is obvious that the control of the switch under resistive damping excels the corresponding with the step pulse in both OFF-ON and ON-OFF transitions slightly sacrificing in the switching time. Finally, in Fig. 6, the power consumption of the switch under the previously mentioned actuation control modes is presented. It is clearly shown that under resistive control mode the switch requires much less power to be actuated.

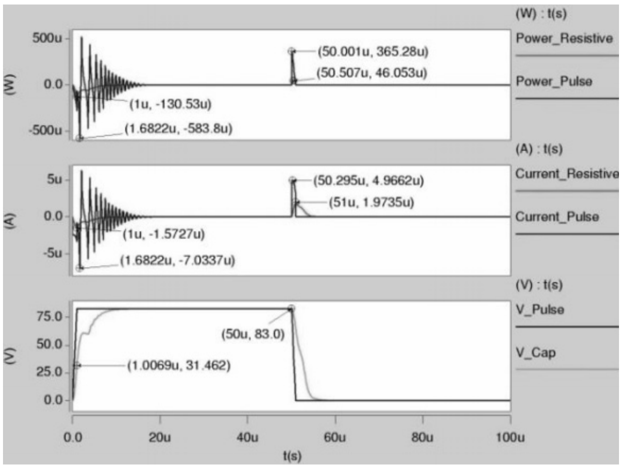

Fig. 6. Power requirements under Pulse and resistive damping modes.

References

[1] L. CASTANER, S. SENTURIA, *Speed-Energy Optimization of Electrostatic Actuators Based on Pull-In.*, IEEE, Journal of Microelectromechanical Systems, **8**, September 1999.

[2] L. CASTANER, *et al*, *Analysis of the extended operation range of electrostatic actuators by current-pulse drive.*, Elsevier, Journal of Sensors and actuators, **90**, pp. 181–190. 2001.

[3] R. NADAL-GUARDIA, *et al*, *Current Drive Methods to Extend the Range of Travel of Electrostatic Microactuators Beyond the Voltage Pull-In Point*, Journal of Microelectromechanical Systems, **11**, 2002.

[4] V. JIMENEZ, *et al*, *Transient dynamics of a MEMS variable capacitor driven with a Dickson charge pump*, Elsevier, Journal of Sensors and Actuators, pp. 89–97, 2006.

[5] J. PONS-NIN, *et al*, *Voltage and Pull-In Time in Current Drive of Electrostatic Actuators*, IEEE, Journal of Microelectromechanical Systems, **11**, 2002.

[6] J. LEE, και C. GOLDSMITH, *Numerical simulations of novel constant-charge biasing method for capacitive RF MEMS switch*, San Francisco, CA, In Proceedings of NanoTech Conference, pp. 396–399, 2003.

[7] J. BLECKE, *et al*, *A Simple Learning Control to Eliminate RF-MEMS Switch Bounce*, IEEE, Journal of Microelectromechanical Systems, **18**, 2009.

[8] Z. GUO, N. McGRUER and ADAMS, *Modeling, simulation and measurement of the dynamic performance of an ohmic contact, electrostatically actuated RF-MEMS switch, Journal of micromechanics and microengineering*, IOP Publishing, pp. 1899–1909, 2007.

[9] M. VAREHEST, *et al*, *Resistive Damping of Pulse-Sensed Capacitive Position Sensors*, Transducers, international Conference on Solid-state Sensors and Actuators, IEEE, Chicago, June 16-19, 1997.

Millimeter Wave CRLH CPW Band-Pass Filter on Silicon and Ceramic Substrate

Gheorghe SAJIN[1], Florea CRACIUNOIU[1], Alina-Cristina BUNEA[1], Andrei A. MULLER[1], Adrian DINESCU[1], Marian ZAMFIRESCU[2], Razvan DABU[2]

[1]National Institute for Research and Development in Microtechnologies, IMT Bucharest, Str. Erou Iancu Nicolae 126A, 077190 Bucharest, Romania
Phone: +40-21-269 0775

[2]National Institute for Laser, Plasma and Radiation Physics
Atomistilor 409, PO Box MG-36, 077125 Magurele, Bucharest, Romania
Phone: +40-21-457 5066

Abstract. This work deals with the development of a Composite Right / Left Handed (CRLH) band-pass filter (BPF) structure in the millimeter-wave range, working at 40 GHz. The design consists of CRLH artificial lines in a coplanar waveguide configuration (CPW) exhibiting metamaterial properties. Two substrates were used for the fabrication of the BPF structure. The device was firstly processed on a 0.5 mm thick silicon substrate with a 2000 Å Au / 500 Å Cr metallization layer. The silicon substrate offers the possibility of future integration in complex mm-wave circuits. The second substrate used was a super-aluminous ceramic substrate of 0.6 mm thickness. A first layer of 800 Å Ti was deposited, followed by a 4000 Å Au layer. The structures were measured and the results analyzed.

1. Introduction

The Composite Right/Left Handed (CRLH) transmission line is an artificial transmission line with metamaterial behavior, made up of series connected capacitances and parallel short ended inductances.

Taking advantage of the dual frequency response of CRLH structures, cf. [1], various types of devices, operating in the microwave frequency range have been developed, on copper plated substrates. Chebyshev band-pass and band-stop filters [2], filters with a dual-band filtering behavior at two arbitrary frequencies [3], dual-band-pass coplanar waveguide configuration filters [4], filters using capacitive-coupled or split ring resonators [5]-[7] and a lot of other constructions were reported.

This paper describes the design (done in IE3D-Zeland), fabrication and measurement of a millimeter wave (MMW) BPF structure.

The device was designed as a CRLH structure in CPW configuration, using series interdigital capacitors and short ended transmission lines as inductors.

Two substrates were used in the manufacturing process: a silicon substrate with a dielectric constant $\varepsilon_{r,Si}$ = 11.9 and a resistivity ρ = 5 kΩ.cm with a 1μm SiO_2 layer grown through thermal oxidation (ε_{r,SiO_2} =4.7) and a super-aluminous ceramic substrate with a dielectric constant $\varepsilon_{r,ceramic}$ = 9.6.

2. Overview

The layout of the CPW CRLH elementary cell used in this design is shown in Fig. 1. The cell is composed of two series connected interdigitated capacitors and a ground connected CPW line as inductor.

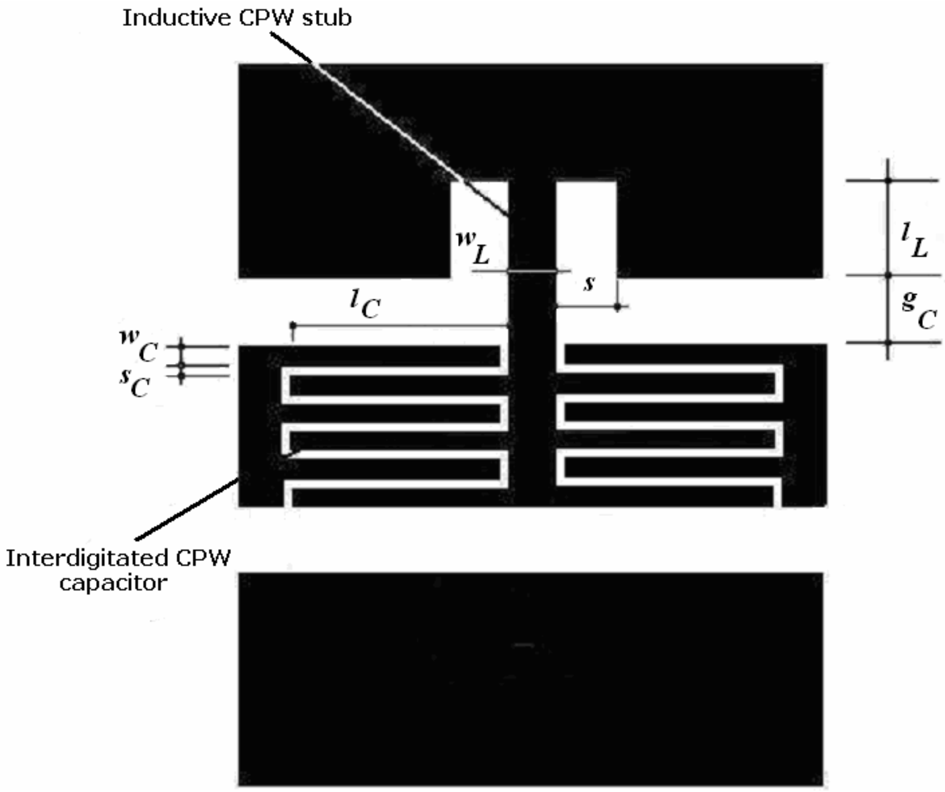

Fig. 1. Layout of the CPW CRLH elementary cell.

The equivalent circuit of the CRLH cell is given in Fig.2 where $2C_{Cs}$, $L_{Cs}/2$, and $2C_{Cp}$ are the capacitance, inductance and the equivalent parasitic capacitance of the interdigitated capacitor, respectively. The equivalent inductance and parasitic capacitance of the inductive grounded line are L_{Lp} and C_{Lp}, respectively.

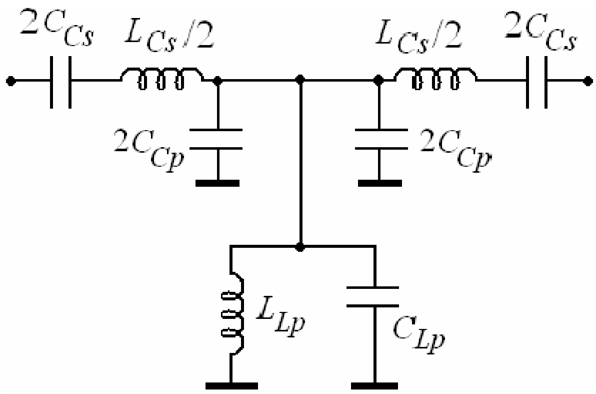

Fig. 2. CRLH cell equivalent circuit consisting of the series interdigitated capacitor and of the ground connected inductor.

The two capacitors and the inductive line were designed (cf. [8]) with the purpose of obtaining a series resonance frequency, given by C_{Cs} and L_{Cs} equal to the parallel resonance frequency, given by L_{Lp}, C_{Lp} and C_{Cp}, therefore attaining a balanced structure. The relations for this design are:

$$C_{Cs} = \frac{k}{4\pi\, f_0\, Z_c} \tag{1a}$$

$$L_{Lp} = \frac{k\, Z_c}{4\pi\, f_0} \tag{1b}$$

$$C_p = \frac{1}{\pi\, f_c\, RH\, Z_c} = C_{Lp} + 4C_{Cp} \tag{1c}$$

The values of C_{Lp} and L_{Cs} were computed for the CRLH structure to be balanced at the frequency f_0 with the formula:

$$L_{Cs}\, C_{Cs} = L_{Lp}\, C_p = \frac{1}{(2\pi\, f_0)^2} \tag{2}$$

It should be remembered that $f_{C_{LH}} = \dfrac{1}{4\pi\sqrt{L_{Lp} C_{Cs}}}$ is the cut-off frequency of the LH (Left-Handed) mode and $f_{C_{RH}} = \dfrac{1}{\pi\sqrt{L_{Cs} C_p}}$ is the cut-off frequency of the RH (Right-Handed) mode. The introduction of a parameter k > 1 is useful in the design process, in such a way that:

$$f_0 = \sqrt{f_{cLH} \cdot f_{cRH}} = k \cdot f_{cLH} = \frac{f_{cRH}}{k} \tag{3}$$

The minimum and maximum frequencies related to the CRLH frequency bandwidth may be computed as

$$f_{\min} = \frac{f_{cRH}}{2}\left[\sqrt{1+\frac{4f_{cLH}}{f_{cRH}}}-1\right] \tag{4a}$$

and

$$f_{\min} = \frac{f_{cRH}}{2}\left[\sqrt{1+\frac{4f_{cLH}}{f_{cRH}}}+1\right] \tag{4b}$$

respectively.

Taking into account the substrate thickness, the upper frequency limit was imposed to f_{max} = 75 GHz. Also, the lower frequency limit was imposed to f_{min} = 20 GHz. Using the previous relations, f_{cLH} = 30 GHz, f_{cRH} = 52 GHz, $f_0 \approx$ 40 GHz and k ≈ 1,3 were computed.

The parallel resonant circuit formed by L_{Lp} and C_{Lp} was modeled with an inductive CPW ground connected line with the characteristic line impedance Zcl ≈ 25 Ω. Computing for Zc = 50 Ω, the following values were obtained: $2C_{Cs} \approx$ 106 fF, LCs ≈ 0,3nH, CCp ≈ 25 fF, $L_{Lp} \approx$ 0,13 nH, $C_{Lp} \approx$ 20 fF. The resonance of the inductance is: $f_{0_L} = \dfrac{1}{2\pi\sqrt{L_{Lp} C_{Lp}}} \cong 97 GHz$ (the electrical length at this frequency is 90^0).

The CRLH cell layout was designed such as the length of the interdigitated capacitor be much smaller than the wavelength corresponding to f_0: Lc << 2000 μm (see Fig. 1). The value $2C_{Cs}$ = 106 fF was obtained for the following geometrical dimensions: w_C = 10 μm, s_C = 5 μm, L_C = 250 μm and number of digits equal to 10. For the inductive ground connected line the values obtained were: L_L = 277 μm, w_L = 42 μm and s_L = 10 μm.

The BPF structure consists of one, two or four series connected CRLH cells. The simulation results for a BPF structure with one CRLH cell having the above computed dimensions are presented in Fig. 3.

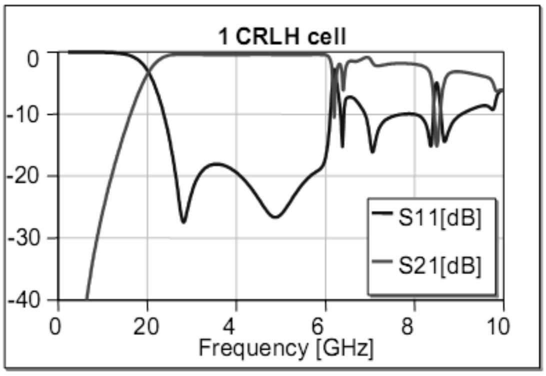

Fig. 3. S_{11} and S_{21} of BPF. Simulated values for one CRLH cell structure on high resistivity silicon substrate.

The maximum frequency obtained by simulation (60 GHz) – see Fig. 3 – is lower then the initially imposed one (75 GHz) due to the influence of the substrate thickness on the maximum working frequency of the circuits.

3 Experimental Results and Comments

A. BPF structures processed on a silicon substrate

The BPF structures were fabricated using standard photolithography. A silicon wafer with 500 μm thickness and 5 kΩcm resistivity was used as substrate. A 1 μm thick SiO_2 surface layer was grown on the silicon wafer. The Si wafer was plated through a sputtering process with a metallic layer of 2000 Å Au / 500 Å Cr.

In Fig. 4 (a) and (b) photos are presented showing the results of the photolithographic process on silicon. Fig. 4 (a) shows band pass filter structures with one, two and four CRLH cells. Fig. 4 (b) presents a detail of the interdigitated capacitor (Scanning Electron Microscopy – SEM – image). Very good line definitions were obtained, with almost no rounding at the corners.

a)
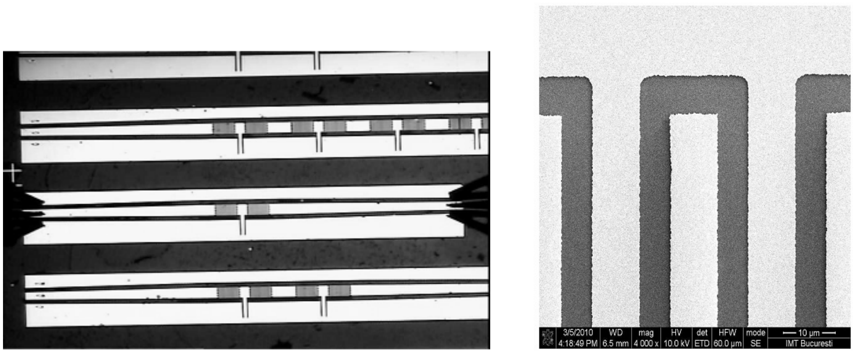
b)

Fig. 4. BPF structures on silicon (a) and a detail of an interdigitated capacitor (b).

The electrical measurements on the BPF obtained through photolithography were done with a ANRITSU 37397D Vector Network Analyzer (VNA) with a 110 GHz maximum working frequency combined with a Karl Süss on-wafer characterization equipment. A BPF structure supporting the probe-tips of the on wafer measuring system is shown in Fig.4 (a). The S parameter measurement of a one-cell CRLH BPF structure processed on silicon is given in Fig. 5.

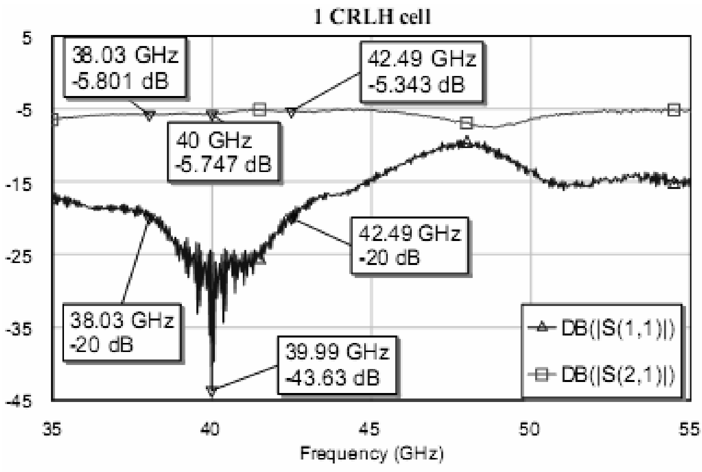

Fig. 5. S11 and S21 parameters of a one CRLH cell BPF structure on silicon.

For one CRLH cell, the S parameter distribution for a frequency scan between 35 GHz and 55 GHz shows a value S11 < -20 dB in the frequency range 38 GHz ÷ 42.5 GHz with the maximum value of -43.63 dB at 39.99 GHz. The losses in the same frequency range are about 5-6 dB. The frequency band is 4.5 GHz (for S11 < -20dB).

B. *BPF structures processed on a super-aluminous ceramic substrate*

The same structure was processed on a super-aluminous substrate (AlSiMag 614 made by American Lava Corp.) with a dielectric constant $\varepsilon_{r,ceramic}$ 9.6 = and a thickness of 0.6 mm. The resistivity can be considered infinite. The process used was the same standard photolithographic process consisting of a one mask exposure / wet etching technique.

A optical microscopy photo is presented in Fig. 6, showing a one CRLH cell BPF structure on ceramic substrate. The interdigital capacitor and the inductive grounded CPW line are visible.

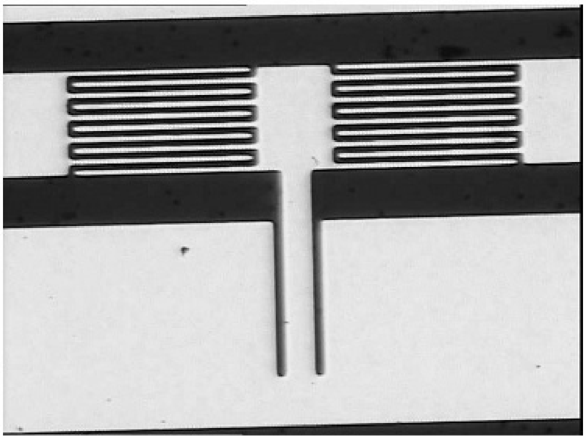

Fig. 6. A processed BPF structure on ceramic substrate.

The technological results were not as accurate as was the case for silicon, with a over-etching effect visible in Fig.7. This in turn influenced the values of the capacitance and hence the working frequency of the BPF. The poor results in maintaining the geometrical sizes of the structure processed on ceramic substrate were determined by an imperfect exposure process, due to the slightly curved shape of the ceramic surface.

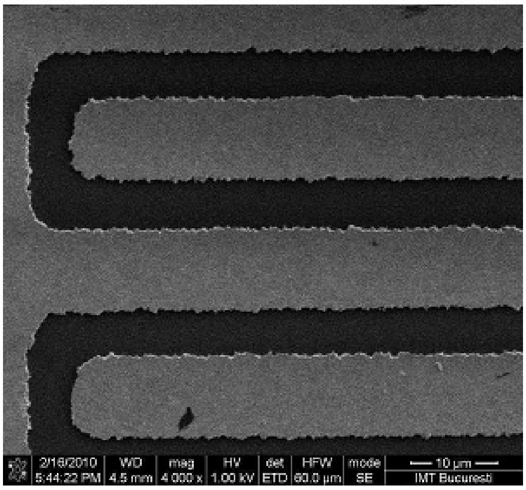

Fig. 7. SEM image of a BPF structure on ceramic substrate: a detail of an interdigitated capacitor.

The measurement of the S parameters was done with the same setup as for the structures on silicon. The results for a one CRLH cell BPF are given in Fig. 8.

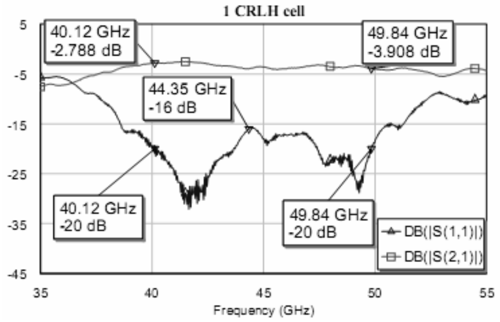

Fig. 8. S parameters of a BPF structure with one CRLH cell on ceramic substrate.

S11 shows a good matching, with values better then -16 dB for a frequency band between 40.12 GHz ÷ 49.84 GHz. The losses are very low in this frequency band with S21 between -2.8 dB ÷ -3.9 dB. This decrease of the losses, in comparison to the silicon case, can be attributed to the practically infinite resistivity of the ceramic substrate. The passband is almost double (9.72 GHz) compared to the structures processed on the silicon substrate.

4. Conclusions

A MMW BPF structure, designed with CRLH-TLs, in CPW configuration is described in this paper. The structure was processed on two different substrates: silicon and alumina ceramic. While the silicon substrate can be easily integrated in more complex millimeter wave circuits, the ceramic substrate showed a much larger frequency band and reduced losses.

Measurements of the BPF structure consisting of one CRLH cell on silicon revealed a 40 GHz working frequency with a 4.5 GHz band. The frequency band for the structures processed on a ceramic substrate was almost 10 GHz. The high losses in the silicon case can be explained due to the low resistivity substrate.

The frequency shift observed for the ceramic substrate is caused mainly by the altered capacitance value due to the over-etching effect.

References

[1] C. CALOZ, T. ITOH, *Electromagnetic metamaterials: Transmission line theory and microwave applications*, John Wiley & Sons, Cap. 5, 2006.

[2] C. LIU, W. MENZEL, *On the Relation between Composite Right-/Left-Handed Transmission Lines and Chebyshev Filters*, International Journal of Microwave Science and Technology, Volume 2009, Article ID 184895, DOI:10.1155/2009/184895.

[3] Oscar GARCÍA-PÉREZ, Javier HERRAIZ, Vicente GONZÁLEZ-POSADAS, Daniel SEGOVIA-VARGAS, *Design of a dual-band active filter using CRLH structures*, 19th International Conference on Applied Electromagnetics and Communications, Dubrovnik, September 2007.

[4] Mao SHAU-GANG, Chuen YU-ZHI, Wu MIN-SOU, *Asymmetric dual-passband coplanar waveguide filters using periodic composite right/left-handed and quarter-wavelength stubs*, IEEE Microwave and Wireless Components Letters, **17**(6), pp. 418–420, ISSN 1531-1309.

[5] C. LI, K.-Y. LIU, F. LI, *Composite right/left-handed coplanar waveguide band-pass filter using capacitively-coupled zeroth-order resonators*, Appl. Phys. A **87**, 317–319, 2007.

[6] Yuanyuan SUN, Yewen ZHANG, Fuqiang LIU, Li HE, Hongqiang LI, Hong CHEN, *A novel filter based on zeroth-order resonance by means of CRLH transmission line*, Microwave and Optical Technology Letters, **49**(5), pp. 1015–1018.

[7] M. GIL, J. BONACHE, J. SELGA, J. GARCIA-GARCIA, F. MARTIN, *High-pass Filters Implemented by Composite Right/Left Handed (CRLH) Transmission Lines Based on Complementary Split Rings Resonators (CSRRs)*, PIERS online, **3**(3), 2007.

[8] S. SIMION, G. SAJIN, R. MARCELLI, F. CRACIUNOIU, G. BARTOLUCCI, *Microwave Directional Coupler with CRLH cells on Silicon Substrate*", Proceedings of the 50th International Symposium "Electronics in Marine" ELMAR, pp. 195–198, Zadar, Croatia, 10–13 Sept. 2008, ISSN 1334-2630; ISBN 978-953-7044-06-0.

Tapered Walls Via Holes Manufactured Using DRIE Variable Isotropy Process

D. VASILACHE, S. RONCHIN, S. COLPO, B. MARGESIN, F. GIACOMOZZI, S. GENNARO

FBK-irst, via Sommarive 18 - 38123 Trento, Italy;
Tel.: +39 0461 914677

Abstract. This paper describes a method to manufacture through wafer via holes with tapered walls for RF applications. The main purpose was the need to obtain via holes with tapered walls that allow depositing seed and barrier layers by Physical Vapor Deposition (PVD) to enable gold electroplating. Method consists in consecutively using of the two basic process types for DRIE technique: isotropic and anisotropic etchings. Thus via holes with 20µm and 100µm diameter having tapered walls with angles between 14° and 18° were manufactured. Thin metal layers were also deposited on the walls by e-beam technique.

1. Introduction

Through wafer via holes manufacturing can be done using different techniques, but Deep Reactive Ion Etching (DRIE) showed its superiority to all other techniques, mainly in respect of pattern transfer accuracy, minimum achievable dimensions and aspect ratio, side effects or wall roughness [1].

The commonly used materials for via holes filling are copper or heavily doped polisilicon, due to their deposition properties [2, 3]. Our aim was to develop this connection type using gold, avoiding in this way problems regarding the resistivity or contamination. Less used as conductive material, method of filling via's by gold electroplating consists in using a sacrificial material as support for the seed layer on the wafer backside and electroplating starting from only one side, without a barrier layer between gold and substrate - as described in [4].

To be able to obtain a continuous seed layer (CrAu) on the walls, we manufactured tapered walls using dry etching with a variable isotropy. We developed this process in such a way to control with a very good precision the angle of the walls. Such a process could be helpful for instance in encapsulation processes, when on devices side small areas are needed, to reduce the chip size, while on the other side contact pads or wire bonding are needed.

2. Manufacturing Method

One of the most important advantages of the DRIE technique for MEMS technology comes from the possibility of using both isotropic and anisotropic etching processes. Moreover, by simply changing of plasma and process parameters (power, gas flow and pressure, substrate bias) it is possible to change the process isotropy during the same run [5-6].

The Bosch type processes, consisting in frequently alternating vertical etching and deposition of protective polymers on the side walls, provide the possibility to obtain an important anisotropy and very high etching rates and this is the main process used in case deep cavities with almost vertical walls are wanted [7]. Isotropic etching, less used, allows to obtain unique structures (mainly as complementary process to the anisotropic one) or to release movable / suspended parts in MEMS devices [6, 8-9].

The complex process developed to achieve the intended purpose, consists in mixing these two processes in the same run in order to obtain tapered walls, allowing the deposition of the seed layer using PVD methods. During manufacturing process alternatively anisotropic and isotropic etching processes are used: anisotropic etching to achieve the depth, while the isotropic etching to enlarge via's on one side in order to obtain the desired angle. Developed method consists in successive anisotropic and isotropic etching cycles, step by step reaching the depth and enlarging via.

To achieve our shape, the passivation polymers deposited on the walls by the Bosch processes have to be removed by a supplementary oxygen plasma cleaning before isotropic etching steps [5].

The main problem of this method remains the dependence of the etching rate on the aspect ratio (ARDE effect–Aspect Ratio Dependent Etching), the usual problem for the DRIE processing. The process needs to be fine tuned for every hole dimension and manufacturing in the same step of via holes with different opening size will be difficult if not impossible.

3. Experimental Results

Manufacturing process starts with thermal oxidation of the wafers, resist deposition and patterning of the via windows (circular holes with 20μm and 100μm diameter) and SiO_2 etching (by RIE) from the holes. Further, both resist and the SiO_2 layer were used as mask for the DRIE process. The tapered via hole process started with a Bosch process. Then, in order to remove the passivation layer deposited over the walls during anisotropic process, an oxygen plasma step was performed. The whole cavity so obtained was enlarged using the isotropic etching process. Without an oxygen plasma step in this process, due to the passivation deposited over the walls in the previous step, internal cavities connected by vertical channels will be obtained, like in [6]. The whole cycle of anisotropic etching /

oxygen plasma / isotropic etching was then repeated until the bottom surface of the wafer was reached. To maintain the desired dimension of the via's on the bottom side of the wafer, as it was patterned on the top side, the whole etching process was completed with an anisotropic etching step.

Three different recipes were tested for the anisotropic etching steps–the characteristics of each one are presented in table 1.

Table 1. Summary of drie anisotropic etching recipes

Recipes (anisotropie etching)	Recipe characteristics	Expected results
1. HER (High Etching Rate)	High gas flow/pressure high power; long etching time.	High etching rate (> 10 μm/min, depending of mask); high roughness due to specific Bosch process profile (scalloping)-up to 1 μm.
2. SDE (Silicon Deep Etch)	Smaller gas flow/pressure and power comparing with HER recipe; substrate bias was increased.	Smaller etching rates (-50% of HER rate) smaller roughness-400…500 nm.
3. LR (Low Roughness)	Gas flow/pressure and power grady reduced comparing with the previous recipes.	Much smaller etching rate (20…25% of HER etching rate); very smooth walls (-30nm).

Isotropic etching steps differ from the previous ones basically by the removal of the passivation gas (C4F8) from the recipe and substrate biasing.

As a first test through silicon via's (TSV) were obtained using HER recipe on 200μm thick silicon wafers (<100> oriented, high resistivity).

Results, presented in figure 1, show that holes were enlarged by about 12μm on each side of the top side, which implies an angle of about 3.8º-the angle was computed considering average tilt angle, taking into account front and bottom side via openings. Wall roughness in this case is in the range of 1μm due to the scalloping, specific to the Bosch process (figure 2.a). Measurements performed showed an etching rate of about 16,6μm/min during anisotropic etching steps (HER recipe), while for the isotropic process etching rate was about 2μm/min.

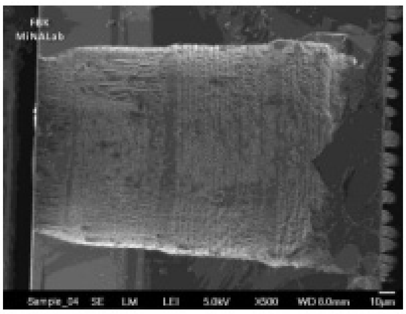

Fig. 1. TSV manufactured using HER recipe.

To reduce the corrugation it was used the procedure proposed by Shikida *et al*. [10] to smooth the asperity by wet etching- but KOH etching solution was replaced with a TMAH one - 25% at 74ºC for 10 minutes (figure 2.b).

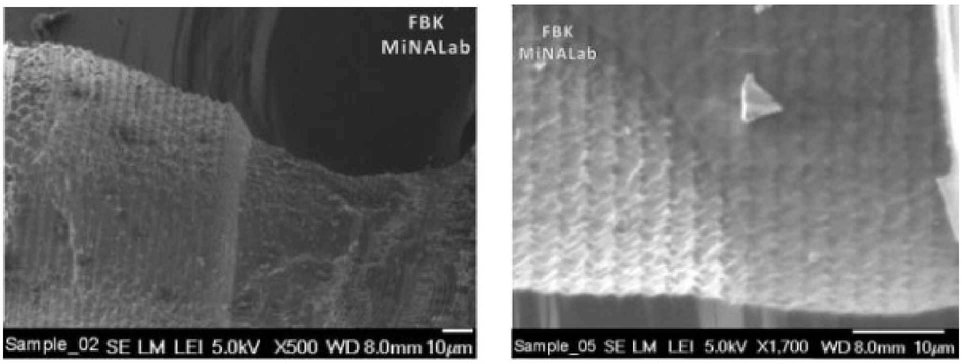

Fig. 2. Scalloping–due to the Bosch effect after via hole manufacturing (a) and after 10min selective corrugation removal in TMAH 25% (b).

Finally, Cr/Au barrier and seed layers were deposited inside the manufactured TSV's - results are presented in figure 3. As we can see, although the corrugation was reduced by wet etching, at the bottom side of the via's there are still some problems due to the walls roughness, deposited layers are not continuous also due to the small angles.

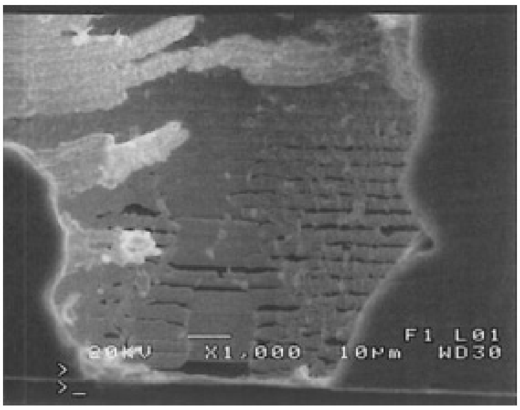

Fig. 3. Seed layer (Cr/Au, 5/150nm).

Since the etching rates strongly depend on the used mask, results obtained were used for a rough estimation of the etching rates for the next experiments with holes dimension. SDE and LR anisotropic recipes were used for tapered via manufacturing, the target being angles of about 20°. Two different hole dimensions

(20µm and 100µm) were used to reach 200microns depth on 500µm thick silicon wafers (<100> oriented wafers); process used involves five anisotropic and four isotropic etching steps for each recipe.

Figures 4-5 present the results obtained for holes with 100µm initial diameter using SDE or LR recipes for anisotropic etching. Measurements performed showed for first recipe an enlargement of the holes of about 50µm on each side for a depth of 195µm, which means an angle of about 14.4º (14.28º ÷ 14.52). For the second recipe (LR), obtained angle was of about 18º (17.74º ÷ 18.04º), but in this case the etching depth was 159µm and the lateral etching was (due to the isotropic etching) in the same range.

For the holes with the second diameter, 20µm, due to the ARDE effect all etching rates are smaller–in this case etching depths were about 128µm when SDE recipe was used, while for the LR recipe was of about 110µm.

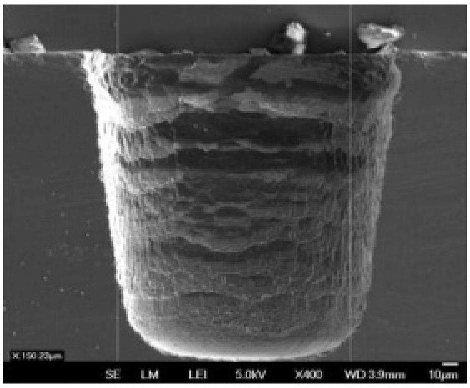

Fig. 4. Via performed using SDE recipe, 100µm diameter.

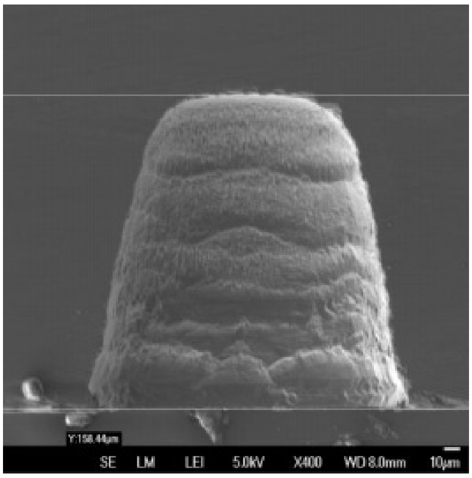

Fig. 5. Via performed using LR recipe, 100µm diameter.

In both cases isotropic etching provided an enlargement of the holes of about 30µm, so that the obtained wall angles were of about 15º for SDE recipe and 17.25º for LR recipe–figures 6 and 7.

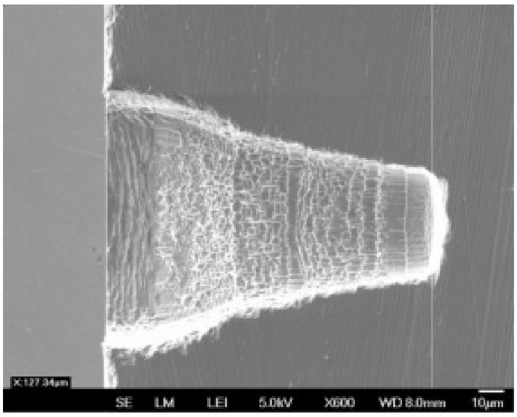

Fig. 6. Via performed using SDE recipe, 20µm diameter.

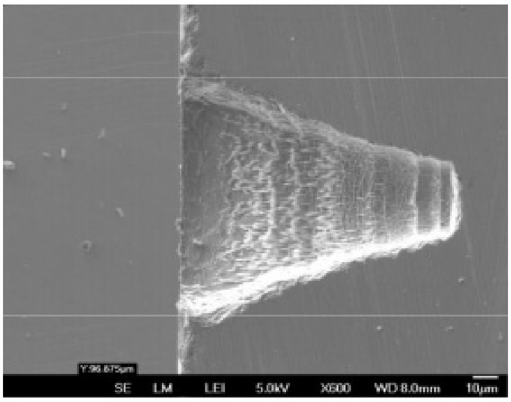

Fig. 7. Via performed using LR recipe, 20µm diameter.

Figures 4-7 show that the walls roughness was reduced–we can assume that this was not only the effect of changing the anisotropic etching recipe (LR and SDE recipes instead HER), but also due to longer isotropic etchings to obtain higher angles (having a polishing effect over the surfaces). Using low roughness recipes (LR and SDE) we can observe the appearance of nanometer peaks on the walls – more evident for 20µm diameter holes and bigger for LR recipe. One method to remove these peaks is to increase the temperature during DRIE processing [11], but this method lead to increasing the etching rate of resist layer used as mask. Finally, a small bowing effect can be seen in these cases, missing when HER recipe was used.

Structures obtained by using LR recipe were used to deposit barrier and seed layers (Cr/Au, 5/100nm) by e-beam, to verify the quality of these layers - figures 8 and 9.

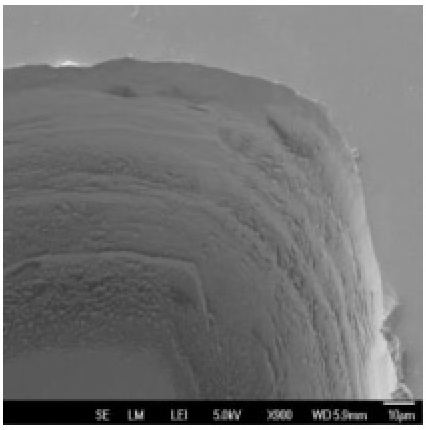

Fig. 8. 100µm diameter via, after seed layer deposition (top view).

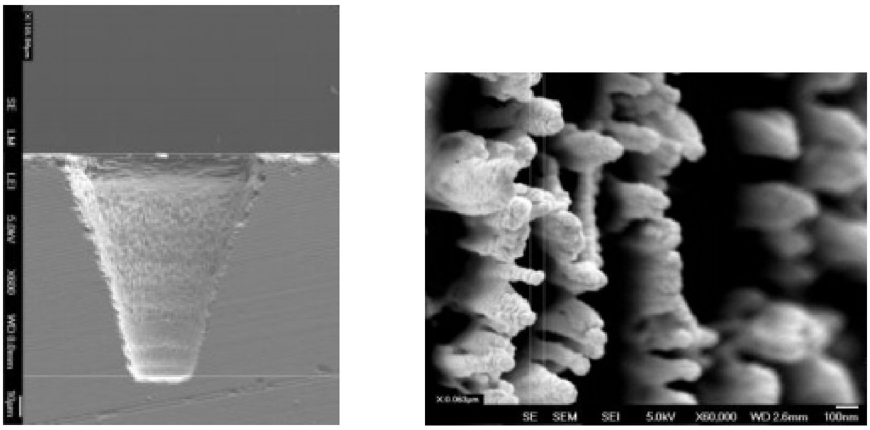

a) b)

Fig. 9. 20µm diameter via, after seed layer deposition – cross section (a) and detail of the nanometer peaks (b).

Figures 8 and 9 show that the seed layer was continuously deposited over the walls, providing better coverage than for the HER recipe (but the angle was bigger for the last two recipes).

4. Conclusion

In this paper we proved that using a variable isotropy process (based on mixing of isotropic and anisotropic etching process during the same etching run) it was possible to obtain tapered via holes with a good control over the wall angle-in this case angles obtained were between 14º and 18º. Also, after via manufacturing, it was possible to deposit a continuous seed layer which can be used for via filling by electroplating, improving the adhesion over the walls and having a barrier layer (chromium in this case).

Although the process needs to be optimized for each mask dimension and for each depth (due to the sensitivity of the etching rate with depth, decreasing sharply with depth mainly in small cavities), this technique provides an easier and reliable way to obtain tapered via's, with a very good control over the walls angles that can easily be adapted to any ICP type equipment.

Acknowledgement. The authors acknowledge the European Space Agency (MIGNON project ARTES 5.1 – 5C.091) for the support in this work.

References

[1] A. POLYAKOV, T. GROB, R.A. HOVENKAMP, H.J. KETTELARIJ, I .EIDNER, M.A. DE SAMBER, M. BARTEK, J.N. BURGHARTZ, *Comparison of Via-Fabrication Techniques for Through-Wafer Electrical Interconnect Applications*, Electronic Components and Technology Conference, p. 1466, 2004.

[2] C.S. PREMACHANDRAN, R. NAGARAJAN, C. YU, B. XIOLIN, C.S. CHOONG, *A Novel Electrically Conductive Wafer Through Hole Filled Vias Interconnect For 3D MEMS Packaging*, Electronic Components and Technology Conference, p. 627, 2003.

[3] N. LIETAER, P. STORAS, L. BREIVIK, S. MOE, *Development of cost-effective high-density through-wafer interconnects for 3D Microsystems*, J. Micromech. Microeng., **16**, pp. S29–S34, 2006.

[4] S.N. Subbarao, *et all*, *Method for Fabricating Via Holes in a Semiconductor Wafer*, US Patent (4), 348,253, Sep.7, 1982.

[5] D. VASILACHE, S. COLPO, S. RONCHIN, F. GIACOMOZZI, B. MARGESIN, *V-shape through wafer via manufactured by drie variable isotropy process*, International Semiconductor Conference (CAS), Sinaia-Romania, p. 235, 2010.

[6] F. MARTY, L. ROUSSEAU, B. SAADANY, B. MERCIER, O. FRANÇAIS, Y. MITA, T. BOUROUINA, *Advanced etching of silicon based on deep reactive ion etching for silicon high aspect ratio microstructures and three-dimensional micro-and nanostructures*, Microelectronics Journal, **36**, p. 673, 2005.

[7] B.L.P. GASSEND, L.F. VELÁSQUEZ-GARCÍA, A.I. AKINWANDE, *Design and Fabrication of DRIE-Patterned Complex Needlelike Silicon Structures*", J. MEMS **19**, p. 589, 2010.

[8] B.L.P. GASSEND, L.F. VELÁSQUEZ-GARCÍA, A.I. AKINWANDE, *Design and Fabrication of DRIE-Patterned Complex Needlelike Silicon Structures*, J. MEMS **19**, p. 589. 2010.

[9] C.-L. DAI, F.-Y. XIAO, Y.-Z. JUANG, C.-F. CHIU, *An approach to fabricating microstructures that incorporate circuits using a post-CMOS process*, J. Micromech. Microeng., **15**, p. 98, 2005.

[10] M. SHIKIDA, N. INAGAKI, H. SASAKI, H. AMAKAWA, K. FUKUZAWA, K. SATO, *The mechanism of selective corrugation removal by KOH anisotropic wet etching*, J. Micromech. Microeng., 20, 015038, 2010.

[11] R. LI, Y. LAMY,W.F.A. BESLING, F. ROOZEBOOM, P.M. SARRO, *Continuous deep reactive ion etching of tapered via holes for three-dimensional integration*, J. Micromech. Microeng., **18**, 125023, 2008.

Magneto-Mechanical Modeling and Simulation of MEMS Sensors Based on Electroactive Polymers

F.J.O. RODRIGUES, L.M. GONÇALVES, J.H. CORREIA, P.M. MENDES

University of Minho, Dept. Industrial Electronics, Guimarães, Portugal

Abstract. Mechanical oscillations have been suggested for many applications, such as: acoustic sensors and actuators, telemetric links, or energy harvesting. In common, all these applications require a readout mechanism to translate mechanical oscillations on electrical signals. PVDF (Poly(vinylidene fluoride)), is a polymer with outstanding electroactive properties, which can be used as a readout mechanism. Combined with a permanent magnet layer on a MEMS device, PVDF may provide a passive and resonant magnetic field sensor. The full system simulation becomes very challenging, since it includes three different domains: magnetic, mechanical and piezoelectric. This paper reportson the full system simulation, from an external magnetic field, till the piezoelectric response of the PVDF. From the developed methodology, it was possible to accurately predict the interaction of all the physical variables, and optimize the MEMS device, leading to better sensitivity or harvesting ability.

1. Introduction

Despite being around from more than 10 years, Microelectromechanical systems (MEMS) continues to be an exciting and challenging multidisciplinary field with tremendous progress taking place in research and commercialization. From the beginning, MEMS have been taking advantage of well-established manufacturing methods routinely used in the integrated circuit industry to develop devices capable of sensing, actuating and processing information [1]. In fact, MEMS can be classified in two major categories: sensors and actuators. As a microsensor, it consists of mechanical structures that predictably deform or respond to a specific physical (or chemical) variable.

The recent year's developments in the compatibility of the piezoelectric thin films with the IC technology are increasing the importance of this research driver in the microsystems applications [2]. Among polymers, PVDF (Poly(vinylidene fluoride)) and VDF (vinylideneflouride) copolymers, has remarkable properties leading to electro-optics, electro-mechanical and biomedical applications. The semicrystalline nature of PVDF, combined with the occurrence of at least four crystalline phases (α, β, δ and γ) implies a challenging physical microstructure [3]. The most frequently described and important phase is the βone, due to its high piezo and pyro-electric properties, when compared to theother crystalline phases, and even compared to otherpolymeric materials [4].

Combining a MEMS device with a layer of PVDF, placed at proper positions, is known as a piezoelectric readout mechanism. The changes in PVDF charge (piezoelectricity) results on detectable voltage amplitude variation, which are proportional to the magnitude of the stimulus sensed. This mechanism may be used to detect mechanical variations, though being used to sense and generate mechanical waves, as well to harvest energy from mechanical wave.

A MEMS device may also be used to detect RF electromagnetic waves based on the Lorentz force [5].

That solution requires a current flowing through the MEMS device, which encloses the challenge of routing enough current along the MEMS device, without degrading its mechanical properties. Moreover, that current will contribute for power consumption.

Instead of a current, a layer of a permanent magnet may be applied. In this way, the MEMS device has the benefit of being sensitive to magnetic fields, without the drawback of compromising the MEMS device anchors with routing lines. More extraordinary, is the fact that such MEMS device translates a magnetic field into a detectable voltage, without using any power supply. This leads to more power efficient sensors, for wireless applications, and opens the possibility to harvest energy from magnetic fields, like those produced by the many railways available in our cities. Fig. 1 shows the concept.

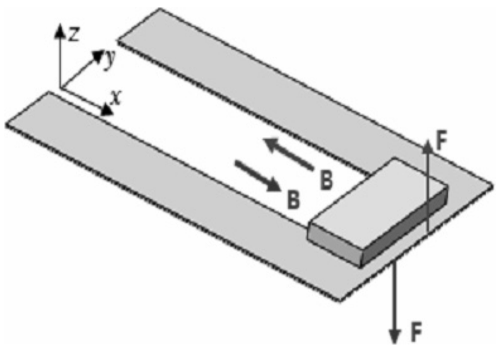

Fig. 1. RF MEMS device based on PVDF and permanent magnetic layer to detect RF magnetic fields.

It is a silicon cantilever, with a top layer of PVDF, and an area with a permanent magnet (represented by the box with applied forces). As seen in figure, the permanent magnet does not interfere with the structure mechanical behavior, if its weight is controlled.

This paper will present a methodology on how to simulate this complex three domain problem. It will show how this structure behaves and a model validation is also presented, where the simulation results are compared to measurements and good agreement is obtained.

2. MEMS Device Modeling

A. U-shaped cantilever was selected to develop this methodology since it allows, simultaneously, to study all the required physical variables and domain interactions, keeping the simulation times at acceptable levels.

Figure 2 shows the proposed MEMS simulation domain simulations may be found in Table 1.

Table 1. Material properties

	CANTILEVER	MAGNET
Material	**PVDF**	**Neodymium**
Length (x) Width (y) Thickness (z)	25 mm 18 mm 110 µm	4 mm 10 mm 1 mm
Density	$1800 \frac{Kg}{m^3}$	$7400 \frac{Kg}{m^3}$
Young's Modulus	$3 \cdot 10^9 \ \frac{N}{m^2}$	1.7×10^{10} N/m^2
Poisson Ratio	0.35	0.281
Piezoelectric strain coefficient	-28×10^{11} m/V	-
Residual magnetism	-	1.43 T
Coercive field strength	-	9.3×10^5 A/m

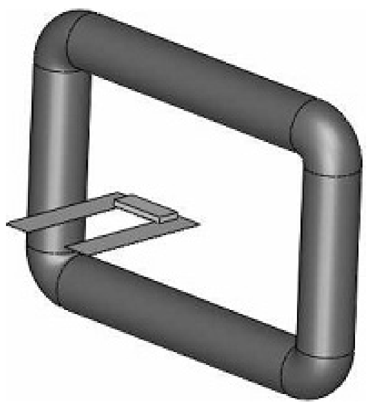

Fig. 2. MEMS device model, including the cantilever and magnetic coil to generate real magnetic field lines.

A. U-shaped cantilever description

As it is shown in Fig. 1, a force (F) acts on the cantilever when it is exposed to an external magnetic field (B). When the magnet is polarized along the z axis and the applied magnetic field vector has a component on x axis, a force (Lorentz force) will lead to a displacement in z axis. However, this MEMS structure will move only when the Lorentz force overcomes the elastic force, which means a minimum magnetic field must be applied in order to force the structure to move [5]. This "minimum" magnetic field can be reduced since the cantilevers' displacement is greater the closer are the frequencies of the external magnetic field and the eigenfrequency of the cantilever.

B. Magnetic Field Generator

Instead of assuming a specific magnetic field line distribution, a magnetic field was generated with a coil and applied to the cantilever, placed 2 mm away, as shown in the Fig. 2. The cantilever was aligned with both axis of the coil, so then it would be possible to maximize the magnetic field for the same voltage.

To mimic the measuring setup, the coil has 200 turns of copper, with 200 micrometers in diameter. It was fed by a signal generator, at the resonant frequency, with a signal of 5 V in amplitude. It was also possible to change the frequency of this signal, depending on the cant displacement.

3. MEMS Device Simulation

A. Introduction

Due to the multiplicity of simulation domains, simulations were performed using *Ansys Multiphysics*. This very powerful software allows the simulation of different environments, being the reason why is used in so many different industries and universities.

Once the simulation of this system encompasses piezoelectric, electrical, magnetical and mechanical magnitudes it comes mandatory the use of more than one single element. The adopted methodology was based on building the final result by iteratively combining the simulation in each simulation domain. That requires the use of the called "coupled-field analysis", where results moves from one domain to other through "import" features available in Ansys.

The "load transfer coupled-field analysis" was used to perform a magneto-structural analysis, in which it was given the voltage at the coil as an input and it returned the cantilever displacement as an output. So, this method is the combination of different engineering disciplines that interact to solve a global engineering problem. In this case, a magnetic simulation and a mechanical simulation (normally referred as magneto-mechanical simulation) were performed to analyse the displacement of the cantilever in function of the voltage on the coil.

As final step, the final displacement was used as an input in the piezoelectric analysis. However, the magnetic and the mechanical simulations were performed with the 3D model and piezoelectric on a 2D model.

B. Magnetic Simulation

Fig. 3 shows view of the model used for magnetic and mechanical simulation. Instead of attempting to simulate the full model, shown in Fig. 2, symmetry facilities were used to reduce the simulation domain. So, to perform the magneto-mechanical simulation it was used a halfsymmetry model, where the outer box is an air shell involving the entire model. The coil is the U shaped volume and the smaller box is another box of air containing half cantilever and half magnet inside.

The Solid97 was the element selected for the magnetic simulation. It is an eight-node 3D magnetic solid element and it is appropriate to simulate magnetic vector potential together with the VOLT degree of freedom. A 3D static magnetic analysis was performed using this element, together with different voltages at the coil.

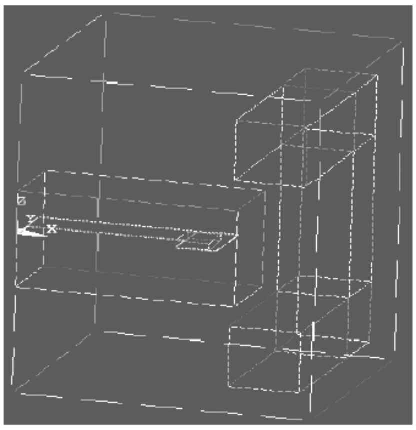

Fig. 3. Simulation model, showing all boundary lines for the simulated volumes.

After simulation, with proper coil voltages and using magnetic properties of the neodymium magnet listed on Table 1, the magnetic force at the magnet was obtained. This magnetic force on the magnet was then used as an input to the displacement simulation of the cantilever.

C. Mechanical Simulation

After the magnetic simulation, all the volumes and attached nodes representing the coil and the outer air shell are deleted and just the inner air shell, cantilever and magnet remains to the next simulation domain. Then, all the volumes are meshed with the Solid98 element (with displacement degree of freedom) and the force vector values in the database are imported and applied to the new magnet elements. Together with this, mechanical properties listed in Table 1 were used.

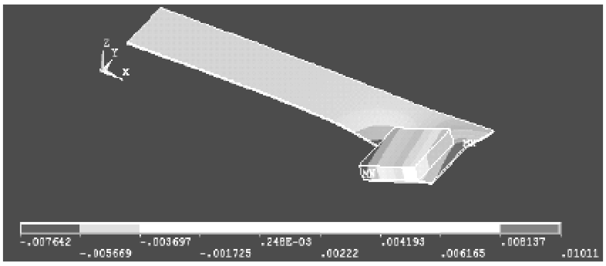

Fig. 4. Cantilever deformation, for a coil voltage of 5 V.

After performing a static simulation, the deformed cantilever is obtained, as shown in Fig. 4. From the Fig. 4 it is possible to observe that the structure deformation is not uniform. This means that proper design of this type of devices should rely on advanced simulations, rather than on simple equations modelling interaction between the different physical variables.

D. *Piezoelectric Simulation*

In order to allow the use of the cantilever as a magnetic field sensor, the PVDF performance is a key factor. Effectively, larger piezoelectric coefficients will provide higher voltages for a given deformation. In the thickness mode, piezoelectric actuators increases or decreases its thickness following the inverse piezoelectric relation:

$$\varepsilon_3 = d_{33} E_3 \tag{1}$$

where ε_3 is the strain of the actuator, d_{33} is the piezoelectric coefficient and E_3 is the applied electric field. In eq. (1), the index 3 means that only the cantilever thickness (z direction) is considered.

Theoretical calculations lead to a value of $|d_{33}| \sim 25.19$ pC.N^{-1} [6], which is closed to the experimentally obtained $|d_{33}| \sim 28$ pC.N^{-1}[7]. This experimental piezoelectric coefficient was the one used as input in the piezoelectric simulation.

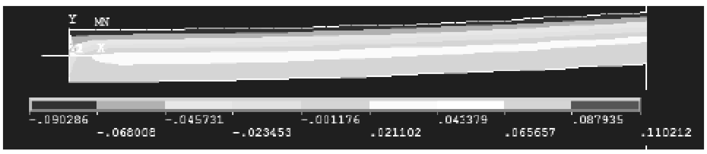

Fig. 5. PVDF voltage in the simulated cantilever beam.

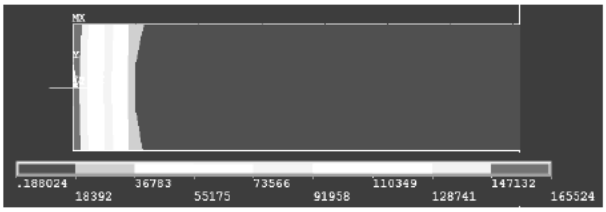

Fig. 6. PVDF electric field distribution.

The piezoelectric simulation was performed by a 2D model, using the 8 node coupled-field solid element Plane223. This element has the piezoelectric analysis capability, so that the maximum displacement was given (about 1 cm from the mechanical simulation) as an input load and it returned the voltage and electric field distribution as shown in Fig. 5 and Fig. 6.

The simulated cantilever beam was 100 µm thick and 2.5 cm long. Fig. 5 and Fig. 6 shows only one beam end, because, as it can be seen on Fig. 7, it was the region where the experimental readout was implemented. In Fig. 5, the resulting voltage amplitude (corresponding to the maximum displacement and voltage on the coil–from the mechanical and magnetic simulations) is around 90 mV, which means a 180 mV peak-to-peak signal.

4. Experimental Results

The experimental setup that was used to validate the simulated structures and models is shown on Fig. 7.

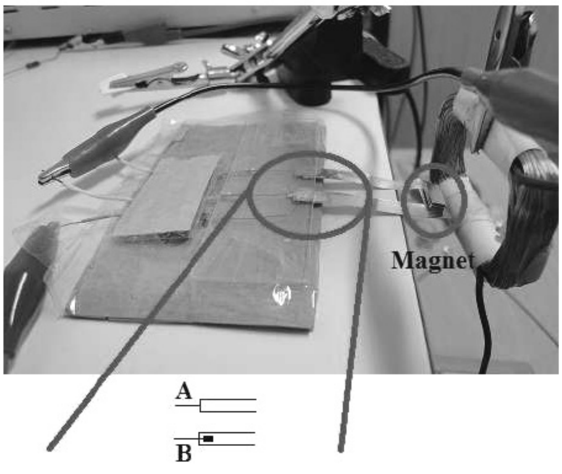

Fig. 7. Experimental setup.

The electrodes are on the base of the cantilever and they were connected to an acquisition system, and the measured result when a 5 V *ac* signal was applied on the coil is shown on Fig. 8.

The output of the cantilever was connected to an acquisition board from NI, and the signal was recorded when a voltage was applied on the coil. The measured result was a 200 mV peak-to-peak signal, which is just 20 mV more than the value from the simulation. Fig. 8 shows the circuit schematic that was used as a receiver. The electrodes (from the cantilever) that can be seen in Fig. 7 are connected to this amplifier.

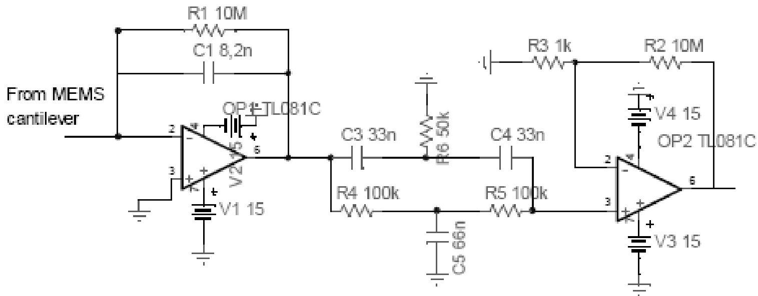

Fig. 8. Charge amplifier schematic.

It is a charge amplifier, followed by a 50 Hz notch filter and a voltage amplifier. With this circuit, it was possible to detect the signal shown in Fig. 9.

It was possible to receive a 200mV, 12 Hz signal, frequency that corresponds to the resonant frequency of this cantilever with the magnet.

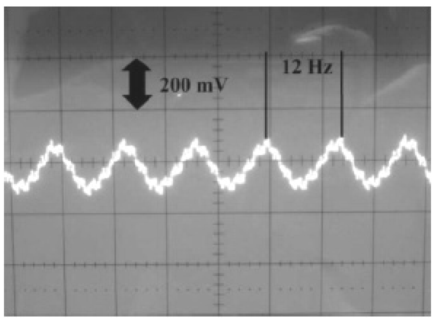

Fig. 9. Signal obtained from the vibrating cantilever, after amplification and filtering.

5. Conclusions

Despite the use of piezoelectricity, as a readout mechanism, has not been widely used so far, due to lack of piezoelectric materials integration technology.

The presented work takes advantage from the recent developments to predict its behaviour on a MEMS device. After modelling and simulation, a MEMS resonant structure was used to establish a low-frequency RF link.

The type of finite element coupled-field analysis implemented allowed to simulate the cantilever behaviour in the presence of an RF magnetic field generated by an external coil. The full model domain was simulated, from the generation of the external magnetic field till the voltage generated by the PVDF. The model is feasible and stable.

An experimental validation was performed, where good agreement between measurements and simulations was observed. However, improvement to a 3D piezoelectric, simulation is still possible, where a realistic cantilever may be simulated instead of only a beam.

Acknowledgement. This work was supported by grants from the Portuguese Foundation for Science and Technology (SFRH/BD/62608/2009) and FCT/PTDC/EEATEL/65283/ 2006 – MEMS Micro-Antennas for Wireless Biomedical Devices.

References

[1] D. POLLA and L. FRANCIS, *Processing and characterization piezoelectric materials and integration into microelectromechanical systems*, in Annual Review Materials Science, **28**, pp. 563–597, 1998.

[2] S. BEEBY, M. TUDOR and N. WHITE, *Energy harvesting vibration sources for Microsystems applications*, in Measurement Science and Technology, **17**, pp. 175–195, 2006.

[3] R. LAMEIRO, F. RODRIGUES, L. GONÇALVES, S. LANCEROS-MENDEZ, J. CORREIA, P. MENDES, *Small Antenna based on a MEMS magnetic field sensor that uses a piezoelectric polymer as translation mechanism*, in MME 2010 Abstracts: 21st Micromechanics and Micro systems Europe Workshop, University of Twente, Transducers Science and Technology, Enschede, The Netherlands, September 2010.

[4] V. SENCADAS, R. GREGORIO FILHO, S. LANCEROS-MENDEZ, *Alpha - to - beta phase transformation and microstructural changes of PVDF films induced by uniaxial stretch*, in Journal of Macromolecular Science part B- Physics, **48**, pp. 514–525, 2009.

[5] L.A. ROCHA, P.M. MENDES, *Electrically Small MEMS Antenna for Wireless Biomedical Microsystems*, Proc. 38th European Microwave Conference 2008 (EuMC), pp. 262–265, Amsterdam, 28-29 October 2008.

[6] K. TASHIRO, M. KOBAYASHI, H. TADOKORO, E. FUKADA, *Calculation of elastic and piezoelectric constants of polymer crystals by a point charge model: application to Poly(vinylidene fluoride) form I*, in Macromolecules, **13**, pp. 691–698, 1980.

[7] Y. JIANG, Y. YE, J. YU, Z. WU, W. LI, J. XU, G. XIE, *Study of thermally poled and corona charged Poly(vinylidene fluoride) films*, in Polymer Engineering & Science, **47**, 2007.

Near Millimeter-Wave Building Blocks Based on Novel Coaxial to SIW Transition

Valentin BUICULESCU, Alina CISMARU

IMT - Bucharest, Erou Iancu Nicolae no.32B, 077190 Bucharest, Romania

Abstract. The paper presents a new connection topology intended for flexible integration of substrate-integrated waveguide (SIW) components, based on a building blocks concept, due to configuration circular symmetry and possible location on both SIW wide walls. This type of connection was experimentally validated on a scaled down model made of FR-4 substrate, by using printed circuit board (PCB) technology, with a bandwidth exceeding the regular 5 GHz unlicensed telecommunications frequency range. The measured results are in excellent agreement with simulated two-port parameters. The transition can be made compatible with either surface mounted assembly or miniature coaxial connectors (SMA, K or Q-type) depending on dimension limits vs. frequency range.

1. Introduction

Many passive components have been implemented in substrate-integrated waveguide (SIW) technology, due to reduced insertion loss and radiation compared with their microstrip and coplanar transmission line counterparts, mainly in the mm-wave frequency range. Antennas, directional couplers and especially the filters and frequency diplexers can be mentioned among relevant SIW applications [1]-[5]. The specific structure of these components is based on low loss dielectric substrates, having the wide top and bottom planes covered with thin metal layers which are connected by two periodic arrays of metal plated via holes or metal posts. Due to their dielectric filling, SIW structures can be seamlessly integrated with microstrip or coplanar transmission lines (TL). However, the connection of a narrow TL to the wider SIW component has to be performed with specially designed transition geometries, in order to achieve a broadband response [5]-[8].

The coplanarity condition between input/output coupling lines and the wide upper SIW plane somehow limits the chained components relative placement inside their integration area. Moreover, all system integrated components - including the SIW structures - can not be physically separated for electrical characterization, hence their individual measurement requires either to produce and test them as independent components or to insert line gaps between any two adjacent components, and corresponding ground contacting pads too, all for vector network analyzer (VNA) coupling by using on-wafer test probes. These probes have a fixed range of discrete distance values between contacting fingers, therefore any design should be restricted to it. The gaps can be closed in a subsequent technological process, possibly expensive and hazardous.

A typical example of RF and microwave on-wafer probe family is ACP (Air Coplanar Probe) series [9], with a characteristic ground-signal-ground coplanar waveguide (CPW) configuration.

The paper presents a new approach for microwave and near-millimeter wave systems integration by utilizing a recently developed transition from miniature coaxial connectors to SIW structures [10], which can be adapted as a component connection mean, more flexible regarding the transmission line interfaces intended to form a junction, compared with presently used connection types. The proposed transition can be also tested from reliability point of view, mainly for stand-alone SIW components used in lower frequency applications.

2. The Novel Coaxial to Siw Transition

The usual coupling structures to a SIW component (Fig. 1) consist of folded extension slots for coplanar lines [5]-[6] and tapered (linear or stepped) transitions in case of microstrip lines [6]-[8].

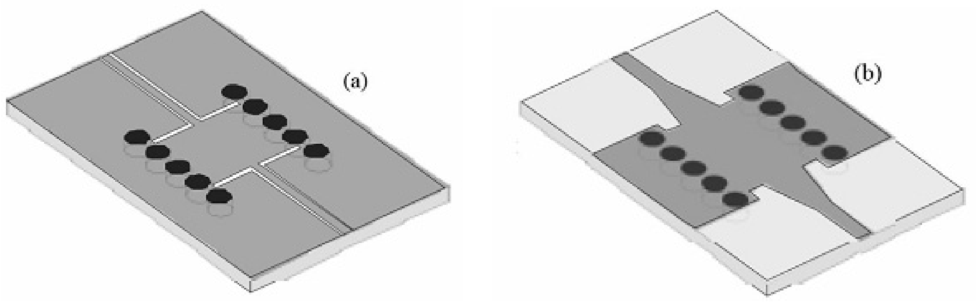

Fig. 1. Example of SIW transitions to coplanar line (a) and to microstrip line (b)

The distinctive element defining the novelty of coaxial to SIW transition is the probe coupling structure placed inside the SIW area, at certain offset from the longitudinal guide axis (PBO) and distance (PBD) from the end-of-guide shorting wall (Fig. 2).

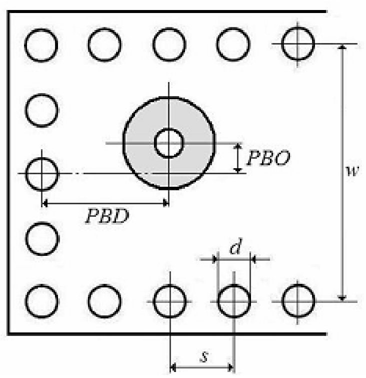

Fig. 2. The offset probe used for coaxial-to-SIW transition (bottom view).

The probe configuration, with minimum two metal plated cylindrical coaxial sections, usually having different diameters, is presented in Fig. 3. One probe end - detail (1) in Fig. 3, surrounded by an annular copperless area - detail (2) in Fig. 3, identifies the signal transfer „top" plane port. A small circular pad, electrically connected to each „top" probe end, has to be provided for reliable assembly. The other probe end is connected to the ground „bottom" plane, so that the microwave signal does not pass through it.

Both „top" and „bottom" definitions here are circumstantial ones, but they help us to have a reference plane for the only possible signal transfer place within a given transition. This probe design does not incorporate any other hidden or exposed element (either metal or dielectric), therefore the processing technology is maintained simple and fully compatible with all SIW components containing only metalized via holes, mainly filters and diplexers.

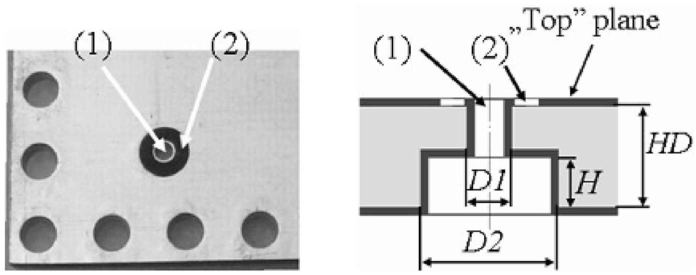

Fig. 3. Coupling probe details: "top" probe end, also connector's center insertion point (1); annular copperless area (2).

In case of an n-port SIW circuit (n ≥ 2), the „top" plane of a coupling structure can become the „bottom" plane of any other coupling structure, if the system design requires it, thus contributing to the overall assembly flexibility.

In other words, any transition may be placed upon any of two available SIW's wide walls. Additionally, due to its circular symmetry, the transition allows free angular relative positioning of two coupled circuits.

3. Building Block Concept

The coaxial-to-SIW coupling structure described above is not polarized, *i.e.* two similar transitions can be paired if their top probe ends are collinear and corresponding ground pads or areas are available, without any restriction related to the transmission line type at the other transition end.

This property permits us to imagine a spatially assembled structure (Fig. 4) composed not only by SIW „bricks" but also of other components using traditional planar transmission lines. The following conditions apply: (i) all circuits are provided with compatible transitions or probes, (ii) the connecting probes are coaxial and (iii) unobstructed mechanical contacts are required for soldering purpose.

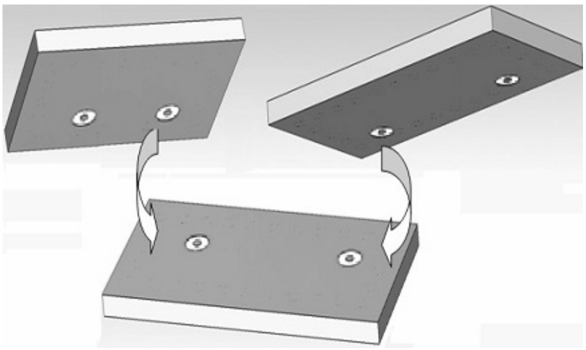

Fig. 4. Illustration of building blocks concept.

Some microwave components assembled on circuit boards having microstrip or grounded CPW signal transmission lines can be also made compatible with the new coaxial-to-SIW transition, as surface mounted devices. In this case, all microwave signal connection pads should be embedded in the bottom ground plane, similar to the coupling probe details presented in Fig. 3 for a miniature coaxial connector. The new top-to-bottom via hole has an inductive behaviour, requiring a carefully designed reactance compensation.

4. Simulation Results

Certain limits are expected regarding available working frequency bands due to dimension constraints introduced by finite diameter measure of the coaxial connectors' center conductors: 0.305 mm for K-type and 0.24 mm for V-type models. Also, some technological restrictions may occur in case of building block assembly of surface mounted components. Consequently, starting with general design rules [8], a test circuit containing a short SIW segment inserted between two coaxial to SIW transitions was proposed for analysis and optimization.

The simulation process was based on the characteristic SIW dimensions presented in Fig. 2, the target bandwidth covering full 23.5-30 GHz frequency range, so that both 24.0 to 24.25 GHz (ISM band) and approx. 26 to 30 GHz (MMDS band - USA) possible applications could benefit from the optimization results. CST Studio Suite™ [11] simulation and optimization software was used for the entire project development.

The following constant parameters were chosen for this design:

d (via diameter) = 400 μm

s (via pitch) = 1000 μm

w (distance between via rows) = 4000 μm

HD (dielectric height) = 900 μm

ε_r (relative permittivity) = 5.9 (lossy A6M Ferro dielectric material) The simulated circuit response, after optimization of PBO, PBD, D1 and D2 variables as listed below, is presented in Fig. 5.

PBO = 820 μm

PBD = 1650 μm

D1 = 300 μm

D2 = 1045 μm

H = 450 μm

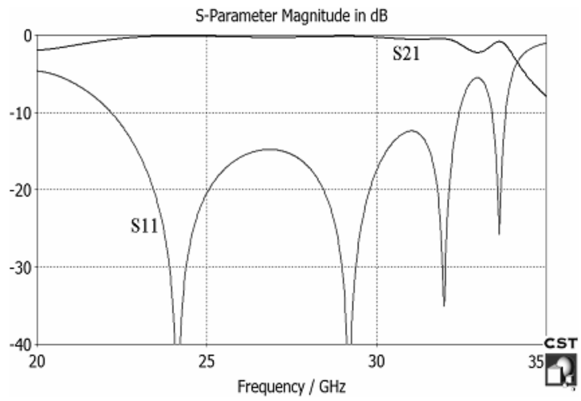

Fig. 5. Simulation results for the 26-30 GHz transition model.

The height H was considered to be half of the dielectric substrate height, although it may be changed by other optimization runs if the technological processes, like multi-layer low temperature co-fired ceramic (LTCC), tolerate to define a certain value range, usually with discrete values.

5. Experimental Results and Model Validation

The structure presented in previous section was scaled down to 5 GHz frequency band and produced of regular FR-4 material, in order to validate the proposed concept. The circuit is presented in Fig. 6, after SMA connectors assembly.

The scaled SIW dimensions are: d = 3 mm; s = 6 mm; w = 24 mm; HD = 5 mm. The corresponding results after structure optimization are PBO = 5.5 mm, PBD = 10 mm, $D2$ = 8 mm, while the probe dimension H is half of dielectric height. The external diameter of annular copperless area was decided according to 50 Ω SMA connector dielectric outer nominal diameter (about 4 mm) and D1 = 1.5 mm (it allows insertion of 1.27 mm SMA center conductor).

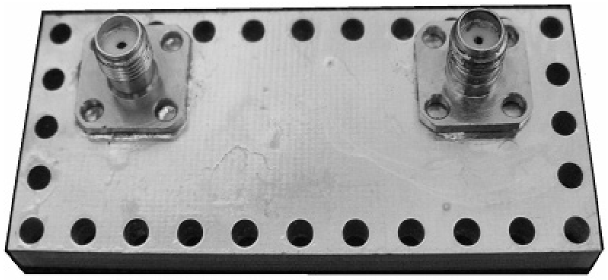

Fig. 6. The scaled test structure (5GHz band).

The measured circuit response shows an excellent agreement with simulated behavior (Fig. 7), consequently confirming the possibility to extend the use of the new transition type for flexibly structured mm-wave circuits based on SIW components.

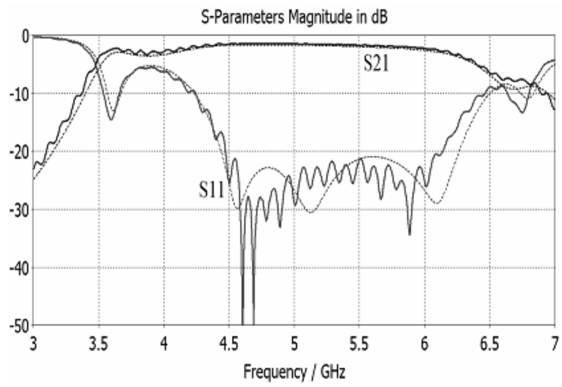

Fig. 7. S parameters of the scaled model: measured (continuous lines) and simulated values (dotted lines).

6. Conclusions

A new and flexible solution for SIW structures connection to other components, having either similar or different transmission line interfaces (coaxial line, microstrip, CPW), has been presented. The placement of these transitions is not more restricted to the top of SIW components, as it happens with present coupling sections to planar transmission lines, so that it can be located on each of wide SIW walls, depending on particular requirements. A scaled down model was produced by using PCB technology on FR-4 substrate; the measured results are in excellent agreement with circuit simulations. It is expected that the proposed solution could be also extended to surface-mounted components.

Acknowledgement. The research presented in this paper is supported by the Sectoral Programme Human Resources Development (SOP HRD), financed from the European Social Fund and by the Romanian Government under the contract number POSDRU/89/1.5/S/63700.

References

[1] D. STEPHENS, P.R. YOUNG and I.D. ROBERTSON, *W-band substrate integrated waveguide slot antenna*, Electron. Lett. **41**(4), 17th February 2005.
[2] M. HENRY, C.E. FREE, B.S. IZQUEIRDO, J. BATCHELOR and P. YOUNG, *Millimeter wave substrate integrated waveguide antennas: design and fabrication analysis*, IEEE Trans. Adv. Packag. **32**(1), pp. 93–100, February 2009.
[3] V.A. LABAY and J. BORNEMANN, *Simplified design of multilayered substrate-integrated waveguide Riblet–Saad couplers*, Microwave Opt. Technol. Lett. **52**(5), pp. 1142–1144, May 2010.
[4] H.M. HIZAN, I.C. HUNTER and A.I. ABUNJAILEH, *Integrated SIW Filter and Microstrip Antenna*, in 40th European Microwave Conf. Proc., pp. 184–187, 2010.
[5] A. ISMAIL, M.S. RAZALLI, M.A. MAHDI, R.S.A.R. ABDULLAH, N.K. NOORDIN and M.F.A. RASID, *X-Band trisection substrate-integrated waveguide quasi-elliptic filter*, Progress In Electromagnetics Research, PIER 85, pp. 133–145, 2008.
[6] Ke WU, D. DESLANDES and Y. CASSIVI, *The substrate integrated circuits - a new concept for high-frequency electronics and optoelectronics*, 6th Intl. Conf. TELSIKS, pp. 3-10, Oct. 2003.
[7] D. STEPHENS, P.R. YOUNG and I.D. ROBERTSON, *Millimeter-Wave Substrate Integrated Waveguides and Filters in Photoimageable Thick-Film Technology*, IEEE Trans. Microw. Theory Tech., **53**(12), pp. 3832–3838, December 2005.
[8] J.E. RAYAS-SANCHEZ and V. GUTIÉRREZ-AYALA, *A general EM-based design procedure for single-layer substrate integrated waveguide interconnects with microstrip transitions*, 38th European Microwave Conf. Proc., pp. 983–986, 2008.
[9] http://www.cmicro.com/products/probes/rf-microwave/ acp-probe/air-coplanar-probe
[10] V. BUICULESCU, S. COSTOVICI, A. CORNEL, *A novel coaxial connector transition to substrate-integrated waveguide components for stand-alone applications*, Accepted for presentation at PLUMEE, 30 May-1 June 2011, Limoges, France, 2011.
[11] *** CST Studio Suite TM software modules

Distributed MEMS Tunable Phase Shifters on CMOS Technology for Millimeter Wave Frequencies

Gustavo REHDER[1], Benjamin BLAMPEY[2], Trang VO[2], Philippe FERRARI[2]

[1]Laboratory of Microelectronics, University of São Paulo, CP 61548, CEP 05424-970, São Paulo, SP, Brazil
E-mail: grehder@lme.usp.br

[2]IMEP-LAHC–Grenoble University-CNRS 5130, 3 Parvis Louis Néel, BP257, 38016 Grenoble Cedex 1, France
E-mail: philippe.ferrari@ujf-grenoble.fr

Abstract. The concept of a slow-wave MEMS tunable phase shifter that can be fabricated using the CMOS back-end and an additional maskless post-process etch is presented. The tunable phase shifter concept is formed by a conventional slow-wave transmission line. The metallic ribbons that form the patterned floating shield of this type of structure are released to allow motion when a control voltage is applied, which changes the characteristic impedance and the phase velocity. For this device a quality factor greater than 32 can be maintained, resulting in a figure of merit on the order of 0.85 dB/360° and a total area smaller than 0.065 mm^2 for a 60-GHz working frequency.

1. Introduction

New applications and services using large amounts of data that tend to saturate the available frequency bands and bandwidths. Telecommunication systems with applications such as high-speed short-range wireless personal area network (WPANs), real time video streaming at rates of several Gb/s (60 GHz), automotive radars (77 GHz), and RF-imaging (frequencies from 60 GHz to more than 140 GHz) are examples [1], [2].

Traditionally, millimeter-wave (mmW) devices are based on monolithic microwave integrated circuits (MMICs), fabricated with Gallium Arsenide (GaAs) due to its higher electron mobility, higher breakdown voltage, and the availability of high quality-factor passive circuits leading to a reduced insertion loss compared to silicon. However, GaAs technology is expensive, which results in prohibitive costs for consumer applications. For several applications, a beam forming architecture will have to be used in order to increase the transmitted and received power. This is especially important for low-cost fully integrated transceivers, in which the integrated antenna has low efficiency due to the silicon substrate and due to the high absorption of the atmosphere. In such systems, tunable phase shifters are of particular interest, since they are required in networks of scanning antennas for beam forming.

The development of low cost mmW communication system depends on the ability to integrate all the passive elements in low cost CMOS technology. For tunable phase shifters it will be necessary to improve the insertion losses, reduce surface area and increase power limitations comparing the active and passive tunable phase shifters presented so far [3]-[6].

The topology of the phase shifter presented in this paper, using distributed micro-mechanical-electrical systems, could provide an answer to these three problems simultaneously.

2. Tunable Phase Shifter Principle

The tunable phase shifter is based on the slow wave coplanar waveguides (S-CPW) implemented on the classic CMOS Back-End-Of-Line (BEOL) [7], [8]. Normally, the CPW is formed by the thick metal layer (upper most) or combination of several metal layers, in order to increase metal thickness and reduce conduction losses. In these structures a shielding plane, formed by a lower metallic layer, is used to prevent the electric field from reaching the silicon substrate. The shielding plane is made of narrow ribbons that are 200 nm to 600 nm wide and typically 0.5 μm to 1 μm apart that can be connected by metallic vias to the ground plane.

In this type of structure, the capacitance per unit length (C) can be essentially controlled by the distance between the CPW and the shielding plane. By controlling C, it is possible to control the phase velocity $v_{\varphi} = 1/\sqrt{LC}$, where L is the inductance per unit length), thus the phase.

Therefore, by modifying the S-CPW with a post-CMOS maskless etch step, it is possible to remove the insulator (SiO_2) of the BEOL and free the shielding plane, rendering it mobile, as illustrated in Fig. 1. The application of a dc voltage between the CPW and the shielding plane will cause the shielding plane to move towards the CPW, due to the electrostatic force. Thus, the capacitance per unit length will increase, reducing the phase velocity. If a second set of ribbons (DC electrodes) are included underneath the shielding plane, electric voltage can be applied between this set of ribbons and the shielding plane, causing the latter to move away from the CPW, decreasing C. The DC electrodes should have the same dimensions of the ribbons of shielding plane and should be located directly underneath them to avoid blocking the magnetic field.

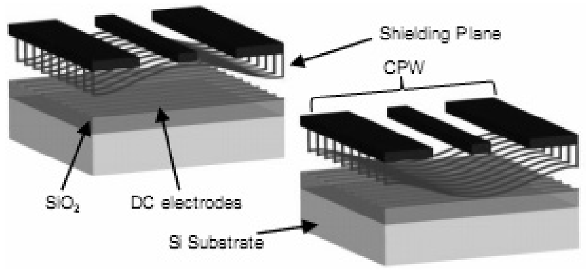

Fig. 1. Distrubuted MEMS tunable phase shifter principle.

Considering a commercial CMOS process such as AMS 0.35 µm, the top metal layer M4 can be used to form the CPW, while M3 is used for the shielding plane and M2 for the DC electrodes.

In order to obtain an improved performance of the phase shifter, the CPW dimensions were optimized using HFFS (ansoft) for a nominal (without actuation of the shielding plane) characteristic impedance of 70 Ω and a maximized quality factor. This nominal value of 70 Ω leads to the optimal condition in order to obtain a minimum Voltage Standing Wave Ratio over the whole range of phase variation.

The optimized CPW transmission line has a 15-µm wide center conductor, 12.5-µm wide ground conductors that are 55 µm away from the center conductor. Further, according to the design rules of the AMS 0.35 µm technology, the M3 metal layer (shielding plane layer) is 1 µm below the CPW (M4). The minimum feature of this technology is 0.6 µm, which is used for the width of the ribbons. The thickness of the M3 layer is also 0.6 µm. The ribbons are spaced 1 µm apart in order to maximize the quality factor. The DC electrodes are located 0.64 µm below the shieling plane.

The pull-in voltage for the ribbons of the shielding plane can be calculated using [9] that takes into account the fringing field capacitance and the induced axial stress due to the non-linear stretching. Assuming a Young's modulus and Poisson's ratio for aluminum, 70 GPa and 0.35 respectively, and no residual stress in the M3 layer, pull-in voltages between the central conductor and shielding plane and between the shielding plane and the DC electrodes were calculated to be 7.7 V and 5.7 V, respectively. This value is a first estimation for this structure, since the material properties for the AMS 0.35 µm are not know and will have to be determined for a more rigorous analysis. However, this first estimation is promising, indicating that a low voltage can be used to command the phase shifter.

3. Performance of the Phase Shifter

As indicated by [9], the shielding plane will collapse onto the central conductor and DC electrodes at approximately $0.4 \cdot d_0$, where d_0 is the initial gap. For this reason, a continuous phase shift is not possible.

Nevertheless, by connecting the ribbons in groups, it is possible to obtain several bits of phase shift. The ribbons can be connected underneath the ground strips, where they are anchored, and do not influence the quality factor of the phase shifter. Each group of ribbons can be in three distinct positions: at rest, attached to CPW (UP position) or attached to the DC electrodes (DOWN position).

In practice, each group of ribbons should not be longer than the wavelength of the RF signal divided by twenty. At 60 GHz, this leads to approximately 25 μm for the S-CPW described in this paper. Therefore, each group of ribbons should be divided into sections of 25 μm distributed along the transmission line.

Taking into account these considerations, the performance of the proposed tunable phase shifter was analyzed by 3D finite element simulations using HFSS (Ansoft). The deformation of the ribbons in the UP and DOWN position was approximated to the deformation of a fixed-fixed beam with a concentrated load at the center [10]. A thin (40 nm) SiO_2 insulator was considered over the entire structure to prevent DC short circuits. This thin insulator can be deposited after the structure is released.

Table 1 shows the performance *i.e.* quality factor (Q), characteristic impedance (Z_c) and effective relative permittivity (ε_{reff}) of the tunable phase shifter for the three distinct positions.

Table 1. Performance of tunable phase shifter

	Q factor	Zc (Ω)	ε_{reff}
UP	32.6	25.7	75.8
Rest	36.7	68.9	11.7
Down	38.8	80.3	8.8

In Table 1, it is possible to see that the quality factor is around 32 and 39 no matter the position of the shielding plane. This result was corroborated experimentally with fixed shielding planes using standard CMOS technology [2].

Further, the effective relative permittivity, ε_{reff}, varies from 75.8 to 8.8. These strong variations allow a significant phase shift with quite small changes in Z_c, because the inductance of S-CPW transmission lines is constant and does not vary with the position of the shielding plane position. The characteristic impedance varies from 25.7 Ω to 80.3 Ω. This leads to a Voltage Standing Wave Ratio lower than 2, *i.e.* a modulus of the return loss S_{11} better than 10 dB.

The quality factor of transmission lines directly affects the insertion loss of the tunable phase shifter, shown by the figure of merit (insertion loss per degree of phase) given by (1).

$$dB/^{\circ} \approx 2\pi/360 \cdot 8.69/2Q \quad (1)$$

The phase shifter presented in this paper is based on a transmission line with a figure of merit of 0.85 dB/360°.

For a beam forming application, a phase shift of 180^o is required [ref]. The length of the phase shifter required for a 180° phase shift is given by (2).

$$l = \frac{c}{2f \cdot \left(\sqrt{\varepsilon_{reff\,\max}} - \sqrt{\varepsilon_{reff\,\min}} \right)} \qquad (2)$$

Where *f* is the frequency and c is the speed of light. For a tunable phase shifter working at 60 GHz, with ε_{reff} between 75.8 and 8.8, the total length of the proposed structure would be 436 µm. These results were obtained for a 150-µm wide phase shifter, which leads to a total area smaller than 0.065 mm^2.

Today, the state of the art CPW has a quality factor of 15, for a transmission line made on SOI HR substrate with 65 nm technology [3]. If the quality factor of varactors are taken into account (lower than 6 at 60 GHz [5]), this would lead to an overall quality factor of 4.2 for the entire phase shifter. This gives a figure of merit of 6.5 dB/360°. Further, due to the low C_{max}/C_{min} of the varactors, the length of the transmission line would have to be 2λg (about 4 mm) to achieve a 360^o phase shift.

This would require a silicon area of 4 mm × 0.1 mm = 0.4 mm², considering a CPW or microstrip transmission line 100-µm wide.

As described above, the proposed tunable phase shifter shows a significant improvement in performance and consumes considerably less silicon surface. Further, no varactors are needed to achieve the required phase shift, thus the power handling limitations are considerably higher.

4. Sample Fabrication and Preliminary Results

As mentioned, a maskless etching process is used to free the shielding plane that is embedded in silicon dioxide (SiO_2) in order to allow it to move under the application of an electric field. The SiO_2 is removed from selected areas of the structure using the silicon nitride (Si3N4) passivation layer of the conventional CMOS process as mask. The SiO_2 is etched with HF vapor at ambient temperature. To avoid condensation of the HF vapor, the samples are kept at 40^{o}C, preventing the metallic layer (aluminum) to be etch away. By controlling the etching time, it is possible to free the shielding plane while maintaining the second set of ribbons attached to the SiO_2.

The maskless etching process of the oxide layer has already is been demonstrated by other teams [4] and do not pose a major problems, as seen in Figure 2. In this figure, it is possible to see several sets of ribbons that can be used to form the shielding plane. The ribbons shown here are 50 to 200-µm long and 0.6 or 2-µm wide. No deformation due intrinsic stress can be seen. Different metal levels (M4 and M3) from AMS 0.35 µm CMOS process were used to obtain the ribbons. Metallic vias are used to anchor the ribbons to a lower oxide layer that is not removed in the etching process.

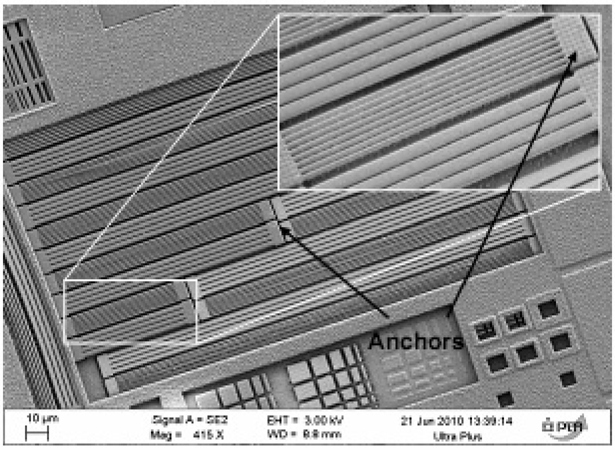

Fig. 2. Ribbons with different dimensions (50 to 200 µm × 0.6 or 2 µm) released using HF vapor.

6. Conclusion

A new concept of millimeter wave phase shifter using CMOS technology was proposed. The expected performance can consider the eventual integration of phase shifters for controlling scanning antennas, which generally represents a major technological breakthrough. The "price" to pay is a maskless post-CMOS etching step.

Acknowledgement. The authors wish to acknowledge the finatial support of the Brazilian agency of FAPESP.

References

[1] R.C. DANIELS and R.W. HEATH, *60 GHz Wireless Communications : Emerging Requirements and Design Recommendations*, IEEE Vehicular Technology Magazine, **2**(3), pp. 41–50, Sept. 2007.

[2] N. GUO, R.C. QIU, S.S. MO and K. TAKAHASHI, *60-GHz Millimetre-Wave Radio : Principle, Technology, and New Results*, EURASIP Journal on Wireless Communications and Networking, ID 68253, 2007.

[3] S. KISHIMOTO, N. ORIHASHI, Y. HAMADA, M. ITO and K. MARUHASHI, *A 60-GHz Band CMOS Phased Array Transmitter utilizing Compact Baseband Phase Shifters*, RFIC, Boston, USA, 2009.

[4] P.B. VADIVELU, P. SEN, S. SARKAR, D. DAWN, S. PINEL and J. LASKAR, *Integrated CMOS mm-wave Phase Shifters for Single Chip Portable Radar*", IMS, 7-12 June, Boston, USA, 2009.

[5] K.-J. KIM, K. H. AHN, T.H. LIM, H.C. PARK and J.-W. YU, *A 60 GHz Wideband Phased-Array LNA With Short-Stub Passive Vector Generator*, IEEE Microwave and Wireless Components Letters, **20**(11), pp. 628–630, Nov. 2010.

[6] M. PARLAK, J.F. BUCKWALTER, *A Low-Power*, W –Band IEEE MWCL, **20**(11), Nov. 2010.
[7] T.S.D. CHEUNG, *et al*., *Shielded passive devices for silicon-based monolithic microwave and millimeter-wave integrated circuits*, IEEE JSSC, **41**(5), May, pp. 1183–1200, 2006,.
[8] D. KADDOUR, *et al*., *High-Q Slow-Wave Coplanar Transmission lines on 0.35-µm CMOS Process*, IEEE MWCL, **19**(9), pp. 542–544, Sep. 2009.
[9] S. PAMIDIGHANTAM, R. PUERS, K.BAERT and H.A.C. TILMANS, *Pull-in voltage analysis of electrostatically actuated beam structures with fixed–fixed and fixed–free end conditions*, J. Micromech. Microeng., **12**(4), pp. 458–464, July 2002.
[10] R.J. ROARK and W.C. YOUNG, Formulas for Stress and Strain, New York: McGraw-Hill, 1989.
[11] C-L. DAI, *et al*., *A maskless wet etching silicon dioxide post-CMOS process and its application*, Microelectronic Engineering, **83**(11-12), pp. 2543–2550, Nov.-Dec. 2006.

Design and Modeling of Membrane Supported FBAR Filter

Alexandra STEFANESCU, Dan NECULOIU, Alina Cristina BUNEA

IMT Bucharest, 32B, Erou Iancu Nicolae str., 077190 Bucharest, Romania
Tel.: +40212690775

Abstract. This paper introduces a novel technique for the electromagnetic modeling of the Film bulk acoustic resonator (FBAR) filters. The piezoelectric equations are coupled to the Maxwell's equations through a Lorentz dispersive model. First, FEM (Finite Element Method) simulations are performed for an FBAR resonator in order to observe the resonant behaviour of the device. Then, the Lorentz model is extracted from the FEM results and is introduced in the electromagnetic (EM) design of the FBAR filter.

1. Introduction

With the development of mobile and satellite communication as well as data transmission (WLAN), film bulk acoustic resonators (FBAR) have attracted a major interest in the fabrication of radio frequency (RF) filters. These applications need small size, high quality factors and monolithic integration with active electronic devices. FBAR devices have the potential advantages to act as key components for wireless communication and sensing network systems [1], [2].

The most common wide band gap (WBG) materials are SiC, GaN and AlN, the last two with pronounced piezoelectric properties. The sub-micron thickness of the GaN or AlN membrane in FBAR devices will result in an operating frequency up to 6 GHz and above. Recently the first FBAR structures manufactured on GaN membranes have been reported [3], [4].

Most of the designs presented thus far are based on equivalent circuits - 1D Mason's model [5, 6] or distributed models based on Krimtholz, Leedom and Matthaei circuit (KLM) [7]. Since one of the main challenges in designing FBAR structures is to avoid the unwanted resonances, different numerical techniques have been used in literature, most of them based on Finite Element Method (FEM) [8, 9]. All these methods analyze the FBAR structure from the mechanical and electrical point of view. The relative high frequencies and the metallization thickness comparable with the piezoelectric membrane thickness impose the development of an advanced modeling technique.

This paper proposes a novel method for design and modeling of the FBAR filters (Fig. 1). The method consists in linking the FEM piezoelectric simulations for a simple configuration of FBAR composed of metal/piezoelectric-film/metal layers with symmetric top and bottom electrodes with the electromagnetic design of a complete three resonator band-pass filter by including a Lorentz dispersive model for the piezoelectric material in CST Microwave Studio. This method permits a complete 3D detailed modeling that also analyzes the microwave behaviour of the FBAR filter.

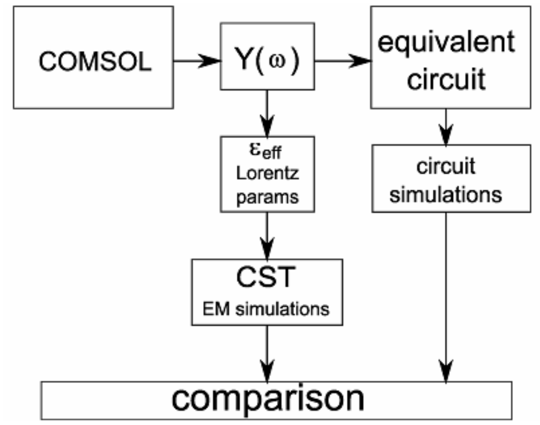

Fig. 1. Flow chart of the modeling technique.

A coupled analysis of the EM modeling with the solution of the acoustic equations for the Thin Film Bulk Acoustic Resonators has been developed by Farina and Rozzi in [10].

The paper is organized as follows. Section 2 presents the modeling of the FBAR resonators used in the filter design and Section 3 describes the electromagnetic simulation results obtained with CST Microwave Studio for the FBAR filter. Finally, we conclude and propose future paths of research in Section 4.

2. Fem Simulation

Simulations with Finite Element Method (FEM) software, COMSOL [11] were carried out to investigate the frequency response analysis for two BAW resonators. In both cases, the lowest layer is Molybdenum (50 nm thick) that operates as ground electrode. Next, the buffer layer (composed from AlGaN) is 0.3 μm thick and the GaN undoped layer has also 0.3 μm. On top of the resonator there is another Molybdenum electrode: resonator A – 50 nm thick and 100 μm wide – and resonator B – 50 nm thick and 150 μm wide. The relation between the strain, electric field and electric displacement field in a strain-charge form is given by the piezoelectric constitutive equations (1) and (2):

$$S = s_E T + d^T E \tag{1}$$

$$D = dT + \varepsilon_T E \tag{2}$$

where **S** represents the strain matrix, **T** is the stress matrix, **E** is the electric field applied to the resonator, D is the electric density displacement matrix, d, s_E, and ε_T are piezoelectric material constants. The piezoelectric strain constants, permittivity and density are taken from [12]. The model geometry (Fig. 2) is a symmetric section in the centre of the layout. For the frequency analysis the geometry was extended with perfectly matched layer (PML) domains at the membrane edges, in order to increase the length of the resonator. These layers have the property of absorbing the energy of the acoustic waves that cross the exterior boundaries of the model.

The boundary conditions are set as follows: the bottom electrode (grounded, V_0=0) is fixed, and an electric potential is applied on the top electrode (V_0=1). The rest of the boundaries are free zero charge, excepting the truncation boundaries which are fixed.

In the frequency response analysis the admittance of the resonator is estimated with (3):

$$Y(\omega)=\frac{J_{ns}}{V_0} \tag{3}$$

where J_{ns} is the current through the top electrode and ω is the angular frequency.

The geometry of resonator A is presented in Fig. 2. The insets represent the electric potential variations for the resonant and antiresonant frequencies.

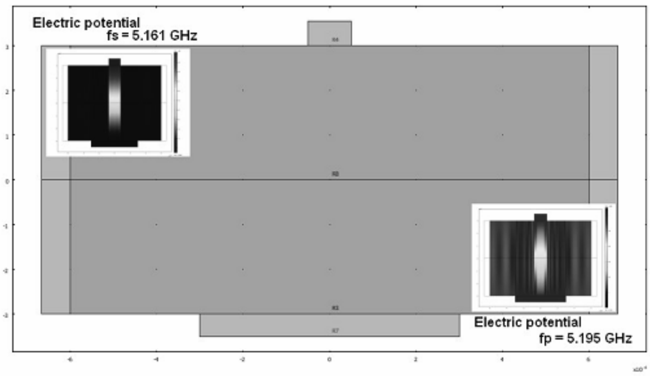

Fig. 2. FEM model for FBAR (inset – simulation results for resonator A).

Figure 3 shows the graph of the admittance as a function of frequency. For both resonators a series resonant frequency at 5.161 GHz and one parallel resonant frequency at 5.195 GHz have been obtained. As expected, an increase in the static capacitance is observed with the increase of the top electrode area.

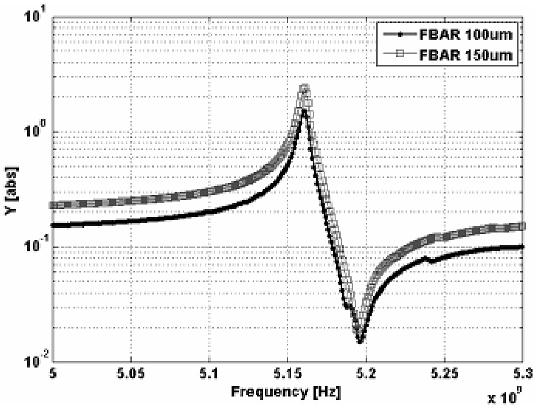

Fig. 3. Compared simulated electrical admittance versus frequency for the two FBAR structures.

The equivalent Butterworth – Van – Dyke circuit representation [1, 13] is used in the resonators modeling process (Fig. 4) in order to extract the optimum areas for the electrodes by fitting the results obtained with COMSOL:

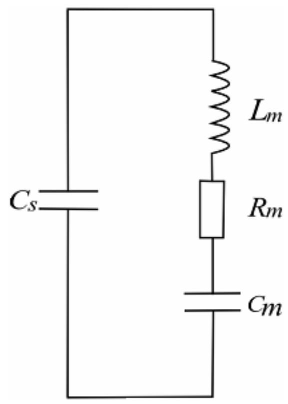

Fig. 4. Butterworth – Van – Dyke equivalent circuit of the FBAR resonator.

The circuit includes a static capacitance, C_s and a motional arm having a dynamic inductor L_m, a dynamic capacitance C_m and a dynamic loss R_m.

The values extracted from the equivalent circuit for the two resonators are depicted in Table 1.

Table 1. Characteristics of each FBAR used in designing the FBAR filter

FBAR component	FBAR A	FBAR B
Area Size [μm^2]	100 μm × 300 μm	150 μm × 300 μm
C_s [pF]	0.225	0.222
C_m [pF]	18.2	18.8
R_m [Ω]	0.5	0.48
Lm [nH]	4.136	2.152

The structure is similar to a parallel plate capacitor which allows the evaluation of the permittivity of the dielectric material, ε [12] with (4):

$$\varepsilon(\omega)=\frac{|Y(\omega)|}{\omega\frac{A}{t}}, \quad (4)$$

where A represents the electrodes area and t is the thickness of the dielectric layer (GaN).

3. Electromagnetic Simulation and Modeling

The FBAR filter has a standard pass band configuration, containing two series connected resonators (A) and a parallel one (B). The performance of the filter is dictated by the individual performances of the resonators [14].

The FBAR filter topology is represented in Fig. 5. This configuration was chosen due to the backside metallization of the membrane that has the key role of an electrode with floating potential. The access electrodes are defined on the front side.

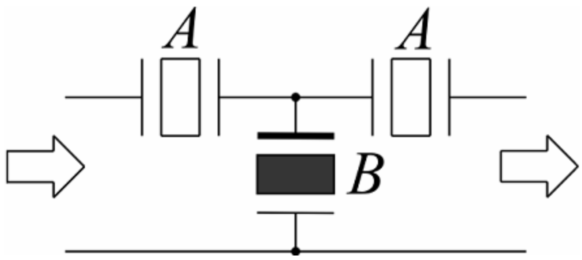

Fig. 5. FBAR Filter topology

A 3D view of the structure is shown in Fig. 6. The two lateral resonators have a width of 100 μm and a length of 300 μm, while the central one has a width of 150 μm and the same length.

The filter is fed by means of 50/100/50 μm coplanar waveguide transmission lines.

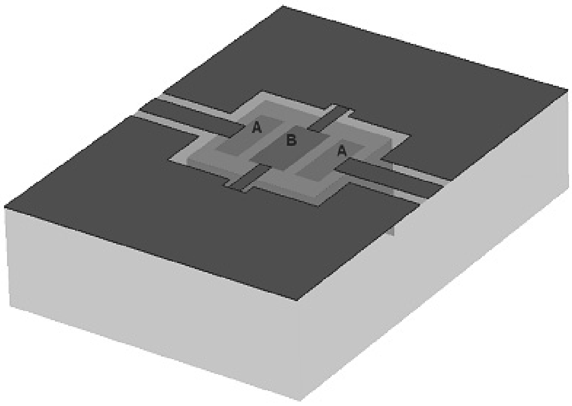

Fig. 6. EM model for FBAR.

The main dimensions of the layout are shown in Fig. 7. The inset presents a schematic cross section of the active part of the structure.

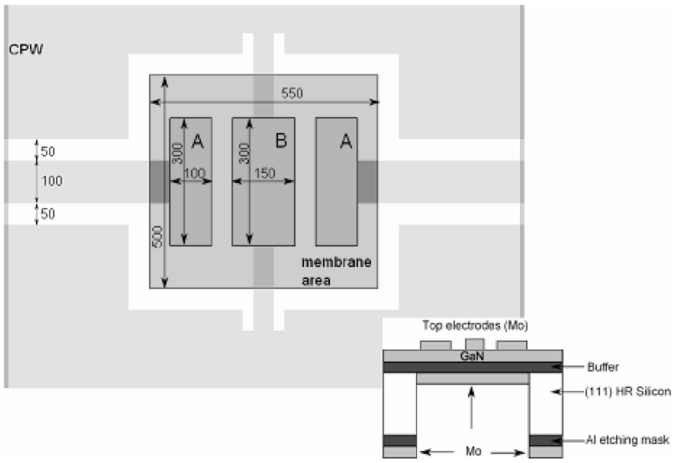

Fig. 7. Layout of the simulated structure (inset – cross section).

The above design is simulated with CST Microwave Studio (MWS) [15]. The port definition and S parameter extraction are optimized for electric field distribution (ideal for waveguide port and planar ports with multiple pins definition feature). For this structure, the Frequency Domain Solver has been used.

In order to solve the coupled piezoelectric/electromagnetic equations, we need to define a material dispersion curve for the electric permittivity so that the electrical displacement (5) used in the full-wave EM analysis

$$D = \varepsilon_T E \tag{5}$$

to comprise the piezoelectric effect. To catch the resonance behaviour of the piezoelectric material, the Lorentz model is applied for the electric permittivity (ε) obtained with (4):

$$\varepsilon_r(\omega) = \varepsilon_\infty + \frac{(\varepsilon_s - \varepsilon_\infty)\omega_0^2}{\omega_0^2 - \omega^2} \tag{5}$$

where ω_0 is the resonance frequency and ε_∞ is the relative permittivity of the Gallium Nitride material. The dielectric loss tangent (tanδ) of the piezoelectric film is not added in the model.

Figure 8 shows the real (ε') and imaginary parts (ε'') of the relative permittivity extracted for resonator A, demonstrating the material resonance at the resonance frequency (Table 2).

Table 2. Material parameters used for Lorentz model

	FBAR A	FBAR B
ε_∞	9	9
ε_s	8.66	8.66
f resonance [Hz]	5.12e9	5.23e9
f damping [Hz]	22e7	26.6e7

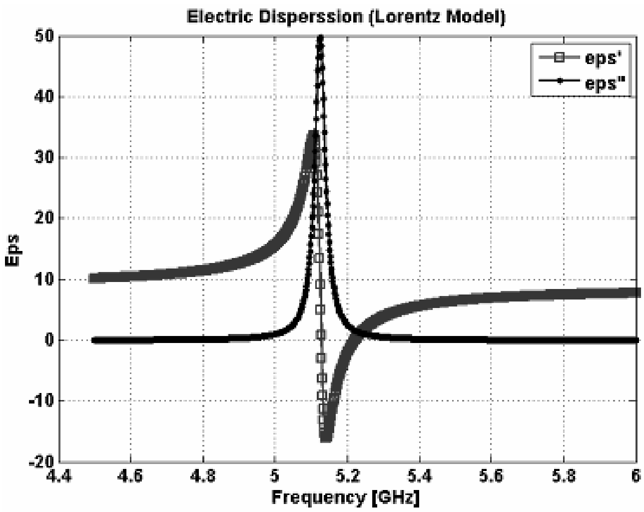

Fig. 8. Resonance behaviour of GaN extracted with Lorentz model for the electrodes type A.

The simulated transmission and reflection parameters are reported in Fig. 9. The filter is centered at 5.2 GHz.

Figure 10 shows the transmission parameter for the filter simulated with an electrical circuit software simulator.

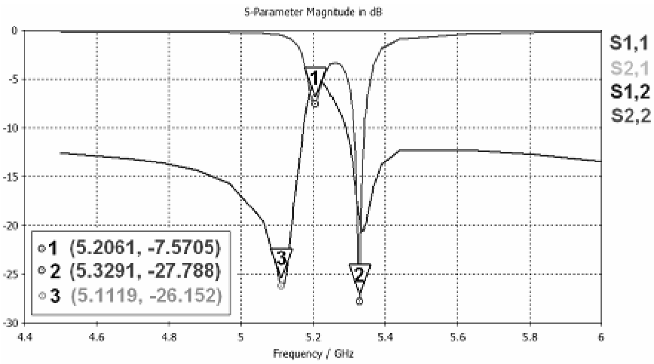

Fig. 9. FBAR filter characteristics. Transmission response S21 (dark) and reflection S11 (dashed).

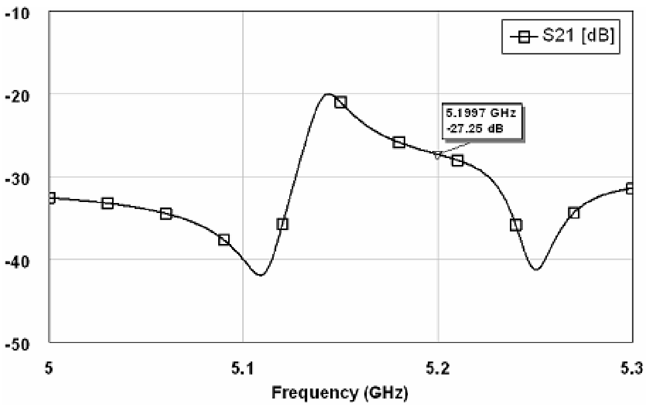

Fig. 10. Simulated transmission parameter for the FBAR filter structure.

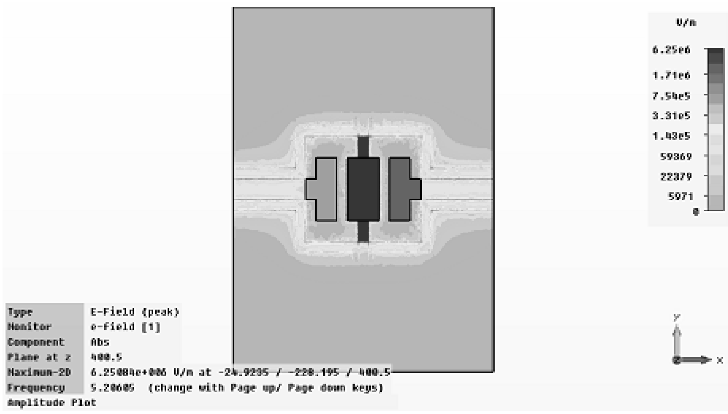

Fig. 11. Electric field distribution at 5.206 GHz.

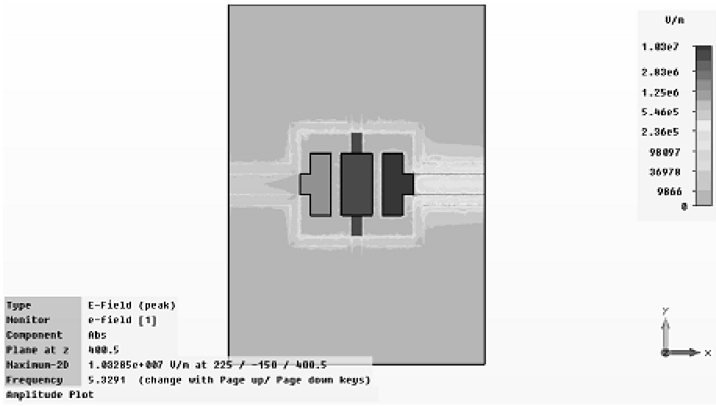

Fig. 12. Electric field distribution at 5.321 GHz.

Figures 11 and 12 show the electric field distribution in the xy plane at the frequencies marked with 1 (5.206 GHz) and 2 (5.321 GHz) in Fig. 9.

4. Conclusion

FEM and EM simulations have been carried out for the membrane supported FBAR filter. A novel modeling approach that links the piezoelectric simulation (COMSOL Multiphysics) of the device with the electromagnetic model (CST Microwave Studio) is presented. This work will be used for the design, characterization and parameter extraction of the membrane supported FBAR filter.

Acknowledgement. The author Alexandra Stefanescu acknowledges the support of the Sectoral Operational Program Human Resource Development (SOP HRD) financed from the European Social Fund and by the Romanian Government under the contract number POSDRU/89/1.5/S/63700.

References

[1] C.M. FANG, S.C. LIN, Y.C. CHIN, P.Y. CHEN, H.R. LIN, P.Z. CHANG, *5.4 GHz high-Q bandpass filter for wireless sensor network system*, Sensors, IEEE, 2009.

[2] H-W CHOI, J-Y. JUNG, S-K. LEE, Y-S. PARK, K-H. KIM, *The Designing of an Air-gap Type FBAR Filter using Leach Equivalent Model*, Transactions on Electrical and Electronic Materials, **7**(4), 2006.

[3] D. NECULOIU, G. KONSTANTINIDIS, A. MÜLLER, A. KOSTOPOULOS, D. VASILACHE, K.MUTAMBA, C. SYDLO, H. L. HARTNAGEL, L. BARY, R. PLANA, *Microwave FBAR Structures Fabricated using Micromachined GaN Membranes*, International Microwave Symposium Digest, IEEE MTT-S, pp. 877–880, 2007,.

[4] A. MÜLLER, D. NECULOIU, G. KONSTANTINIDIS, A. STAVRINIDIS, D. VASILACHE, A. CISMARU, M. DANILA, M. DRAGOMAN, G. DELIGEORGIS and K. TSAGARAKI, *6.3-GHz Film Bulk Acoustic Resonator Structures Based on a Gallium Nitride/Silicon Thin Membrane*, Electron Device Letters, IEEE, **30**(8), pp. 799–801, 2009.

[5] W. PANG, H. ZHANG, H. YU, E.S. KIM, *Analytical and Experimental Study on Second Harmonic Response of FBAR for Oscillator Applications above 2GHz*, Ultrasonics Symposium, IEEE, **4**, pp. 2136–2139, 2005.
[6] Y. ZHANG, Z. WANG, J. DAVID N. CHEEKE, *Resonant Spectrum Method to Characterize Piezoelectric Films in Composite Resonators*, IEEE Transactions on Ultrasonics, Ferroelectrics and Frequency Control, **50**(3), pp. 321–333, 2003.
[7] C. COLLADO, E. ROCAS, J. MATEU, A. PADILLA, J.M. O'CALLAGHAN, *Nonlinear Distributed Model for Bulk Acoustic Wave resonators*, IEEE Transactions on Microwave Theory and Techniques, **57**(12), 2009.
[8] H. CAMPANELLA, E. MARTINCIC, P. NOUET, A. URANGA, J. ESTEVE, *Analytical and Finite-Element Modeling of Localized-Mass Sensitivity of Thin-Film Bulk Acoustic-Wave Resonators (FBAR)*, IEEE Sensors Journal, **9**(8), pp. 892–901, 2009.
[9] J. VERDU, P. DE PACO, O MENDEZ, *Electric Equivalent Circuit for the Thickened Edge Load Solution in a Bulk Acoustic Wave Resonator*, Progress in Electromagnetic Research M, **11**, 2010.
[10] M. FARINA, T. ROZZI, *Electromagnetic Modeling of Thin Film Bulk Acoustic Resonators*, IEEE Transactions on Microwave Theory and Techniques, **25**(11), 2004.
[11] COMSOL webpage: www.comsol.com
[12] http://ioffe.ru
[13] H. CAMPANELLA, *Acoustic Wave and Electromechanical Resonators, Concept to Key Applications*, Artech House Integrated Microsystems Series, 2010.
[14] Tuomas PENSALA, *Thin Film Bulk Acoustic Wave Devices. Performance Optimization and Modeling*, VTT publication 756, phd Thesis, 2011
[15] CST webpage: www.cst.com

Characteristics of Smooth-Walled Spline-Profile Horns for Tightly Packed Feed-Array of RATAN-600 Radio Telescope

N. POPENKO[1], R. CHERNOBROVKIN[1], I. IVANCHENKO[1], C. GRANET[3], V. KHAIKIN[2]

[1]Usikov Institute for Radiophysics and Electronics of the National Academy of Sciences of Ukraine, 12 Ak. Proskura St., Kharkov, 61085, Ukraine
E-mail: ireburan@yahoo.com

[2]Special Astrophysical Observatory of Russian Academy of Sciencies/NRTT Lab, Polytechnicheskaya 21 off.201, 194021 St.Petersburg, Russia
E-mail: vkhstu@mail.ru

[3]BAE Systems Australia, 40-52 Talavera Road, North Ryde 2113, Australia
E-mail: christophe.granet@baesystems.com

Abstract. In this paper we present a design of highly packed multi-beam receiving array. The requirements to the individual element of antenna array are formulated and the smooth-walled spline-profile horn as the adequate candidate is proposed. The utilization of such array in the RATAN-600 radio telescope will allow for providing the minimum beam spacing about (1.16-1.32) HPBW that is close to the best results in the highly packed multi-beam receiving array.

1. Introduction

In order to expand essentially the field of view and receive both the multi-pixel radio images of some extent of the sky area and a quickly variable cosmic source without mechanical scanning the multi-beam receiving array with tightly packed feed elements is required. With respect to the millimetre wavelenght range the use of the phased focal plane array is not always acceptable due to small aberrations in the case of feed removal from the main mirror focus and the large insertion loss in the radiation forming matrix. Therefore, the non-phased focal receiving feed-array is a more preferable one for the millimetre radio telescopes. Here, the highly sensitive compact receiving module with a cross section less than the horn's cross section follows the each feed of the array [1]. The characteristics and optimization method of highly packed multi-beam receiving array with stripline radiators are considered in [2]. The resonance nature of such radiators allows one to achieve the cross section less than /2 λ thereby realizing densely packed multi-beam receiving array. However, the low radiation efficiency and narrow bandwidth make these radiators undesirable for radio astronomy applications.

In this paper the problems concerning a design of the highly packed multi-beam receiving array are discussed and the preferable single radiator as a feed of tightly packed array of RATAN-600 radio telescope is presented.

2. A Tightly Packed Multi-Beam Receiving Focal Array for the Radio Telescope

As a distinctive feature of the multi-beam receiving array is the ability to form the multi-pixel image in the wide field of view without mechanical scanning and special phasing techniques. A property like that is achieved by means of employing in the modern radio telescopes the low aberration long-focus optics and packing density as much possible (ideal) of the focal array. Under the ideal packed of the multi-beam receiving focal array we understand the satisfaction of the spatial sampling theorem conditions in accordance with the Rayleigh criterion. In this case the neighbouring beams of radio telescope are overlap at the half power level and the distance between the adjacent beams equals to the half power beam width (HPBW). It allows one to create a map of the sky part under investigation without the "holes".

The main limitation of the hight packing density achievement is the impossibility to agree the physical size (diameter) of the primary feed (horn) with the physical size (diameter) of the focal spot (FS). In accordance with the Gaussian beam optics, the intensity of EM field within the limits of FS decreases 2e times (86.5%) at the distance 0 w from the reflector axis thereby determining the effective radius of the FS [3]:

$$\omega_0 = 0.22\,\lambda \frac{f}{D}\sqrt{T_e}$$

where f is the focal length, D is the aperture size, T_e is the edge taper level of the reflector in dB. Than the diameter of FS for $D/f = 0.4$ equal $2w_0 \approx 1.12\ \lambda$.

At the array step $2w_0$ the spacing of beams of the radio telescope is close to be optimal and equal (1.16 -1.32) HPBW depending on the decreasing level of radiation on the aperture edge (-10 ÷ -13*dB*). However, the practically attainable aperture diameter of the efficiency horn is usually larger than 1.12 λ. As a result, the radio telescopes with the most closely packed multi-beam receiving array in the millimetre wavelength range have the spacing of beams (1.8 − 2.8) HPBW [3]. In this case the minimum is usually achieved by meance of the pre-focal quasi-optical focusing. This allows one to optimize the size and shape of the FS.

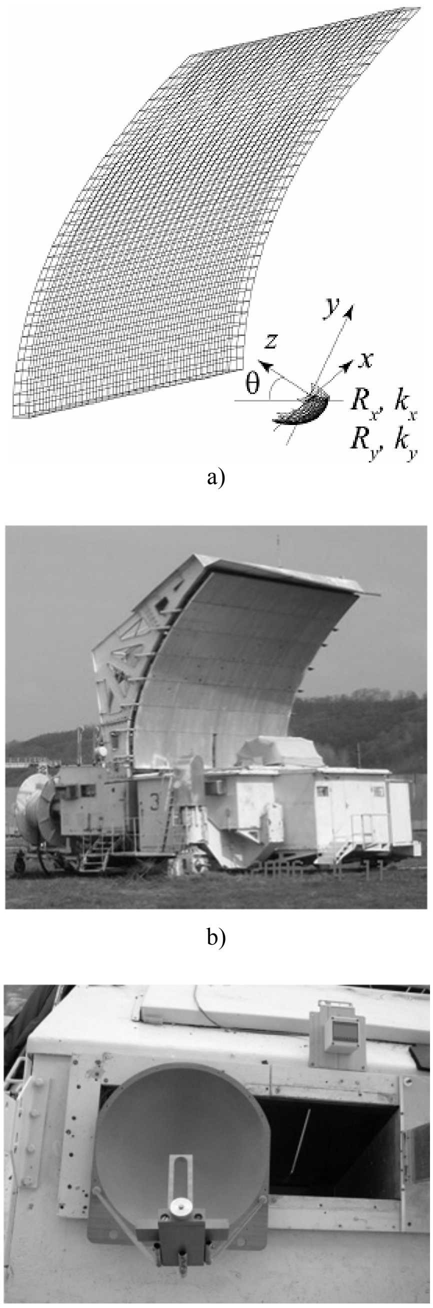

Fig. 1. Model of the secondary and the tertiary mirrors (a), photo of the secondary (b) and the tertiary mirrors (c).

Figure 1. shows a standard focusing optics with the secondary mirror and new tertiary mirror installed in the secondary focus. The tertiary mirror has the non-symmetrical quasi-elliptical form.

The feed of the highly packed multi-beam receiving array has to provide the high aperture efficiency (more than 98%) and to have a reduced aperture cross section to diminish the step of the focal plane array. Therefore, the reasonable compromise between the high aperture efficiency and the acceptable side-lobe level this feed should be found. To this end, the comparative analysis of characteristics of the corrugated horn, the horn with a dielectric filling, and the smooth-walled spline-profile horn has allowed us for choosing the latter as the best feed. By employing the horn optimization method described in [4], the smooth-walled spline-profile horn has been optimized.

The feed prototype consists of the smooth-walled spline-profile horn with a transition from the rectangular waveguide to the circular one. Sixteen individual feeds for the multi-beam focal plane array have been manufactured and tested (Fig. 2). The radiation patterns were measured on the experimental set-up described in [5], while the input reflection coefficient was measured on the Agilent Network Analyzer PNA-L N5230A. By taking into account that the input reflection coefficient and radiation pattern are virtually the same for all sixteen feeds, we show this coefficient (Fig. 3) and readiation pattern (Fig. 4) only for a one of them. The discrepancy of calculated and measured results can be caused by the small dimensional deviations during the manufacturing process. The radiation patterns were measured at 34GHz, 36GHz and 38GHz. As one sees from this picture the radiation pattern is virtually the same in both principal planes. The side-lobe levels are less than -18dB in both planes for all the frequencies and the cross-polarization level is less than -20 dB. The maximum gain is 18dBi at a top of the frequency band.

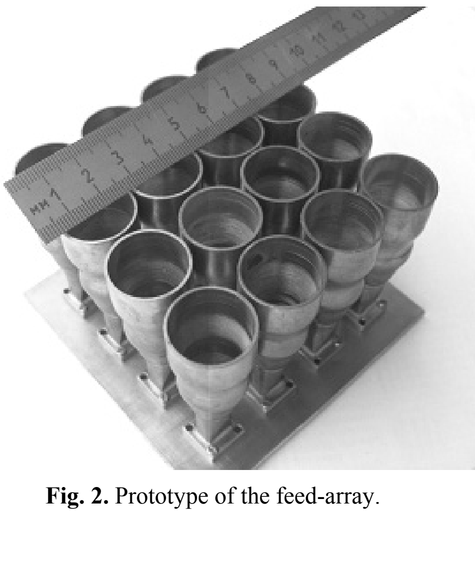

Fig. 2. Prototype of the feed-array.

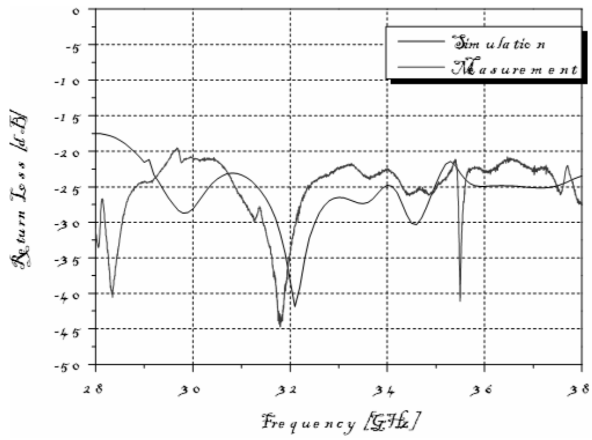

Fig. 3. Simulated and measured input return loss of the smooth-walled spline-profile horn.

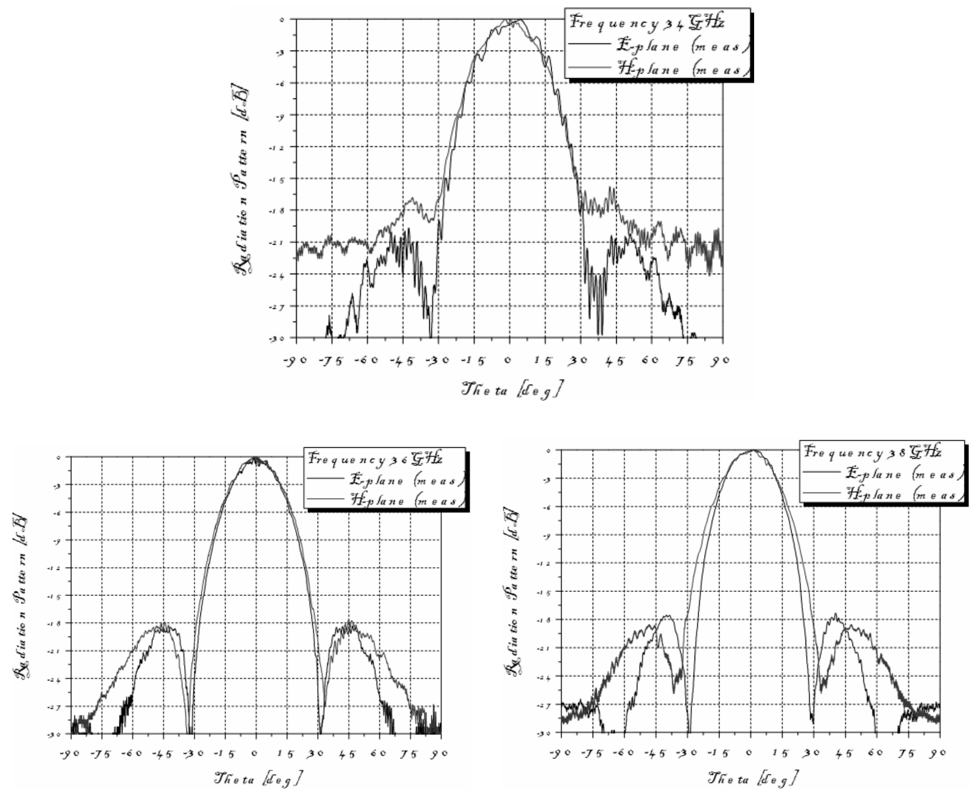

Fig. 4. Measured radiation pattern of the smooth-walled spline-profile horn.

As it follows from simulations, the feed-array composed of such the smooth-walled spline-profile horns will allow one to achieve the beam spacing of the radio telescope RATAN-600 about (1.16 −1.32) *HPBW*. This value is close to the best results in the highly packed multi-beam receiving array without applying the special pre-focal quasi-optics.

3. Conclusion

The features in designing the highly packed multi-beam focal array for RATAN-600 have been examined.

The experimental investigations of the smooth-walled spline-profile horn have shown that the individual radiator design like that meets to stringent requirements to the size and efficiency of the compact radiators from their applications in the highly packed multi-beam focal array located in the tertiary focus of the radio telescope point of view. The measured beamwidth of the optimized smooth-walled spline-profile horn at the level -10dB is less than 45^0 in the H- and E-planes. The side lobe level is less than -18dB in both principal planes and the input reflection coefficient is better than -20dB in the frequency range 30GHz-38GHz. The experimental results are in good agreement with simulated ones in the operational frequency band 34GHz-38GHz. The use of the proposed feed in the RATAN-600 radio telescope will allow for providing the minimum beam spacing about (1.16 − 1.32) *HPBW* and the compact array packaging close to the ideal.

References

[1] V.B. KHAIKIN, V.R. ZAKAMOV, V.I. SHASHKIN, S.E. KUZMIN and V.N. RADZIKHOVSKY, *A wideband receiver-module for passive mm wave imaging array: optimization and test results*, In Proceed. of MSMW, pp. 45–47, Kharkov, Ukraine, June 2010.

[2] E.K. MAJROVA, V.B. KHAIKIN, *Characteristics of radio telescopes with multi-element strip focal arrays*, Izv. VUZov. Radiofizika, v..XLVIII, N2, pp. 245–251, 2005.

[3] P. GOLDSMITH, Quasioptical Systems, IEEE, New York, 1998.

[4] C. GRANET, G.L. JAMES, R. BOLTON and G. MOOREY, *A smooth-walled spline-profile horn as an alternative to the corrugated horn for wideband millimeter-wave applications*, IEEE Trans. Antennas Propag **52** (3), pp. 848–854, 2004.

[5] A.S. ANDRENKO, I.V. IVANCHENKO, D.I. IVANCHENKO, S.Y. KARELIN, A.M. KOROLEV, E.P. LAZ'KO, N.A. POPENKO, *Active Broad X-Band Circular Patch Antenna*, IEEE Antennas and Wireless Propagation Letters **5**, pp. 529–533, 2006.

Compact Planar Dielectric Disk Antennas for X- and KU- Bands

Igor V. IVANCHENKO, Maksym M. KHRUSLOV,
Nina A. POPENKO

Usikov Institute for Radiophysics and Electronics of the National Academy of Sciences of Ukraine, 12 Ac. Proskura st., 61085, Kharkov, Ukraine
e-mail: buran@ire.kharkov.ua

Abstract. The influence of edge effects on the characteristics of the dielectric disk antenna is investigated. The regularity in beamforming is determined depending on the geometrical and electrical parameters of antenna. Two modes of antenna operation are analyzed. It is shown that the antenna can produce both the multi-beam and mono-beam radiation pattern. The number of antenna prototypes overlapping X- and KU bands are manufactured and tested.

1. Introduction

The major disadvantage of microstrip circular disk antennas is their narrow bandwidth. One of the approaches to overcome this problem is replacing the metal patch with a dielectric disk of low-loss, high-dielectric material [1]. It has already been shown that thin-disk dielectric patch antennas may possess radiation characteristics substantially different from those of conventional metal patches [2, 3]. Here, in the strict problem formulation the radiation pattern of such the antenna with an infinite ground plane under resonance conditions is omni-directional in the horizontal plane while in the vertical plane antenna produces no field along zenith direction. However, the experimental investigations point out that in practice the finite ground plane availability is a reason of visible transformations in the radiation pattern shape which became multi-beam one [4]. Nowadays, there is a need and practical interest in designing high efficiency and low cost planar antennas with mono-beam radiation pattern for various RF wireless communication applications at higher frequencies. In this paper, we establish the regularity in correlation of geometrical and electrical parameters of the dielectric disk antenna (DDA) with radiation characteristics to create the compact planar DDA for X- and K_U-bands.

2. Antenna Design

DDA under studying consists of the dielectric disk (0.5mm of thickness) having the relative permittivity ε_d=90 and radius a. The disk of the radius a is located above the grounded substrate with different relative permittivity ε_s and radius R (Fig. 1).

In experiments the axial-symmetrical excitation is realized by a 50-Ohm coaxial feed placed strongly at the antenna center. In accordance with [1, 2] the geometrical and electrical parameters of DDA are chosen to excite the necessary TM mode in the structure. The measurements were carried out on the experimental stands allowing the recording of the near-fields in the inductive region of antenna, as well as radiation patterns and return loss data [5].

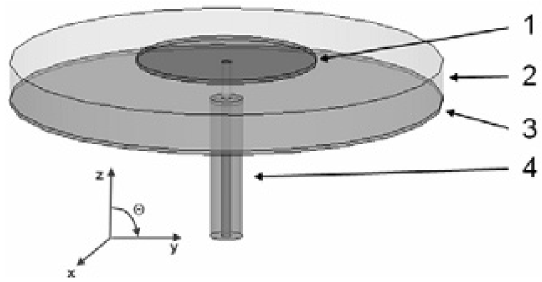

Fig. 1. Schematic view of the DDA: 1 – dielectric disk; 2 – substrate; 3 – ground plane; 4 - coaxial feed.

3. Results and Discussion

In accordance with theoretical calculations [1, 2] the ratio between the dielectric disk radius and substrate height of DDA for the infinite polystyrene substrate (ε_s=2.04) was selected to excite necessary TM modes in the structure. On the basis of experimental results the antenna with substrate radius R=110 mm operates in the multi-frequency mode (Fig. 2a). In particular, the analysis of near-fields in the inductive region of DDA pointed out the two possible modes of antenna operation, namely: (i) the “disk resonator mode” (Fig. 2b) and (ii) the “spatial diffraction lattice mode” (Fig. 2c). As one sees from these pictures, one has the visible field concentration close to the disk surface for the first mode of operation (Fig. 2b). Note that just such complete near-field distributions determine the multi-beam radiation in the far-zone [4].

We have also determined that the substrate size reduction gives rise to reducing the number of lobes, resonance frequencies, and interference circus in the near field. Moreover, the decreasing of power loss in this case leads to the antenna efficiency increasing. At the same time, the antenna bandwidth decreases due to increasing of the working mode Q-factor. The subsequent investigations pointed out the existence of the thresholds in the grounded substrate dimensions corresponding to the transition from the multi-beam radiation pattern to the mono-beam one. For example, the aforementioned transition for antenna under study is observed for the ratio of dielectric disk and grounded substrate radii more than 3.6. The DDA characteristics for R=15mm is shown in Fig. 3.

With the aim to improve the antenna performance, the substrate with low permittivity (ε_s=1.07) has been employed. It has been not a surprise because for such the antenna design the power losses associated with the dielectric substrate modes excitation are minimized. Just the near-field distributions in the inductive region of antennas illustrate the aforementioned statement. The near-field distributions of DDA with a foam substrate are shown in Fig. 4 for different substrate dimensions.

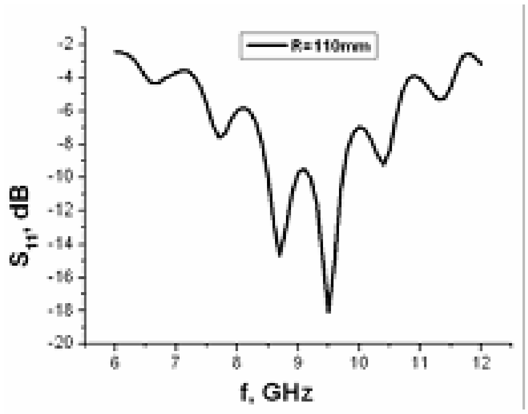

a)

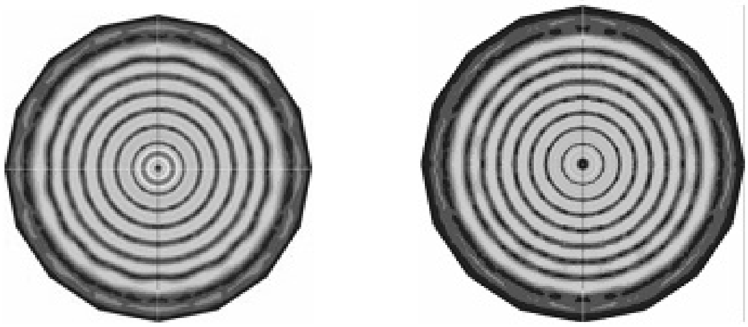

b) c)

Fig. 2. Input return loss (a) and near-fields of DDA with the grounded polystyrene substrate of radius R=110mm and disk radius a=12.5mm at f=8.7GHz (b) and f=9.5GHz (c), respectively.

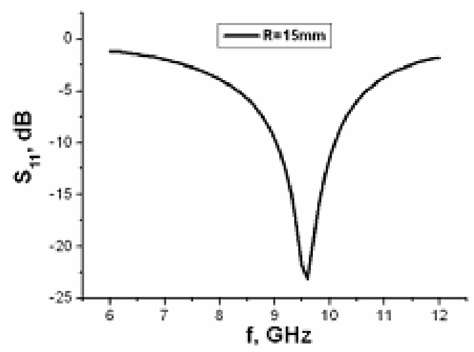

a)

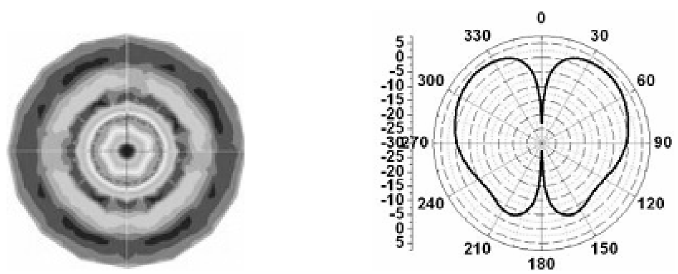

Fig. 3. Input return loss (a), near-field (b), and radiation pattern (c) of the DDA with the grounded polystyrene substrate of radius R=15mm and disk radius a=12.5mm at f=9.6GHz.

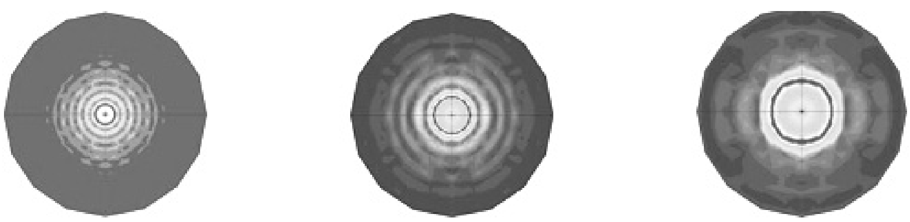

a) b) c)

Fig. 4. Near-field distributions of the DDA with a foam substrate: R=110mm r_d=12.5mm, h=1mm, f=14GHz (a); R=45mm, r_d=12.5mm, h=1.25mm, f=14.5GHz (b); R=15mm, r_d =12.5mm, h=1.25mm, f=14.4GHz (c).

As can be seen from these distributions the antenna operation corresponds to the “disk resonator mode”. By reducing the substrate radius, the number of interference circles decreases and for the DDA with R=15mm the interference picture vanishes virtually. The corresponding radiation patterns are shown in Fig. 5. We can observe the mono-beam radiation pattern in the broadside direction of the DDA and power radiation increasing in the backside direction.

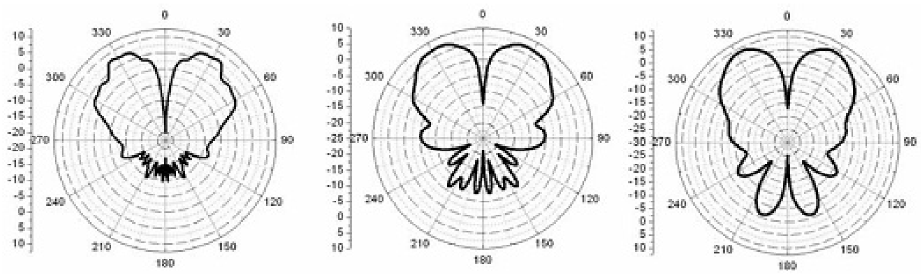

Fig. 5. Radiation patterns of the DDA: R=110mm rd=12.5mm, h=1mm, f=14GHz (a); R=45mm, r_d=12.5mm, h=1.25mm, f=14.5GHz (b); R=15mm, rd=12.5mm, h=1.25mm, f=14.4GHz (c).

As a result of the comprehensive investigations the effect of disk and substrate radii, as well as the substrate height on such antenna characteristics as the resonance frequency, radiation pattern, bandwidth and efficiency has been analyzed. For example, the resonance frequency of the DDA with the fixed grounded substrate size moves toward higher frequencies when reducing the dielectric disk radius (see Fig. 6). In this case, the impedance bandwidth and efficiency of the antenna increases.

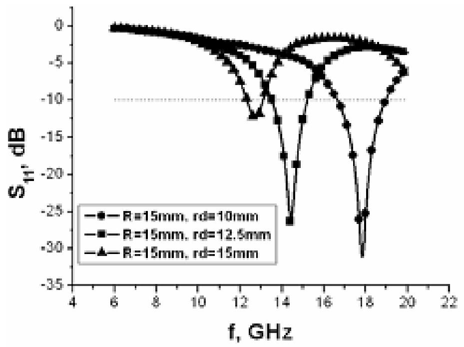

Fig. 6. Input return loss of the DDA versus the dielectric disk radius.

Fig. 7. Antenna prototype.

Based on the results noted above the number of compact antenna prototypes have been manufactured and tested. The measured antenna characteristics are in good agreement with simulations. These antennas demonstrate the mono-beam radiation pattern in the impedance bandwidth and overlap the frequency range 8 – 20GHz. The photo of antenna prototypes is shown in Fig. 7.

4. Conclusions

The finite grounded substrate of dielectric disk antennas with the ratio of dielectric disk and grounded substrate radii more than 3.6 and relative substrate permittivity more than 2 leads to the multi-frequency mode of operation and multi-beam radiation pattern. Based on the analysis of field distributions in the inductive region of antennas under study it has been shown that two types of operation modes with close frequencies called as “disk resonator mode” and “spatial diffraction lattice mode” can be realized. For both cases the spatial field distribution along the grounded substrate radius appears to be similar to the divergent interference circles, but for the “disk resonator mode” the field is concentrated close to the disk surface. The effect of geometrical and electrical parameters of antenna on its characteristics has been analyzed. The compact antenna prototypes producing the mono-beam radiation pattern in the impedance bandwidth no worse than 12% for the frequency range 8 – 20GHz have been manufactured and tested.

References

[1] Y.P. ZHANG, C.W.Y. ANG, C.S.C. LEE and M.A. DO, *Bandwidth Enhancement of a Patch Antenna of Very High-permittivity material*, Microw. Opt. Technol. Lett., **28**, pp. 98–99, 2001.

[2] N. BLIZNYUK and A. NOSICH, *Numerical modeling of axially symmetric dielectric disk antenna excited by veryical electric dipole*, AP2000 Conference Book of Abstracts. Davos, Switzerland, p. 394, 2000.

[3] A. NOSICH and N .BLIZNYUK, *Radiation of axisymmetrically excited resistive and thin-dielectric disk antennas*, Proc. of 16th Intern. Conf. on Applied Electromagnetics and Communications, pp. 247–249, Dubrovnik, Croatia, 1-3 Oct. 2001.

[4] A. ANDRENKO, I. IVANCHENKO, N. POPENKO, M. KHRUSLOV, *Near-field Characterization and Radiation Properties of Circular Dielectric Patch Antennas*, Proc. of 2nd Intern. Conf. on Electromagnetic Near-Field Characterization & Imaging (ICONIC’05), pp. 174–179, Barcelona, Spain, 8-10 June, 2005.

[5] I. IVANCHENKO, D. IVANCHENKO, A. KOROLYUV, N. POPENKO, *Experimental Studies of X-band Leaky-wave Antenna Performances*, Microwave and Optical Technology Letters, **35**, pp. 281–283, Nov. 2002.

Effect of Working Environment on Stiction Mechanisms in Electrostatic RF-MEMS Switches

U. ZAGHLOUL[1,2,3], G. PAPAIOANNOU[1,2, 4], B. BHUSHAN[3],
P. PONS[1,2], F. COCCETTI[1,2,5], R. PLANA[1,2]

[1]CNRS; LAAS; 7 avenue du colonel Roche, F-31077 Toulouse, France
[2]Université de Toulouse; UPS, INSA, INP, ISAE, LAAS, F-31077 Toulouse, France
[3]NLBB Laboratory, The Ohio State University, Columbus, OH 43210, USA
[4]University of Athens, Solid State Physics, Panepistimiopolis Zografos, Athens, Greece
[5]Novamems, 10 av. De l'Europe, F-31520 Toulouse, France

Abstract. In this work, an in depth investigation of the major stiction mechanisms occurring in electrostatic RF-MEMS switches is presented. Stiction is caused by two main mechanisms: dielectric charging and meniscus formation resulting from the adsorbed water film between the switch bridge and the dielectric layer. The effect of each mechanism and their interaction were investigated by measuring the adhesive force under different electrical stress conditions and relative humidity levels. An atomic force microscope (AFM) was used to perform force-distance measurements on the nanoscale. The study provides a comprehensive understanding of the phenomena and highlights the crucial role of the working environment hence of the packaging.

1. Introduction

Among various reported reliability concerns for electrostatic capacitive MEMS switches, the dielectric charging and its resulting stiction is considered the main failure mechanism of these devices [1]. On the other hand, capillary condensation of water vapour results in the formation of meniscus bridges between contacting and near-contacting asperities of two surfaces in close proximity to each other. This leads to an intrinsic attractive force, which may lead to high adhesion and stiction [2]. The meniscus formation is also reported to be highly affected by the electric field [3, 4]. Thus, the applied bias used to actuate MEMS switches and the resulting dielectric charging are expected to affect the meniscus formation at the interface between the switch bridge and the dielectric film. Therefore, the adhesion or stiction between the switch bridge and the dielectric film could be also affected by the meniscus formation. The individual impact of the two different stiction mechanisms (charging induced and meniscus force induced) and their interaction under different electrical stress conditions and relative humidity levels are not understood and have not been studied before. Moreover considering the limitations in the accurate assessment of working environment within packaged RF-MEMS microvolume, (which in worse case scenario may even drift with time), and the impact of environment on the device performances, the relevance of accurate investigation technique is apparent.

In this study a novel characterization technique is presented in order to study different stiction mechanisms which exist in MEMS switches. The proposed methodology makes use of the AFM tip in order to simulate a single asperity contact with the dielectric surface [5, 6]. For the first time the adhesive force measured on the nanoscale under different relative humidity levels and electrical stress conditions is presented. The induced surface potential over the dielectric surface was measured, and used in order to explain the obtained results. Force-distance measurements was performed on the nanoscale and are used to measure the adhesive force. The individual and combined influence of the meniscus force and dielectric charging on adhesive force was studied. This provides an accurate evaluation of the individual effect of each stiction mechanism.

Finally, a correlation between the obtained nanoscale results and the literature reported data from MEMS switches measurements, was performed.

2. Experimental Details

The investigated samples consist of PECVD SiNx films with 300 nm thickness deposited over 500 nm Au layers, which were evaporated over Si substrates (see inset figure in Fig. 1). Since no photolithography steps are required in order to prepare the required samples, the proposed technique provides a low cost and quite fast assessment solution compared to other characterization methods. The adhesion experiments were performed under different relative humidity levels in order to study the effect of meniscus force. For each humidity level, the adhesive force was measured while different bias amplitudes were applied to the Au layer underneath the SiNx film. Due to the dielectric charging, the SiNx film is charged and this results in an induced surface potential over the dielectric film. The applied bias, therefore, corresponds to the voltage used to actuate the MEMS switch and/or the induced surface potential over the dielectric film due to the dielectric charging.

Force-distance measurements were used to measure the adhesive force between the AFM tip and the SiNx film as well as the adsorbed water film thickness over the SiNx surface [2]. An example of the force-distance curve for the investigated samples is presented in Fig. 1.

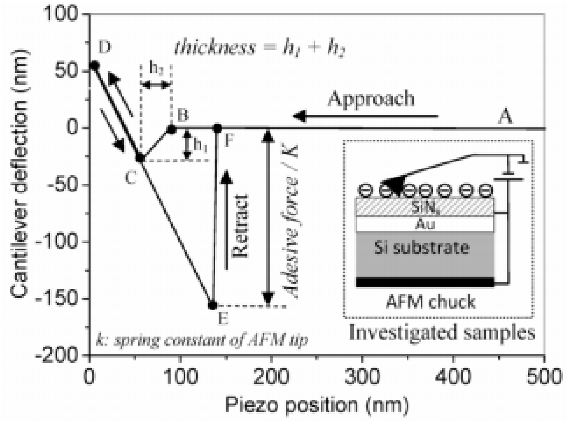

Fig. 1. Force-distance curve for the investigated samples.

The force-distance measurement starts at a large separation (point A) where there is no deflection of the cantilever. As the piezo moves towards the sample, a sudden mechanical instability occurs between point B and point C, and the tip jumps into contact with the adsorbed water film and wicks up around it to form a meniscus. The cantilever bends downwards because of the attractive meniscus force acting on the tip. As the piezo further approaches the SiNx surface, the deflection of the cantilever increases while the tip travels in the water film and eventually contacts the underlying SiNx surface at point C, and then the cantilever starts to bend upwards. Once the piezo reaches the end of its designated ramp size at point D, it is retracted to its starting position. The tip goes beyond zero deflection (point E) and enters the adhesion region. At point E, the elastic force of the cantilever becomes equivalent to the adhesive force, causing the cantilever to snap back to point F. The piezo travel distance used in this study is 500 nm which is comparable to the air gap of MEMS switches.

The adhesive force, which is the force needed to pull the tip away from the sample, can be calculated from the force distance curve by multiplying the vertical distance between E and F with the stiffness of the cantilever as explained in Fig. 1. Also, as the tip travels in the adsorbed water film from point B to C, it is deflected as well. The tip deflection occurs in the same direction as the piezo travels for the AFM used in this study. The water film thickness is therefore the sum of the travel distance of the piezo (h_1), and the deflection of cantilever (h_2) as highlighted in Fig. 1 [2].

3. Results and Discussion

A. Effect of meniscus formation when no-bias is applied

Figure 2 shows that the adhesive force increases considerably when the relative humidity (RH) increases from 1% to only 20%, and the increase tends to saturate at larger RH. The measured thickness of the adsorbed water film over the SiNx surface also increases with humidity as highlighted in the figure. The increase of the water film thickness enhances the meniscus formation, and consequently results in increasing the adhesive force. Though the measured increase in the water film thickness when increasing RH from 1% RH to 80% RH is found to be relatively small, the adhesive force increases considerably. In addition, when the RH increases, the meniscus becomes easier to form and more difficult to rupture [7]. This leads to stronger attractive capillary force between the tip and the sample, and hence larger adhesive force with increasing the RH. The considerable change in the adhesive force when RH increases to only 20% indicates that the SiNx material is very sensitive to any tiny amount of water molecules adsorbed over its surface.

B. Effect of applied bias on adhesive force

The separate and combined effect of the two mentioned stiction mechanisms were studied by using three different groups of samples (A, B, and C). Group A and B were dehydrated just before performing the experiments through two cycles of heating (150 °C) and cooling steps under vacuum.

This removes a considerable amount of the adsorbed water over the dielectric surface. Then, group A was measured under a very low RH level (1%), while group B was stored under high RH (60%) for 60 min, and then was measured under 60% RH. Group C was not dehydrated, and was measured under a low humidity level (1%) similar to group A. The thickness of the adsorbed water layer for group A is therefore smaller than groups B and C. Consequently, the contribution of the meniscus force to the measured adhesive is expected to be much smaller for group A compared to groups B and C. Comparing groups A and B, the influence of the water molecules adsorbed during a time duration of 60 min under high relative humidity (60%) could be assessed. Also, the comparison between groups A and C reveals the influence of the annealing step.

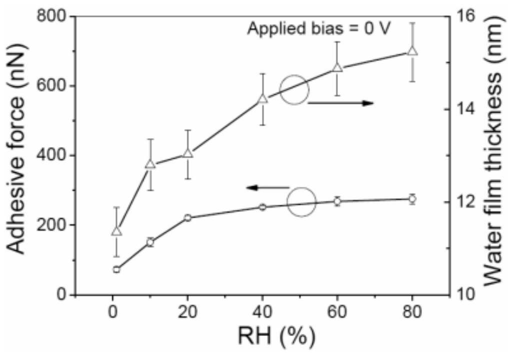

Fig. 2. The influence of the relative humidity on adhesive force and adsorbed water film thickness.

Figure 3 presents the measured adhesive force under different applied bias for the three mentioned sample groups (A, B, and C). For the three groups, the adhesive force is found to increase with the applied bias as shown in Fig. 3a. This increase is attributed to the increase in the attractive electrostatic force between the AFM tip and the SiNx surface as the applied bias increases. In addition, the increase in the adhesive force with bias is found to be very small for group A compared to groups B and C. In these experiments, the adhesive force was measured while the bias is applied between the AFM tip and the sample. So, the SiNx film is charged, and this results in an induced potential over the dielectric surface which reduces the effective applied bias between the AFM tip and the sample. The induced surface potential for the three groups of samples were measured, and the effective applied bias is calculated, and the results are plotted in Fig. 3a.

Figure 3a highlights that for a given applied bias, the effective bias is much smaller for group B compared to group A. Therefore, the electrostatic attractive force for group B is much smaller than group A for all investigated applied bias. In spite of that, the adhesive force measured under different bias for group B is found to be much larger compared to group A. The measured adhesive force as a function of the effective bias is shown in Fig. 3b. It is evident from the figure that at the same effective bias, hence the same electrostatic force, the adhesive force for group B is much larger compared to group A.

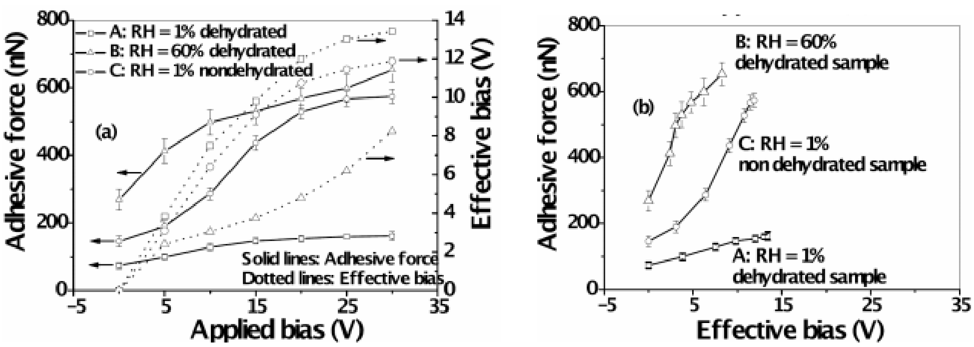

Fig. 3. The impact of applied bias on adhesive force.

Also the increase in the adhesive force with the effective bias is much higher for group B compared to group A. Therefore, the difference in the trend of the adhesive force versus the applied bias between both groups cannot be attributed to the electrostatic attractive force. Additionally, the relatively small difference in the adhesive force between the two groups when no bias is applied clearly indicates that the large difference between both groups at higher bias cannot be explained by the liquid mediated meniscus formation. Since the individual impact of the attractive electrostatic force and the liquid mediated meniscus formation does not explain the high difference in the adhesive force between groups A and B, there must be other adhesion mechanisms.

There are different mechanisms behind the meniscus formation as shown in Fig. 4. When mechanical instability occurs (between points B, C in Fig. 1), the tip jumps into contact with the adsorbed water film and wicks up around it to form a meniscus (Fig. 4a). This is called liquid mediated meniscus. It has been also reported that the adsorbed water film between the AFM tip and the sample surface grows under the influence of the electric field, forming a meniscus that becomes unstable when a critical field is reached [3, 4]. At this point, the meniscus suddenly forms a bridge between the tip and surface as shown in Fig. 4b. This is called a field-induced meniscus. A modeling study shows that the height of the water film under the tip almost doubles upon the formation of the field-induced meniscus [3]. Therefore, the increase in the water film thickness caused by field-induced meniscus is much higher compared to the increase in the water film thickness caused by increasing the relative humidity (see Fig. 2). Also, due to the attraction of water molecules towards the tip under the electric field, the volume of the meniscus surrounding the tip will increase considerably.

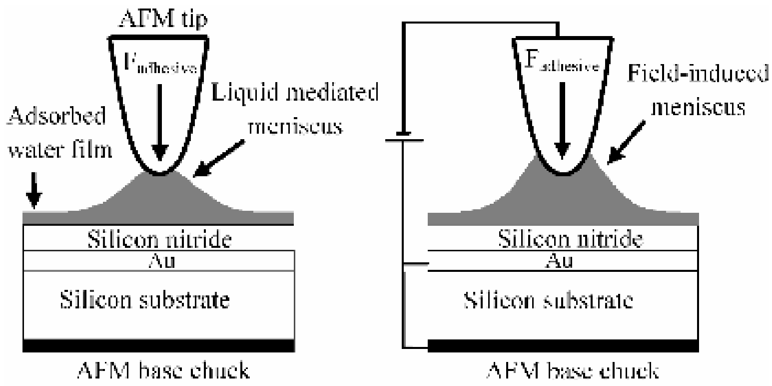

a) b)

Fig. 4. Different mechanisms of meniscus formation between the AFM tip and the sample surface.

This leads to the conclusion that the field-induced meniscus and its resulting considerable increase in the water film volume surrounding the tip will result in increasing the adhesive force between the AFM tip and sample surface considerably. Also, the influence of the field-induced meniscus on the adhesive force is expected to be much higher compared to the liquid mediated meniscus formed when no bias is applied.

The threshold voltage required to induce the formation of water bridges between a metallic tip and a flat metallic sample is given by [4]

$$V_{th} = 3.5D\sqrt{\ln\left(1/RH\right)} \qquad (1)$$

where D is the distance at which the field-induced meniscus forms, and RH is the employed relative humidity. Based on Eq. 1, for a given tip-sample separation, the required threshold field for the formation of water bridges decreases considerably when the relative humidity increases. For example, at 5 nm tip-sample separation, the calculated value of V_{th} for RH of 1% and 60% are found to be 24.7 V and 8.2 V, respectively.

Figure 3b shows that for sample group B the adhesive force increases considerably at relatively small effective bias (around 5 V), and this increase is attributed to the field-induced meniscus formation. The considerable increase in adhesive force indicates obviously that the threshold field required to induce the formation of liquid bridges between AFM tip and the SiNx surface has been reached. This is supported by the small calculated value of the threshold voltage at 60% RH from Eq. 1 which is 8.2 V. In addition, higher RH would lead to a stronger attractive capillary force since the adhesive force becomes longer ranged as explained earlier. According to that, the field-induced meniscus can persist at a longer tip-sample separation before bridge rupture [7]. Therefore the adhesive force measured at 60% RH (group B) will increase considerably by the field-induced meniscus formation. For group A of samples, the maximum effective bias is found to be larger compared to group B as shown in Fig. 5d. In spite of that the increase in the adhesive force with the effective bias for group A is found to be smaller compared to group B. This indicates that for group A the threshold field required for the field-induced meniscus has not been reached by the range of applied bias used in these experiments. Comparing the adhesive force for groups A and B at higher bias, it can be concluded that at higher RH levels the adhesive force resulting from the field-induced meniscus is much higher compared to the adhesive force caused by the attractive electrostatic force and/or the liquid mediated meniscus.

Two categories of capacitive MEMS switches (switch-A and switch-B) are assumed, which employ the sample groups A and B. When no bias is applied and assuming that the surfaces of both the dielectric film and the switch bridge come in contact with each other, the interface will look like Fig. 5a and Fig. 5b for switch-A and switch-B, respectively. The figures shows that the interfaces of both switches have many contacting and near-contacting asperities. Also the liquid mediated meniscus in switch-B is much higher than switch-A.

When bias is applied in order to actuate the switch, field-induced meniscus will be formed in the positions of contacting and near-contacting asperities for switch-B (Fig. 5d). This might also occur in switch-A if the actuation voltage is large enough to reach the threshold voltage (Fig. 5c). Under any condition, the formation of the field-induced meniscus will be much higher in switch-B compared to switch-A, similar to the obtained results for samples B and A. This results in the formation of a water meniscus between the near-contacting asperities in switch-B as shown in Fig. 5d. Also, the volume of liquid mediated meniscus previously formed at the contacting asperities will increase in switch-B. When the applied bias is removed, the adhesive force between the switch bridge and the dielectric layer occurs under the effect of induced surface potential over the dielectric surface. Since the induced surface potential in sample B is much larger compared to sample A (Fig. 2), the enhancement of the field-induced meniscus in switch-B is much larger compared to switch-A. Also, the attractive electrostatic force in switch-B will be much higher compared to switch-A. Based on this analysis, the adhesive force between the switch bridge and the dielectric film will be much larger in switch-B compared to switch-A.

Based on the previous analysis, the adhesion or stiction between the switch bridge and the dielectric will be much faster in switch-B compared to switch-A. This explains why MEMS switches operated at larger RH have shorter lifetimes as reported in [8]. For switch-B, the main mechanism behind the stiction is the field-induced meniscus formation which is enhanced by the dielectric charging phenomenon. For MEMS switch-A, if the induced surface potential reaches the critical threshold, field-induced meniscus will be formed, and the high resulting adhesive force will cause the switch stiction. If the induced surface potential in the long time range does not reach the threshold voltage, the stiction will be caused by the electrostatic attractive force.

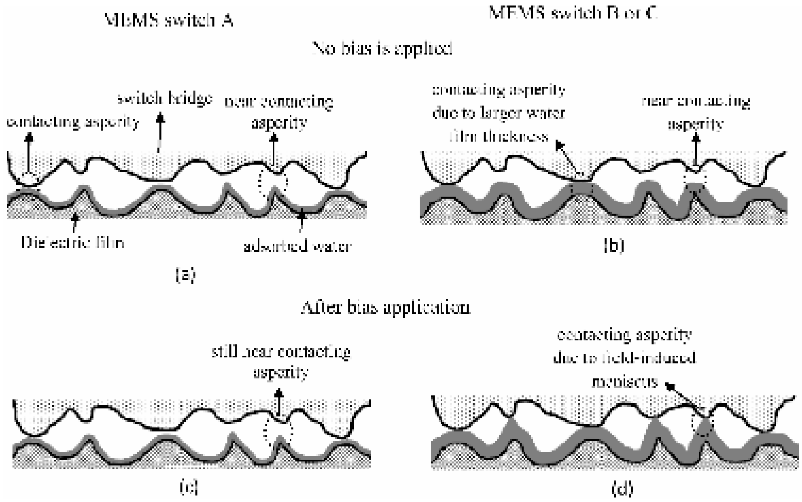

Fig. 5. A cartoon showing the meniscus formation at the interface between the switch bridge and the dielectric film for MEMS switches.

Figure 2 also highlights that the increase in the adhesive force with the applied bias for sample group C is much higher compared to group A. The effective applied bias, hence, the electrostatic force, is relatively smaller for group

C compared to group A. Therefore the higher increase rate of adhesive force with the applied bias for group C compared to group A is attributed to the field-induced meniscus formation. Once again, two types of MEMS switches are assumed, switch-A and switch-C, which resembles the investigated samples A and C, respectively. When bias is applied to actuate switch-C, the volume of the meniscus surrounding the contacting asperities will increase due to the field-induced meniscus formation (Fig. 5d). Also, bridging the near-contacting asperities by water will be further supported by the field-induced meniscus in switch-C. This is because the gap between the near-contacting asperities will be smaller due to the thicker water film in switch-C, and therefore the threshold voltage will be smaller. In other words the field-induced meniscus formation is expected to be much higher in switch-C compared to switch-A. Based on this analysis the stiction between the switch bridge and the dielectric film for switch-C will be much faster compared to switch-A. This explains why annealing MEMS switches increases the device lifetime as reported in [1].

4. Conclusion

The individual impact of the charging induced stiction and meniscus induced stiction in electrostatic capacitive RF-MEMS switches is presented. Also, the interaction between both stiction mechanisms was investigated. The adhesive force resulting from the field-induced meniscus is found to be a dominant stiction mechanism. The adhesive force induced by meniscus formation due to the adsorbed water layer is found to be relatively small when the dielectric layer is not electrically stressed. When bias is applied, the adhesive force increases considerably for dielectric films which have not been annealed even after being measured at a very low humidity level, due to the field-induced meniscus. For the annealed samples, the contribution of the field-induced meniscus is found to be very high when the sample is stored under larger relative humidity for a short time. The nanoscale characterization performed in this study explains well the crucial role of a controlled MEMS packaged environment to control and minimize relative humidity and enhance lifetimes. Also, it explains why annealing MEMS switches increases the device lifetime.

References

[1] P. CZARNECKI, X. ROTTENBERG, P. SOUSSAN, P. EKKELS, P. MULLER, P. NOLMANS, W. DE RAEDT, H. TILMANS, R. PUERS and L. MARCHAND, *Effect of substrate charging on the reliability of capacitive RF MEMS switches*, Sens. Actuator A-Phys. **154**, pp. 261–268, 2009.

[2] B. BHUSHAN, *Nanotribology and Nanomechanics*, An Introduction, third edition, Springer-Verlag, Heidelberg, Germany, 2011.

[3] S. GÓMEZ-MONIVAS, J.J. SÁENZ, M. CALLEJA and R. GARCIA, *Field-induced formation of nanometer-sized water bridges*, Phys. Rev. Lett. **91**, 056101, 2003.

[4] G. SACHA, A. VERDAGUER and M. SALMERON, *Induced water condensation and bridge Formation by electric fields in Atomic Force Microscopy*, J. Phys. Chem. B, **110**, pp. 14870–14873, 2006.

[5] U. ZAGHLOUL, G.J. PAPAIOANNOU, F. COCCETTI, P. PONS and R. PLANA, (2010a), *A systematic reliability investigation of the dielectric charging process in electrostatically actuated MEMS based on Kelvin probe force microscopy*, J. Micromech. Microeng. **20**, Art.# 064016, 2010.

[6] U. ZAGHLOUL, G.J. PAPAIOANNOU, H. WANG, B. BHUSHAN, F. COCCETTI, P. PONS and R. PLANA, (2011b), *Nanoscale characterization of the dielectric charging phenomenon in PECVD silicon nitride thin films with various interfacial structures based on Kelvin probe force microscopy*, Nanotechnology , "in press", 2011.

[7] M. YUMEI, X. ZHANG, W. WANG, *Capillary liquid bridges in atomic force microscopy: Formation, rupture, and hysteresis*, J. Chem. Phys. **131**, 184702, 2009.

[8] W. van SPENGEN, P. CZARNECKI, R. POETS, J. van BEEK and I. De WOLF, *The influence of the package environment on the functioning and reliability of RF-MEMS switches*, Proc IEEE Int. Reliability Physics Symposium, pp. 337–341, IEEE, New York, 2005.

The Discharge Current Through the Dielectric Film in MEMS Capacitive Switches

M. KOUTEOURELI, L. MICHALAS, G. PAPAIOANNOU

Solid State Physics Section, Physics Dpt. National and Kapodistrian University of Athens
Athens, Greece
E-mail: mkoutsoureli@phys.uoa.gr

Abstract. A new method to determine the bulk discharge current in the dielectric film of MEMS capacitive switches is presented. The method is based on the elementary theory of the discharge process in dielectric materials and the physical model of MEMS capacitive switches with non uniform trapped charge and air gap distributions. The shift of the bias for the minimum of the pull-up capacitance allows the calculation of current densities in the order of picoAmpere per unit area. Assessment of switches with silicon nitride dielectric film shows that the discharge current transient obeys the stretched exponential law. Finally the proposed method is applied to assess the discharge of electrical stressed devices.

Key words: MEMS capacitive switch, dielectric charging, lifetime, reliability.

1. Introduction

Capacitive RF MEMS switches although are very promising components for radio frequency applications their commercialization is still hindered by reliability problems. The key issue problem in these electrostatically actuated devices is the dielectric charging because it causes erratic device behavior and limits the device lifetime [1–3]. So far the dielectric charging of MEMS switches has been investigated by recording the shift of pull-in and pull-out voltages as a function of electrical stress conditions [1], [4-7] or the shift of the bias for the pull-up capacitance minimum [8]. In order to obtain a better understanding of the charging processes the electrical properties of the dielectric films have been investigated with the aid of MIM capacitors [9-11], which although cannot simulate the charging through roughness and asperities can provide the same information when the decay of top electrode potential is monitored [12]. Finally, the assessment of both MIMs and MEMS [13] revealed that the shift of bias for minimum capacitance is thermally activated.

Recently the Kelvin Probe Force Microscopy (KPFM) method [14-16] has been employed to investigate the dielectric charging. This method allowed the monitoring of surface charge dissipation when injection occurs through a single asperity, simulated by AFM tip, or over a large area when charging occurs through the contacting armature. The method also allowed the determination of the influence of ambient on the discharge process [15, 16].

The lifetime of a MEMS capacitive switch is determined by the rates of injected charges during the pull-down state and the collected, by the bottom electrode, charges during the pull-up state. The charge decay rate, which is related to the current paths in the bulk of dielectric film, has been attempted to be determined by monitoring the discharge current in MIM capacitors. As shown in [17], in MIM capacitors the discharge current in the external circuit measured with thermally stimulated depolarization current (TSDC) method and in earlier papers with the discharge current transients (DCT) method [11] arises from collection of charges located in the vicinity of the injecting electrodes. Taking into account the recovery time of a charged MEMS capacitive switch we are easily led to the conclusion that the discharge current of a MIM capacitor measured in external circuit is several orders of magnitude larger than the current through the bulk material. Here it must be pointed out that recently has been attempted to measure the discharge current in MEMS capacitive switches [18]. In this experiment the duration of the current transient was limited to about 150 sec thus providing little information on those parameters that determine the switch lifetime.

The aim of the present work is to demonstrate a new method that allows the determination of the discharge current in MEMS capacitive switches. Transients with duration in excess of 103 sec have been monitored and current densities of the order of pico Ampere per unit area or even less have been calculated. The method takes into account the model of a real MEMS switch with non uniform trapped charge and air gap distributions [19]. The rate of the shift of bias for minimum pull-up capacitance and the dielectric film thickness allow the calculation of the discharge current. The discharge current, determined by mechanisms such as hopping, percolation etc, which are expected in an amorphous and disordered dielectric, provides valuable information that can be used for further optimization and/or engineering of the dielectric material.

2. Theoretical Background

The dielectric charging/polarization in an insulating film arises from charges, injected through surface roughness and asperities, and/or redistributed throughout the dielectric material, the orientation of dipoles and presence of charges at the dielectric interface [21]. In the case of a MEMS capacitor the depolarization process will induce a discharge current density transient through the dielectric film that is given by:

$$.J_{dis}(t) = -\frac{d}{dt}\psi(t) \quad (1)$$

where ψ(t) is the surface charge density.

In order to calculate the switch discharge current transient, the present work device model adopts both the model proposed in [19]. For this we consider the setup in Fig. 1 that includes a fixed nonflat metal plate of area A which is covered with a dielectric layer of uniform thickness d_ε, dielectric constant ε_r, and volume charge density, $\rho(x, y, z)$. Above it a rigid but nonflat movable metal plate is fastened with a linear spring k to a fixed wall above the dielectric layer at a rest position $d_0(x, y)$.

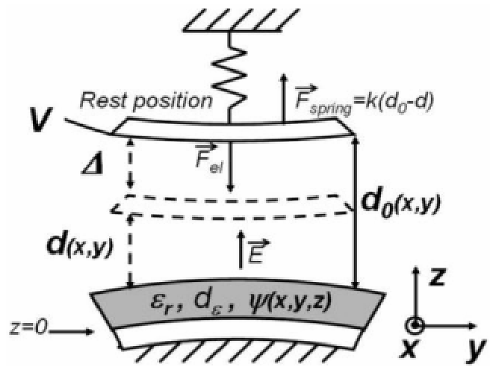

Fig. 1. Model of a capacitive switch with non uniform trapped charge and air gap distributions [12].

A dc bias source of amplitude V is applied to the two plates. Following the procedure analyzed in [19] we find that the electrostatic force F_{el} can be written in a compact form of

$$F_{el}(\Delta) = \frac{A}{2\varepsilon_0}\left[\left(V\mu_\alpha - \mu_\beta\right)^2 + V^2\sigma_\alpha^2 + \sigma_\beta^2 - 2V\,\mathrm{cov}_{(\alpha,\beta)}\right] \quad (2)$$

where μ, σ_2, and cov denote the mean, variance, and covariance, respectively, of the α(x, y, Δ) and charge β(x, y, Δ) distributions:

$$\alpha(\alpha, y, \Delta) = \frac{\varepsilon_0}{\left[d_0(x,y) - \Delta\right] - \frac{d_\varepsilon}{\varepsilon_r}} \quad (3)$$

which is the distribution of capacitance per unite area and

$$\beta(x, y, \Delta) = \frac{d_\varepsilon}{\varepsilon_r\,\varepsilon_0} \cdot \psi_{eq}(x,y) \cdot \alpha(x,y) \quad (4)$$

the distribution of charge density induced at armature area and $\psi_{eq}(x, y)$ and Δ are the equivalent surface charge distribution and the displacement from equilibrium respectively. At equilibrium positions the system is determined by equating the electrostatic and spring forces that reduce to

$$\frac{2\varepsilon_0 k \Delta}{A} = \left(V\mu_\alpha - \mu_\beta\right)^2 + V^2\sigma_\beta^2 - 2V\,\mathrm{cov}_{(\alpha,\beta)} \tag{5}$$

Depending on the adopted device model the above equations can lead to different level complexity approaching in an improved manner the behavior of real MEMS switch. In the general case of distributed equivalent charge [$\psi(x, y, z)$], and air gap [$d_0(x, y)$, (2) cannot be simplified. The bias at which the capacitance in the up state attains minimum (V_m), for which the electrostatic force becomes minimum independently of the charge and air gap distributions is given by

$$V_m = \frac{\mu_\alpha\,\mu_\beta\,\mathrm{cov}_{(\alpha,\beta)}}{\mu_\alpha^2 + \sigma_\alpha^2} \tag{6}$$

which can be further written as:

$$V_m = \frac{1}{1+\left(\sigma_\alpha \big/ \mu_\alpha\right)^2}\cdot\left(\frac{\mu_\beta}{\mu_\alpha} + \frac{\mathrm{cov}_{(\alpha,\beta)}}{\mu_\alpha^2}\right) \tag{7}$$

According to this the shift of the bias for capacitance minimum consists of two components, the one arising from the net surface charge and the other from the covariance of the capacitance and charge distribution. Since the covariance depends on the magnitude of the capacitance and charge variances, the contribution of $\mathrm{cov}_{(\alpha,\beta)}$ can be mitigated by properly choosing a switch where $\left(\sigma_\alpha \big/ \mu_\alpha \ll 1\right)$ the discharge current density, will be given by:

$$J_{disch}(t) = -\frac{\overline{d\psi_{eq}}(t)}{dt} = -\frac{\varepsilon_r\,\varepsilon_0}{d_\varepsilon}\cdot\frac{dV_m(t)}{dt} \tag{8}$$

where is the mean value of equivalent surface charge density.

Here it must be pointed out that (8) describes the average net charge discharge current density. Therefore in a switch where the net charge is zero Eq. 8 will lead to a zero current and only the nanoscale assessment with KPFM method can be used to obtain information on the surface potential decay only and not on the discharge current in the bulk dielectric.

3. Experimental

The switches utilized in the present work were fabricated with a standard photolithographic process on high resistivity silicon wafers on top of which SiO_2 film was deposited. The dielectric film is PECVD Si_3N_4 deposited at 300°C. Switches with 250 nm dielectric were fabricated. The membrane is an evaporated titanium-gold seed layer electroplated to a thickness of 2μm. Under no applied force, the membrane is normally suspended about 2.5μm above the dielectric. The sacrificial layer was removed with resist stripper and the switches were dried using a critical point dryer. The active area of the switches was about 2.5×10^{-5} cm^2.

The pull-up capacitance voltage (C-V) characteristics were monitored with a Boonton 72B capacitance meter while sweeping the voltage in 50 mV. The pull-in voltage was 25V and each switch was stressed at 30V and 40V before assessment. In all cases the discharge process was monitored for 14000 sec. The bias for pull-up state capacitance minimum was determined by fitting a parabola to the experimental data. This allowed also the determination of the magnitude of the capacitance minimum. Finally, in the present work for the sake of simplicity it was assumed that the capacitance variance is very small so that to satisfy the conditions to apply Eq.8. A switch complying to this condition can be selected with the aid of *i.e.* an optical profilometer or can be properly designed.

4. Results and Discussion

Figure 2 shows the evolution of the capacitance-voltage characteristic in the pull-up state of a switch stressed at 30 Volt for 5 min. In all devices and for all stress conditions the bias for capacitance minimum (V_m) was found to decrease with time and simultaneously the capacitance minimum (C_m) to decrease too. Since the stress was unipolar, the increase of capacitance minimum after stress can be attributed to non uniform charging [14] and creep.

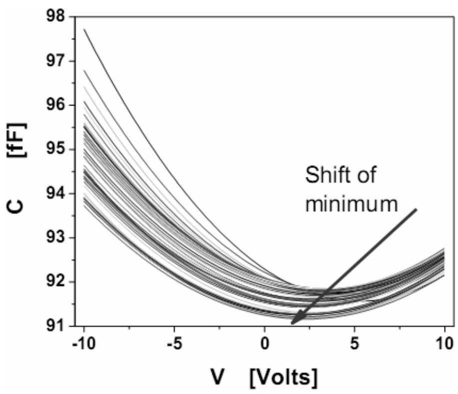

Fig. 2. Evolution of pull-up state capacitance-voltage characteristic of a switch stressed for 5 min at 30V.

Here it must be emphasized that Eq. 8 can be applied, even in the presence of non uniform charge distribution, as long as the capacitance variance is low, as assumed for the sake of simplicity in the present work.

The transient of bias for capacitance minimum, for a switch subjected to stress at 30V for 5 min, is presented in Fig. 3. The variation of V_m with time clearly reveals the presence of a very long time discharge mechanism with a characteristic time much larger than the time window of observation (14000 sec) used in the present experiment. This is the reason the value of V_m still remains large beyond 10 sec (fig. 3). Furthermore, taking into account that the dielectric film is amorphous silicon nitride we expect that the decay of the charge, which may arise from dipole orientation and space charge polarization, will obey the stretched exponential law.

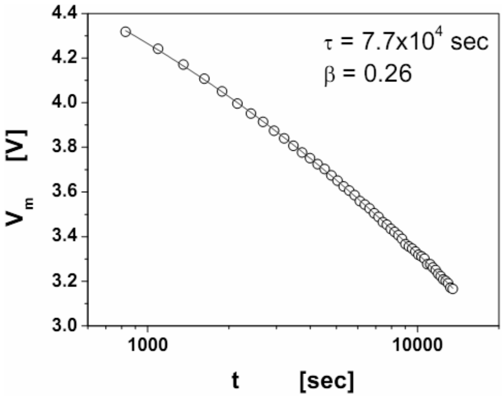

Fig. 3. Bias for capacitance minimum (V_m) transient for a switch stressed for 5 min at 30V.

The fitting revealed a time constant of 7.7×10^4 sec and a value for stretch factor of 0.26, indicating a long discharge time and a complex process.

$$V_m(t) = V_0 \cdot \exp\left[-\left(\frac{t}{\tau}\right)^{\beta}\right] \tag{9}$$

The discharge current transient, calculated form (8) by derivation of (9), is presented in Fig. 4. According to this the discharge current will be given by:

$$J_{disch}(t) = \overline{\psi_0} \cdot \frac{\beta}{\tau} \cdot \left(\frac{t}{\tau}\right)^{\beta-1} \cdot \exp\left[-\left(\frac{t}{\tau}\right)^{\beta}\right] \tag{10}$$

where $\overline{\psi_0} = \frac{\varepsilon_r\,\varepsilon_0}{d_\varepsilon} \cdot V_0$

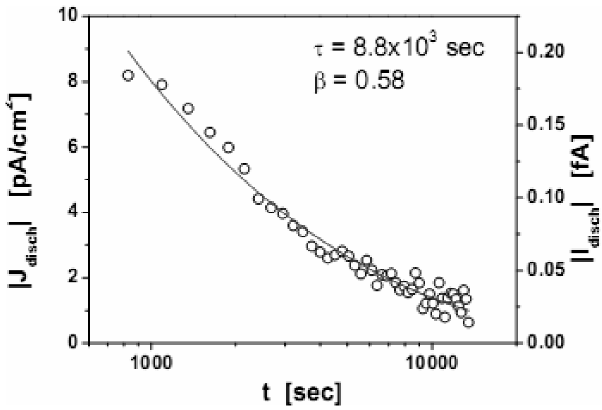

Fig. 4. Calculated discharge current transient for a switch stressed for 5 min at 30V.

The fact that both decays obey the stretched exponential law is not surprising because the same behavior has been observed in the discharge current transient of MIM capacitors and dielectric films assessed with KPFM methods [12]. A close examination of the discharge current reveals the time constant is shorter and the stretch factor larger than the ones determined from V_m decay. The differences must be attributed to the fact that V_m is determined from the contribution from all present charging mechanisms, several of which persisting beyond the time window of the present experiment (see Fig. 3). On the other hand the discharge current is practically determined by the mechanism which dominates the discharge process in the time window of the experiment. Obviously the use of longer time window of observation will provide more information.

The increase of stress conditions, bias of 40 Volt for 15 min, affects both the discharge current and the decay characteristic time constant due to larger amount of injected charge and different occupancy of trapping centres. The decrease of stretch factor with the electric field intensity increasing has been also observed in the discharge current transients in MIM capacitors [15, 20].

5. Conclusion

A new method to calculate the long term discharge current in the bulk of the dielectric film of RF MEMS capacitive switches is presented for first time. The applied method takes into account the constrains of a real MEMS switch with non uniform trapped charge and air gap distributions. The rate of the shift of bias for minimum capacitance in the pull-up state and the dielectric film thickness are used to determine the discharge current. The discharge current has been found to lie in the range of pico Amperes per unit area, a much lower value with respect to any reported one. Such a low current level seems plausible if we take into account the long discharge time of heavily charged MEMS switches. On the other hand these low current levels can be easily attributed to mechanisms such as hopping, percolation etc, which can be expected to occur in amorphous and disordered dielectrics under the presence of intrinsic and gradually vanishing electric fields. Here it is essential to emphasize that the knowledge of the magnitude and time dependence of the bulk discharge current provides valuable information that can provide feedback on the further optimization and/or engineering of the MEMS dielectric films.

Acknowledgment. The authors would like to acknowledge the support from ESA projects AO/1-5288/06/NL/GLC and AO/1-5851/08/NL/NA as well as by ENIAC-2010 NANOCOM project.

References

[1] C.L. GOLDSMITH, J. EHMKE, A. MALCZEWSKI, B. PILLANS, S. ESHELMAN, Z. YAO, J. BRANK AND M. EBERLY, *Lifetime Characterization of Capacitive RF MEMS Switches*, IEEE MTT-S Int. Microwave Symp. Digest, pp. 227–230, 2001.

[2] J. WIBBELER, G. PFEIFER and M. HIETSCHOLD, *Parasitic charging of dielectric surfaces in capacitive microelectromechanical systems (MEMS), Sensors and Actuators*, SensorsActuators, **A 71**, pp. 74–80, 1998.

[3] G.M. REBEIZ, *RF MEMS Theory, Design and Technology*, Haboken, (New Jersey 2003), J. Willey and Sons.

[4] S. MELLE, D. De CONTO, L. MAZENQ, D. DUBUC, B. POUSSARD, C. BORDAS, K. GRENIER, L. BARY, O. VENDIER, J.L. MURARO, J.L. CAZAUX, R. PLANA, *Reliability Modeling of Capacitive RF MEMS, IEEE Tans. on Microwave Theory and Techniques*, Microelectronics Reliability, **45**(9-11), pp. 1770–5, 2005.

[5] W. Merlijn van SPENGEN, Robert PUERS, Robert MERTENS and Ingrid de WOLF, *A comprehensive model to predict the charging and reliability of capacitive RF MEMS switches*, J. Micromech. Microeng., **14**, pp. 514–521, 2004.

[6] Z. PENG, X. YUAN, J.C.M. HWANG, D.I. FOREHAND and C.L. GOLDSMITH, *Dielectric Charging of RF MEMS Capacitive Switches under Bipolar Control-Voltage Waveforms*, International Microwave Symposium, pp. 1817–1820, 2007.

[7] D. MARDIVIRIN, D. BOUYGE, A. CRUNTEANU, A. POTHIER, P. BLONDY, *Study of Residuel Charging in Dielectric Less Capacitive MEMS Swithes*, International Microwave Symposium, pp. 33–36, 2008.

[8] R.W. HERFST, H.G.A. HUIZING, P.G. STEENEKEN and J. SCHMITZ, *Time and voltage dependence of dielectric charging in RF MEMS capacitive switches*, IEEE 45th Annual International Reliability Physics Symposium, pp. 417–420, 2007.

[9] X. YUAN, J.C.M. HWANG, DA. FOREHAND and C.L. GOLDSMITH, *Modeling and Characterization of Dielectric-Charging Effects in RF MEMS Capacitive Switches*, International Microwave Symposium, pp. 753–756, 2005.

[10] E. PAPANDREOU, M. LAMHAMDI, C.M. SKOULIKIDOU, P. PONS, G. PAPAIOANNOU and R. PLANA, *Structure dependent charging process in RF MEMS capacitive switches*, Microelectronics Reliability **47**, pp. 1812–1817, 2007.

[11] M. LAMHAMDI, P. PONS, U. ZAGHLOUL, L. BOUDOU, F. COCCETTI, J. UASTAVINO, Y. SEGUI, G. PAPAIOANNOU, R. PLANA, *Voltage and temperature effect on dielectric charging for RF-MEMS capacitive switches reliability investigation*, Microelectronics Reliability, **48**(8-9), pp. 1248–1252, 2008.

[12] U. ZAGHLOUL, M. KOUTSOURELI, H. WANG, F. COCCETTI, G. PAPAIOANNOU, P. PONS, R. PLANA, *Assessment of dielectric charging in electrostatically driven MEMS devices: A comparison of available characterization techniques*, Microelectronics Reliability, **50**, pp. 1615–1620, 2010.

[13] G. PAPAIOANNOU, J. PAPAPOLYMEROU, P. PONS and R. PLANA, *Dielectric charging in radio frequency microelectromechanical system capacitive switches: A study of material properties and device performance*, Applied Physics Letters **90**, pp. 233–507, 2007.

[14] R.W. HERFST, P.G. STEENEKEN, J. SCHMITZ, A.J.G. MANK and M. van GILS, *Kelvin probe study of laterally inhomogeneous dielectric charging and charge diffusion in RF MEMS capacitive switches*, 46th Annual International Reliability Physics Symposium, Phoenix, pp. 492–495, 2008.

[15] U. ZAGHLOUL, F. COCCETTI, G. PAPAIOANNOU, P. PONS, R. PLANA, *A novel low cost failure analysis technique for dielectric charging problem in electrostatically actuated MEMS devices*, IEEE International Reliability Physics Symposium (IRPS), pp. 237–245, Anaheim, USA, 2010.

[16] U. ZAGHLOUL, B. BHUSHAN, P. PONS, G.J. PAPAIOANNOU, F. COCCETTI and R. PLANA, *On the influence of environment gases, relative humidity and gas purification on dielectric charging/discharging processes in electrostatically driven MEMS/NEMS devices*, Nanotechnology **22**, pp. 035–705, 2011.

[17] M. KOUTSOURELI, L. MICHALAS and G. PAPAIOANNOU, *The Effect of Temperature on Dielectric Charging of Capacitive MEMS*, 2011 IEEE International Reliability Physics Symposium (IRPS), Monterey CA USA, 2011.

[18] D. MOLINERO and L. CASTANER, *Modeling and measuring transient discharge current of microelectromechanical switches after dielectric charging by voltage stress*, Appled Physics Letters **94**, pp. 043503, 2010.

[19] X. ROTTENBERG, I. De WOLF, B.K.J.C. NAUWELAERS, W. De RAEDT and H.A.C. TILMANS, *Analytical Model of the DC Actuation of Electrostatic MEMS Devices With Distributed Dielectric Charging and Nonplanar Electrodes*, J. of Microelectromechanical Systems, **16**(5), pp. 1243–1253, 2007.

[20] U. ZAGHLOUL, G. PAPAIOANNOU, F. COCCETTI, P. PONS, R. PLANA, *Dielectric charging in silicon nitride films for MEMS capacitive switches: Effect of film thickness and deposition conditions*, Microelectronics Reliability, **49**, pp. 1309–1314, 2009.

[21] J. VANDERSHUEREN and J. CASIOT, *Thermally stimulated relaxation in solids*, P. Braunlich (Ed.) Topics in Applied Physics **37**(ch. 4), pp. 135–223, Springer-Verlag, Berlin, 1979.